Alma Mater Studiorum – Università degli Studi di Bologna

DOTTORATO DI RICERCA IN GEOFISICA – GEO/10

XXIV CICLO

SEA LEVEL VARIATIONS FROM DECADES TO MILLENNIA: A FEW CASE STUDIES

Settore Concorsuale di afferenza: 04/04

Presentata da:

GABRIELLA RUGGIERI

Relatore:
Chiar.mo Prof.

GIORGIO SPADA

Esame finale anno 2012

Contents

Preface

The study of Glacial Isostatic Adjustment (GIA) is gaining a central issue in the sea level change community. The main goals of this Ph.D. study are to investigate the regional and global geophysical components related to present polar ice melting and to provide independent cross validation checks of GIA models using both geophysical data detected by satellite mission, and geological observations from far field sites, in order to determine a lower and upper bound of uncertainty of GIA effect.

The present Thesis was partially supported by funding to the *ice2sea* programme from European Union 7th Framework Programme, grant number 226375, by COST Action ES0701 *Improved constraints on models of Glacial Isostatic Adjustment*, and by the University of Urbino. The subject of this Thesis is the sea level change from decades to millennia scale. Some key findings concerning the causes of sea level change and the associated instruments to detect this variations ranging from remote sensing to geological observations are presented in Chapter 1. Within *ice2sea* collaboration, we developed a Fortran numerical code to analyze the local short-term sea level change and vertical deformation (Chapter 4) resulting from the loss of ice mass. This method is used to investigate polar regions, Greenland and Antarctica (Chapter 4). With regard to Greenland Ice Sheet we have studied the geophysical consequences of a new mass balance derived from repeated surface elevation measurements from NASA's ice cloud and land elevation satellite (ICESat) for the time period between 2003 and 2008. With regard to Antarctica we have simulate the loss of ice mass through a plausible mass balance model. In both case studies, we investigated the vertical uplift and subsidence, geoid height variations, global patterns of sea–level change (or fingerprints), and regional sea–level variations along the coasts of polar regions. Long–wavelength uplifts and gravity variations in response to past ice thickness variations are obtained solving the Sea Level Equation, which accounts for both the elastic and the visco–elastic components of deformation. To capture the short–wavelength components of vertical uplift in response

to current ice mass loss, which is not resolved by satellite gravity observations, we have specifically developed a high–resolution regional elastic rebound model. The elastic component of vertical uplift is combined with estimates of the visco–elastic displacement fields associated with the process of Glacial–isostatic adjustment (GIA), according to a set of published ice chronologies and associated mantle rheological profiles. We related the combined feature of GIA and present ice melting to the vertical velocity recorded by Global Positioning System (GPS) placed along the coasts of polar regions. Most of the satellite missions (e.g. GRACE and ICESat) are sensitive to GIA effect. This is due to the fact that, while the GRACE mission is able to accurately detect large scale changes in mass over the polar continents, the technique itself is not able to distinguish between mass change due to GIA and that due to ongoing ice loss or gain. Gravity field variations are often estimated neglecting rheological effects and thus assuming a fully elastic response of the Earth. In Chapter 3, we aimed to describe the ongoing surface movements resulting from recent glacial instabilities, also taking into account the effects associated with crustal and upper mantle rheologies. In order to model the geophysical response to recent melting of polar continents, we evaluated the vertical deformation related to a small scale surface loads, considering the following earth models: elastic model, Maxwell model, Burger model and Caputo model. These latter allow to analyze the transient behaviour of crust resposnse to a load at century and decade time scales. In addition we introduce a low viscosity zone within the upper mantle and within the lithosphere. This was first motivated by geophysical evidence indicating a significant rheological stratification of the lithosphere and by seismic data suggesting the existence of a low velocity zone except beneath cold cratonic areas. All the computations are performed using ALMA program that provides the vertical and horizontal displacements to study the response of the Earth to finite-sized surface loads or more complex loading function.

The coastal areas are affected by the long wavelength component of GIA process. Hence understanding the response of the Earth to loading is crucial in various contexts, ranging from the interpretation of modern satellite geodetic measurements (e. g. GRACE and GOCE) to the projections of future sea level trends in response to climate change. Based on the hypothesis that Earth mantle materials obey to a linear rheology, and that the physical parameters of this rheology can be only characterized by their depth dependence, in the last two Chapters we investigate the Glacial Isostatic Effect upon the

far field sites of Mediterranean area using an improved SELEN program (3.2 version).

We investigated (Chapter 5) the RSL for the last 2000 years along the coast of central Italy. The rate of sea level change during the last 2000 years is a major scientific challenge nowadays. Precise determination of sea level rise along the study area improves our understanding on the secular, instrumentally observed, variations across the Mediterranean. We presented new and revised observations for archaeological fish tanks located along the Tyrrhenian and Adriatic coast of Italy. In spite the large diffusion of fish tank along the Tyrrhenian sea, only one is found along the Italian coast of Adriatic sea. Data are based on morphological characteristics of eight submerged Roman fish tanks constructed between 31 BC and AD 69. Underwater geomorphological features and archaeological remains related to relative sea level and to the shoreline during the late Holocene have been measured and afterwards corrected using recorded tidal values. We elaborated the sea level scenario for the last 2000 years. Using glacial isostatic adjustment model we explained how the sea level change departs from the eustatic signal. In this context the revising relative sea level during Roman period allows to provide a reference to isolate the long wavelength contribution to sea level change from the secular sea level rise. In order to achieve this goal we use two approach. First we estimated the range of GIA correction testing a set of various plausible scenarios of the global melting history since the Last Glacial Maximum and the Earth rheological profile. Second we compared the observations with RSL predictions in order to validate ice global models and add new data to constrain the end of melting of Late Pleistocene ice sheets.

In Chapter 6 we focused on the RSL since 6000 years ago in Tunisia area. The tectonically stable part of the south Tunisian coast is of particular interest because it seems to provide evidence for mid-Holocene sea level above the present-day level. In contrast with the well recognized middle to late Holocene highstand in equatorial ocean basins, mid-Holocene highstands seem not to exist in the Mediterranean as a whole. Data are based on beachrocks outcrop in SE Tunisa (El Grine area). Analysing these samples using sedimentological, petrographic cathodoluminescence, and stratigraphic methods we obtained a much more accurate and precise constraint of the possible relative sea level highstand than currently available. Using preliminarily OSL data we determined the mid-Holocene sea-level index point of SE Tunisia. We explained the palaeo sea-level observations in term of glacial isostatic adjustment. We have accomplished this goal through a set of computations based on a spherically layered incompressible Earth

model and two different available ice chronologies. Because the improved SELEN 3.2 GIA program takes into account the shoreline migrations, it is the appropriate code to be used to asses the sea-level curve predictions on sites placed along the Gabes Gulf, characterized by a large and shallow continental shelf. After to solve the sea level equation for the SE Tunisa area, we analyze separately the factors that could affect the sea-level in this region. Among these factors, the glacio-isostasy, hydro-isostasy, shoreline migration and catastropic rise events shall be treated in detail. We evaluated, also, the SE Tunisia coast regarding its potential sensitivity to the melting history of Antarctic ice sheet.

List of abbreviations

A1IS	Antarctic Ice Sheets included within modified ICE-5G
A2IS	Antarctic included within modified ANU05
AIS	Antarctic Ice Sheet
APLO	Atmospheric Pressure Loading Service
ANU	Australian National University
BP	Before Present
CHAMP	Challenging Minisatellite Payload
CL	Cathodoluminescence method
EAIS	East Antarctic Ice Sheet
ER	Elastic Rebound
ESL	Equivalent Sea Level
GER	Global elastic Rebound
GFs	Green's functions
GRACE	Gravity Recovery And Climate Experiment
GIA	Glacial Isostatic Adjustment
GNET	Greenland GPS Network
GOCE	Gravity field and steady-state Ocean Circulation Explorer
GPS	Global Positioning System
GrIS	Greenland Ice Sheet
ICESat	Ice, cloud and land Elevation Satellite
InSAR	Interferometric Synthetic Aperture Radar
IPCC	Intergovernmental Panel of Climate Change
ITRF	International Terrestrial Reference Frame
IPR	Ice Penetrating Radar
LDC	Load Deformation Coefficients
LGM	Last Glacial Maximum
MSL	Mean Sea level
MWP	Melt Water Pulse
N	Geoid surface
PSMSL	Permanent Service for Mean Sea Level
POLENET	Polar GPS Network
PREM	Preliminary Reference Earth Model
RSL	Relative Sea Level
S	Sea level variations surface
SAR	Synthetic Aperture Radar
SGC	Self Gravitation Consistent

SLE	Sea Level Equation
U	Earth bedrock surface
UNEP	United Nations Environment Programme
WAIS	West Antarctic Ice Sheet
WGI	World Glacier Inventory Program
WMO	World Meteorological Organization

Chapter 1

Background and motivation

1.1 Causes and time scales of sea level change

Here we focus on the processes and feedback can cause the sea level variations. Sea level change results by complex interaction of geophysical processes within the Earth system, including interactions among the solid Earth, atmosphere, ocean, cryosphere, and hydrosphere (Shum et al., 2008). Sea level change encompasses a broad range of time scales, with different mechanisms associated with change over different times. Recalling the work of Geophysic Study Committee (1990) we summarize mechanisms of sea-level change by time scale in Table 1.1 and we include the geophysical processes that is disturbed. As shown in Table 1.1 changing sea-level is the result of processes occurring within the Earth (U, N), the cryosphere and the oceans. From geophysical point of view the sea level variations (S) is the offset between the geoid surface (N) and the solid surface of the Earth (U) (Peltier, 2004). The geoid (N) surface is an equipotential surface at mean sea level (MSL). MSL is a measure of the average height of the surface of oceans averaged over a period of time long enough to remove high-frequency oscillations (halfway point between the mean high tide and the mean low tide; Douglas,1997). Following the terminology used by Suess (1906) the change in sea level related to to a change in water volume within oceans assuming a rigid Earth and no geoid changes hypothesis, corresponds to the eustatic (S_E) component of sea level change. However, non-uniform process in space and time perturbing sea surface and causing non-uniform sea level change as well as changes in the global mean sea level (Houghton et al., 1990; Church et al., 2001; Gehrels, 2009). Hence the use of relative sea level term (RSL) is used to separate the local amplitude of sea level change from the global magnitude of sea level change.

The time scales at which sea level change occurs vary between 10^{-4} and 10^{8} years.

Table 1.1: Some Mechanisms of Sea-Level Change.

Mechanisms	Time scale (years)	Surface variations
Ocean Steric volume Changes		S_E
Shallow (0 to 500 m)	10^{-1} to 10^{2}	
Deep (500 to 4000 m)	10^{1} to 10^{4}	
Glacial Accretion and Wastage		S_E, U, N
Mountain Glaciers	10^{1} to 10^{2}	
Greenland Ice Sheet	10^{2} to 10^{5}	
East Antarctic Ice Sheet	10^{3} to 10^{5}	
West Antarctic Ice Sheet	10^{2} to 10^{4}	
Liquid Water on Land		S_E
Ground water Acquifers	10^{2} to 10^{5}	
Lakes and Resservoirs	10^{2} to 10^{5}	
Plate tectonics		
Lithosphere Formation and Subduction	10^{5} to 10^{8}	U, N
Glacial Isostatic Rebound	10^{2} to 10^{4}	S_E, U, N
Continental Collision	10^{5} to 10^{8}	U, N
Sea floor and Continental Epeirogeny	10^{5} to 10^{8}	U, N
Sedimentation	10^{4} to 10^{8}	U
Earthquake	10^{-4}	U

On decadal time scale, RSL at any particular location results from many processes, mostly related to recent climate change (e.g. ocean steric volume changes, glacial accretion and wastage listed in Table 1.1). After earthquake, the changes in ocean volume, related with the warming of shallow layers is the faster mechanism among those summarized in Table 1.1. Sea level will rise about 100 mm for every degree of temperature increase throughout the uppermost 500 m (Wunsch et al., 2007). However, feedbacks related with the thermal expansion are beyond the scope of this Thesis, and are not discussed any further. On longer time scale, at millennia scale, the geodynamic framework of the area and the delayed response of Earth to past climate change are the most important mechanisms. This latter is referred to Glacial Isostatic Adjustment (see Section 1.2.1 for further details). However observation data of secular sea level change result by simultaneous combination of the short time scale of recent ice mass loss and by the longer time scale of Glacial Isostatic Adjustment (GIA) effect. The present Greenland and Antarctica ice sheets are remnants of the late Pleistocene ice sheets and contain enough water to raise global sea level by about 60 m and 6 m respectively (Solomon et al., 2007).

Hence, the ice sheets of Greenland and Antarctica have the potential to make the largest contribution to sea-level rise, but they are also the greatest source of uncertainty. The study of past and present ice chronology of Antarctica and Greenland provide valuable insights and spurs contentious debate over issues pertaining to global climate change. In Table 1.2 we summarize the instruments that provide to constrain the geophysical processes accompanying the mass redistributions associated with GIA and with present ice melting. In the last two decades, GPS network (King et al., 2010) and satellite based systems like GRACE (Gravity Recovery and Climate experiment) (Shum et al., 2008), have been installed or lunched. They, together provide excellent data coverage that gives a detailed picture of the adjusting processes. This satellite instruments combined with field observations represent an important constraint for GIA modeling. In the Chapter 4 we use geophysical data detected by ICESat observations and GPS (Table 1.2) in order to analyze the present-days pattern of geophysical processes related to polar ice melting and long-wavelength GIA effect. Moreover we use archaeological field observations (Chapter 5) and sedimentological RSL indicators (Chapter 6) in order to investigate the sea level change for the last 2000 years and 6000 years, which give further insight into the Earth rheology and ice history.

Table 1.2: Instruments that provide to constrain the geophysical processes accompanying the mass redistributions associated with GIA and with present-days ice melting. S: sea level variation; N: geoid surface; U: solid surface of the Earth; MB: mass balance.

	S	**N**	**U**	**MB**	**Time scale**
Altimeter		X		X	last two Decades
GRACE		X		X	Decade[a]
ICESat				X	Decade[a]
GPS			X		Decades[a]
Tide Gauges	X				Centennial
Archaeological remains	X				Last 2 kyrs [b]
RSL	X				Millennia[c]

[a] See Chapter 4; [b] See Chapter 5; [c] See Chapter 6;

1.2 Sea level variations during the last millennia

There are four major climate cycles that recur with periods between 20,000 and 400,000 years - the so called "Milankovitch Bandwith"- which are collectively referred to as

Milankovitch Cycles. These climate cycles result from the actions and interactions of the Earth's orbital cycles (ellipticity, precession and obliquity cycles) (Zachos et al., 2001). The strongest control on climate is probably the summer length and temperature in which ever hemisphere is the most land-dominated, because this has the greatest impact on the buildup of glacial ice from season to season. Major episodes of continental glaciation have been documented from the geologic record for the Late Proterozoic, Ordovician, Pennsylvanian, and Quaternary. Since the most recent of these cycles, the Last Glacial Maximum (LGM, 21 kyrs BP; by Peltier, 2004), the sea level have continued to change, essentially everywhere on the earth's surface through the so-called glacial isostatic adjustment (GIA) process. In regions that were previously glaciated, such as Canada and Northwestern Europe, the rates of sea level variation that are still observed as a consequence of ongoing glacial isostatic adjustment are non negligible (e. g., Peltier, 1999). RSL continues to fall at a rate which may exceed 1 cm/yr (e. g., in the Hudson Bay region Peltier, 2004; and in the Gulf of Bothnia, Steffen and Wu, 2011).

1.2.1 Glacial Isostatic Adjustment

The Glacial Isostatic Adjustment (GIA) is the ongoing viscoelastic response of Earth to the redistribution of mass on its surface that accompanied deglaciation (Figure 1.1) of the Pleistocene ice sheets since the LGM. The GIA theory of sea level change emerged between 1864 and 1888 with the seminal works by Agassiz (1840); Croll (1867); Woodward (1888). In the twentieth century, after a century of eclipse, the theory was recovery by Milutin Milankovic between 1920 and 1941 with astronomical theory of insolation. In 1976 the theory received new confirmation from the paleostratigraphic work of James Hayes, John Imbrie, Nicholas Shackelton, and others who documented the astronomical signals in a number of independent proxy climate records. In the 1976 Farrell and Clark (1976) formulated the sea level change theory into mathematical equation, nowadays known as Sea Level Equation (see Chapter 2). During the LGM large and thick ice caps covered not only Greenland and Antarctica but also North America and Eurasia, while the global sea level was 120-130 m lower than present (Lambeck et al., 2002).

GIA includes three mains geophysical processes: vertical displacements of the surface topography, variations of the shape of the geoid, and changes of sea level. The deformation of the solid Earth related to GIA may be observed in the present day using Global Positioning System (GPS) receivers to measure vertical and horizontal deformation

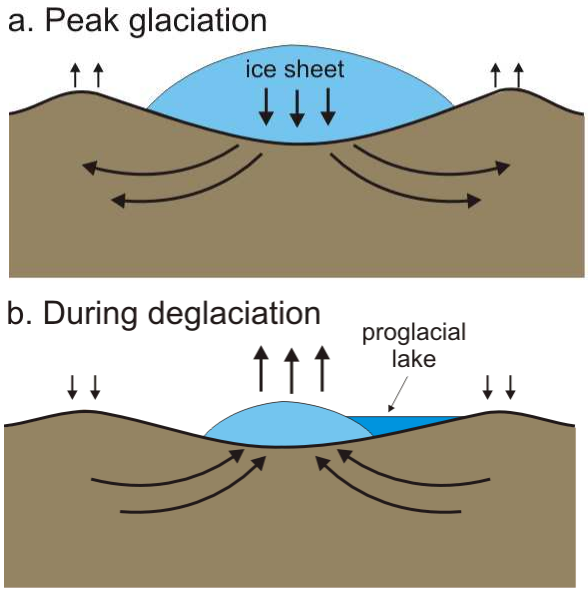

Figure 1.1: *a* At peak glacial conditions the Earth surface is depressed beneath the ice sheet and slightly elevated outside the ice sheet owing to mantle flow. *b* During deglaciation the depressed region rises and peripheral regions subside. Uplift of the Earth's surface is frequently observed as relative sea level fall in recently deglaciated areas. During the initial stages of recession proglacial lakes formed in the Puget Lowland. Shoreline features of these lakes are now tilted up to the north. By *http://www.nrcan.gc.ca/earth-sciences/*.

rates relative to the centre of the Earth or centre of the mass (King et al., 2010). However, the reference frame is difficult to establish because the motion of the reference frame is that it cannot be measured directly, but must inferred from tracking of Earth-orbiting satellites. The best effort to do so is represented by the International Terrestrial Reference Frame (ITRF) (Altamimi et al., 2011). In this Thesis we use the GPS velocity based on ITRF2005 (Khan et al., 2008; Thomas et al., 2011).

The motion of mantle material that flows within the deglaciated regions contributes to gravity field changes. This signal is observable in the rate of change of the present-day gravity field, such as that measured by the GRACE satellite (Tapley et al., 2009). Moreover present-day rates of relative sea-level change are measured using tide gauges and satellite altimetry (Nerem, 1995). However, in order to understand the temporal evolution of GIA it is also useful to make observations which relate to past relative sea-level positions. These are recorded as raised or submerged shorelines, or in terms of salinity changes as determined from diatom analysis of lake sediments. It is important to be able to determine both the height and the age of any relative sea-level marker

for it to be of use in reconstructing relative sea-level change over time (Pirazzoli, 1991; Whitehouse, 2009).

1.2.2 RSL Indicators

Palaeo-records of sea level history provide a crucial basis for understanding the chronologies of Pleistocene ice sheets and the rheological property of Earth. They allow to detect the background variations of sea level upon which the sea level rise related to modern processes is superimposed. Moreover RSL indicators provide one of the few reliable means to infer GIA beyond the instrumental period. The RSL indicators are from coasts that are tectonically stable and are based on the four types of proxies spanning the past 6000 years:

1. archaeological indicators;
2. sedimentological indicators;
3. paleontological indicators;
4. geomorphological indicators.

Obtaining shoreline-related data involves a number of procedures and interpretations. The usual procedure consists in identifying former sea-level indicators, locating the position of a former water plane and measuring the elevation of this paleo-level, and determining the time at which water stood at this specific level (Pirazzoli, 1991). However sea-level indicators need to elaborate due consideration for the uncertainties that surround both the determination of vertical relationships between the position of the sea-level indicators and the MSL, and for the errors associated with the age determinations (Lambeck et al., 2004a). We give a brief description of the RSL indicators used in this Thesis: archaeological indicators and sedimentological indicators.

Archaeological indicators

People have always lived along the coast, as a source of food and transportation. This trend continues today, with 100 million people worldwide presently living within 1 m of mean tide level (Houghton et al., 1990). The advantages of archaeological data are that dating, particularly with classical culture of Mediterranean, can be very precise, often to within decades using pottery and other artefacts. Moreover the relations between

the evidence and mean sea-level, can also be drown fairly precise (Kearney, 2001). The most useful archaeological remains are obviously those related to the sea, in particular from areas of small tidal range, such as fish tanks (Schmiedt, 1972; Pirazzoli, 1976; Lambeck et al., 2004b), harbours installations (Flemming, 1999), docks (Anzidei et al., 2010) and wells (Sivan et al., 2004). Different archaeological markers provide sea-level estimates with different accuracies and it is not possible to assign the same error bars to all data. For instance, the altitude of RSL based on the Roman fish tank (Figure 1.2), depends on hydraulic role of feature within the fish tank (Evelpidou et al., 2011, in press). In Chapter 5 fish tanks will use as archaeological indicators and some of the advantages and issues surrounding the fish tanks as archaeological data will be discussed.

Figure 1.2: Mattonara fish tank of Roman period, placed along the Tyrrhenian coast, closed to S. Marinella.

Sedimentological indicators

Marine deposits are most common and their shape or stratigraphy may be clearly identifiable as typical coastal features (beachrock, littoral bar, estuary or lagoon floor). Easily datable by reworked shell or coral fragments, these features can imply wide vertical uncertainty ranges when they are used to reconstruct former sea level positions, due to tidal range and to possible storm events (Pirazzoli, 1991). Over the past several decades speleothems (i.e., stalagmites and flowstones) have emerged as powerful proxy records for

long periods of Quaternary paleoclimate history (Tuccimei et al., 2011, in press). There are at least two reasons for this. Diagenetic changes occurring in near shore, within marine carbonates, can be used to deduce diagnostic criteria in terms of sea level position. Beach rock is constituted from clastic shoreline deposits cemented by calcitic-magnesitic or aragonitic carbonates in or near the intertidal zone, often at the interface of the fresh-water-marine phreatic flow (Alexandersson, 1969). This precipitation can be exceptionally fast, of the order of 10 years and, depending on local conditions, this interface may occur above or below mean sea level. In particular, supratidal cementation by carbonate cements is common and much debate still exists about the uppermost level of cementation. Beachrock outcrops commonly consist of sequences of bands, which usually dip seaward and may be associated with sedimentary structures and lithofacies diagnostic of the depositional conditions of the constituent sediments (Vousdoukas et al, 2007). Former shoreline position is obtained from detailed microstratigraphic and sedimentological analysis of deposits. Optical luminescence dating of beachrock is nowadays the most important method (Thomas, 2009) to date this deposits. In Chapter 6, beachrock will be used as sedimentological indicators of former sealevel for the last 6000 years. We include, within this chapter diagnostic character of beachrock deposits such as sedimentary structure, diagenetic setting, stratigraphic relationship in order to minimize the uncertainties of former sea level.

1.3 Present Sea level variations

Since 1900 the trend of sea-level is characterized by a significant acceleration in sea-level rise, coinciding with the Industrial Revolution (Figure 1.3). In this figure the observed sea-level rise is based on data from geological observations, tide gauges and from multiple mission satellite altimetry. To highlight the problem of global climate change, including sea-level rise and potential antropogenic effect on sea-level rise, the WMO (World Meteorological Organization) and the United Nations Environment Programme established the IPCC in 1988. Since 1990 the IPCC estimated global sea-level rise during the 20th century with a trend of 1-2 mm/yr in 1990 (Houghton et al., 1990), although with a high degree of uncertainty, and 1.5 mm/yrs in 2001 (Church et al., 2001). Published estimates of sea level budget since 1993, listed by Cazenave and Llovel (2010) within the IPCC AR4, are shown in Table 1.3. Two time spans are considered: 1993-2007 and 2003-2007. Over 1993-2007 (second column of Table 1.3), the altimetry-based rate of sea

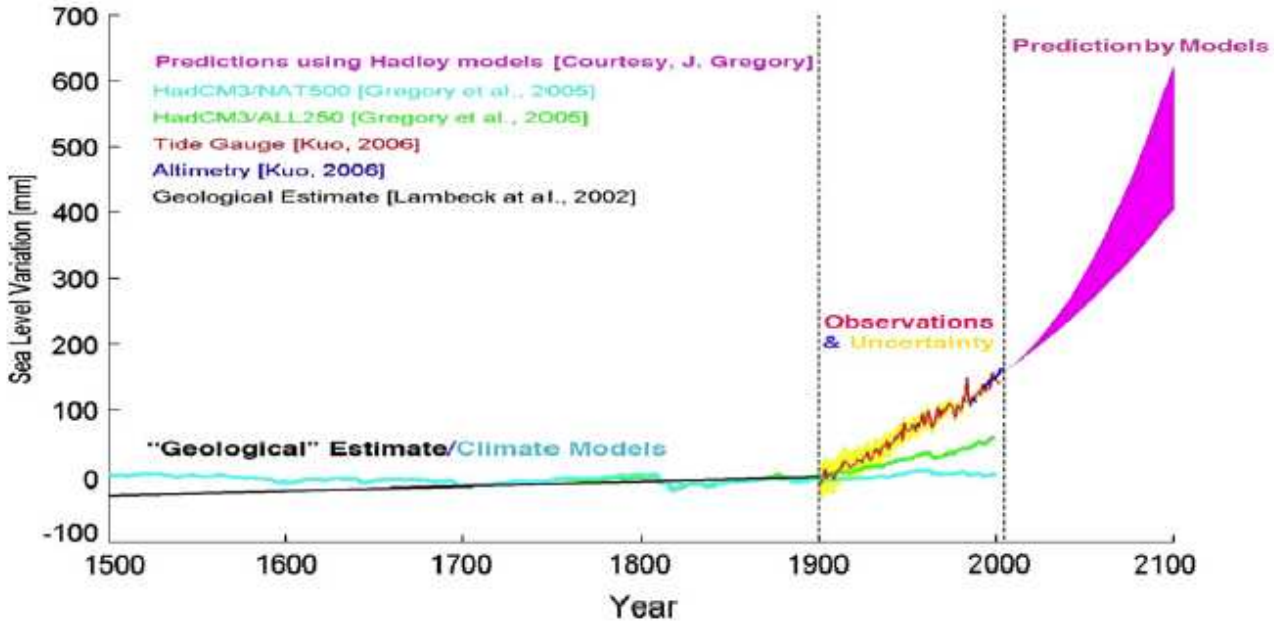

Figure 1.3: Estimated, observed, and predicted global sea-level rise over the period 1500–2100, by Shum et al. (2008). Before the 20th century sea level variation is based on geological interpretations. Between 1900 and 2005 observed sea-level rise is based on tide-gauges. The last two decades observed sea-level rise is based on data from tide gauges and from multiple mission satellite.

level rise was 3.3 ± 0.4 mm year^{-1}. Mean thermal expansion rate based on Levitus etal. (2009) is 1.0 ± 0.3 mm year^{-1}. The rate difference between observed sea level rise and mean thermal expansion is 2.3 mm year^{-1} (Cazenave et al., 2009). This represents the ocean mass increase probably due to ice loss. Considering the contribution of glaciers to sea level rise elaborated by Meier et al. (2007) leading to a value of 1.1 ± 0.25 mm year^{-1} and that an average ice sheet mass loss is 0.7 ± 0.2 mm year^{-1}, the residual rates is 0.45 mm year^{-1}. This value shows the difficulty reconciling climate model predictions with the observed data Considering the third column of Table 1.3, Cazenave and Llovel (2010) show increased contribution from the glaciers and polar ice sheets component to the estimate the sea level budget between 2003 and 2007 compared with the the time span 1993-2007. There is evidence that the land ice melt contribution has increased significantly over the last decade. This larger contribution of ice melting to sea level rise

allows a better reconciliation with the observed data (residual value of -0.05 mm year^{-1}.

Table 1.3: Sea level budget for two time spans. First between 1993 and 2007. Second between 2003-2007. By Cazenave et al. (2009)

Sea level rise mm yr^{-1}	1993-2007	2003-2007
Observed	3.3 ± 0.4	2.5 ± 0.4
Thermal expansion	1.0 ± 0.3^a	0.25 ± 0.8^b
Ocean mass	2.3 ± 0.5^c	2.1 ± 0.1^d
Glaciers	1.1 ± 0.25^e	1.4 ± 0.25^f
Total ice sheets	0.7 ± 0.2	1.0 ± 0.2
Greenland Ice Sheet	0.4 ± 0.15	0.5 ± 0.15
Antarctic Ice Sheet	0.3 ± 0.15	0.5 ± 0.15
Land waters		-0.2 ± 0.1^g
Sum	2.85 ± 0.35	2.45 ± 0.85
Observed rate minus sum	0.45	-0.05

1.3.1 Measuring Sea Level

Sea level can be observed in three ways. The first is the relative sea level (the height of the water relative to the land), measured using tide gauges. The second is Satellite altimetry measures the distance between an Earth-orbiting satellite and the surface of the ocean (Figure 1.4). Knowing accurately the position of the satellite we can know the height of the ocean relative to the centre of the Earth. The third is GRACE, but it measures only the changes in gravity caused by local changes in water mass. On the other hand, altimetry and GRACE data can be combined in order to evaluate sea level variations.

Tide gauge measurements available since the late nineteenth century show significant sea level rise during the twentieth century (Douglas, 2001). The sea level change of past century comes from tide gauge measurements taken along continental coastlines and islands. The largest tide gauge database of monthly and annual mean sea level records is the Permanent Service for Mean Sea Level (PSMSL, available at *http://www.pol.ac.uk/psmsl*) (Woodworth and Player, 2003), which contains data for the twentieth century from $\sim$ 2000 sites. Unfortunately, the records are somewhat inhomogeneous in terms of data length and quality. The number and distribution of tide gauges in the past cannot compare to today dense network, thus older data are incomplete. For long-term sea level studies, for instance, only 10% of the data set is useable. Moreover tide gauges measure sea level relative to the ground (S), hence correction is needed to

interpret tide gauge measurements in terms of global mean sea level change (N). In recent years, precise positioning systems, i.e., the global positioning system (GPS), have been installed at a few tide gauge sites to monitor land motions (U). But the equipped sites remain few and the GPS records minimal (Woppelmann et al, 2007).

Since the early 1990, satellite altimetry (Figure 1.4) has become the main tool for precisely and continuously measuring sea level with quasi-global coverage and short revisit time. The quantity of interest in oceanography is the sea-surface height above

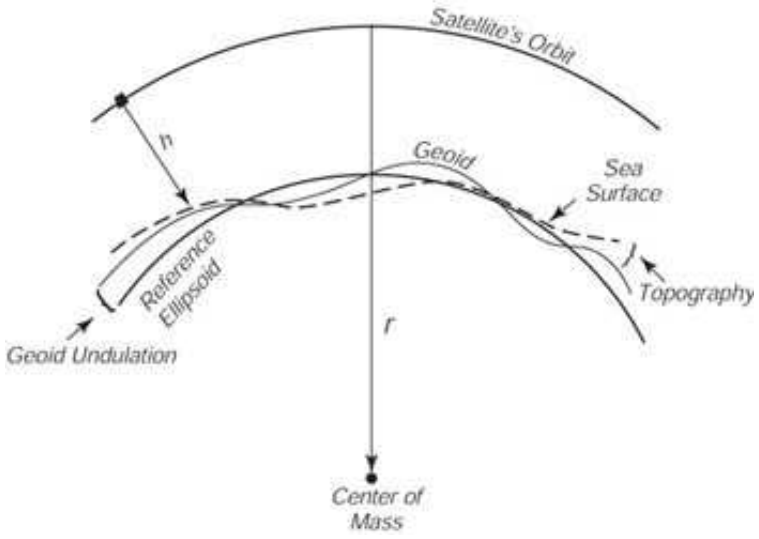

Figure 1.4: A satellite altimeter measures the height (**h**) of the satellite above the sea surface. When this is subtracted from the height **r** of the satellite orbit, the difference is sea level relative to the center of mass of the Earth. The shape of the surface is due to variations in gravity, which produce the geoid undulations, and to ocean currents which produce the oceanic topography, the departure of the sea surface from the geoid. The reference ellipsoid is the best smooth approximation to the geoid. The variations in the geoid, geoid undulations, and topography are greatly exaggerated in the figure. By Stewart (1985).

a reference fixed surface (typically a conventional reference ellipsoid); it is obtained by the difference between the altitude of the satellite above the reference (deduced from precise orbitography) and the range measurement. The estimated sea-surface height requires correction for various factors due to atmospheric delay and biases between the mean electromagnetic scattering surface and the sea at the air-sea interface. Moreover corrections due to geophysical effects e.g. solid Earth ocean tidal effects, are also applied. In 1992, the Topex/Poseidon altimetry missions have been launched. The altimetry-derived sea-surface height coming from this mission, allowing precise detection of ocean

dynamics for the first time with precision below 10 cm (Nerem, 1995). The pattern of sea level change that will emerge from the ongoing sequence of satellite altimetry missions will be the net contribution of all processes shown in Table 1.1. Recent reviews (Cazenave et al., 2009) show that the most up to date estimates of mean rate of sea level rise for the 20th century are converging on around 1.7 to 1.8 mm year^{-1}, with uncertainties of around 0.2 to 0.3 mm year^{-1}.

1.3.2 Mass balance

Considering that thermal expansion, ocean mass and land ice loss are the main causes of global sea level change (see Table 1.3), a number of satellite missions, in Europe and the United States, are aimed at improving our knowledge of the sea level problem (Sabadini and Maier-Reimer, 2002). Challenging Minisatellite Payload (CHAMP), Ocean Circulation Explorer (GOCE) and GRACE mission provide estimates of the static gravity field with different accuracy and spatial resolution (Reigber et al., 2004; Visser et al, 2002; Tapley et al., 2009). The main characteristics of the, GRACE and GOCE missions are summarized in Table 1.4. Inspection of Table 1.4 underlines that these missions are limited in spatial resolution and temporal behaviour. Mass balances of present polar ice sheets (Velicogna, 2009; Wouters et al., 2008; Wu et al., 2010) indicate a contribution to sea level rise ranging between 0.075 mm yr^{-1}and 0.52 mm yr^{-1}for AIS (Zwally and Giovinetto, 2011) and between 0.1 and 0.8 mm (Velicogna and Wahr, 2005; vanderBroeke et al., 2009) for GrIS (Chapter 4 includes a overview of the recent mass balances obtained from Antarctica and Greenland. However glacier changes are having impacts on secular sea level rise (Meier et al., 2007) (as Table 1.3 showed). The World Glacier Inventory Program (WGI) attempts to measure and classify all the perennial ice masses of the world. They estimate that the total area of these glaciers and ice caps to be about 785 $\pm$ 100 10^3 km^2 with a total volume of 260 $\pm$ 65 10^3 km^3 equivalent to 0.65 $\pm$ 0.16 m of sea level rise (Dyurgerov and Meier, 2005).

There are three major techniques employed to measure ice sheet mass balance: the mass budget method, the gravity method and the elevation change method. Historically, the first technique is the mass budget method, which compares the input and output of ice mass to the continent. The information of accumulation comes primarily from ice cores, and the calving/discharge can be determined from Interferometric Synthetic Aperture Radar (InSAR) measurements of glacier velocities together with the ice thickness. The

mass budget approach compares two large numbers (total accumulation vs total loss) with large uncertainties, hence requires very precise measurements of both (Rignot, 2011). The major challenge with the mass budget method is the lack of accurate data for determining the various contributions to the mass budget equation.

The GRACE twin satellites were launched during 2002. Primary goal of the GRACE satellite mission is to obtain accurate global models of the Earth's gravity field, of both the static and time varying component (Tapley et al., 2009). The mission consists of two satellites in low Earth orbit, working together to measure the global gravitational field and document gravity anomalies (Wahr et al., 2000). The time-variations in the gravity field can be used in many different applications, for instance in ice sheet mass balance studies (Velicogna, 2009; Wouters et al., 2008; Wu et al., 2010). The gravity method is also called the weighting method, since an observed change in gravity is directly associated with a change in mass. Indeed, GRACE space gravimetry is sensitive to solid Earth mass change, in particular, that associated with GIA (Sørensen et al., 2011). Estimates of present-day GIA are crucial for determining current ice mass balance estimates over Antarctica and Greenland ice sheets (Tapley et al., 2009). This is due to the fact that, while the GRACE mission is able to accurately detect large scale changes in mass over the Polar continents, the technique itself is not able to distinguish between mass change due to GIA and that due to ongoing ice loss or gain (Riva et al., 2009). Over Antarctica, where the GIA effect is of the same order of magnitude as the ice mass change, the poorly known GIA correction is a source of significant uncertainty (Cazenave and Llovel, 2010). In spite of these problems, satellite-based sensors clearly show accelerated ice mass loss from the ice sheets over the recent years (Rignot, 2011). Published estimates of GRACE–only solutions for the average Greenland Ice sheets mass balance during the last decade vary between -177 ± 6 Gt yr^{-1} for the period 2003–2009 (Luthcke et al., 2010) and -237 ± 20 Gt yr^{-1} for the period 2003–2008 (vanderBroeke et al., 2009). GRACE results indicate accelerated ice mass loss from coastal regions of the Greenland ice sheet since 2002/2003, especially in Jakobshavn Isbrae glacier on the west coast of Greenland (Spada et al., 2010, subm.). Estimates of recent changes in Antarctic land ice based on GRACE data, range from losing -87 $\pm$ 43 Gt yr^{-1} (Wu et al., 2010) to over -190 $\pm$ 77 Gt yr^{-1} for the period 2002-2009 (Chen et al., 2009).

Differently from the low resolution of GRACE mission (400 km), ICESat measurements offers higher resolution (between 25 and 50 km) (Riva et al., 2009). The

Table 1.4: Characteristics of the CHAMP, GRACE and GOCE satellite missions. By Schotman (2008).

Mission	Accuracy cm	Maximum degree l	Resolution km	Launch
CHAMP	5	50	400	2000
GRACE	1-5	∼60	250-200	2002
GOCE	1-2	200	100	2008

Ice Cloud and land Elevation Satellite (ICESat) laser altimetry mission, lunched in 2003, consists of surface elevations for the large ice sheets (Zwally et al., 2011) and allows monitoring ice sheet elevation change. Problems with the lasers on-board ICESat early in the mission, have reduced the measurements to two or three months every year, and this has also reduced the spacial coverage of the satellite (Ewert et al., 2011). Furthermore the tracks are not repeated exactly, and this makes deriving rates of elevation changes difficult (Gunter et al., 2009). A major limitation for altimetry is the contamination of the radar signal near the coast when the reflection of the radar pulse is partly due to the oceans surface and partly to land. As a consequence, standard altimetry data are unreliable at distances closer than 40 km to the coast (Slobbe et al., 2009). Improved data processing techniques are being developed for coastal regions, but they have not yet been implemented operationally (Gommenginger et al., 2009). Different methods for deriving elevation from the ICESat altimetry was developed by Sørensen (2010), from which volume changes are derived. In particular she derived the volume change of the Greenland Ice sheets by correcting the observed elevation changes for snow/ice densities model and firn compaction. Moreower elevation change corrections applied are the bedrock movement related both the elastic signal and glacial isostatic adjustment (Sørensen, 2010). Due to its orbit inclination (94^o) and pointing angle (nearly nadir), ICESat data do not cover latitudes higher than about 86^o (Riva et al., 2009). This limit implies a data gap within the polar ice cap. Published estimates of ICESat solutions for the average Greenland Ice sheets mass balance during the last decade, vary between -139 $\pm$ 6 Gt yr $^{-1}$ for the period 2003-2007 (Slobbe et al., 2009) and -240 $\pm$ 28 Gt yr^{-1} for the period 2003-2008 (Sørensen et al., 2011). In spite the large number of published estimated of GRACE solutions for Greenland ice sheets mass balance, the ICESat solutions for Antarctica mass balance not has yet available. However temporal variations inferred from GRACE gravity measurements, combined with ICESat altimetry data, provided a better

estimate of changes in ice sheet mass balance for Greenland and Antarctica. Potential error sources in measuring mass balance include uncertainties in postglacial rebound, and under sampling and compaction errors. By combining ICESat and GRACE data, the postglacial rebound error is expected to be reduced (Wahr et al., 2000).

Chapter 2

Theory

This chapter is devoted to the study of the Sea Level Equation (SLE), that has been introduced in Section 1.2.1. The observed change in relative sea level is the change in distance between the ocean floor and the ocean surface. The surface of the equilibrium ocean is always at constant gravitational potential, and this surface defines the geoid. As ice melts on the surface of the Earth and matter within the Earth flows to compensate for the changing surface-mass distribution, the combined mass transfers affect the geoid. In the following derivations (Section 2.2), the notation of Spada and Stocchi (2007) has been adopted and we refer to works of Spada and Stocchi (2006; 2007) and Spada et al. (2011b) for details. Further insight into the theoretical aspects of the sea-level equation, presented here, can be found in Farrell and Clark (1976); Clark et al. (1978); Nakada and Lambeck (1989); Milne and Mitrovica (1998); Peltier (1999, 2004).

2.1 Basic equations

From a geophysical point of view the GIA problem is based on the analyses of deformation in continuum mechanics by surface pressure, associated with the ice masses. The relation between stresses and induced strains is expressed by constitutive equations that approximates the response of that material to external forces and concern the rheology of material. The first foundamental equation is the equation of momentum. Considering that the volume force $\vec{F}$ is balanced by the surface stresses σ_{ij} on the infinitesimal block situated somewhere inside the Earth and that we displace the block by an infinitesimal amount $\vec{u}$. Furthermore we assume that the Earth is laterally homogeneous and radially stratified and hydrostatistically pre-stressed. We also neglected the Earth rotation. If we assume that the force is the gravity $\vec{F} = -\nabla\phi$, and no other forces or loads acting on its

surface, the equation of momentum reads:

$$-\nabla\sigma - \nabla(\rho_o g\vec{u}\,\hat{e}_r) - \rho_0\nabla\phi_1 - \rho_1 g_0\hat{e}_r = 0\,, \tag{2.1}$$

(e. g. Ranalli, 1995) where:
$-\nabla\sigma$ is the negative gradient of stress σ,
ρ_0 denotes the density before the perturbation,
ρ_1 denotes the perturbate density where $\rho_1 \ll \rho_0$,
g is the gravitational acceleration,
$\vec{u}$ is the displacement vector,
$\hat{e}_r$ is the radious of Earth,
The first term of Eq. (2.1) describes the contribution from the stress, the second term describes the advection of the pre-stress (hydrostatic), the third term the changed gravity (self gravitation) and the fourth term the changed density (compressibility). In cases where self-gravitation is neglected, the third term will be zero, while in the case of incompressibility the fourth term will be zero. The continuity equation for an incompressible fluid reads:

$$\vec{\nabla}\dot{u} = 0\,, \tag{2.2}$$

The perturbed gravitational potential ϕ_1 satisfies the Poisson equation

$$\nabla^2\phi_1 = -4\pi G\rho_1\,, \tag{2.3}$$

where G is the universal gravitational constant. In the case of incompressibility, the right-hand term of Eq. (2.3) will be zero

$$\nabla^2\phi_1 = 0\,. \tag{2.4}$$

The Eq. (2.1), (2.3) and (2.4) need to supplemented with a constitutional equation describing how stress and strain (or strain rate) are related to each other (e. g., Fung, 1965).

2.2 Developments of Sea Level Equation

The sea-level change, induced by an assumed known history of glaciation and deglaciation reads:

$$S(\theta,\lambda,t) = \frac{\rho_i}{\gamma}G_s\otimes_i I + \frac{\rho_w}{\gamma}G_s\otimes_o S + S^E - \frac{\rho_i}{\gamma}\overline{G_s\otimes_i I} - \frac{\rho_w}{\gamma}\overline{G_s\otimes_o S}\,, \tag{2.5}$$

where:
S is sea-level change,
θ and λ is colatitude and longitude respectively,
t is time,
$\rho_i = 913$ kg m^{-3} is the densities of ice,
$\rho_w = 1000$ kg m^{-3} is the densities of water,
γ is the reference surface gravity,
G_s is the sea–level Green 's function
$I = I(\theta, \lambda, t)$ is the ice thickness variation,
$S^E = S^E(t)$ represents the eustatic term (i. e., the ocean–averaged value of S),
$\otimes_i$ and $\otimes_o$ denote spatio–temporal convolutions over the ice and ocean covered regions, and the overbar indicates an average over the surface of the oceans that ensures mass conservation (Farrell and Clark, 1976).

Because the unknown field $S(\theta, \lambda, t)$ appears both on the left-hand side of Eq. (2.5) as well as under the three-dimensional convolution integral, Eq. (2.5) is clearly an integral equation. This imply that we need to solve through a iterative procedure.

In the literature, the solution of the SLE in the form Eq. (2.5) is referred to as gravitationally self-consistent solution, since it has been obtained imposing that the geoid is that particular equipotential surface constrained by the requirement of mass conservation. In this Thesis we refer to *SGC* predictions when the results are based on the solution of SLE in the form of Eq. (2.5). Key variables and terms are defined within below Sections 2.2.1, 2.2.2, 2.2.3.

2.2.1 Green's function

Within the study of deformations of Earth when it is a point-like, impulsive load is applied to the surface of the Earth, the Green's functions (henceforth GFs) able to describe the geophysical quantities involved within GIA process. In particular the GFs provide a way to quantify the three dimensional displacements and the variation of the gravitational potential when a point-like, impulsive load is applied to the surface through the Love numbers ϕ, h, l (Love, 1909), respectively of a spherically symmetric, layered Earth model. The G_s is the sea-level Greens function and represents the offset between the geoid surface and the topography. It is defined as:

$$\frac{G_s}{\gamma}(\theta, \lambda, t) \equiv \frac{G_\phi}{\gamma} - G_u \,, \tag{2.6}$$

where G_ϕ is the GFs for the incremental gravitational potential and G_u is the GFs relative to the vertical component of displacement. Obviously this geophysical displacements are function of the rheology of the Earth.

We consider a localized point mass M placed at the surface of a *rigid*, spherically, symmetric Earth. By Newton Law of gravitation, the gravity potential at an external point P per unit time exerted by the localized mass is inversely proportional to the distance $d(\theta) = 2a\sin(\frac{\alpha}{2})$ between the mass and P. Since the point mass adds to the background potential of the Earth, we refer to incremental gravitational potential defined for a rigid Earth as:

$$G^r_\phi \equiv \frac{\phi^r(\alpha,t)}{m_s} = \frac{a\gamma\delta(t)}{2m_e\sin(\frac{\alpha}{2})}\,, \tag{2.7}$$

(e.g. Farrell, 1972) where m_s represents the intrinsic (or static) mass of point mass M, $\delta(t)$ is Dirac's delta, m_e is the mass of the Earth and γ is the surface gravity acceleration. An equivalent expression for the GF can be obtained recalling the Legendre sum:

$$\sum_{t=0}^{\infty} Pl(\cos\alpha) = \frac{1}{2\sin(\frac{\alpha}{2})}\,, \tag{2.8}$$

where $P_l(\cos\alpha)$ is the Legendre polynomial of harmonic degree l. hence, from Eq. (2.7)

$$G^r_\phi = \delta(t)\sum_{l=0}^{\infty}\phi^r_l P_l(\cos\alpha)\,, \tag{2.9}$$

where $\phi^r_l \equiv \frac{a\gamma}{m_e}$.

For an *elastic* spherically, symmetric Earth the action of the impulsive mass produces two related effects. First the planet yields under the pressure exerted by the load. Second, there is a variation of the gravitational potential following the change of the shape of the Earth. The corresponded GF for the incremental gravitational potential for a elastic Earth is defined as:

$$G^e_\phi = \delta(t)\sum_{l=0}^{\infty}\phi^e_l P_l(\cos\alpha)\,, \tag{2.10}$$

which is in phase with G^r_ϕ as a consequence of elasticity. Furthermore, since Earth responds linearly to the imposed forces, the spectral coefficents ϕ^e_l are proportional degree-by-degree to ϕ^r_l

$$\phi^e_l = k^e_l\phi^r_l\,, \tag{2.11}$$

where the non-dimensional number k_l^e is the elastic load-deformational coefficient (LDC) (or Love numbers) for the incremental gravitational potential. The spectral form of GF for a elastic Earth is:

$$G_\phi = \delta(t)\frac{a\gamma}{m_e}\sum_{l=0}^{\infty}(1+k_l^e)P_l(\cos\alpha)\,. \tag{2.12}$$

At the surface of the Earth, the elastic displacement induced by the applied load can be expressed as:

$$\vec{u}(\alpha,t) = G_u(\alpha,t)\hat{r} + G_v(\alpha,t)\hat{\alpha}\,, \tag{2.13}$$

where $\hat{r}$ and $\hat{\alpha}$ are unit vectors in the directions of increasing radius and colatitude, and G_u and G_v are the GFs relative to the vertical and horizontal components of displacement, respectively.

By virtue of the spherical symmetry of the Earth, the longitudinal component of displacement perpendicular to both $\hat{r}$ and $\hat{\alpha}$ vanishes identically. Hence the GFs relative to the vertical and horizontal components of displacement depend on the elastic GFs only, where GFs of dimensional displacements for a rigid Earth is:

$$G_u^r(\alpha,t) = G_v^r(\alpha,t) = 0\,, \tag{2.14}$$

The GFs pertaining to vertical and horizontal displacement can be expressed in spectral form by means appropriate LDCs h_l^e and l_l^e respectively in the following manner:

$$G_u^e = \delta(t)\frac{a}{m_e}\sum_{l=0}^{\infty}h_l^e P_l(\cos\alpha)\,, \tag{2.15}$$

and

$$G_v^e = \delta(t)\frac{a}{m_e}\sum_{l=0}^{\infty}l_l^e\frac{P_l(\cos\alpha)}{\partial\alpha}\,, \tag{2.16}$$

we observe that G_u^e and G_v^e have dimensions of displacements per unit time and per unit mass.

Assuming a Maxwell *viscoelastic* spherically, symmetric Earth the action of the impulsive mass produces a delayed response relative to the viscous part. In this case the GF relative to the total incremental gravitational potential reads:

$$G_\phi(\alpha,t) = G_\phi^r(\alpha,t) + G_\phi^e(\alpha,t) + G_\phi^v(\alpha,t)\,, \tag{2.17}$$

where the rigid and elastic components are given by Eq. (2.9) and (2.12) respectively, while the viscous part is defined as:

$$G_\phi = H(t)\frac{a\gamma}{m_e}\sum_{l=0}^{\infty}\left(\sum_{j=1}^{M} k_{lj}e^{s_{lj}t}\right)P_l(\cos\alpha)\,, \tag{2.18}$$

where $H(t)$ is the Heaviside step function:

$$H(t) = \begin{cases} 1, & t \geq 0 \\ 0, & t < 0 \end{cases} \tag{2.19}$$

k_{lj} are the viscoelastic $LDCs$ for the incremental potetiantial, and s_{lj} describe the relaxation of the Earth to the imposed impulsive unit load:

$$s_{lj} = -\frac{1}{\tau_{ij}}\,, \tag{2.20}$$

where τ_{ij} are the relaxation times of the Earth model (Haskell, 1935). The couple $s_{lj}$and τ_{ij} is referred to as the j-th viscoelastic mode of degree l. The Eq. (2.20) indicates that the quantities s_{lj} are real and negative, even if a rigorous proof of this statement valid for any Earth model is still to come. In the case of an incompressible viscoelastic body, the term s_{lj} $(i = 1, ..., M)$ describe the relaxation of the Earth to the imposed impulsive unit load, with M depending on the number of layers of the Earth model employed and on the nature of the interfaces between the layers.

The GFs pertaining to the vertical and horizontal components of displacements can be similarly written like Eq. (2.17) as the sum of elastic and viscoelastic parts, with:

$$G_u(\alpha, t) = G_u^e(\alpha, t) + G_u^v(\alpha, t)\,, \tag{2.21}$$

and

$$G_v(\alpha, t) = G_v^e(\alpha, t) + G_v^v(\alpha, t)\,, \tag{2.22}$$

where we have used Eq. (2.14), (2.9) and (2.12) for the elastic compoment of the displacement. In analogy with the viscoelastic $LDCs$ for the incremental potetiantial (k_{lj}) we use the h_{lj} and l_{lj} relative to the radial and horizontal components of displacement respectively to calculate the G_u and G_v GFs. The GFs for a viscoelastic Earth can be rewrite using the viscoelastic $LDCs$ (Farrell and Clark, 1976) as:

$$\begin{Bmatrix} \frac{1}{\gamma}G_\phi \\ G_u \\ G_v \end{Bmatrix}(\alpha, t) = \frac{a}{m_e}\sum_{l=0}^{\infty}\begin{Bmatrix} k_l \\ h_l \\ l_l \end{Bmatrix}(t) + \begin{Bmatrix} 1 \\ 1 \\ \partial_\alpha \end{Bmatrix}. \tag{2.23}$$

2.2.2 Ice thickness

The term $I(\theta, \lambda, t)$ of Eq. (2.5) is the spatio-temporal variation of ice sheets that is defined as:

$$I(\theta, \lambda, t) = T(\theta, \lambda, t) - T_0 \,, \tag{2.24}$$

where $T(\theta, \lambda, t)$ is the ice thickness given at point P of coordinates (θ, λ) at a given time t and T_0 is the ice thickness at P at remote reference time t_0. The localized impulsive load associated with changes of the thickness of the ice sheets is:

$$L_i(\theta, \lambda, t) = \rho_i I(\theta, \lambda, t) \,, \tag{2.25}$$

with ρ_i the density of ice (931 kg m^3). For an ice load with fixed margins,the following factorization is possible:

$$L_i(\theta, \lambda, t) = \sigma(\theta, \lambda) f(t) \,, \tag{2.26}$$

where $f(t)$ is the load time-history and $\sigma(\theta, \lambda)$ is the load function that defines the spatial features of the surface load. Usually simple loading episode is simulated employing the loading history $f(t) = H(t)$. The surface loads are characterised by load functions of the type:

$$\sigma(\theta, \lambda) = \begin{cases} H_{\mathcal{D}} & if \;\; (\theta, \lambda) \in \mathcal{D} \\ c & if \;\; (\theta, \lambda) \notin \mathcal{D} \end{cases} \tag{2.27}$$

where $\mathcal{D}$ is the load function domain, $H_{\mathcal{D}}$ is a function defined on $\mathcal{D}$ and c is a constant. All most of the surface loads considered in this Thesis are characterized by load functions of the type disc load (with rectangular cross section). In this case the load function is:

$$\sigma(\theta) = \begin{cases} \rho_{ih} & if \;\; 0 \leq \theta, \leq \alpha \\ 0 & if \;\; \alpha < \theta, \leq \pi \end{cases} \,. \tag{2.28}$$

However we use, in Chapter 3 a parabolic cross section to simulate ice accretion. The accumulation and ablation of Pleistocene ice sheets (L_i), together with the complementary variation in ocean bathymetry, constitute the surface load wich drives the glacial isostatic adjustment process:

$$L(\theta, \lambda, t) = L_i(\theta, \lambda, t) + L_o(\theta, \lambda, t) \,, \tag{2.29}$$

$L_i(\theta, \lambda, t)$ are given by Eq. (2.26), and L_o is the water load. To define it, we need to introduce the sea level SL and the sea level change S (Figure 2.1):

$$S(\theta, \lambda, t) = SL(\theta, \lambda, t) - SL_0(\theta, \lambda, t_0) \,, \tag{2.30}$$

where $SL_0(\theta, \gamma, t)$ is the sea level measured at the reference time t_0, and $SL(\theta, \lambda, t)$ is the sea-level measured as the difference between the Earth geoid surface and the Earth solid surface. The water load is

$$L_o(\theta, \lambda, t) = \rho_w S(\theta, \lambda, t) \mathcal{O}(\theta, \lambda, t)\,, \tag{2.31}$$

where ρ_w is the density of water (1000 kg m^3) and $\mathcal{O}$ is the ocean function:

$$\mathcal{O}(\theta, \lambda) = \begin{cases} 1, & (\theta, \lambda) \in \text{oceans} \\ 0, & (\theta, \lambda) \notin \text{oceans} \end{cases}\,. \tag{2.32}$$

In analogy with the ice load Eq. (2.26), the ocean surface load can be defined by:

$$L_i(\theta, \lambda, t) = \sigma^{oc}(\theta, \lambda) f(t)\,, \tag{2.33}$$

where $f(t)$ is the load time-history and $\sigma^{oc}(\theta, \lambda)$is the ocean load function that defines the spatial features of the surface load:

$$\sigma^{oc}(\theta, \lambda) = \frac{m_s^{oc}}{A_{oc}} \mathcal{O}(\theta, \lambda)\,, \tag{2.34}$$

where A_{oc} is the area of the surface of the oceansm_s^{oc} is the static mass of the ocean load:

$$m_s^{oc} = a^2 \int_\Omega \sigma^{oc} d\Omega\,, \tag{2.35}$$

and Ω is the unit sphere.

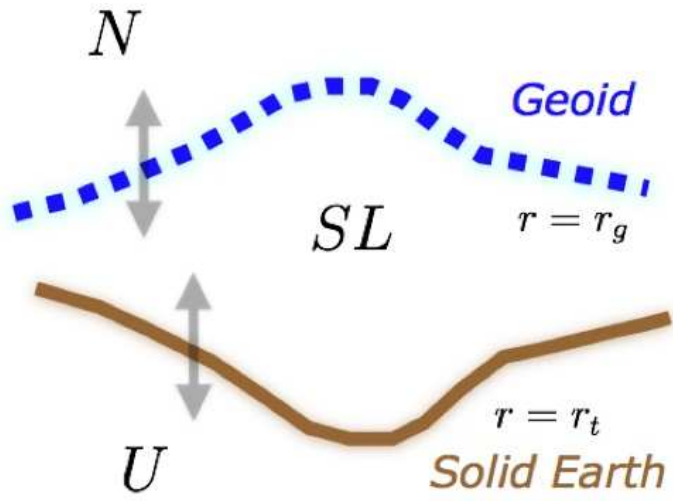

Figure 2.1: the sea level (SL) s the sea-level measured as the difference between the Earth geoid surface (N) and the Earth solid surface (U).

2.2.3 Eustatic term

The eustatic sea level variation is referred to the modification of the oceanic water volume which follows the mass exchange between the cryosphere and the hydrosphere in the absence of any deformational and gravitational effect.

Given a change $m_i(t)$ in the ocean mass, eustasy imposes a spatially uniform sea level change of opposite sign

$$S_E(\theta, \lambda, t) = -\frac{m_i(t)}{\rho_w A_o}\,. \tag{2.36}$$

The S_E plays an important role in solving the SLE. As mentioned in Section 2.2, the unknown sea level variation S appears explicitly to left-hand side of Eq. (2.5), but it is also embedded in spatio-temporal convolution products at the right-hand side. Solving the SLE in absence of any deformational and gravitational effect, we obtain $S = S_E$. In this manner S_E is first solution of the SLE . This is substituted to S on the right-hand side of Eq. (2.5). In this way, a new estimate S is iteratively obtained at the left-hand side. The experience has shown that this procedure quickly converges to a stable solution (Peltier, 1999).

2.2.4 Convolution term

The vertical displacement U and the variation of the gravitational potential N at point ω with coordinates (θ, λ) and time (t) result from displacements and potentials due to changes of the ice and of the oceanic mass distributions at any point (θ', λ') and times $t' \leq t$. This involves a spatial integration over the whole surface of the Earth and a time convolution which accounts for the load time-history and time-dependent response of the viscoelastic mantle. Since GFs for vertical displacement G_u and gravitational potential G_ϕ have similar forms, the spatio-temporal convulutions can be compacted as:

$$\left\{ \begin{array}{c} U \\ N \end{array} \right\}(\omega, t) = \int_{-\infty}^{t} dt' \int_{\Omega} dA' \left\{ \begin{array}{c} G_u \\ G_\phi \end{array} \right\}(\alpha, t - t') L(\omega', t')\,, \tag{2.37}$$

where L is the total load:

$$dA \equiv a^2 \sin\theta d\theta d\lambda\,, \tag{2.38}$$

and α implicitly dependes upon ω and ω' via the cosines formula $\cos\alpha = \cos\theta\cos\theta' + \sin\theta\sin\theta'\cos(\lambda' - \lambda)$. It is useful to intruduce the concise notation:

$$G \otimes_d L(\omega, t) \equiv \int_{-\infty}^{t} dt' \int_{d} dA' G(\alpha, t - t') L(\omega', t')\,, \tag{2.39}$$

where G is a generic GF, L is a generic load and d is a subset of the Earth surface. Hence, using Eq. (2.29) and (2.39) the vertical displacement U the variation of the gravitational potential N related to the ice and oceanic components of the load can be express:

$$\left\{ \begin{array}{c} U_i \\ N_i \end{array} \right\} (\omega, t) = \left\{ \begin{array}{c} G_u \\ G_\phi \end{array} \right\} \otimes_i \rho_i I \,, \tag{2.40}$$

and

$$\left\{ \begin{array}{c} U_o \\ N_o \end{array} \right\} (\omega, t) = \left\{ \begin{array}{c} G_u \\ G_\phi \end{array} \right\} \otimes_o \rho_w S \,. \tag{2.41}$$

By its own definition Eq. (2.29), the total load L depends both on the ice thickness and the sea level variations. While the former can be reasonably assumed to be known from geological or geophysical evidence, the latter will depend, beside on the amount of water exchanged between the ice sheets an the oceans, also on vertical displacement of the solid Earth and geoid height changes, which can only be determined once the sea level changes themselves are known.

2.2.5 Mass Conservation

To obtain the SLE, we need first to evaluate how the surface of the geoid has changed from the reference state to the current state. Both states are characterized by an arbitrary distribution of ice and ocean masses, and they differ by the mass contained in these reservoirs the total mass being unaltered. We assume that solid Earth and geoid slight depart from a sphere having radious $r = r_0$, characterised by a radially varying density. Here we denote with $m_i(t)$ the ice mass variation, where conventionally a positive change denotes accretion. We recall that we are assuming fixed shorelines, so that the shape of the continents is unaltered by the exchange of mass between the ice sheets and the oceans. However in spite many equipotential surfaces

$$r = r_0 + \frac{\Phi}{\gamma} + c \,, \tag{2.42}$$

Φ is the variation of the total gravitational potential with respect to the reference state. Only the one that satisfies the conservation of mass constraint is the radius of the sea surface (G). In this case, the sea level equipotential surface reads:

$$N = \frac{\Phi}{\gamma} + c(t) \,, \tag{2.43}$$

we refer to N as the offset between two equipotential surfaces. where the constant $c(t)$ is introduced in order to ensure the mass conservation, The requirement of mass conservation

can be stated as $\Delta M = 0$, where the mass variation of the system ice + oceans is:

$$\Delta M = m_i(t) + \int_o S\rho_w dA\,. \tag{2.44}$$

Recalling Eq. (2.30), we can write the sea level variations as the difference between the geoid surface N and vertical displacement of the solid surface U. as:

$$S = \frac{\Phi}{\gamma} + c - U\,, \tag{2.45}$$

Substituting S in Eq. (2.44) using Eq. (2.45) we obtain:

$$m_i(t) + \int_o \rho_w \left(\frac{\Phi}{\gamma} + c - U\right) dA = 0\,, \tag{2.46}$$

that gives

$$m_i(t) + c\rho_w \int_o dA + \rho_w \int_o \left(\frac{\Phi}{\gamma} - U\right) dA = 0\,, \tag{2.47}$$

where we assume a constant water density, hence:

$$m_i(t) + c\rho_w A_o + \rho_w A_o \overline{\left(\frac{\Phi}{\gamma} - U\right)} = 0\,, \tag{2.48}$$

where the overbar denotes the average over the surface of the oceans $\overline{(\cdot)} \sim \frac{1}{A_o}\int_o (\cdot) dA$.

Solving Eq. (2.45) for the costant c, we finally provides:

$$c = -\frac{m_i(t)}{\rho_w A_o} - \overline{\left(\frac{\Phi}{\gamma} - U\right)}\,. \tag{2.49}$$

For a rigid Earth, the constant $c(t)$ introduced to conserve mass corresponds to the amount of water exchange between the continental ices and oceans:

$$c(t) = S_E = -\frac{m_i(t)}{\rho_w A_o}\,. \tag{2.50}$$

2.3 SELEN program

To

calculate the GIA effect the improved SELEN 3.2 (Spada and Stocchi, 2007), publically-available program (see *http://www.fis.uniurb.it/spada/SELEN/minipage.html*), is used in this Thesis. The SELEN, writing in Fortran double precision, adopts the pseudo-spectral method of solution, first introduced by Mitrovica and Peltier (1991). The pseudo-spectral approach applies a spatial discretization of the all variables involved (time, ice thickness, vertical and horizontal displacement, gravitational potential, ocean function). The spatial

discretization of the variables is accomplished by means of Spherical Harmonics (SH) expansions, using complex4π-normalized harmonics:

$$\mathcal{Y}_{lm}(\theta,\gamma) = \mu_{lm} P_{lm}(cos\theta) e^{im\lambda}\,, \tag{2.51}$$

where $P_{lm}(cos\theta)$ is the associated Legendre function of degree l and order m, μ is normalization constant. The ice chronologie is discretized assuming a stepwise in the interval $0 \leq t \leq t_N$, where $t = 0$ marks the beginning of deglaciation and $t = t_N$ is present time. The ice models are discretized with the aid of the icosahedral pixelization (Tegmark, 1996), which provides a of equal-weight integration points that allows for a straightforward, nearly optimal quadrature on the sphere, with:

$$\int_{\Omega} f(\omega,t) d\omega \sim \frac{4\pi}{N} \sum_{J=1}^{N_p} f(\omega_j,t)\,, \tag{2.52}$$

where $f(\omega,t)$ is any function defined on Ω, t is time, N_p is the number of pixels, and ω_j is the centroid of pixels coordinates with (θ,γ) colatitude and longitude. Most of the numerical computation performed at global scale, in this Thesis, have been carried out using l_{max} =128 and a geometrical resolution 48 (r) in the Tegmark algorithm that generates the pixels coordinates. We chose l_{max} =128 as good compromise between low CPU time requirements and solution accuracy. According to Tegmark (1996) the number of pixels that compose the sphere (Ω) is $N_p = 40r(r-1)+12 = 90252$ that largely exceeds the minimum number of pixels $N_p^{min} = \frac{l_{max}^2}{3} = 5462$ that ensures an optimal quadrature on the sphere. However at regional scale, in order to capture the short-wavelength component of vertical uplift response to current ice mass loss (see Chapter 4) we push the resolution until l_{max} =1024 and l_{max} =10^5.

SELEN solves the SLE based on Earth radially stratified and incompressible and the various layers are characterized by a linear viscoelastic rheology. In Chapter 3, we test a multi-layered rheological profile according to ALMA publically-available (see *http://www.fis.uniurb.it/spada/ALMA_minipage.html*) code (Spada, 2008). The improved versions SELEN 3.2 takes into accounts the shoreline migration and the rotational feedback. In the following Sections we describe the two key input models to solve the SLE: ice models (Section 2.3.1) and rheological models (Section 2.3.2).

2.3.1 Ice models

The ice sheet history model is needed as input in GIA modeling. The ice models are composed of an aggregate of axis-symmetrical disk-shaped ice element with thickness time

dependent until the LGM. In this study, two different ice histories are used, to predict GIA contribution to GPS data, altimetry, across the polar ice sheets and to coastal sites of Mediterranean area (Figure 2.2). ICE-5G (Peltier, 2004), and ice model developed by the Research School of Earth Sciences (RSES) group at Australian National University (ANU) (Lambeck and Purcell, 2005). We defined this latter ice model as ANU05. Moreover we test the Antarctica regional ice model IJ05 by Ivins and James (2005) to analyze the viscoelastic contribution to GPS data across the Antarctica. In Figure 2.2 the Frames (a) and (b) show (with the thick gray line) the Equivalent Sea Level (ESL) as a function of time of the regional ice history of Antarctica, assumed by IJ05. Also we elaborate two present-day ice melting scenario of GrIS and AIS (see Chapter 4).

ICE-5G

The most widely-used global ice model is the ICE-5G (Peltier, 2004). This is constrained by geological data, changes in gravity as well information from VLBI. ICE-5G is an updated version of ICE-3G and ICE-4G models (Tushingham and Peltier , 1991). It was developed following the introduction of improved ice-dynamic modelling and the availability of new data, including new far-field sea-level histories from equatorial regions(Yokoyama et al., 2000), ice margin data from Siberia (Svendsen et al., 1999), GIA data from the British Isles(Peltier et al, 2002) and geodetic and gravity data from North America (Argus et al, 1999), and finally RSL data from Greenland (Johnsen et al., 1995). ICE-5G assumes 22720 disk of 1 degree of half-amplitude. It defines the time-dependent loads of ice since the Last Glacial Maximum (LGM) occur 21 kyr BP. In particular ICE-5G is characterized by 127.15 m of Equivalent Sea Level (ESL). Most of it is stored in the Laurentide ice sheet (Tarasov and Peltier, 2002) (Figure 2.2). ICE-5G should be used in conjunction with the VM2 Earth model (Peltier, 2004). Recently a improved ice global models ICE-6G was been proposed by Toscano et al. (2011), but has not yet available. Figure 2.2 (a) summarizes the ESL as a function of time of the major land-ice source included within ICE-5G.

ANU05

The ANU05 ice model (Lambeck et al., 2004b) has been based on a combination of field data for ice margins and on inversion of geological sea level and shoreline data. These inversions have been complemented with simple glaciological models when the field

data was incomplete. The ANU05 model includes several regions: Northern Hemisphere, Antarctica, Fennoscandia, Northern Hemisphere Glaciers, Southern Hemisphere Glaciers. The Fennoscandian part of this model, which also covers the Barents Sea, is known as FBK8 (Lambeck, 1995). The GREEN model (Fleming and Lambeck, 2004) describes the Greenland part of ice global model that was been constrain with the RSL indicators across the island. The BK4 British Isles ice model (Lambeck, 1993), and the ANT3 Antarctic model (Nakada and Lambeck, 1988) are include within the ANU05 global ice model. In spite of ICE-5G model, within the Northern Hemisphere Glaciers, ANU05 model include the glaciers of Swiss also. With 29813 ice elements, ANU05 describes a melting rates since 30 kyrs BP, characterized by ESL of 129 m since the LGM set to 21 kyr BP (Fleming et al., 1998). Figure 2.2 (b) summarizes the ESL as a function of time of the major land-ice source included within ANU05.

2.3.2 Rheological models

To analyze the loading effect requires a model, in time and space, for the ice load (analyzed within the above Section 2.3.1) and a model for the Earth structure. The Earth model is used as input to determine a loading Greens functions (Section 2.2.1), which are weighed sums of load Love numbers. SELEN, based on spectral methods, assumes a spherically symmetric, self-gravitating Maxwell visco-elastic Earth. The elastic structure of the Earth is based on the seismic model PREM (Dziewonski and Anderson, 1981) while the thickness of the elastic lithosphere and the viscosity of the mantle are the two variables of the earth model input. One of the earliest estimates of viscosity, based on Holocene RSL curves in Scandinavia, is from Haskell (1935). He finds an average mantle viscosity of 10^{21} Pa s from the base of the lithosphere to a resolving depth of about 1400 km (Mitrovica, 1996). The ICE-3G deglaciation history (Tushingham and Peltier , 1991), constrained by geomorphological data and Holocene sea-level curves, was inferred using a slight deviation from the above mentioned model, by increasing the viscosity of the lower mantle (LM) to $2{\cdot}10^{21}$ Pa s, using a lithospheric thickness (LT) of 120 km (VM1); Tushingham and Peltier, 1991). Peltier (2004) developed a further ice-load history ICE-5G for which the new VM2 viscosity stratification was derived. VM2 rheological profile, assumes a lithospheric thickness of 90 km, an average upper mantle of 0.5 10^{21} Pa s and an average lower mantle viscosity of 2.7 10^{21} Pa s. However lateral variation in material properties occurs within the upper mantle and that corresponding variations in mantle temperature and

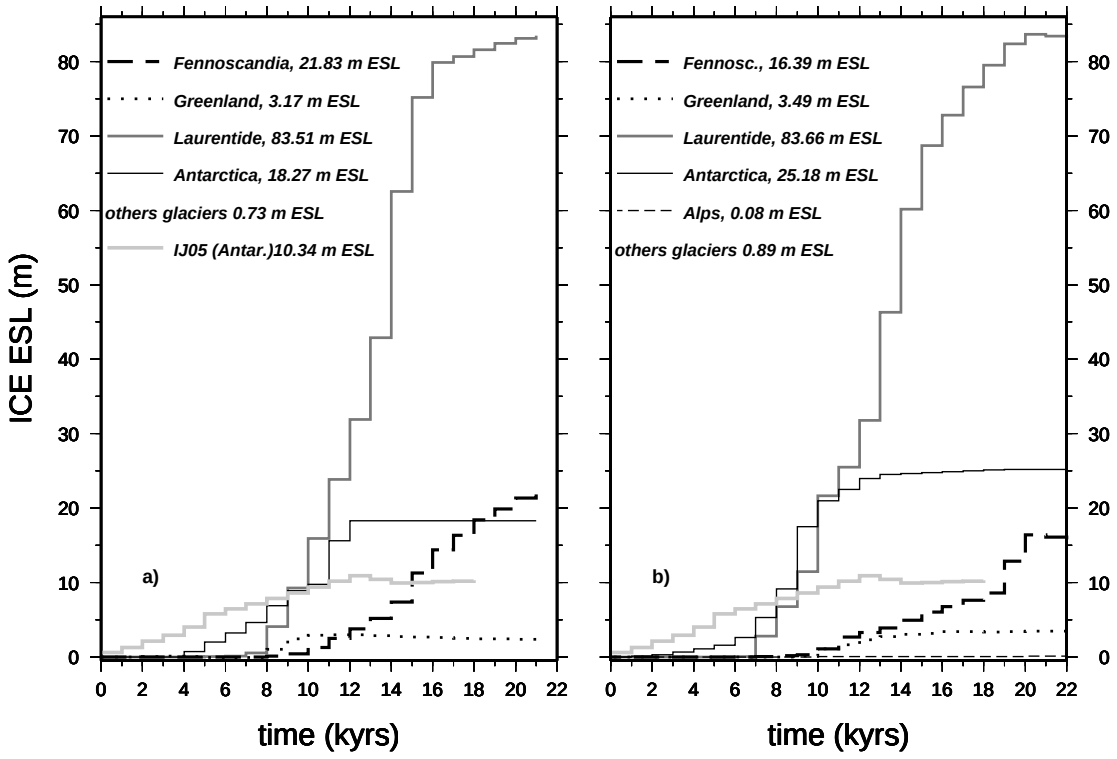

Figure 2.2: The ESL as a function of time of the major land-ice source, constituents of the global ice models. ICE5G in the frame (a) and ANU05 in the frame (b). In both frames we show (with the thick gray line) the ESL as a function of time of the regional ice history of Antarctica, assumed by IJ05.

hence upper mantle viscosity can be expected. Lambeck and Chappell (2001) suggest to overcame this unresolved GIA question using a regional models representative of the region of interest. This imply a wide range error when global GIA predictions are computed (see Chapter 5). Whitehouse (2009) notes that even if regional Earth models are used, the sea-level equation must still be solved in the global domain to ensure the correct redistribution of meltwater in the oceans. The main rheological profiles used in this Thesis are summarized in Table 2.1.

Seismic data (Stein and Wysession, 2003) indicate a low-viscosity zone (LVZ) within the asthenospheric mantle with an order of magnitude smaller the the upper mantle viscosity. This low-velocity zone is associated with ductile flow of mantle convection and

Table 2.1: Radial viscosity profile (Lithospheric thickness (LT) and mantle viscosity η) used to create the ice models described in Section 2.3.1. ANU05 data are taken from Fleming and Lambeck (2004) and Lambeck and Purcell (2005). The volume–averaged VM2 viscosity values are based on (Peltier, 2004). IJ05 rheological profile is employed by Ivins and James (2005).

Layer	Outer radius[a] km	η 10^{21} Pa s	η 10^{21} Pa s	η 10^{21} Pa s	η 10^{21} Pa s	η 10^{21} Pa s
		ICE–5G	ANU05	ANU05	ANU05	IJ05
η_{LM}	5701	2.7	5	10	20	6
η_{UM}	5971	0.5	0.2	0.3 - 0.4	0.5	0.4
η_{LVZ}	6281	0.5	0.2	0.3 - 0.4	0.5	0.4
LT(km)	6371	90	50	80	100	90

[a] The outer radius refers to ICE-5G. However the others models assume different LT thickness and hence different outer radius of LVZ, while outer radius of UM and LM remain the same for all viscosity profile models.

it is strongly dependent on thermal regime. Evidence of LVZ is not found in old and cold cratonic areas as the Baltic Shield (e.g. Steffen and Kaufmann, 2005). In Chapter 3 we aim todescribing ongoing surface movements resulting from recent glacial instabilities, also taking into account the effects associated with shallow upper mantle and crustal rheologies.

Chapter 3

Rheology Models and secular ice sheets fluctuations

3.1 Introduction

Over the last few years there has been a rising interest in the possible effects of low viscosity crustal and asthenospheric layers upon the response of the Earth to surface loading. This was first motivated by geophysical evidence indicating a significant rheological stratification of the lithosphere (Ranalli and Murphy, 1987), and by seismic data suggesting the existence of a low velocity zone except beneath cold cratonic areas (Schubert et al., 2001). Second, the improved spatial resolution of ongoing satellite gravity missions motivates further research in this direction. According to Schotman (2008), results from the ESA's ongoing GOCE mission (http://www.esa.int/SPECIALS/GOCE/index.html) can be used in principle to detect spatial signatures to scales down to $\sim$ 100 km, characteristic of crustal low viscosity zones (Vermeersen, 2003; van der Wal et al., 2004). Nowadays, the potential effects of these rheological features are investigated using various observations related to Glacial Isostatic Adjustment (GIA), ranging from Late Holocene relative sea level data (Kendall et al., 2003) to present–day geodetic measurements (Di Donato et al., 2000; Barletta et al., 2006), in an attempt to constrain their thickness and lateral extent. As recently summarized by Schotman et al. (2009), adopted viscosity values for the "soft" crustal layers, with a typical thickness of $\sim$ 10 km, may range between 10^{17} and 10^{20} Pa·s , e. g. at least one order of magnitude smaller that the traditional GIA value of $\sim 10^{21}$ Pa·s (Haskell, 1935; Tushingham and Peltier , 1991; Spada et al., 1992). For the asthenosphere, similarly low viscosity values are used, consistently with those proposed in the seminal work of Cathles (1975) and in Fjeldskaar (1994).

Within the framework of linear rheologies, the response of the crust and of the shallow upper mantle to surface loads on decade to century time scales is further complicated by possible transient rheological effects (for which the strain rate is not constant in a creep experiment, see e. g. Christensen 1982), which can be modeled using Generalized Maxwell Bodies (GMB). A well known example of transient rheology is given by the Burgers body, in which a steady–state Maxwell and a transient Kelvin–Voigt elements are connected in series (Christensen, 1982; Ranalli, 1995). The resolving power of GIA observations appears to be insufficient to constrain the values of this four–parameters rheological body as well as of other possible GMBs (Yuen et al., 1986; Peltier et al., 1986; Körnig and Müller, 1989; Rümpker and Wolf, 1996). However, on decade to century time scales, it is now clear that transient rheological effects contribute significantly to the post–seismic deformation both on a regional (Pollitz, 2003) and on a global scale (Melini et al., 2008), and therefore they may influence the response of the Earth to recent cryospheric forcing, as first suggested by Sabadini et al. (1988) considering harmonic degree two signatures. For the sake of parsimony, in our study we will consider only one GMB in addition to the Burgers model, namely the Caputo rheology for which Körnig and Müller (1989) have determined a set of best–fitting parameters constrained by relative sea level observations in Fennoscandia and North America. The Caputo rheology (Caputo, 1967), which is characterized by a stress–strain relationship containing fractional time–derivatives (e. g., Mainardi, 2010), remains transient on all time scales. On the other hand, the transient relaxation of the Burgers body is limited to the Kelvin–Voigt element which is disposed in parallel to the Maxwell element in its mechanical analogue (e. g., Mainardi, 2010).

The purpose of this Chapter is two–fold. First, by analyzing the response of a significant number of linear rheological models for the shallow upper mantle and the crust, we aim to determine how surface displacements, at a given harmonic degree, are amplified with respect to the elastic response on time scales from decades to centuries. This is addressed computing loading Love numbers (Love, 1909; Farrell, 1972; Longman, 1962a,b; Munk and MacDonald, 1960) for vertical and horizontal displacements by means of a recently re–discovered numerical method (Spada and Boschi, 2006; Spada, 2008) particularly suitable for complex viscosity profiles in the presence of transient rheological effects. Second, we study the effect of steady–state and transient rheologies in the spatial domain, computing the vertical displacement field in response to the accretion of an ice

sheet with simple geometry. In particular, we focus on the spatial pattern and the time scale of vertical displacements at the ice sheet margins, which are relevant to interpret present and future sea level changes in response to the current continental cryosphere fluctuations. Our results may have contribute to a better assessment of the effects of sudden ice melting upon future sea level rise, which is traditionally estimated using elastic (Mitrovica et al., 2009) or traditional viscosity models (Bamber et al., 2009). The results shown in this Chapter have been published in 2009 within Tectonophiscs (*ice2sea* manuscript number 003) with a title: " Shallow upper mantle rheology and secular ice sheets fluctuations", by Spada, G., Colleoni, F., Ruggieri, G., 2011.

3.2 Methods

All the computations have been performed using ALMA (Spada, 2008), a Love numbers calculator based on the Post–Widder (PW) inverse Laplace formula (Post, 1930; Widder, 1934, 1946). ALMA provides the response functions by–passing the computation of the viscoelastic "normal modes" (Spada and Boschi, 2006), which would demand the solution of a high degree algebraic secular equation whose roots may be difficult to resolve by standard numerical methods (Vermeersen and Sabadini, 1997; Spada, 2008). The basic output of ALMA is constituted by the Heaviside Love numbers h and l (related to vertical and horizontal displacements, respectively) at a given harmonic degree, later employed in Section 3.3.1 to study the response of the Earth to finite–sized surface loads. In view of the geophysical applications in Section 3.3.2, the code has been subsequently modified in order to describe a more complex loading function.

Denoting by $\tilde{x}(s)$ any of the Laplace–transformed Love numbers, the PW formula gives

$$x(t) = \lim_{k \mapsto \infty} \frac{(-1)^k}{k!} \left(\frac{k}{t}\right)^{k+1} \tilde{x}^{(k)}\left(\frac{k}{t}\right) \tag{3.1}$$

(Post, 1930; Widder, 1934, 1946) where t is time, $x(t)$ is the Love number in the time domain, superscript (k) indicates the derivative of order k and the dependence upon the harmonic degree is implicit to simplify notation. The discretization of the derivative and the convergence accelerators, needed to practically employ Eq. (3.1), are detailed in Spada (2008). Following previous experiments by Spada and Boschi (2006) and Spada (2008), carried out using multi–layered PREM models (Dziewonski and Anderson, 1981), all our computations have been performed in a multi–precision environment (Smith, 1989) using

Table 3.1: Density and rigidity profiles for the elastic model and for REF, LVZ, BUR and CAP (see first column of Table 3.2). The numerical values are obtained by volume–averaging the PREM model of Dziewonski and Anderson (1981). Rheological features of mantle layers are described in Table 3.2.

Layer	Radius range (km)	Density, ρ_0 (kg m^{-3})	Rigidity, μ_0 (10^{11} Pa)
Lithosphere	6281–6371	3192	0.596
Shallow upper mantle	5971–6281	3427	0.720
Transition zone	5701–5971	3857	1.064
Lower mantle	3480–5701	4877	2.194
Core	0–3480	10931	0.00

a number of significant digits $D = 64$, and Gaver accelerators of order $N = 8$ (Gaver, 1966; Valkó and Abate, 2004). These settings are suitable also in the case of particularly challenging problems, such as the computation of very high degree Love numbers for finely layered crustal models (see Section 3.3.1).

All the Earth models employed in this study, whose rigidity and density structures are shown in Table 3.1, share an incompressible rheology. The existence of gravitationally unstable Rayleigh–Taylor modes in compressible Earth models (see e. g., Hanyk, 1999) prohibits the use of the PW inversion method implemented in ALMA, which requires regularity of $\tilde{x}^{(k)}$ along the real positive axis of the Argand plane (see Eq. 3.1). Since this work mainly focuses on the response of the shallow upper mantle to short–term surface loading, we keep constant the lithosphere and lower mantle rheological parameters to values listed in Table 3.2 (we have directly verified that the thickness of the lithosphere has negligible effects upon the Love numbers compared to those produced by the rheological layering of the mantle).

The Earth models considered here can be classified into two distinct groups. The first, which encompasses Maxwell (e. g., steady–state) rheological models, includes the elastic model, REF, LVZ and BRL. In the shallow upper mantle, REF and LVZ are characterized by a reference viscosity value of 10^{21} Pa·s and by a low viscosity zone with viscosity ranging between 10^{18} and 10^{20} Pa·s , respectively. BRL is characterized by a finely layered crust that exactly reproduces the rheological structure described by Barletta et al. (2006). The second group accounts for upper mantle rheologies derived from two GMBs (Christensen, 1982; Körnig and Müller, 1989), namely Burgers (BUR, Burgers, 1935) and Caputo (CAP) bodies (Caputo, 1967; Wieczerkowski and Wolf, 1998).

Table 3.2: Shallow upper mantle complex rigidity and rheological parameters used in this study (radius in the range $5971 \leq r \leq 6281$ km). [] Except for BRL, all these models include a homogeneous 90–km thick elastic lithosphere, a lower mantle with viscosity 2×10^{21} Pa · s, and a homogeneous inviscid core (see alsoTable 3.1).

Model	Rheology	Rigidity, $\tilde{\mu}(s)$	Material parameters
Elastic[a]	Elastic	μ	$\mu = \mu_0$
REF	Maxwell	$\dfrac{\mu s}{s + \mu/\eta}$	$\mu = \mu_0,\ \eta = 10^{21}$ Pa·s
LVZ	" "	" "	$\mu = \mu_0,\ \eta = 10^{18} \div 10^{20}$ Pa·s
BRL[b]	" "	$\dfrac{\mu(r) s}{s + \mu(r)/\eta(r)}$	see Barletta et al. (2006)
BUR	Burgers	$\dfrac{\mu s(s+\frac{\mu'}{\eta'})}{s^2+s(\frac{\mu}{\eta}+\frac{\mu+\mu'}{\eta'})+\frac{\mu\mu'}{\eta\eta'}}$	$\mu = \mu_0,\ \eta = 10^{21}$ Pa·s $\mu' = 0.3\mu_0,\ \eta' = 0.1\eta$
CAP[b]	Caputo	$\mu_0 \dfrac{(s\tau_c)^\gamma}{1 + (s\tau_c)^\gamma}$	$\tau_c = 6.3 \cdot 10^9$ s, $\gamma = 0.8$

[a]Mantle elasticity is practically realized using a very large Maxwell viscosity ($\eta = 10^{50}$ Pa · s).

[b]The BRL model is characterized by complex, piecewise radially dependent rigidity $\mu = \mu(r)$ and viscosity $\eta = \eta(r)$ in the crust and in the shallow upper mantle, as described in Table 2 of Barletta et al. (2006).

[c]The numerical value of the time scale τ_c, adopted from Körnig and Müller (1989), is close to the η/μ ratio (e. g., the intrinsic Maxwell relaxation time for the upper mantle) for the REF model.

Differently from the first group, they are characterized by a transient behavior. However, while the response of CAP is fully transient, BUR combines steady state and transient behaviors (e. g., Mainardi, 2010).

3.3 Results

The effects of shallow upper mantle rheological layering are first described in Section 3.3.1 by analyzing the response to individual harmonic components of loading. This is done

considering the vertical (h) and horizontal (l) Love numbers in response to a Heaviside surface load history. Then, in Section 3.3.2, we simulate the vertical displacements induced by the slow accretion of an ice sheet of parabolic cross section, in order to determine the time scales of relaxation when a full spectrum of harmonics are simultaneously accounted for. We focus both on vertical movements at the center and at the margins of the ice sheet. In the context of global climate change, these latter movements are relevant to regional relative sea level variations in response to present and future glaciers and ice sheets fluctuations (Sheperd and Wingham, 2007).

3.3.1 Spectral domain

In this section we consider separately the effects of three important rheological features: *i)* a low viscosity zone in the shallow upper mantle, *ii)* transient components of mantle relaxation, and *iii)* ductile crustal layers. The time evolution of vertical (h) and horizontal (l) Love numbers for the fundamental mode of harmonic degree $n = 2$ which correspond to these three rheological models are shown in left frames of Figures. 3.1, 3.2 and 3.3, respectively. Because we have verified that the sensitivity of the gravitational potential Love number (k) to rheological stratification in the upper mantle is comparable to that of h, we will only display numerical results concerning h and l. Since Eq. (3.1) by–passes the computation of the viscoelastic normal modes (Spada and Boschi, 2006), the analysis in the spectral domain cannot be performed looking at individual relaxation modes and time scales, as done by Rümpker and Wolf (1996) and previously, for a spherical Earth, by Yuen et al. (1986) and Peltier et al. (1986). Since the Post–Widder formula does not provide the relaxation time–scales of the Earth model (Spada and Boschi, 2006), we estimate them studying the Heaviside Love numbers, which provide the "creep response" (Christensen, 1982) of our Earth model. Of course, estimates of the relaxation times could be performed by least squares methods, as done by Hanyk (1999).

To quantify the effects of rheological layering upon a wide range of harmonic degrees, in the right frames of Figures. 3.1, 3.2 and 3.3 we show the rheological amplification ratio (hereafter RA), defined as

$$\mathrm{RA}_n(t) = \left| \frac{x}{x^e} \right|, \tag{3.2}$$

where n is harmonic degree, x indicates any of the Heaviside Love numbers (h or l) for a given viscoelastic rheology while x^e is the same Love number computed for a purely elastic Earth (e. g., neglecting the effects of viscoelastic relaxation).

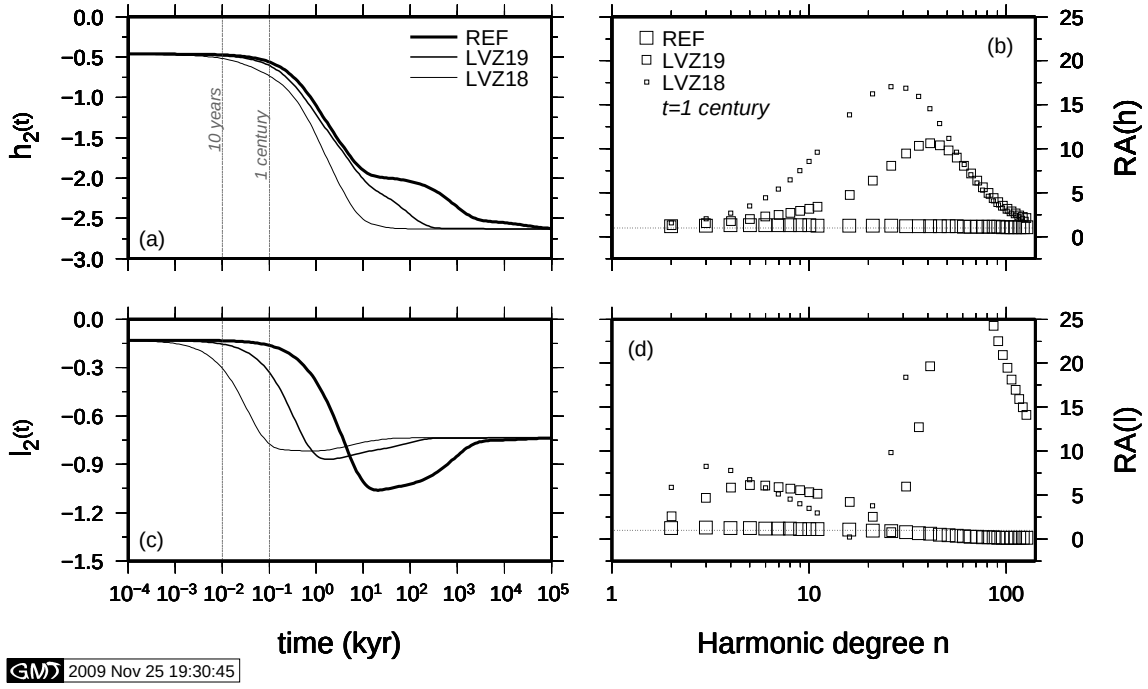

Figure 3.1: Harmonic degree two vertical (a) and horizontal (c) Heaviside Love numbers for the REF and two LVZ models. The Love numbers are displayed across a wide time window ranging from ~ 30 days to 0.1 Gyr. Decade and century time scales are marked by vertical lines. Frames (b) and (d) show rheological amplification factors RA (defined by Eq. 3.2), in the range of harmonic degrees $2 \leq n \leq 128$, for the same models considered in (a) and (c), computed at time $t = 0.1$ kyr. The value RA=1, for which the Love numbers attain their elastic amplitudes, is marked by a dotted horizontal line.

Low viscosity zone

Figures. 3.1a and 3.1c show the time evolution of the vertical and horizontal Love numbers at harmonic degree $n = 2$ for the REF and two LVZ models (characterized by a low viscosity shallow upper mantle), respectively. The Love numbers, displayed in a very broad time window, are characterized by short and long time scales asymptotes corresponding to their "elastic" ($t \mapsto 0$)and "fluid" ($t \mapsto \infty$) responses, and intermediate fluctuations whose amplitude and time scale reflect the rheological layering of the Earth model (see e. g., Vermeersen and Sabadini, 1997). Elastic response only depends on the elastic structure, given in Table 3.1, which does not change between the models; fluid response only depends on buoyancy effects due to internal density contrasts and on the flexural rigidity of the elastic lithosphere. Hence, for a given Earth structure (e. g., density

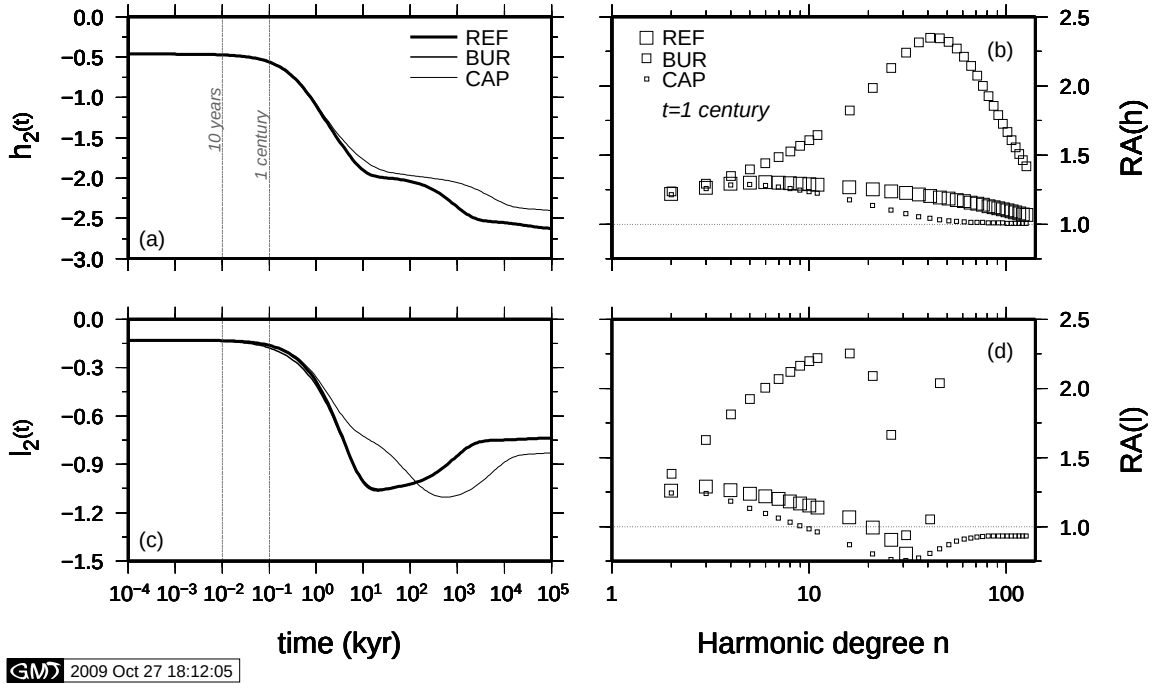

Figure 3.2: Frames (a) and (c) show harmonic degree two Heaviside Love numbers resulting from REF model and from generalized Maxwell rheologies (BUR and CAP), respectively. BUR results are barely discernible in (c). Frames (b) and (c) show RA factors at time $t = 0.1$ kyr as a function of harmonic degree in the range $2 \leq n \leq 128$, for the BUR and CAP transient rheological models.

and rigidity profile) elastic and fluid responses are insensitive to prescribed viscosity values and therefore the asymptotes in Figures 3.1a and 3.1c are the same for the LVZ and REF models.

Since our interest focuses on short term ice sheets fluctuations, in Figure 3.1a we have indicated with vertical lines on the decade and on century time scales. For the REF model, characterized by a mantle viscosity profile that has been long employed in the GIA community (e. g., 10^{21} Pa·s in the shallow upper mantle and transition zone, and 2×10^{21} Pa·s in the upper and lower mantle, respectively, see Tushingham and Peltier , 1991) these long–wavelength Love numbers do not show significant deviations from their elastic asymptotes, even on a century time scale. However, as expected from basic physics, the opposite is true when a LVZ is accounted for, due to the shorter Maxwell relaxation times involved. In this case, the degree two responses deviate from the elastic values, even on the time scale of a few decades. Horizontal movements (Figure 3.1c) show a larger

sensitivity to the presence of the LVZ compared to vertical ones (3.1a), in agreement with previous GIA investigations (e. g., Vermeersen and Sabadini, 1997).

Figures. 3.1b and 3.1d show the ratio RA at time $t = 1$ century for models REF and LVZ. Mantle rheology generally imposes an amplification of the elastic Love numbers (RA ≥ 1) on the range of harmonics considered here ($2 \leq n \leq 128$). For LVZ, peak values (RA ≥ 10) are obtained for $20 \leq n \leq 50$ for the vertical Love number (Figure 3.1b) and even larger effects for $n \geq 20$ are observed on the horizontal ones (Figure 3.1d). Some features of the RA curves in have a straightforward explanation. For instance, the relatively small value of $RA(h)$ for low n values, (Figure 3.1b), is justified by the larger sensitivity of low degree harmonics of vertical displacements to the bulk viscosity of the mantle (Vermeersen and Sabadini, 1997) rather than to relatively small, shallow features as the LVZ. Due to flow channeling, horizontal motions are more affected by the presence of a LVZ, especially for low n values, consistently with Figures 3.1a and 3.1c. This agrees

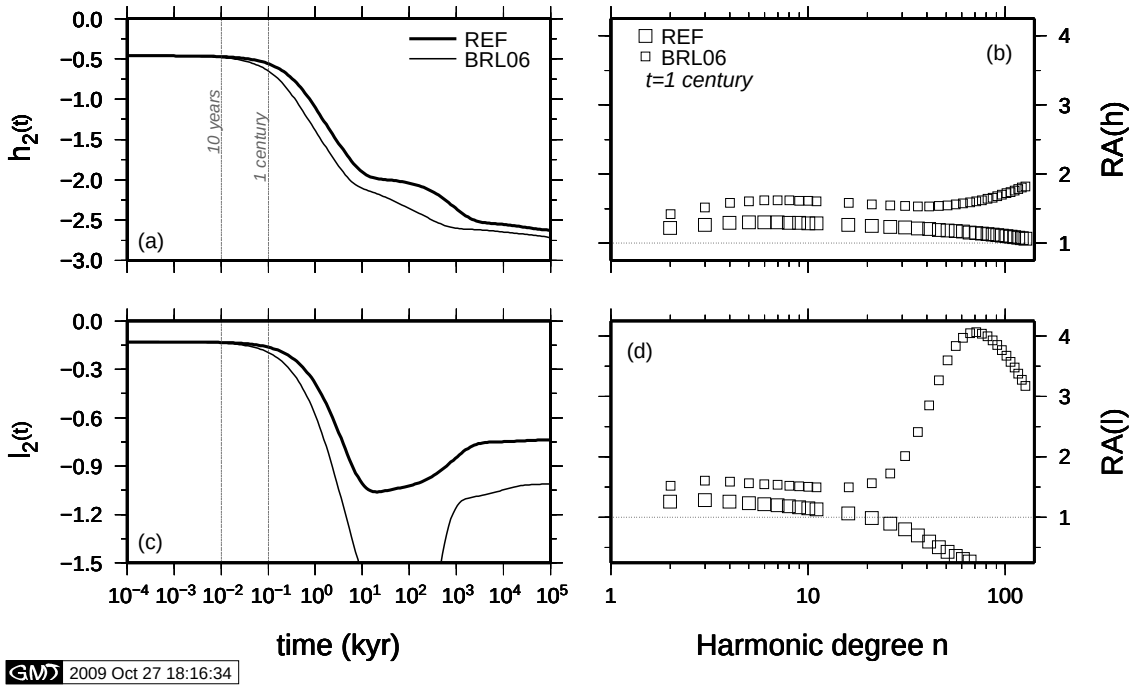

Figure 3.3: In frames (a) and (c) we show harmonic degree two Heaviside Love numbers for the REF model compared with those obtained by the BRL stratification described in Table 2 of Barletta et al. (2006). RA factors at time $t = 0.1$ kyr for the REF and BRL rheological models in the range of harmonic degrees $2 \leq n \leq 128$ are shown in frames (b) and (d), respectively.

with previous results (see e. g., Spada et al., 1992) since the importance of horizontal displacements was first recognized by James and Morgan (1990). The trend of all RA curves is to converge for large n values, when the sub–lithospheric rheology tends to be less important, and the REF and LVZ models are expected to provide comparable (and essentially elastic) responses. Due to the relatively thin lithosphere, however, convergence indeed occurs for $n \gg 128$, the maximum degree considered. The largest values of $RA(h)$ are obtained for LVZ18. This is not the case for l (Figure 3.1d), for which the sensitivity to the LVZ viscosity varies considerably with n. For $n \approx 20$, $RA(l)$ values for LVZ approach REF, and l changes its sign (this causes the cusp feature in Figure 3.1d).

Generalized Maxwell rheologies

The response of the Earth to a harmonic degree two surface load in the presence of transient rheological effects is considered in Fig. 3.2. Numerical values of the material parameters for the Burgers (BUR) and Caputo (CAP, showing a transient behavior at all times) GMBs are given in Table 3.2. Instead of exploring the parameters space of these two rheologies, as done by Rümpker and Wolf (1996) in a flat Earth approximation, here we use the best–fitting values determined in the case of Fennoscandia from the study of Körnig and Müller (1989) (notice, however, that the transient viscosity for the Burgers body is reduced by a factor of ten with respect to the preferred value of Kornig and Müller, which facilitates the study of short–times effects). We limit our attention to the BUR and CAP GMBs, leaving the study of the response of the Lomnitz and of the Q power–law body (see e. g., Körnig and Müller, 1989) to future investigations.

Comparison between Figures 3.2a and 3.2c with the corresponding frames of Figure 3.1 shows that long–wavelength vertical displacemens are by far more sensitive to the Maxwell LVZ than to BUR or CAP transient rheologies. No deviations from the reference model is basically observed even on millennia time scales, and these effects are found to be small for longer periods. BUR results are superposed to REF on all time scales. These findings appear at odds with the analysis of Sabadini et al. (1988), who pointed the importance of mantle relaxation to low degree harmonic loads (up to $n = 9$) even for time scales shorter than a century. However, the results of Sabadini and colleagues pertain to the lower mantle, while here we are only concerned with transient components of shallow upper mantle rheology, which are expected to produce significant effects upon deformations of shorter wavelength. Furthermore, it is well possible that

rheological transient parameters different from those employed here may provide a larger amplification of the harmonic degree two response.

The time evolution of the harmonic degree two horizontal Love number, displayed in Fig. 3.2c, shows some interesting features. In the time window between one decade and one century, no significant relaxation is observed for the CAP solution, which matches closely the REF results. The BUR results are virtually indistinguishable from REF at all time scales. A remarkable finding is the very long time scale required for the CAP model to reach isostatic equilibrium at this harmonic degree, certainly exceeding 10^5 kyrs. However, a isostatic limit will certainly be reached even if CAP is transient at all times, since the CAP complex shear modulus $\tilde{\mu}(s)$ vanishes for long times (e. g., when the complex variable $s \mapsto 0$) as in the case of the steady state Maxwell rheology (see Table 3.2). A similar, but less pronounced, departure from equilibrium is also observed for vertical movements (see Figure 3.2a). The physical reason for the long–standing global isostatic disequilibrium imposed by the CAP rheology is unclear at this stage. From further computations, not shown here, we find that such a long relaxation is not motivated by the form of the effective shear modulus and the numerical values of upper mantle rheological parameters adopted here (see Table 3.2). We therefore argue (but a rigorous demonstration would demand the computation of internal stress fluctuations) that the Caputo rheology enhances the degree of mechanical shear coupling between lower and upper mantle, also possibly delaying the return to equilibrium of compositional internal boundaries which are known to be intrinsically characterized by long relaxation times (e. g., Spada et al., 1992).

The RA factors for generalized Maxwell rheologies, shown in Figures 3.2b and 3.2d, clearly indicate that model CAP is characterized by a modest amplification at all wavelengths with RA close to 1, which makes it similar to REF on the century time scale. For high–degree vertical displacements, CAP is more elastic than REF, while for horizontal displacements, the CAP results are always found below the elastic response. A more complex response is exhibited by BUR, with a response similar to LVZ19 for vertical movements (compare with Figure 3.1b), but an amplitude reduction by a factor of ~ 4. Similarly to the LVZ results, BUR RA factors for horizontal love numbers are bimodal as a function of degree, but their amplitude is greatly reduced.

Ductile crustal layers

Amongst the various models characterized by a ductile crust available from the literature (see the Introduction and the review of the "CLVZ" models in Schotman, 2008), here we consider the one proposed by Barletta et al. (2006) in their study about the vertical uplift in response to the shrinkage of the current alpine glaciers. This model (here referred to as BRL) is inspired to the work of Burov et al. (1999), based on thermo–mechanical modeling of crustal and lithospheric structures beneath the alpine chain. BRL is characterized by a 18.5–km thick effectively elastic upper crust (Maxwell viscosity is 10^{35} Pa·s), a 11.5–km ductile crust with viscosity of 2.15×10^{19} Pa $\cdot$ s, a further 10–km thick crustal layer that includes the Moho, with viscosity of 5×10^{21} Pa $\cdot$ s, and a wide, 630–km thick, low viscosity upper mantle with viscosity 4.64×10^{20} Pa·s. Deeper down, mantle viscosity takes the classical "Haskell value" (10^{21} Pa $\cdot$ s). Hence, differently from our REF model (see Table 3.1), BRL does not include an elastic lithospheric mantle, and its sub–crustal low–viscosity region is ~ 2 times thicker than the REF shallow upper mantle. Numerical values of rheological and physical parameters of BRL, essentially inspired to Burov et al. (1999), are given in Table 2 of Barletta et al. (2006) and will not be repeated here. We are aware that more sophisticated approaches are however possible to describe the rheology of the crust, using the theory of composite materials to account for the presence of rheological heterogeneities (Ivins and Sammis, 1996), and consequently including transient rheological effects.

From Figures. 3.3a and 3.3c it is apparent that significant departures of the BRL results relative to REF are only possible on time scales of approximately one century, as far as we consider the harmonic degree two response. Both vertical and horizontal displacements show a remarkably long relaxation time (longer than the one observed using LVZ models in Figure 3.1), with the latter greatly amplified with respect to REF due to the shear weakness of the relatively thick low viscosity sub–crustal layers in model BRL. With increasing time, deviations of BRL with respect to REF can be attributed to the delayed flow in the ductile crustal layer.

The RA factors for BRL model, shown in Figures 3.3b and 3.3d at time $t = 1$ century, indicates that with the rheological parameters employed for this model, we should not expect dramatic viscoelastic amplifications of vertical movements (RA ≤ 4). This is fairly consistent with the results of Barletta et al. (2006). Nevertheless, horizontal movements, not considered in the analysis of Barletta et al. (2006), show a large peak

in the RA factor for $n \approx 100$, which may have consequences on the interpretation of regional horizontal deformations pattern in the alpine region (Stocchi et al., 2005). The peak of $RA(l)$, already noticed by Klemann and Wolf (1999), can be attributed to the buoyancy mode associated with the density jump across the ductile crustal layer, which is also responsible for the observed increase of $RA(h)$ for large n.

For small scale surface loads, such as those involved in the mass variations occurring across the Alps, a high–resolution approach is required, especially for the assessment of vertical movements in the near field of the glaciers, as pointed by Barletta et al. (2006) (of course, the flat Earth approximation may constitute a valid alternative approach in this context, as discussed by Rümpker and Wolf, 1996). Our implementation of the traditional viscoelastic normal modes method may fail for large harmonic degrees (Spada, 2008) and failures are indeed possible even for fundamental, low degree harmonics (Spada and Boschi, 2006). For these reasons, in order to solve this challenging numerical problem, we use for the first time our numerical implementation of the PW formula for the computation of Love numbers of very large harmonic degree. Validation tests of the PW formula are given in Spada and Boschi 2006. Vertical (left) and horizontal (right) Love numbers for the BRL model, displayed in Figure 3.4, correspond to the elastic

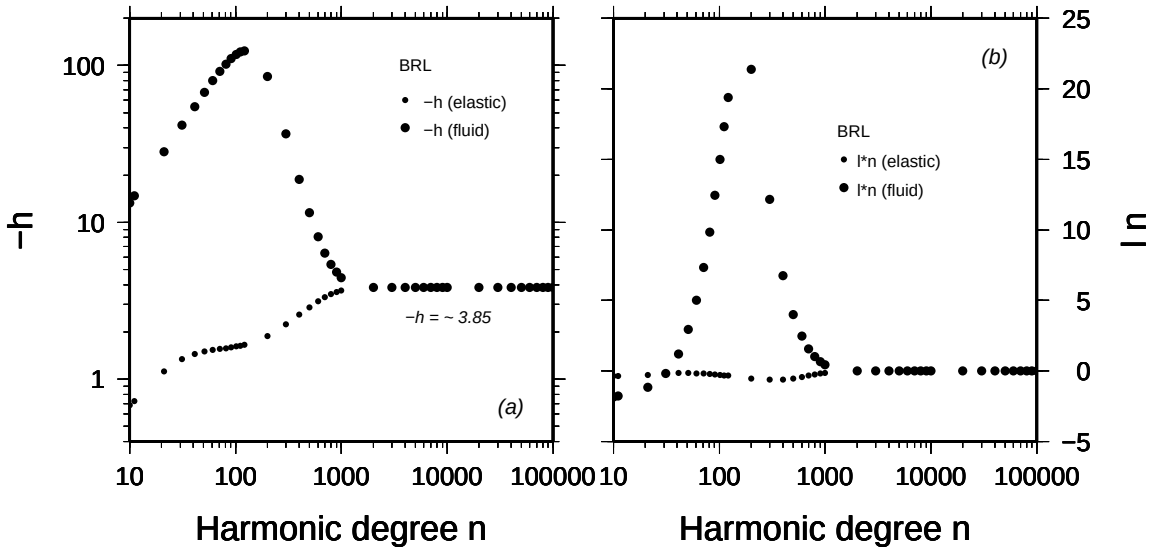

Figure 3.4: Elastic ($t = 10^{-4}$ kyr) and fluid ($t = 10^{6}$ kyrs) asymptotes of vertical (a) and horizontal (b) Love numbers in the range $10 \leq n \leq 100,000$ for model BRL. Note that in (a) $-h$ is shown and the y–axis is logarithmic. In (b), the product $l \cdot n$ is shown.

and fluid regimes, respectively, for degrees in the range $10 \leq n \leq 10^5$. As far as n exceeds $\sim 2,000$, fluid and elastic responses practically coincide, indicating that at these wavelengths the viscoelastic relaxation is totally prevented by the flexure of the elastic crustal layer. Differently from Barletta et al. (2006), very large degree Love numbers have not been extrapolated from values obtained for smaller n values, but directly computed using software ALMA (Spada, 2008). For the vertical Love number, the asymptotic value $h = -3.82$ computed by Barletta et al. (2006) is matched to within 1%. For the horizontal Love number, no comparison with independent computations is presently possible; from Figure 3.4, we observe that product nl vanishes for $n \mapsto \infty$.

3.3.2 Spatial domain

Once the Love numbers are computed, the displacements in the spatial domain can be retrieved by standard methods (see e. g. Spada, 2003). We will focus on vertical displacement, since this is directly related to regional sea level variations. Instead of solving the sea level equation in its complete form (Spada and Stocchi, 2006), we neglect the effects from oceans self–gravitation, which in the near field of the load are blurred by the direct effects of surface loading. This approximation has been also adopted and discussed in the numerical study of Spada et al. (2006). However, differently than in Spada et al. (2006), here vertical displacements accounts for self–gravitation of the solid Earth (e. g., the "k" loading Love number is $k \neq 0$), whose effects are not negligible for long–wavelength deformation (Wu and Ni, 1996). Assuming axially symmetric surface load, sea level change is

$$S(\theta, t) = -U(\theta, t) + S^E(t), \tag{3.3}$$

where U is vertical displacement, S^E is the eustatic (e. g., spatially uniform) component of sea level change, and θ is colatitude with respect to the center of the load (see e. g., Spada and Stocchi, 2006). While $S^E(t)$ is only dependent upon variations of the mass of the ice sheets, vertical displacement is sensitive to rheology. The expression of the Laplace–transformed vertical displacement is

$$\tilde{U}(\theta, s) = \frac{3}{\rho_e} \sum_{n=0}^{n_{max}} \frac{\sigma_n}{2n+1} \tilde{h}_n(s) \tilde{f}(s) P_n(\cos\theta), \tag{3.4}$$

where ρ_e is the average density of the Earth, σ_n is the spectral density of the surface load and $P_n(\cos\theta)$ is Legendre polynomial of harmonic degree n (Spada, 2003). Here we use a load with a parabolic profile of half–amplitude α (see Equation 3.78 in Spada,

2003). Since the load profile is continuous (but its gradient is not) for this geometry, the Gibbs phenomenon is mitigated. Hints on how to deal with load profiles including jump discontinuities are given by Barletta et al. (2006). Due to the factor $(2n+1)$ at the denominator of Eq. (3.4) and to the n–dependence of σ_n and $P_n(\cos\theta)$, the sensitivity of $\tilde{U}(\theta, s)$ to the shallow upper mantle rheology cannot be simply guessed from the spectral Love numbers analysis of Section 3.3.1. Function $\tilde{f}(s)$ represents the Laplace transform of the time history of the surface load:

$$\tilde{f}(s) = \frac{1}{s} \cdot \frac{1 - \exp(-s\tau)}{s\tau}, \tag{3.5}$$

where τ is the duration of the accretion phase (for $\tau \mapsto 0$, $\tilde{f}(s) \mapsto 1/s$, the Laplace transform of the Heaviside step function $H(t)$). The final maximum thickness of the ice sheet is chosen so that its accretion occurs at the constant rate of 10 cm yr^{-1} during a time period of $\tau = 1$ kyr (these rates are comparable with current elevation rates observed in some coastal areas of Antarctica, see Sheperd and Wingham, 2007, and references therein). Eq. (3.4) is inverted in the time domain using the PW formula given by Eq. (3.1). Of course, the meaning of the results below, and particularly the sensitivity of $U(\theta, t)$ to upper mantle rheology, would be unchanged in case of melting (in the case of melt, the rates of displacements would simply reverse sign.)

The vertical displacement obtained using Eq. (3.4) is shown in Figure 3.5 as a function of θ, at time $t = 0.3$ kyr after the beginning of loading, using $n_{max} = 512$. Here $\alpha = 15°$, which results in a disc load comparable to the Antarctic ice sheet (the effects of varying α will be considered at the end of this Section). The results, shown in Figures 3.5a and 3.5b for classical Maxwell and GMBs, respectively, indicate that significant departures from the elastic solution (dashed curves) are expected for many of the rheological models considered, at all the spatial scales. The REF solution is qualitatively similar to the elastic one that shows a slightly enhanced amplitude and negative values on the whole range of colatitudes. Introducing additional rheological features, enhances local compensation and amplifies the deformations beneath the load by a factor ranging between 1 and ~ 3. In addition, we observe a modification of the pattern of vertical movements at the ice sheet margins, showing, for LVZ18 and LVZ19, the development of lateral forebulges whose amplitude amounts to $\sim 1/3$ of the central subsidence; for a stiffer low viscosity zone (LVZ20), the response is similar to REF. On the time–scales considered here, forebulges do not develop when generalized Maxwell rheologies are considered. The history of uplift at the ice sheet center ($\theta = 0$) is shown in Figure 3.6, where we consider separately

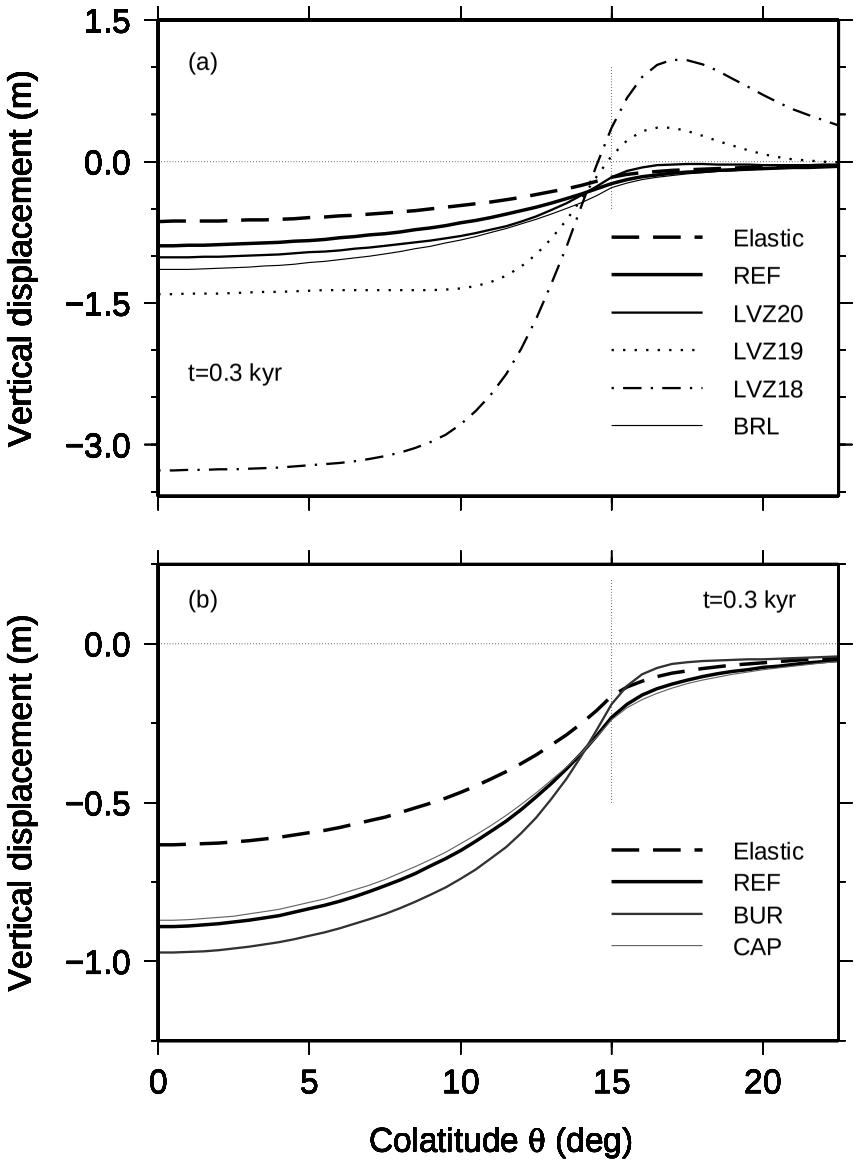

Figure 3.5: Vertical displacement, computed by Eq. (3.4) at time $t = 0.3$ kyr beneath the load and in its near field periphery, for the Maxwell (a) and generalized Maxwell rheologies (b) considered in this study, compared with elastic and REF solutions. The ice sheet extent ($\theta = \alpha$) is marked by a vertical dashed line.

Maxwell (Figure 3.6a) and generalized Maxwell rheologies (Figure 3.6b), in a time window of 0.5 kyr. On these time scales, the rate of deformation as the ice sheets develops is nearly constant for all the models considered, except for LVZ18, which clearly shows an acceleration. As expected on physical grounds, rates of deformation at the ice sheet center increase monotonously with decreasing bulk viscosity in the shallow upper mantle

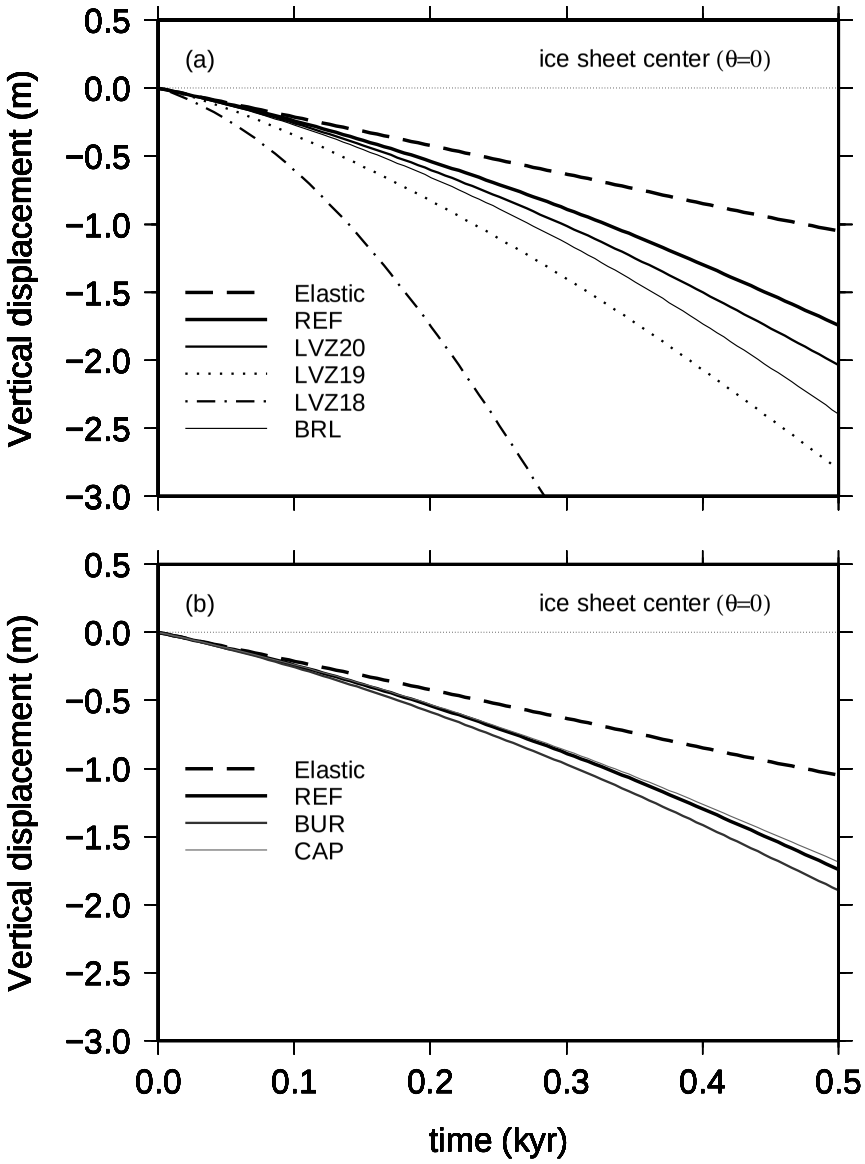

Figure 3.6: Vertical movements at the center ($\theta = 0$) of the ice sheet considered in Figure 3.5, as a function of time after the beginning of loading, for Maxwell (a) and generalize Maxwell rheologies (b).

and it is apparent that deviations from the elastic predictions can only be significant after a few centuries from the onset of the glacial episode, unless we assume model LVZ18. Figure 3.6b shows that the sensitivity of central deformation to transient rheological components is modest, since BUR and CAP results are basically indistinguishable from the REF response. However, on the whole time scale considered, the total viscoelastic displacement the GMB rheologies amounts to ~ 2 times the elastic displacement.

The history of vertical deformation at the ice sheet margin ($\theta = \alpha$) is shown in Figure 3.7, for Maxwell (Figure 3.7a) and generalized Maxwell rheologies (Figure 3.7b), respectively. The elastic solution (thick dashed line), which follows the linear load time history, indicates vertical velocities close to 0.5 mm yr^{-1}. The introduction of a rheological layering in the shallow upper mantle may alter the elastic response in two ways. First,

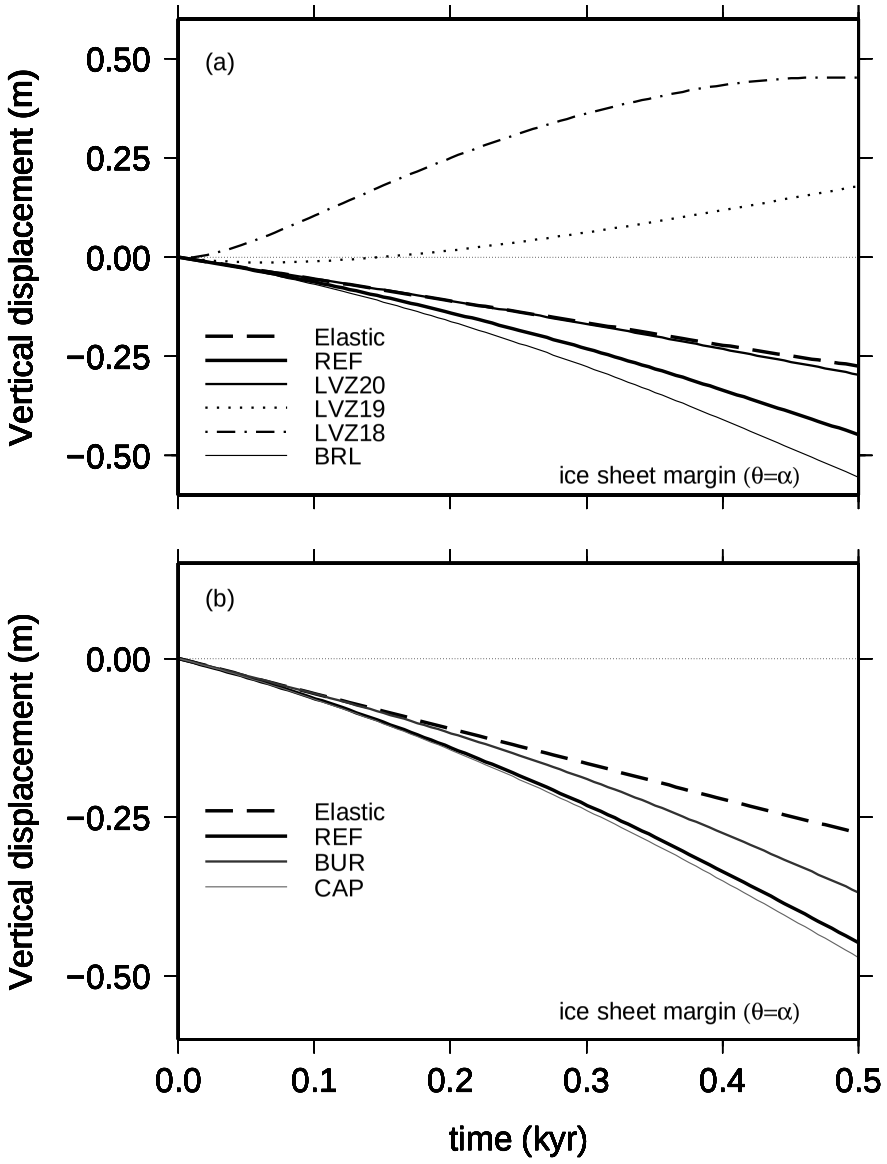

Figure 3.7: Vertical movements at the margin ($\theta = \alpha$) of the ice sheet considered in Figure 3.5, as a function of time after the beginning of loading. Frames (a) and (b) show results for Maxwell and generalized Maxwell rheologies, respectively.

the latter can be subjected to a viscoelastic amplification, without showing a significant acceleration in the time period considered. Such apparently elastic response, also observed by deformations at the load center (Figure 3.6), can be noted when the Maxwell REF and BRL models are employed (Figure 3.7a), but also when transient rheologies are considered (BUR and CAP, Figure 3.7b). Remarkably, for all generalized Maxwell rheologies the responses stand below the elastic solution, which indicates that these GMBs always imply, at the load margins, an amplification of the elastic response of the Earth (this is indeed also true at the center of the load, see Figure 3.6). The second modification of the elastic response is observed in Figure 3.7a for the LVZ models. One one hand, for LVZ19, our predictions show vanishing vertical movements during the first century, and a subsequent deformation at a rate comparable to REF, but with opposite sign (uplift). LVZ18, on the other hand, produces an uplift since the onset of loading, characterized by a complex time evolution. For LVZ20, the history of vertical displacement closely follows the REF predictions.

From GIA investigations (e. g., Spada et al., 1992), we know that the response to surface loading is expected to depend, beside mantle rheological layering, upon the size of the load compared to the thickness of the elastic lithosphere. This sensitivity is studied in Figure 3.8, where vertical displacement at the ice sheet margin ($\theta = \alpha$) is shown for various values of α after three centuries since the onset of loading, keeping fixed the accretion rate of the ice sheet at 10 cm yr^{-1}. The results show two distinct behaviors with varying α. For models REF, BRL and CAP, as well as for the elastic solution, displacements are weakly dependent upon the size of the load and their absolute value decreases with decreasing α. On the contrary, when LVZ and BUR models are considered, it increases with decreasing α until $\alpha \sim 2^\circ$ (for this value, the horizontal extent of the load is comparable with the thickness of the LVZ), and suddenly decreases for smaller values of the load size, when the elastic lithosphere compensates the load by its flexural rigidity. For $\alpha \sim 2^\circ$, a significant divergence from the elastic values is observed. The largest effects are found for model LVZ18 and relatively small values of α, when at the ice sheet margin the response of the asthenosphere enhances the elastic response by a factor of ~ 10. The rheological amplification effect decreases with increasing viscosity in the LVZ and is moderate for the BUR rheology.

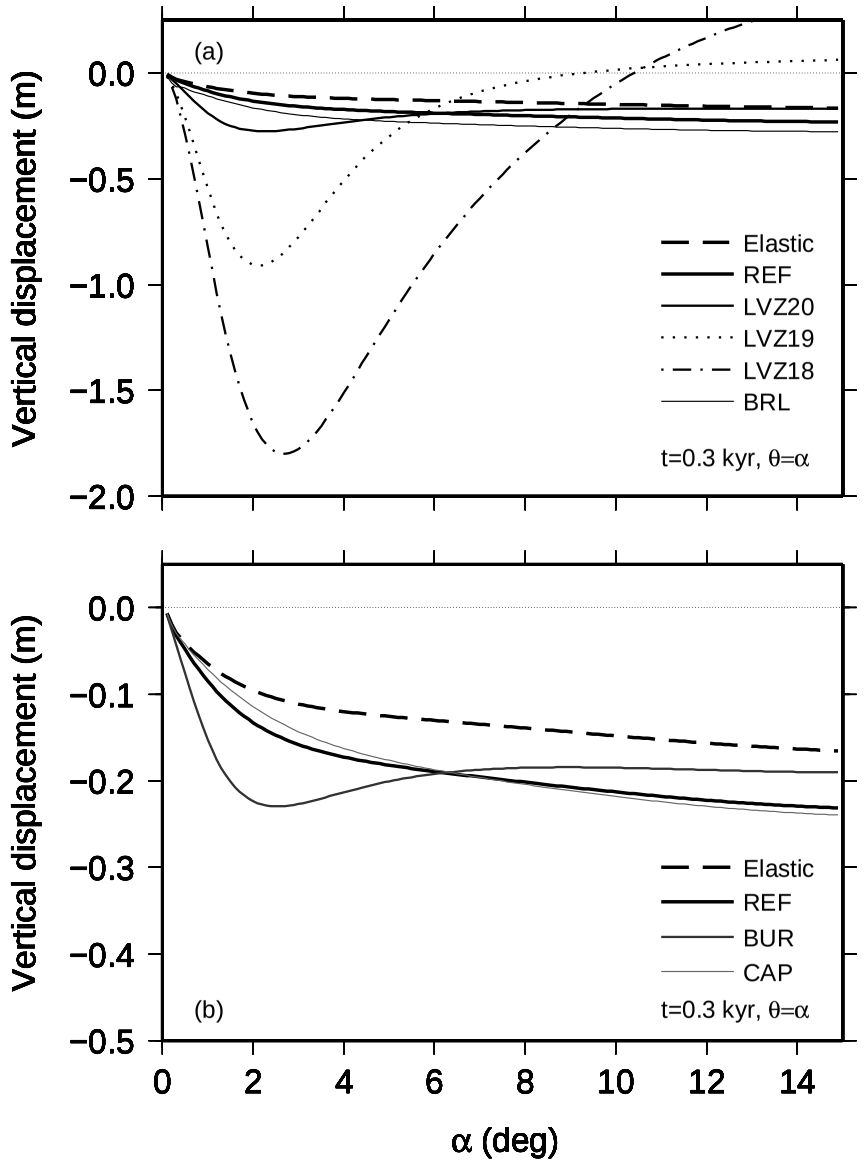

Figure 3.8: Vertical displacement at the load margins ($\theta = \alpha$) as a function of the loads half–amplitude α. Displacements are computed at time $t = 0.3$ kyr. Note that the two frames have different vertical scales.

3.4 Conclusions

Vertical and horizontal Love numbers exhibit different sensitivities to shallow upper mantle rheological layering. When the traditional REF mantle viscosity profile is employed, we have found that the fundamental harmonics of degree two does not show any significant amplification relative to the elastic components on the decade to century

time scale. Since these harmonics are directly related to variations of the inertia tensor (Lambeck, 1980), this indicates that short–term fluctuations of the Earth rotation forced by surface loading are substantially insensitive to shallow upper mantle rheology as far as its viscosity is close to the Haskell value of 10^{21} Pa $\cdot$ s. On the century time scale, the RA factor does not vary substantially with harmonic degree in the range $2 \leq n \leq 128$, reaching a maximum amplitude of ~ 1.5.

Introducing a LVZ with Maxwell rheology and viscosity of 10^{18} or 10^{19} Pa·s significantly alters the Love numbers at all wavelengths. At harmonic degree two, the response of the Earth departs from its elastic asymptote already at a decade scale. This is particularly evident for the horizontal Love number, which shows enhanced oscillations before reaching the fluid regime. In the presence of a LVZ, rheological amplification factors for vertical displacement at $t = 1$ century peaks for harmonic degrees $30 \leq n \leq 40$ with values as large as RA $\sim$ 20. A more complex, bimodal response, is shown by the harmonics of horizontal displacement, which also change their sign with respect to the purely elastic solution. The two transient rheologies tested here, BUR and CAP, affect differently the Love numbers, with the largest amplifications obtained using BUR, but modest effects on the harmonic degree two Love numbers even on a century scale. Furthermore, on the time scales of interest here, a moderate rheological amplification (RA $\sim$ 1.5) of the long–wavelength elastic Love numbers is expected from the relaxation of crustal low viscosity layers, as we have verified using the model previously proposed by Barletta et al. (2006). The implementation of the PW formula has been useful to compute Love numbers for Earth models including thin, low viscosity crustal layers, even in the numerically challenging case of large ($n \sim 100,000$) harmonic degrees.

In the last part of this Chapter, we have modeled the response of the Earth to a simple parabolic cross–section surface load growing at a constant rate, with the purpose of evaluating deviations from the elastic response on time scales of a few centuries. In the vicinity of the load center, the elastic vertical displacements computed by the REF model always constitute a lower bound to values obtained using any other rheological model. In this region, after a few centuries since the beginning of loading, visco–elastic deformations exceed the elastic ones by a factor ranging between 1 and 4. The largest effects are expected in the case of a very soft LVZ with viscosity 10^{18} Pa $\cdot$ s. However, we have found that the sensitivity of vertical deformation to shallow upper mantle rheology is considerably more complex at the ice sheet margin, where vertical movements have

a key–role in the assessment of present and future regional sea level variations (IPCC, 2007; Sheperd and Wingham, 2007). In these regions, a "softening" of the shallow upper mantle rheology does not necessarily imply a larger rate of deformation relative to the elastic case, as we have observed for LVZ20 models. The viscosity of the LVZ determines the pattern and the sign of vertical displacement at the ice margins, and may produce complex vertical movements before a steady–state regime is attained after approximatively one century since the onset of glacial instability. In the presence of a LVZ with viscosity $< 10^{19}$ Pa $\cdot$ s, melting of accretion of relatively small ($\alpha \sim 2^{\circ}$) ice sheets can produce vertical deformations exceeding the elastic ones by a factor of ~ 10 on time scales of a few centuries.

Chapter 4

Sea level change over the last decades

4.1 Introduction

Sea level from the late 19th to the early 21st century shows a rise of 3.2 $\pm$0.4 mm year^{-1} from the satellite data and 2.8 $\pm$0.8 mm year^{-1} from the in situ data (Church and White, 2011). In October 2009, the United Nations Environment Programme (UNEP) released an updated summary of the 2007 Intergovernmental Panel on Climate Change-IPCC Assessment report (UNEP, 2009). In this Climate Change Science Compendium, the authors warned that many of the IPCC forecasted changes were underestimated and that the scale and pace of effects such as sea level rise have and will continue to accelerate. The sea level contribution from glacial sources has been accelerating during the first decade of the 21 st century (Velicogna, 2009).

In the Fourth Assessment Report of the IPCC, it was concluded that a major limitation in predicting future sea–level changes is the contribution from the continental ice sheets (Solomon et al., 2007). It is therefore of utmost importance to constrain the present–day mass balance of the Greenland Ice Sheets (henceforth GrIS) and Antarctic Ice Sheets (henceforth AIS) and to constrain its potential contributions to the future global sea-level rise. By determining the role of current ice sheets in the global climate system, more reliable future scenarios can be obtained. Ice sheet mass balance estimates have improved substantially in recent years using a variety of techniques, over different time periods, and at various levels of spatial detail. Variations in the elevation and thickness of the ice sheet have been measured by various methods including laser altimetry (Krabill et al., 1999), synthetic aperture radar (SAR), echo sounding and ice penetrating radar

(IPR) (Bamber et al, 2001). Repeated surveys carried out over the past 10 years have enabled the estimates of accumulation and ablation rates (Thomas et al., 2000).

In spite of the relatively low horizontal spatial resolution (300–500 km, see Slobbe et al. 2009), GRACE provides the possibility of obtaining monthly mass time series for the harmonic coefficients of the gravity field (Wouters et al., 2008) and to detect possible accelerations of the Arctic and Antarctic ice sheets.

In this chapter, we focus on Greenland and Antarctica ice sheets were the delayed rebounds related to late Pleistocene ice melting and the present-day elastic deformation induced by ice thinning are both active. In the next Section (4.2) we describe the methods used to analyze geophysical components of the two polar ice sheets: Greenland and Antarctica. The recent GrIS mass balance elaborated by Sørensen et al. (2011) allows us to present the pattern of global and regional sea–level variations (Section 4.3.3) and the regional elastic uplift of the GrIS (Section 4.3.3) in response to the current mass loss derived from ICESat observations. This results were recently accepted to the Journal Geophysics Research with title: *Greenland uplift and regional sealevel changes from ICESat observations and GIA modeling* by G. Spada, G. Ruggieri, L. S. Sørensen, K. Nielsen, D. Melini, F. Colleoni. However no new mass balance is currently available for Antarctica, and a simplified model of mass balance for Antarctica is proposed (Section 4.4.2). We analyzed the global and regional pattern of sea level change inferred by the plausible scenario of present-day Antarctica ice melting (Section 4.4.2). After a discussion of the geophysical implications included the sea level fingerprints (respectively in Sections 4.3.3 and 4.4.2), we focus on GIA predictions uncertainty and we compare the viscoelastic predictions with 36 Global Positioning System (GPS) observations along the coasts of Antarctica (Section 4.4.3). Finally we draw our conclusions (Sections 4.3.5 and 4.4.4).

4.2 Methods

We assume that the present–day uplift originates from two major components acting simultaneously across the polar regions. The first is the elastic rebound (ER) associated with the recent ice mass loss across the GrIS and AIS, which hasve been observed by geodetic techniques in the last few decades. In view of the very short time–scales involved, it is generally assumed that the viscous component of this deformation is negligible (Spada et al., 2011a). The second, associated with GIA, results from the viscoelastic

response of the bedrock to the evolution of the polar regions and of the surrounding ice complexes during the last glacial–interglacial period (a complete summary of the state of the art of the GIA theory is presented in the recent report by Whitehouse 2009). These two geophysical processes and the methods employed for their numerical simulation are synthetically described in Table 4.1. Since Greenland is recognized as a tectonically stable region with low seismicity (Chung and Gao, 1997), we can assume that all the present-day vertical uplfit is the result of the combined elastic and viscoelastic rebound (e. g., Khan et al. 2008). However Antarctica experiences of the largest extensional regimes of the West Antarctic rift system (Donnellan and Luyendyk, 2004). Previous studies of geodetic GPS-based analysis (Raymond et al., 2004; Zanutta et al., 2008; Donnellan and Luyendyk, 2004) indicated no significant present motion between East and West Antarctica larger than 1-2 mm yr^{-1}. That is, much of the observed crustal deformation on the continent is attributed to the GIA process (Wahr et al., 2008; Zanutta et al., 2008; Thomas et al., 2011) and recent ice mass loss of AIS .

Though ER and GIA are characterized by distinctly different time–scales and spatial patterns, we know from previous analyses that their amplitudes may be locally comparable, and therefore they are both important for a correct interpretation of GPS observations in Greenland (e. g., Khan et al. 2008) and Antactic (Raymond et al., 2004; Thomas et al., 2011) . In what follows, efforts will be made to estimate modeling uncertainties of the GIA and of the ER component of the total deformation. These uncertainties are related with a limited knowledge of the driving mechanism (i. e. the history of ice thickness variation) and with the response of the solid Earth (i. e. its elastic and viscoelastic structure).

The GIA component of total deformation is evaluated solving the sea-level equation (Farrell and Clark, 1976), which reads:

$$S(\theta,\lambda,t) = \frac{\rho_i}{\gamma} G_s \otimes_i I + \frac{\rho_w}{\gamma} G_s \otimes_o S + S^E - \frac{\rho_i}{\gamma}\overline{G_s \otimes_i I} - \frac{\rho_w}{\gamma}\overline{G_s \otimes_o S}, \tag{4.1}$$

(see Chapter 2) where S is sea–level change, θ is colatitude and λ is longitude, t is time, $\rho_i = 913$ kg m^{-3} and $\rho_w = 1000$ kg m^{-3} are the densities of ice and water, respectively, γ is the reference surface gravity, $G_s = G_s(h,k)$ is the sea–level Green 's function (dependent upon the h and k viscoelastic load–deformation coefficients – LDCs), $I = I(\theta,\lambda,t)$ is the ice thickness variation, $S^E = S^E(t)$ represents the eustatic term (i. e., the ocean–averaged value of S), $\otimes_i$ and $\otimes_o$ denote spatio–temporal convolutions over the ice– and ocean–covered regions, and the overbar indicates an average over the surface of the oceans that

Table 4.1: Synoptic presentation of the geophysical processes considered in this study and of the settings of the numerical methods employed.

Geophysical process:	Elastic Rebound (ER)		Glacial–isostatic adjustment
Method	RER (regional ER)	GER (global ER)	GIA
Forcing	current ice melting	current ice melting	past ice melting
Time scale	decadal	decadal	millennial
Ice model(s)	M3[a]	M3	ICE–5G(VM2)[b]
			ANU05[c]
Ice model(s)		WAIS[d]	IJ05[e]
Rheology	elastic	elastic	Maxwell visco–elastic
Viscosity	–	–	See Table 5.2
LDCs	APLO[f]	APLO	TABOO[g]
	ALMA[g]		
Solver	Eq. (4.4)	SELEN[g] (Eq. 4.1)	SELEN
Ocean load	neglected	gravitationally	as in GER
		self–consistent	
Maximum degree	$\ell_{max} = 128$ and 10^5	60 and 128	128

[a] Greenland Mass balance by Sørensen et al. (2011).

[b] Peltier (2004).

[c] The Greenland component of ANU05 is referred to as GREEN1 by Fleming and Lambeck (2004).

[d] The WAIS ice model represents in simple way, a homogeneous present day ice loss from Western Antarctic Ice Sheets.

[e] Regional ice model of Antarctic by Ivins and James (2005).

[f] Atmospheric pressure loading service, see *http://gemini.gsfc.nasa.gov/aplo/*. The APLO LDCs account for elastic compressibility.

[g] Codes available from: *http://www.fis.uniurb.it/spada/SOFT.html*. ALMA and TABOO LDCs do not account for Earth compressibility. See Spada (2008) and Spada et al. (2011b).

ensures mass conservation (Spada and Stocchi, 2006). Assuming a Maxwell viscoelastic rheology, Eq. (4.1) is solved for S to a maximum harmonic degree ℓ_{max} by the the pseudo–spectral iterative method (Mitrovica and Peltier, 1991) using the code SELEN (Spada and Stocchi, 2007).

In Eq.(4.1) S represents sea–level change with respect to the surface of the solid Earth. Hence

$$S(\theta, \lambda, t) = N - U, \tag{4.2}$$

where N represents the "absolute variation" of the sea surface, measured with respect to the center of mass of Earth (see e.g. Peltier 2001). Vertical displacement can be written as:

$$U(\theta, \lambda, t) = \rho_i G_u \otimes_i I + \rho_w G_u \otimes_o S\,, \tag{4.3}$$

where $G_u = G_u(h)$ is the Green function associated with U and the two terms on the right hand-side account for contributions of the ice and meltwater load respectively. We note that N represents the sea–level change that would be observed by an artificial satellite. The geoid height variation G is related to N by $N = G + c$, where c is the time-dependent constant introduced to ensure mass conservation in the sea level equation (see e.g. Spada and Stocchi 2006). Apart from the notation, these definitions N and G are matching those by Simon et al. (2010). In this study, we are mainly concerned with the trend (i.e. the time–derivative) of the above quantities, which in the body of thesis will be denoted by $\dot{S}$, $\dot{U}$, $\dot{N}$ and $\dot{G}$ respectively, and assumed to be constant over the time period covered by the ICESat observations ($\sim$ 2003–2008).

In the following, the ER problem for Greenland and Antarctica will be solved using both a global and a regional –scale – approach (see Table 4.1). In the following, these will be referred to as GER and RER approaches, respectively. The elastic LDCs required for these methods have been obtained from the Atmospheric pressure loading service (here after abbreviated to as APLO). They pertain to a spherically symmetric, non–rotating, elastic and isotropic (SNREI) Earth model with PREM structure (Dziewonski and Anderson, 1981). They are expressed in the reference frame of center of mass of the system (Earth + Load) and account for the Earth's elastic compressibility. The LDC for vertical displacement (h^{APLO}), is shown in Figure 4.1a as a function of degree ℓ. The asymptote for $\ell \mapsto \infty$ is almost attained, here, for $\ell \approx 10^3$. For a planet of radius a, mass m and gravity γ, $h_\infty = -\frac{\gamma m}{4\pi a^2 \mu}\frac{\lambda+2\mu}{\lambda+\mu}$, where λ and μ are the Lamè constants of the outmost layer of the Earth (Farrell, 1972). Since the ICESat -derived

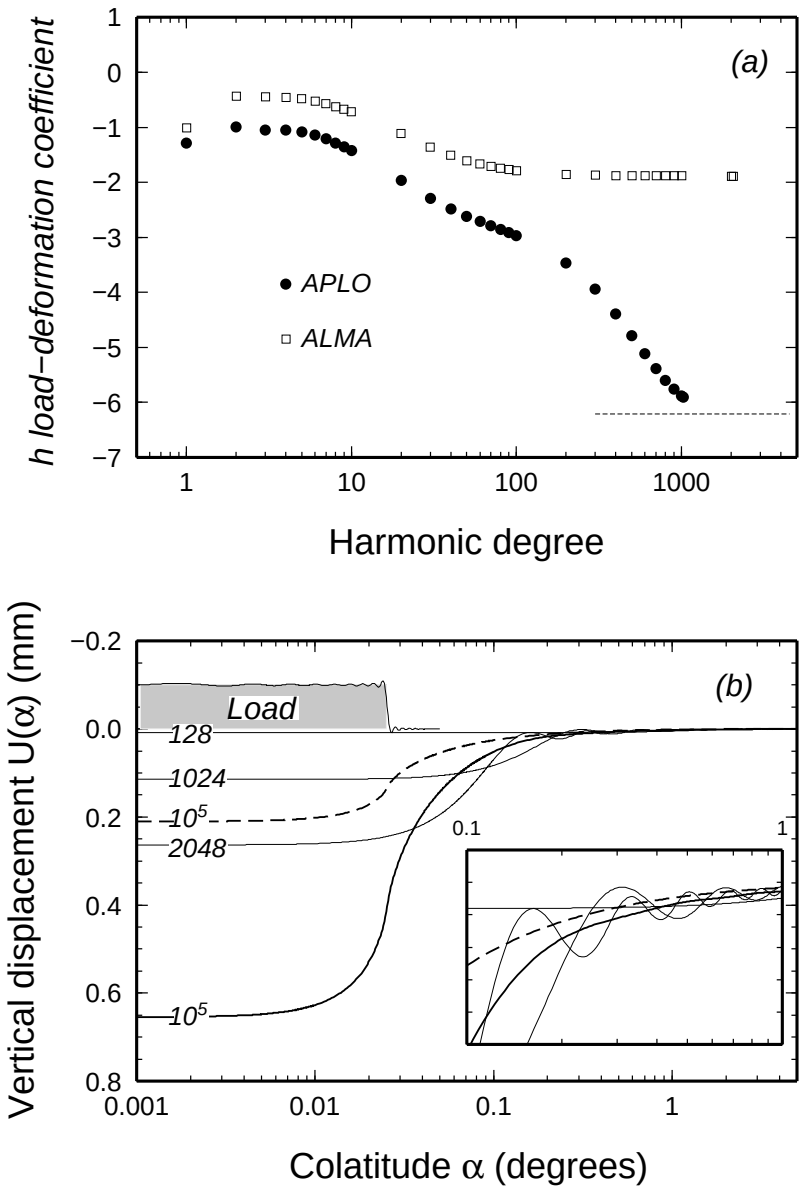

Figure 4.1: *(a)* Vertical LDCs h^{ALPO} (circles) and h^{ALMA} (squares) as a function of degree l. The curve is comparable to that in Figure 1 of Farrell (1972), pertaining to the Gutemberg–Bullen A Earth model and used by Khan et al. (2008). The dashed line shows the asymptote $h_\infty^{APLO} \approx -6.22$. *(b)* Vertical displacement in response to the thickness variation of $\Delta H = -1$ m for a disc load with $\beta = 0.025°$ (the disc profile is shown by the gray hatched area along with its spherical harmonic reconstruction). Note that the x–axis is logarithmic and that the y–axis is positive downward. Solid curves are obtained using $h = h^{APLO}$ and varying ℓ_{max} (an asymptotic value is obtained for $\ell_{max} = \ell_\infty \equiv 10^5$). The dashed curve is obtained using $h = h^{ALMA}$. The inset shows the details of $U(\alpha)$ in the range of colatitudes $0.1° \leq \alpha \leq 1°$.

mass balance of the GrIS is very rich in small wavelength features (see Figure 4.2a), we expect that vertical deformations evaluated by the RER method may be particularly sensitive to the shallow stratification of the Earth. For this reason, in Figure 4.1a we also show h values obtained for an incompressible, PREM–averaged model with 100–layers of uniform thickness (h^{ALMA}). These LDCs, computed by means of the software ALMA (Spada, 2008), have a reduced amplitude compared to h^{APLO}. This is a consequence of incompressibility and of the elastically stiffer outmost mantle layer resulting from the coarse PREM averaging in ALMA (note that $\ell \mapsto \infty$, h_∞ scales inversely with μ). Of course, we are aware that the assumption of incompressibility represents a bad approximation, especially when dealing with the effects of ongoing elastic deformations. However, the use of a finelylayered PREM model could be equally disputed in a regional environment where the actual elastic parameters and density profiles can deviate from the globally averaged values and where lateral variations can play an important role. Therefore, our computations based on ALMA should be meant as an attempt, performed in the framework of spherically layered elastic models, to provide a quantitative assessment of the errors introduced by assumptions about layering. The consequences on the surface vertical velocities will be explored in Section 4.3.4 below.

While GER relies upon the solution of the full Sea level Equation (4.1), in the RER method we simply perform a convolution between the elastic Green functions and each of the elementary disc–shaped elements that discretize the mass budget of the GrIS (see Figure 4.2a) and AIS (see Figure 4.15). Apart from the different Green functions employed, the RER approach thus follows closely the method adopted by Khan et al. (2007, 2008) to evaluate the vertical movements at GPS sites in response to the melting of near–field GrIS glaciers. For a single ice element, vertical displacement is

$$U(\alpha) = 3\ \Delta H \left(\frac{\rho_i}{\rho_w}\right) \sum_{\ell=0}^{\ell_{max}} \frac{\sigma_\ell}{2\ell+1} h_\ell P_\ell(\cos\alpha)\,, \tag{4.4}$$

where α is the colatitude of the observer relative to the source, ΔH is the ice thickness variation, the P_ℓ's are the Legendre polynomials, ℓ_{max} is the maximum harmonic degree, $\sigma_\ell = \sigma_\ell(\beta)$ is the ℓ–th harmonic component of the surface load (a closed–form expression of σ_ℓ for an axisymmetric disc load of half–amplitude β is given in Spada et al. 2011b). A similar expression holds for the variation of the geoid height $G(\alpha, t)$, with h_ℓ substituted by $1+k_\ell$. Once Eq. (4.4) is evaluated for a unit ice thickness variation, the total displacement $U(\theta, \lambda, t)$ corresponding to a regional ensemble of disc loads is obtained by rescaling the

solution and taking advantage, by means of simple geometrical methods, of the axial symmetry of Eq. (4.4) relative to the center of the load. Figure 4.1*b* shows $U(\alpha)$ for an instantaneous melting episode with $\Delta H = -1$ m. The load amplitude is $\beta = 0.025°$, matching the size of the 5 km $\times$5 km ice elements that compose the GrIS M3 mass balance. In spite the high resolution model of GrIS released by Sørensen et al. (2011), the WAIS model assumes a load amplitude of $\beta \approx 0.2°$ corresponding to an area of 500 km^2.

Displacements are shown for increasing values of ℓ_{max} until the oscillations in the periphery of the load (see inset), have disappeared (the final solution corresponds to $\ell_{max} = \ell_\infty \equiv 10^5$). Uplift is attained across a broad area surrounding the load (approximately for $\alpha \leq 16\beta$); for larger values of α, the load is surrounded by a broad peripheral subsidence. As a rule of thumb, a melting episode with $\Delta H = -1.5$ m produces, if h^{APLO} LDCs are employed, a vertical uplift of ≈ 1 mm beneath the load.

Differently from GER, in the RER method, deformation only results from the direct effect of ice melting; meltwater loading and the gravitational interaction between the GrIS and the surrounding oceans are not included in modeling. The GER and the RER approaches have a complementary character. Being "gravitationally self–consistent" (Wu and Peltier, 1982), the GER method allows for estimates of global and regional deformations and gravity changes, and therefore provides, in principle, reliable predictions of sea–level variations at any spatial scale. However, since the computation of short–wavelength deformations by the GER method may be computationally very expensive, for regional and local predictions the RER approach is by far more convenient and, as we will discuss in Section 4.3.2 below, largely consistent with GER on the spatial scale of the GrIS .

4.3 Greenland

4.3.1 Mass Balance of Greenland

The Greenland Ice Sheet is approximately 1.7 million km^2 in area, extending as much as 2200 km north south. The maximum ice thickness is 3367 m, the average thickness is 1600 m (Thomas et al., 2000). The Greenland ice sheet, with a volume of 2.93 10^6 km^3 (Bamber et al, 2001), containing 10% of the Earth ice budget (Duff, 1998), is the second largest ice mass on Earth, after Antarctica. The ice has depressed some bedrock below

sea level, and a little would remain below sea level following ice removal and bedrock rebound (Bamber et al, 2001). However, most of the ice rests on bedrock above sea level and would contribute to the globally averaged sea level rise of 7.3 m if melted completely (Lemke et al. , 2007). A review of the published estimates of the mass balance of the GrIS (and of the associated uncertainties) since the sixties has been recently presented by Ewert et al. (2011).

The table 4.2 gives a review of mass balances recently published. The time intervals covered by the published mass balance estimates varies from few decades to less than one year, in some cases. The mass balances appear to broadly follow the time–evolution of the Greenland coastal temperature and, since the nineties, they are systematically negative. Considering that -360 Gt a^{-1} ice loss is equivalent to 1 mm a^{-1}, the GrIS contributed to sea level rise between 0.1 and 0.8 mm of equivalent sea level.

Table 4.2: GIS mass change trends from altimetry, mass-budget and gravity-change approch.
[a] CSR: solutions produced by the Center for Space Research;
[b] GFZ: solutions of Geo Forschungs Zentrum Potsdam. Release-04;
[c] Mascon: mass concentration, see *http://grace.sgt-inc.com/*

Author	Method	Period	Volume km^3 yr^-1	Mass Gt yr^-1
Krabill et al. (2000)	Airborn LA	Jun 1994-May 1999	-51	$--$
Zwally et al. (2005)	ERS1/2	Apr 1992-Oct 2002	–	$+11 \pm 0.3$
Velicogna and Wahr (2005)	GRACE/CSR	Summers 2002-2004	-82 ± 28	–
Rignot and Kanag. (2006)	InSAR	2005	–	-224 ± 41
Chen et al. (2006)	GRACE/CSR^a	Apr 2002-Nov 2005	–	-219 ± 21
Ramillien et al. (2006)	GRACE/$CNES^b$	Jul 2002-Marc 2005	–	-118 ± 14
Luthcke et al. (2006)	GRACE/$Mascon^c$	Jan 2003-Dec 2005	–	-101 ± 16
Wouters et al. (2008)	GRACE/CSR	Feb 2003-Jan 2008	–	-179 ± 25
Velicogna (2009)	GRACE/CSR	Apr 2002-Feb 2009	–	-230 ± 33

(continued on next page)

(continued from previous page)

Slobbe et al. (2009)	ICESat	Feb 2003-Apr 2007	–	-139 ± 68
Slobbe et al. (2009)	GRACE/CSR	Apr 2002-Jun 2007	–	-218 ± 18
Slobbe et al. (2009)	GRACE/GFZ	Aug 2002-Jun 2007	–	-168 ± 05
vanderBroeke et al. (2009)	GRACE/CSR	2003-2008	–	-237 ± 20
Wu et al. (2010)	GRACE/Altimeter	2002-2008	–	-105 ± 23
Ewert et al. (2011)	ICESat	Sep 2003-Mar 2008	-205	-185 ± 28
Ewert et al. (2011)	GRACE/GFZ	Aug 2002-Jun 2009	-205	-191 ± 21
Sørensen et al. (2011)	ICESat	Oct 2003 to Mar 2008	$--$	-191 ± 23
Sørensen et al. (2011)	ICESat	Oct 2003 to Mar 2008	$--$	-240 ± 28
Sørensen et al. (2011)	ICESat	Oct 2003 to Mar 2008	$--$	-233 ± 27

As reviewed by Alley et al. (2010) (see references therein), the methods employed to constrain the mass balance of the GrIS have so far included pure assessment, surface mass balance techniques, laser and radar altimetry and, recently, gravity observations from the NASA/DLR Gravity Recovery and Climate Experiment (GRACE) satellites (see the overview of Tapley et al. 2009). Published estimates of GRACE–only solutions for the average GrIS mass balance during the last decade, listed by Schrama et al. (2011) vary between -177 ± 6 Gt yr^{-1} for the period 2003–2009 (Luthcke et al., 2010) and -230 ± 33 Gt yr^{-1} for the period 2002–2009 (Velicogna, 2009). A significant part of the error on the GRACE–only mass loss estimates stems from the Glacial–isostatic adjustment (GIA) correction, which contributes a secular gravity signal to the GRACE observations. Efforts have been made to control the amplitude of this correction by forward GIA modeling, using different scenarios for the viscosity profile of the mantle and deglaciation history of the late–Pleistocene continental ice–sheets (see e. g., Velicogna and Wahr 2006a,Wouters et al. 2008).

In a recent study (Sørensen et al., 2011), a new mass balance estimate for the

GrIS during the period (2003–2008) has been proposed, derived from repeated surface elevation measurements from NASA's Ice Cloud and land Elevation Satellite (ICESat , see *http://icesat. gsfc.nasa.gov/*). ICESat is a laser altimetry mission which operated from 2002 to 2009, providing a unique data set for cryosphere studies. For ICESat , the discontinuous temporal coverage (2–3 measurements campaigns of $\sim$ 35 days per year) is compensated by a substantial gain of in spatial resolution ($\sim$ 5 km) with respect to GRACE and by a reduced sensitivity to the amplitude of the GIA correction (Gunter et al., 2009). Furthermore, the altimetry alone cannot provide an estimate of the mass balance (Sørensen et al., 2011), since for all altimeter systems the conversion of volume to mass changes requires modeling of the firn dynamics and of the surface ice densities (Schrama et al., 2011). Depending on the method employed to estimate the elevation change from the (not exactly) repeated altimetry measurements, for the period 2003–2008 the ICESat mass balance proposed by Sørensen et al. (2011) (see their Table 2) varies from -191 ± 23 (model M2) to -240 ± 28 Gt yr^{-1} (model M3). These estimates are in agreement with previous results obtained for the GrIS using other remote–sensing methods during the same time span (see, in particular, the recent summary of GRACE results by Schrama et al. 2011) and substantiate recent ICESat –GRACE comparison studies relative to Antarctica (Gunter et al., 2009). We note that the ICESat mass balance estimates by Sørensen et al. (2011), which does account for firn compaction, elastic uplift and intercampaign bias corrections, exceed significantly the one proposed by Slobbe et al. (2009) (-139 ± 68 Gt yr^{-1}). The spatial pattern of the M3 mass balance proposed by Sørensen et al. (2011), mapped on a quasi–regular geodesic grid, is portrayed in Figure 4.2*a*. In this work, the high-resolution surface load associated with this melting scenario will be employed for providing estimates of time variations of various geophysical quantities. These estimates are essentially based on the solution of the Sea level Equation (SLE, Farrell and Clark 1976) and on the application of well established Green function methods (Farrell, 1972) that permit to capture the shorter wavelength features of the regional uplift patterns (Khan et al., 2007). Predictions include long– and short wavelength vertical deformations in response to unloading, regional sea–level variations along the coasts of Greenland, and global sea–level patterns (or fingerprints) associated with the current mass loss of the GrIS. In the last decade, significant efforts have been devoted to the observation and interpretation of GPS signals possibly associated to the present day vertical movements across Greenland (Wahr et al., 2001; Khan et al.,

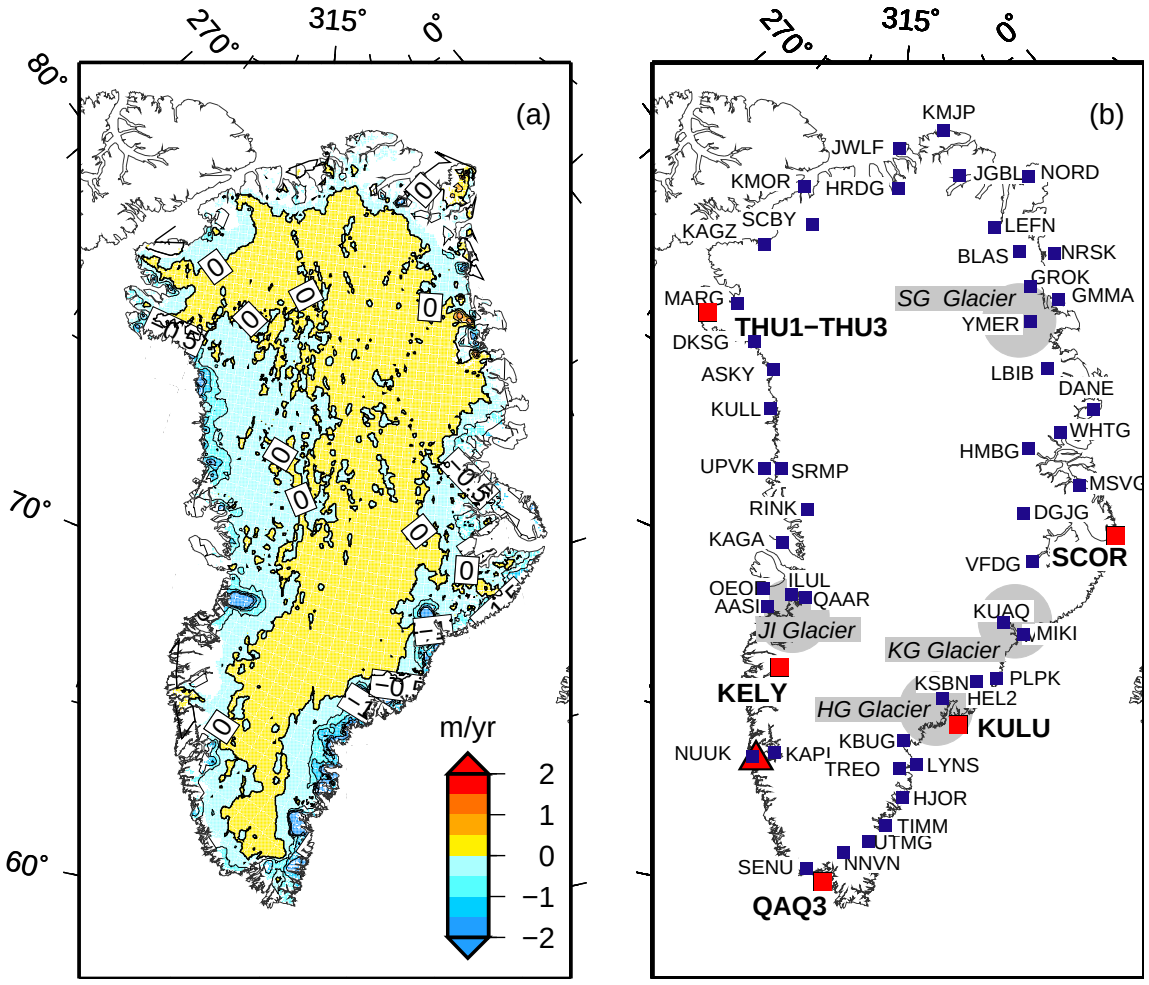

Figure 4.2: *(a)* Mass balance of the GrIS (expressed in units of m yr $^{-1}$) and according to solution M3 of Sørensen et al. (2011), retrieved from ICESat data for the period between October 2003 and March 2008. The whole GrIS is discretized into $\sim 71,000$ equal disc–shaped elements with angular radius $\beta \approx 0.025°$, corresponding to an area of 25 km^2). The total mass balance of M3 is -240 ± 28 Gt yr^{-1}. *(b)* Sites of the Greenland GPS Network (GNET) (coordinates are obtained from the UNAVCO database, see *http://www.unavco.org/unavco.html*) and glaciers mostly contributing to mass loss, with names abbreviations.

2007, 2008, 2010), with the aim of weighing the relative importance of GIA and elastic rebound in response to current ice melting. Using the observations from the few stations that can currently provide a reliable trend of vertical uplift (Khan et al., 2007, 2008), we will address the problem of reconciling the GPS vertical uplift data with GIA and elastic rebound modeling.

4.3.2 Results

4.3.3 Global elastic deformations in response to current mass loss

Figures 4.3*a–c* show the rates of vertical displacement ($\dot{U}$), of sea–level change ($\dot{S}$) and geoid elevation ($\dot{N}$), respectively, based on the GrIS mass budget M3 and obtained by the GER method to degree $\ell_{max} = 128$. The fields are mapped on a quasi–regular geodesic grid with spacing of ~ 25 km, obtained by the icosahedron method of Tegmark (1996). In the considered range of wavelengths, the maximum rate of elastic uplift in *(a)* amount to ~ 10 mm yr^{-1} and are positively correlated with the regions of coastal ice thinning, where mass loss is reaching its largest amplitude according to the mass balance M3 (see Figure 4.2*a*). However, the local vertical uplift is so strong that the whole GrIS is uplifted,

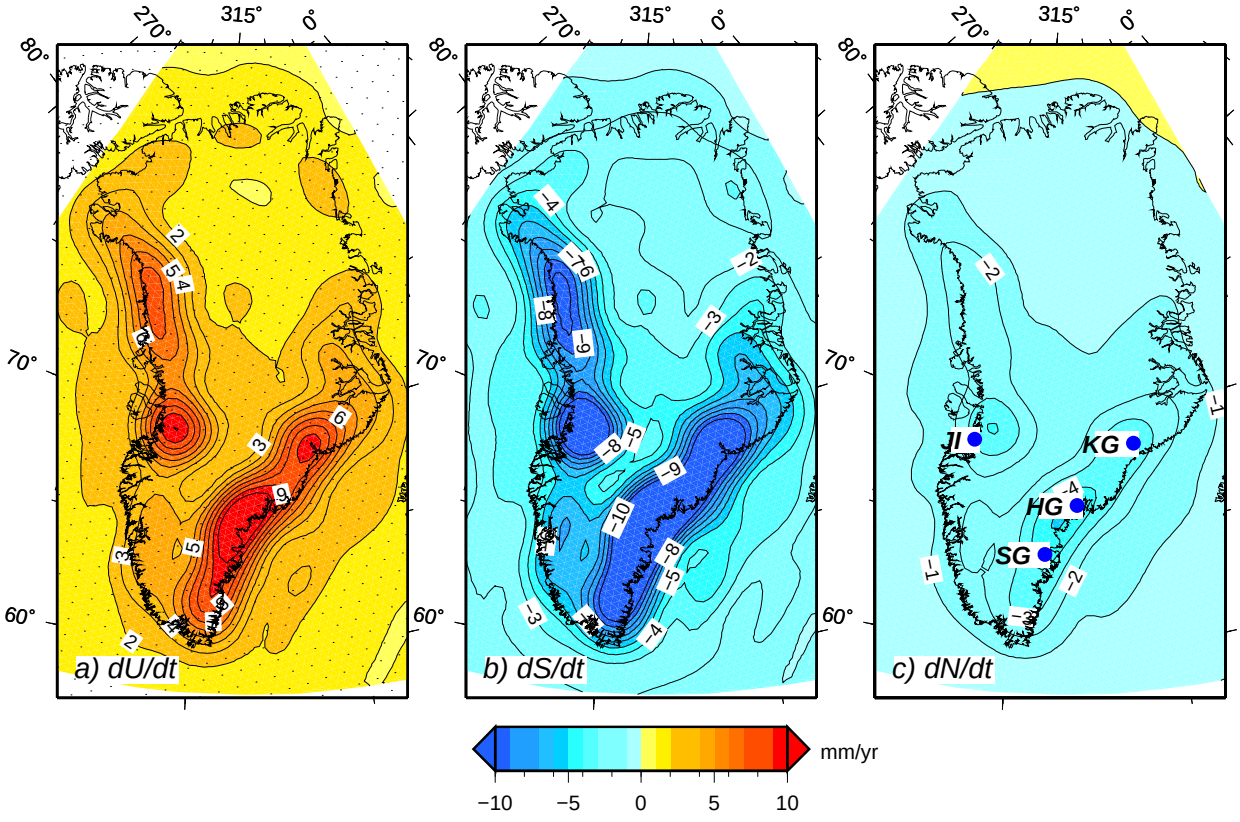

Figure 4.3: *(a)* Elastic vertical velocity ($\dot{U}$) across Greenland, computed by the GER method to degree $\ell_{max} = 128$, according to the M3 ICESat mass balance in Figure 4.2*a*. Dots in *(a)* show the grid pixels. Frames *(b)* and *(c)* show the rates of sea–level change ($\dot{S}$) and of geoid displacement ($\dot{N}$), respectively. In all frames, contour lines are spaced by 1 mm yr^{-1}.

even in the central part where the ICESat –based mass balance indicates ice accumulation and our predicted velocities are in the range of 2 to 4 mm yr^{-1}. Due to the limited spatial resolution of this uplift map, it is not possible to detect areas of local subsidence, which are however suggested by the localized ice thickening along the NE coastline of Greenland in Figure 4.2*a*. The rate of sea–level change $\dot{S}$ (Figure 4.3*b*), which closely (but not exactly) mirrors the map of $\dot{U}$, shows a complex regional pattern along the coasts of Greenland, and reaches its largest amplitude (~ -14 mm yr^{-1}) in the proximity of the Helheim Glacier (HG, see Figure 4.2*b*). Figure 4.3*c*) shows that the sea surface, as seen from the Earths center of mass, is collapsing across Greenland. Furthermore, the pattern of $\dot{N}$ is clearly characterized by smaller spatial variations compared with ($\dot{U}$) and ($\dot{S}$), which is a consequence of the larger energy contained in the lowdegree portion of the gravity field spectrum.

Geophysical pattern of ICESat and GRACE mass balances

In Figure 4.4, a comparison is drawn between the uplift pattern obtained by the ICESat mass balance M3 of Sørensen et al. (2011) and that inferred by observations from the Gravity Recovery And Climate Experiment (GRACE) satellites. Among the various GRACE solutions so far published (e. g., Luthcke et al., 2006; Ramillien et al., 2006; Velicogna and Wahr, 2006a; Chen et al., 2006), here we have used the one by Wouters et al. (2008), who have employed 58 monthly GRACE observations between February 2003 to January 2008, a time span that substantially overlaps the period of the ICESat observations considered by Sørensen et al. (2011). According to the GRACE results of Wouters et al. (2008), the GrIS has lost mass at an average rate of 179 ± 25 Gt yr^{-1}, an amount somewhat smaller than the M3 ICESat estimate of -240 ± 28 Gt yr^{-1} (Sørensen et al., 2011). We note that this GRACE solution better agrees with the mass budget based on method M2 by Sørensen et al. 2011, namely -191 ± 23 Gt yr^{-1}. Since the GRACE mass balance is obtained by an iterative procedure in which Stokes coefficients of the gravity potential are inverted to degree $\ell_{max} = 60$, in Figures 4.4*a* the ICESat – derived uplift rates have been truncated to the same maximum degree and the same sets of APLO vertical LDCs are employed for comparison. For ICESat, the truncation to degree $\ell_{max} = 60$ implies a substantial loss of information, as it can be appreciated by a comparison between Figures 4.4*a* and Figure 4.3*a* (obtained with $\ell_{max} = 128$). The misfit between ICESat and GRACE, portrayed in Figure 4.4*c*, attains

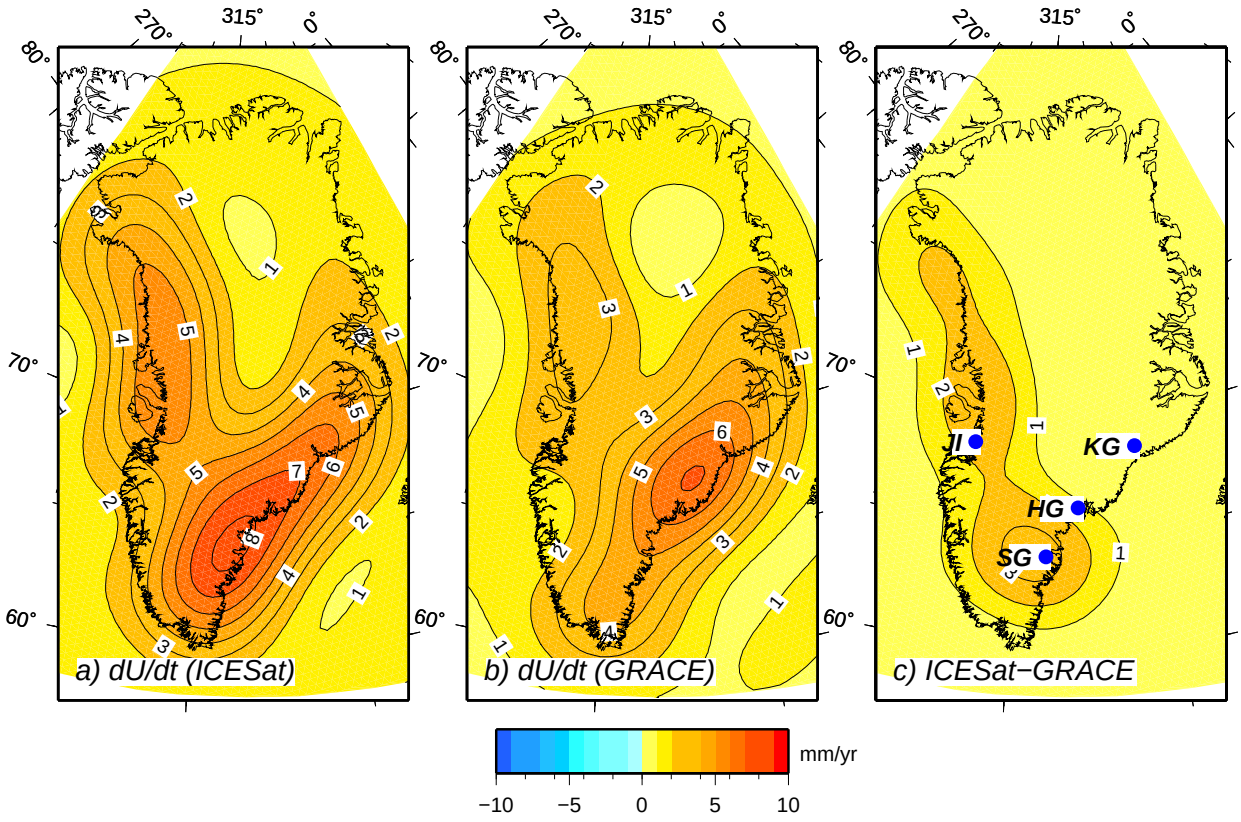

Figure 4.4: *(a)* Regional rate of elastic uplift across Greenland according to the ICESat model M3, using the GER method of solution with $\ell_{max} = 60$. *(b)* As in *(a)*, but using the GRACE mass balance by Wouters et al. (2008) at the same harmonic degree. The difference between the two solutions, shown in *(c)*, is largest around the Southern Glaciers (SG) and in the vicinity of Jakobshavn Isbræ (JI).

its minimum in the bulk of the GrIS and in the North East, where the differences do not exceed 1 mm yr^{-1}. However, the GRACE mass balance does not resolve in detail the ice loss captured by ICESat in the area of the Southeast Glaciers (SG) nor the very localized melting in the area of the Jakobshavn Isbræ (JI), in the North West of the GrIS (see also Figure 4.2). In these regions, the predicted ICESat uplift rate exceeds the GRACE solution by 1–3 mm yr^{-1}. Considering the completely different nature of the two datasets and the different inversion methods, the results of Figure 4.3 support the view that GRACE and ICESat observations are providing, in addition to comparable

gravitational signatures (Sørensen, 2010), consistent scenarios for the long–wavelength elastic uplift patterns during the time span 2003–2008. Differences between the mass balances obtained, and consequently discrepancies in the vertical uplift predictions as shown in Figure 4.3 can be attributed to *i)* under–sampling of the south–eastern part of the ice sheet by ICESat (Sørensen, 2010), *ii)* to the intrinsic limitations that all satellite altimetry systems face along the coastal margins because of the rough topography (Schrama et al., 2011), *iii)* to the different temporal and spatial resolutions of GRACE and ICESat, *iv)* or to the not exact coincidence of the time periods of the ICESat and GRACE time series used for the comparison of Figure 4.4.

Sea level fingerprints

The GER approach based on Eq. (4.1) allows for a "gravitationally self–consistent" evaluation of the global sea–level variations associated with the M3 mass balance model of the GrIS. The sea–level change pattern or "fingerprint" (Mitrovica et al., 2001, 2009; Riva et al., 2010) associated with this mass balance solution is shown in Figure 4.5. With a total mass budget of -240 ± 28 Gt yr^{-1} in the period 2003–2008, according to our computations the GrIS model M3 would provide, on a rigid and non–self–gravitating Earth, an eustatic sea–level variation at a rate of $+0.67 \pm 0.08$ mm yr^{-1}. This estimate agrees well with results found by others. For example, Mitrovica et al. (2001) found, based on completely independent arguments, a secular sea–level rise of $+0.6$ mm yr^{-1}and Wouters et al. (2008) found an estimate of 0.5 ± 0.1 mm yr^{-1} based on GRACE. The estimate is also consistent with previous GRACE satellite gravity observations (Velicogna and Wahr, 2006a) which indicate a mean mass loss between 2002 and 2006 equivalent to a uniform sea–level rise of 0.5 mm yr^{-1}. Since approximately 2003, we note a clear acceleration of ice mass loss from the GrIS , and we underline that the IPCC AR4 (Lemke et al. 2007) with contribution to sea level of 0.21 ± 0.035 mm yr^{-1}underestimated the contribute of GrIS to present-day sea level rise.

Figure 4.5 clearly illustrates significant deviations from eustasy, with maximum $\dot{S}$ values that exceed the average eustatic value (white contours) by $\sim 15\%$ in the regions located in the far field of the GrIS (e. g., in the middle of the Pacific Ocean). This agrees with the recent results of Riva et al. (2010), who estimated a gravitationally driven sea level increase of $\sim 20\%$ greater than the average (eustatic) value at low–latitudes.

In Figure 4.5*b*, the same total mass budget employed in 4.5*a* has been uniformly

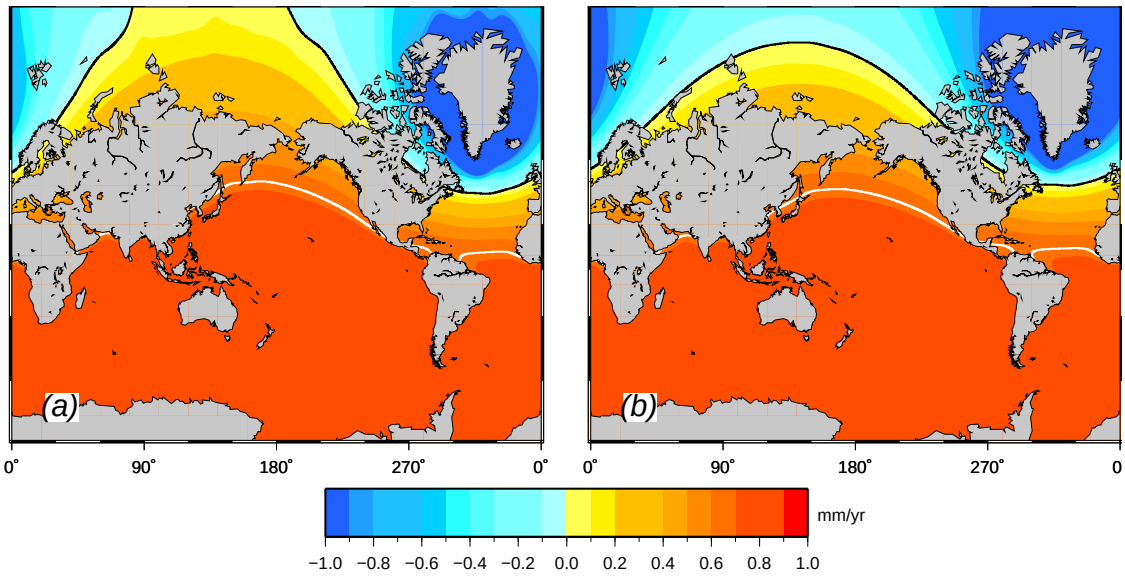

Figure 4.5: *(a)* Global sea–level variation associated with the mass balance M3 of Figure 4.2*a*. In *(b)*, the total volume of ice loss is the same, but uniformly distributed over all the GrIS pixels (note that in both frames the color table is limited to ± 1 mm yr^{-1}). White contours mark the place where sea–level change corresponds to the eustatic change induced by the GrIS meltwater budget ($\dot{S} = \dot{S}^E \approx +0.67$ mm yr^{-1}). The black contour represents the nodal line ($\dot{S} = 0$). The jagged shape of the contour lines in *(a)* reflects the larger energy of short–wavelength harmonics in the GrIS mass budget relative to *(b)*.

distributed over the GrIS, therefore following the same approximation of Mitrovica et al. (2001). The corresponding mass balance, henceforth referred to as M3U, causes the same eustatic sea–level variations of M3. Differences observed with respect to the (normalized) sea–level pattern of Figure 1*b* of Mitrovica et al. (2001) can be attributed to the absence of rotational feedbacks (Milne and Mitrovica, 1998) in this implementation of the SLE, and possibly to a different elastic layering of the mantle. Differences between the maps in Figures 4.5*a* and 4.5*b* are evident (and expected) in the near field of the GrIS. In spite of the significant spatial heterogeneity of the actual mass loss distribution employed in Figure 4.5*a*, associated with the east–west bipolar structure of the mass balance of model M3, differences between the two fingerprints in the remote far field cannot be appreciated at the 0.1 mm yr^{-1} level.

The geophysical significance of the results shown in Figure 4.5 can be better established by a comparison with the secular rates of sea–level change attributed to GIA in key areas as the Mediterranean basin. Figure 4.6 shows the details of the sea–level trends

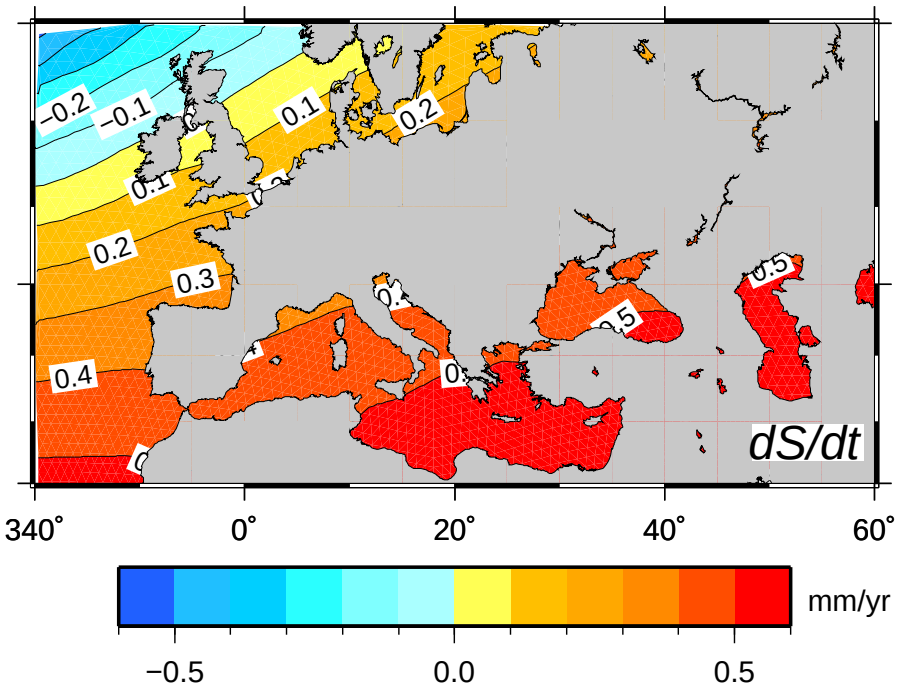

Figure 4.6: Present–day rate of sea–level change (dS/dt) across the Mediterranean and southern Europe associated with the M3 melting scenario of Figure 4.2*a*. Maximum rates (~ 0.6 mm yr^{-1}, i.e. close to the eustatic value) are predicted along the levant coasts. In consideration of the distance from the source of melt water, using the M3U scenario employed in Figure 4.5*b* would not change the details of this map.

across southern Europe and the Mediterranean Sea, adopting the same melting scenario as in Figure 4.5*b*. The $\dot{S}$ values vary smoothly within the basin (approximately from 0.4 to 0.6 mm yr^{-1} from NW to SE), due to the very long wavelength character of the far–field sea–level variations driven by the mass loss in Greenland. Although a precise estimate is thwarted by considerable uncertainties in the mantle viscosity profile, according to Tsimplis et al. (2011), the GIA component of the sea–level variations currently observed at tide gauges located in bulk of the Mediterranean Sea amounts to ~ 0.5 mm yr^{-1}. This estimate, based on the global ice sheet reconstruction ICE–5G(VM2) of Peltier (2004), is consistent with independently derived models of deglaciation (see the very recent work of Lambeck et al. 2011). The GIA secular sea–level trend is comparable with the $\dot{S}$ values shown in Figure 4.6 in the same region, which is only based on the M3 ICESat mass budget. For tide gauge sites located along the continental coasts of the Mediterranean Sea, such as Trieste (northeast Italy), the current melting of

Greenland largely dominates the GIA effects, which according to Tsimplis et al. (2011) may be close to 0.1 mm yr^{-1} (this is consistent with the GIA modeling results by Stocchi and Spada 2009 and Lambeck et al. 2011). Since here we only consider the effects of mass loss from the GrIS during less than one decade, neglecting contributions from Antarctica (e. g., Rignot et al. 2008a) and small glaciers (e. g., Meier et al. 2007), these estimates should be taken cautiously since they may be not representative of secular sea–level trends. However, they indicate that current ice melting of the GrIS is contributing a large fraction of the current sea–level variations observed at tide gauges in the Mediterranean. The marked regional character of the sea–level fingerprints shown in Figure 4.6 should be taken into account for future sea–level predictions in this region, which are often based on the eustatic approximation (e. g., Lambeck et al. 2011).

Regional elastic deformations

The GER method that we have so far employed for modeling elastic rebound of Greenland is based on a solution of the SLE in which only large to intermediate wavelengths are taken into account ($\ell_{max} = 128$). However, the detailed surface load variations provided by ICESat observations, surface density and firn compaction modeling on the 5×5 km grid of Figure 4.2*a* may have the potential of affecting vertical movements (and consequently regional sea–level variations) on a much smaller spatial scale. To improve the spatial resolution of our regional predictions, we have first set up a RER experiment based on Eq. (4.4) and mapped the rate of displacement in the same range of wavelengths considered so far, using the APLO LDCs shown in Figure 4.1*a*. The result, shown in Figure 4.7*a*, are matching well those obtained by the GER method (Figure 4.3). The difference between the GER and RER results for $\dot{U}$, shown in Figure 4.7*b*, is positive across the whole GrIS and reaches its maximum off the coast segments which are more subject to rapid mass loss (and where consequently vertical uplift is maximum). This extra regional uplift in the range of 0.1–0.3 mm yr^{-1} originates from the sea–level fall associated with the decreased gravitational attraction between the melting ice masses and the oceans surrounding the GrIS. This effect, associated with the self–gravitation of the ocean masses, is accounted for in the SLE but totally neglected within the RER modeling. Since its amplitude is substantially negligible compared to the $\dot{U}$ values predicted along the GrIS margins, the results of Figure 4.7 indicate that the RER method provides, on these regional scales, an accurate estimate of the uplift pattern despite the significant simplifying assumptions

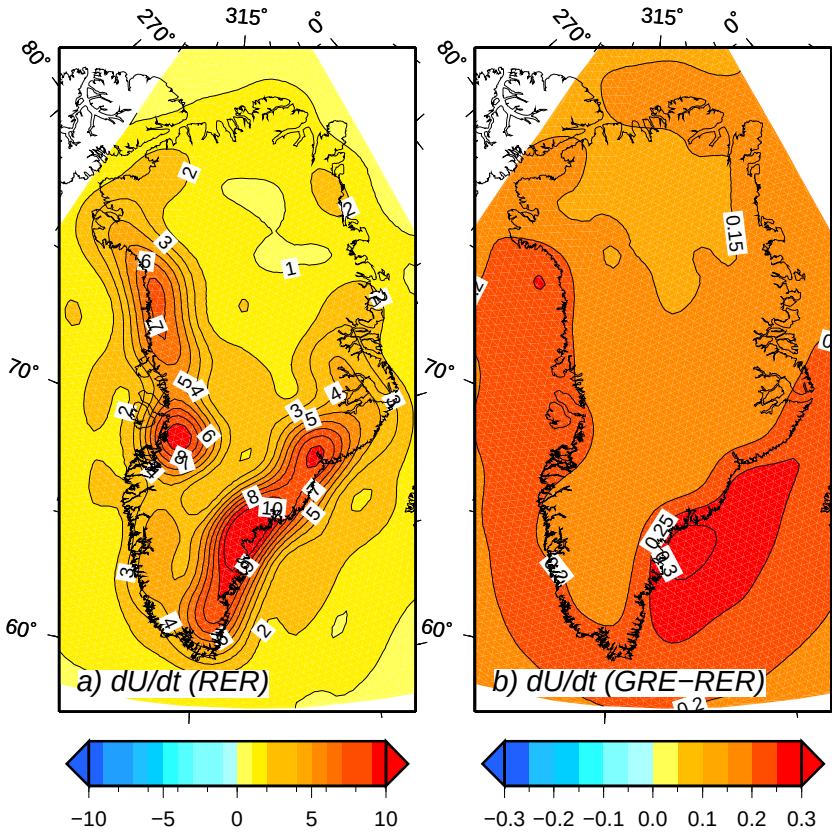

Figure 4.7: *(a)* Elastic vertical velocity across Greenland according to the RER approach to degree $\ell_{max} = 128$. *(b)* Difference between the GER results in Figures 4.3*a* and 4.7*a*, respectively (note the different ranges of color tables). The GER velocity only slightly exceeds the RER solution.

behind its formulation (see Section 4.2). This finding has important practical implications, since, at the same ℓ_{max}, the RER approach is computationally more convenient than the physically self–consistent (but expensive) GER method.

The short–wavelength features of the elastic component of the vertical velocity field and of the geoid are shown in Figure 4.8 on the GrIS spatial scale. Detailed views are shown in the snapshots of Figure 4.9. In both figures, we are showing results of RER computations to harmonic degree $\ell_\infty = 10^5$ based on the h^{APLO} LDCs (the corresponding response function is shown in Figure 4.1*b*). We note that no broad–scale subsidence is observed, even in the central portion of the GrIS where our ICESat mass balance indicates mass increase during period 2003–2008 (see Figure 4.2). This is due to the broad range of the elastic uplift that, according to the results of Figure 4.1, is surrounding the centers of mass loss in spite of their small spatial wavelength (a discussion on this character of the

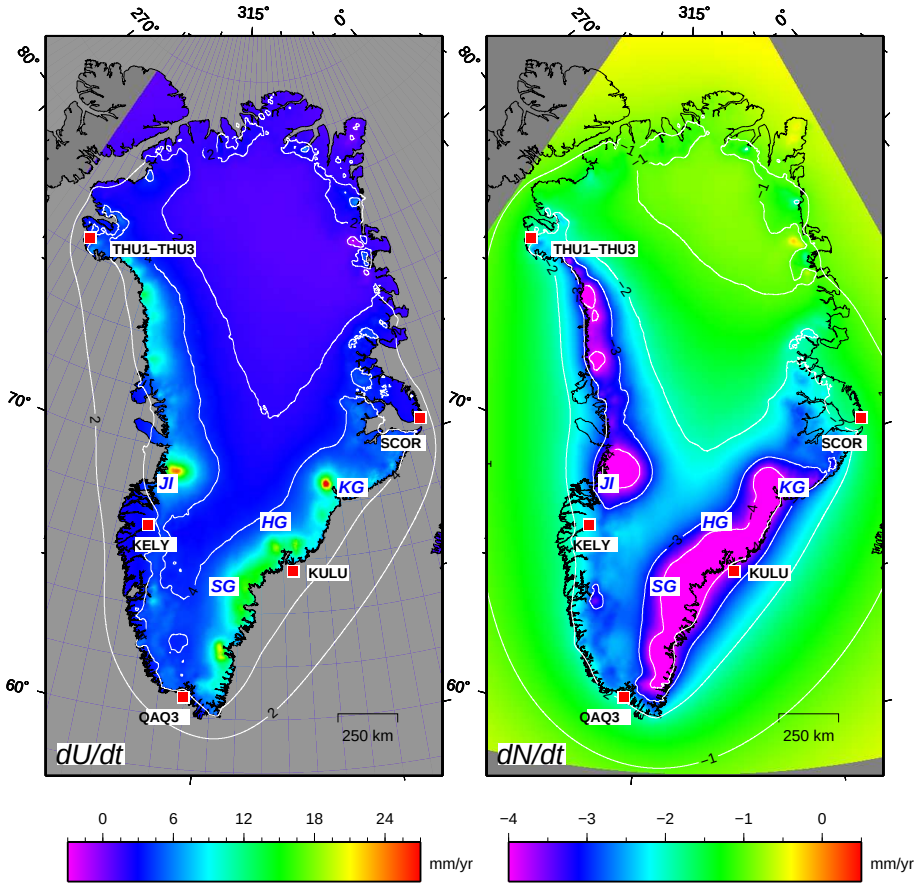

Figure 4.8: Rate of vertical uplift *(a)* and of geoid height variation *(b)* across Greenland, according to RER computations to degree ℓ_∞. The maximum rates ($\dot{U} \approx 25.5$ and $\dot{N} \approx -9.3$ mm yr^{-1}, respectively) are predicted in the vicinity of the Kangerdlugssuaq Glacier (KG). Here, the horizontal resolution is ~ 2.8 km.

elastic response to surface loads is given by Stocchi et al. 2005). This long–range uplift prevails on the subsidence induced by ice accumulation in the central portion of the GrIS. According to Figure 4.8*a*, in the bulk of the GrIS the elastic uplift varies in the range between 2 and 4 mm yr^{-1}, comparable to that estimated by the low–resolution GER method in Figure 4.3*a*. Similarly, the large–scale rate of geoid subsidence is comparable to that of Figure 4.3*c*. However, these highly detailed maps allow to resolve tiny features of the vertical velocity field, whose amplitudes significantly exceed that obtained by the GER analysis. Maximum predicted rates are $\dot{U} \approx 25$ mm yr^{-1}and $\dot{N} \approx -9$ mm yr^{-1}, observed in the vicinity of the Kangerdlugssuaq Glacier (KG). These improved estimates may have an impact on the interpretation of GPS data from stations located close to

glaciers associated with rapid mass loss. This is the case, for example, of the GPS site of KULU, located in the Southern Glaciers (SG) region (see also Figure 4.9*e*). In fact, as shown in Table 4.4, our RER computations at KULU deviate quite significantly (by about $\sim$ 2 mm yr^{-1}) from those obtained by the GER method. In the other GPS sites relevant for this study, located at larger distances from the main drainage basins, the differences are less significant, to indicate that these sites are mostly responding the large scale uplift of the GrIS, which results from the superimposition of the contributions of all elementary ice elements of Figure 4.2*a* and cannot be directly attributed to individual

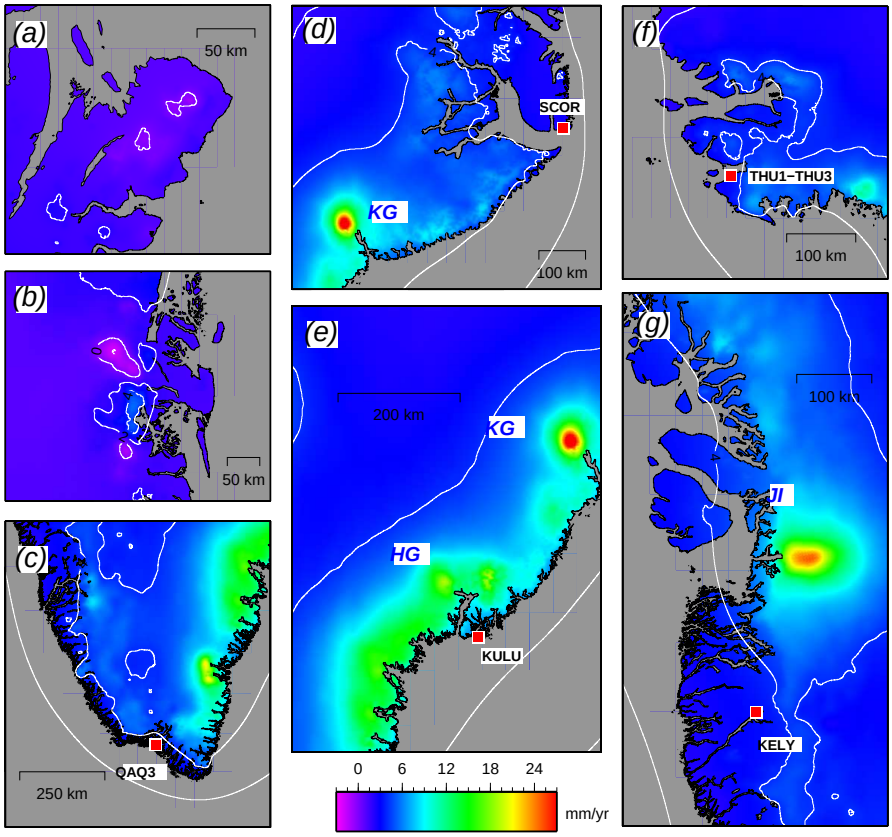

Figure 4.9: Details of the elastic uplift patterns associated with the mass balance M3, obtained by the RER method to harmonic degree $\ell_{max} = \ell_\infty$. Contours lines are 1 mm yr^{-1} apart. Frames *(a)* and *(b)* show areas of subsidence in the regions of the Flade Isblink and Storstrømmen glaciers, respectively. The other frames show detailed uplift maps in areas surrounding the GPS stations of QAQ3 *(c)*, SCOR *(d)*, KULU *(e)*, THUL *(f)* and KELY *(g)*. In these maps, the horizontal resolution is $\sim$ 550 m in the NS direction and varies from 90 to 270 m in the EW direction.

localized glaciers. Due to the different mass balances employed, a direct comparison of our RER computations with the elastic computations of Khan et al. (2007, 2008) is not straightforward (but it will be attempted in Section 4.3.4 below). However, since in Figures 4.8 and 4.9 we account for the whole mass balance, we expect that ICESat – derived vertical rates of displacement may exceed those of Khan *et al.*, who have only used the mass balance from the major drainage systems.

Due to the increased spatial resolution of our RER computations, localized areas of subsidence are now visible in Figure 4.8 on the scale of a few tens of km, particularly along the NE coasts of Greenland. The existence of these subsiding areas could be guessed from Figure 4.2*a*, which is showing localized spots of positive mass balance (Sørensen et al., 2011). In particular, subsidence occurs in the area of the outlet glacier of Storstrømmen (see detail in Figure 4.9*b*), which is recovering from a previous surge that lasted until 1978 (Reeh et al., 1994; Boggild et al., 1994) and where according to our computations the rate of subsidence is reaching an amplitude of ≈ 2 mm yr^{-1}. However, due to the resolution of the ICESat data, the complete mass loss signal might not be captured in the outlet glaciers, meaning that the elastic uplift signal might truly be higher (especially near the glacier front) than what can be seen from ICESat. Another area of subsidence can be recognized in the vicinity of the Flade Isblink glacier, the largest ice cap in Greenland (Figure 4.9*a*). As discussed by Sørensen (2010), at the Flade Isblink ice cap, solution M3 suggests a complex pattern of elevation change. While the north–western part of the ice cap has thickened with maximum values of more than 1 m yr^{-1}, the south–eastern part shows a thinning of up to 0.5 m yr^{-1}. This supports recent results of Kelly and Lowell (2009), who indicate that at present Flade Isblink is growing, though further research is under way by CReSIS (John Paden, personal communication, 2011) to examine this growth. According to our RER computations, the subsidence rate in the Flade Isblink can be estimated at the level of ~ 0.5 mm yr^{-1}. Note that these estimates of subsidence in the NE of the GrIS only account for the current response elastic uplift. In the same regions, strong regional scale uplifts associated with the GIA component of vertical displacement would wipe off these areas of subsidence, at least according to our computations based on model ICE–5G of Peltier (2004)

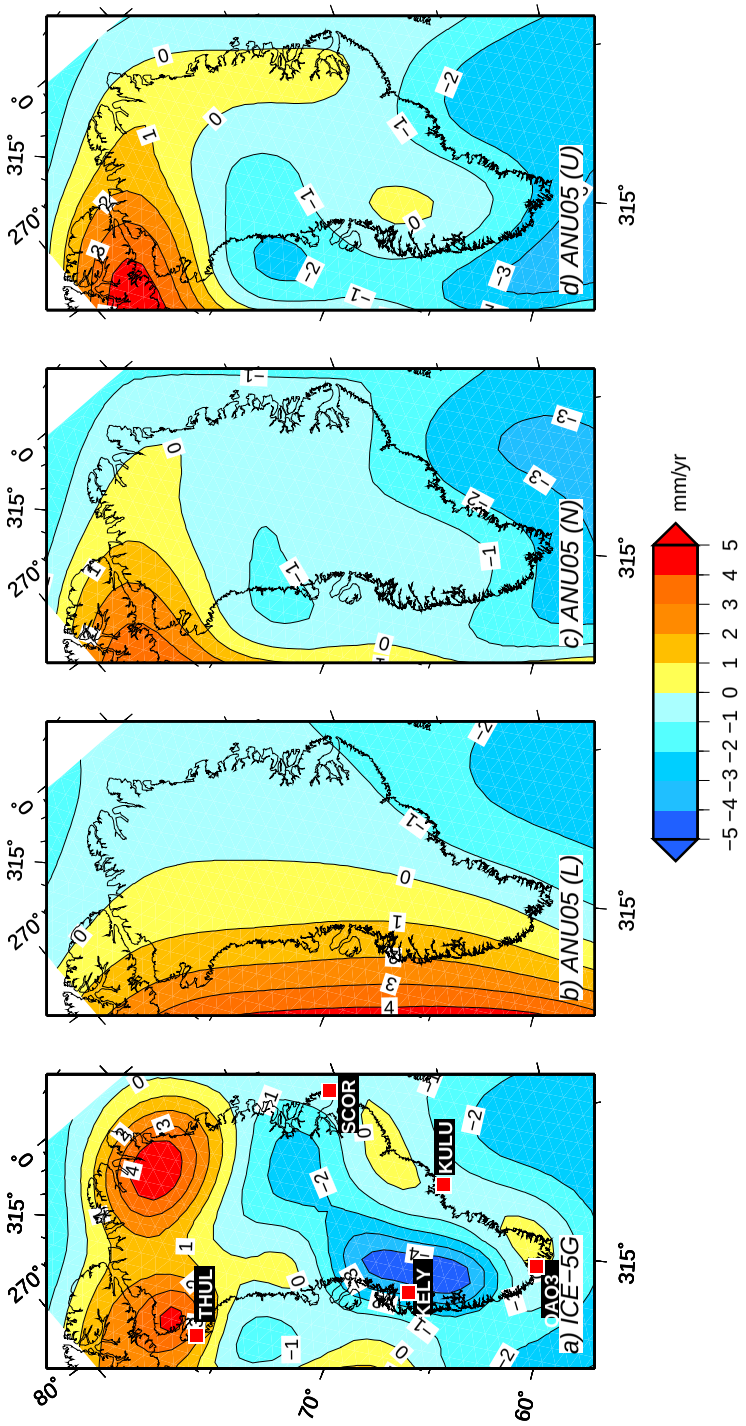

Figure 4.10: Present–day GIA uplift rates computed according to our implementation of the sea-level equation, and using the four models described in the body of the paper and in Table 5.2. Frame *(a)* also shows the locations of the main GPS sites. In all these GIA computations, $\ell_{max} = 128$.

4.3.4 Discussion

Model estimates of uplift due to GIA

The modeling results presented in the previous sections indicate that the elastic uplift of Greenland in response to current mass loss is characterized by an heterogeneous pattern (see, in particular, Figure 4.8). Localized, glacier–scale vertical movements at rates as large as tens of mm yr^{-1} are superimposed on a background GrIS –scale uplift of a few millimeters per year that ultimately results from the interference of the localized sources. Since Greenland is considered a stable continental region with low seismicity (Chung and Gao, 1997), GIA candidates as the second major cause of vertical deformation in the area (seismicity is mainly localized along the coastlines and possibly associated with the GIA process itself, see Chung 2002). To estimate upper and lower bounds of the response of Greenland to the northern hemisphere ice sheets fluctuations (i. e., the GIA component of vertical deformation), we have computed, via Eq. (4.1), the rates of vertical displacement expected across the GrIS according to a set of various plausible scenarios of the global melting history since the Last Glacial Maximum and the Earth rheological profile. This approach, similar to that employed by Velicogna and Wahr (2006a) in order to estimate the range of GIA correction to GRACE observations, differs from previous studies in which a single model of deglaciation has been considered (see e. g., Khan et al. 2008) and can tentatively provide the range of uncertainly associated with GIA modeling. These uncertainties arise as a consequence of the different observational constraints used to reconstruct the history of melting, different assumptions about the rheological profile of the mantle and different numerical implementations of the SLE. We also remark that we did not attempt any simultaneous inversion of GIA parameters based on classical Relative Sea Level (RSL) observations and space geodetic methods, as done for example by Paulson et al. (2007) and, recently, by Wu et al. (2010). Rather, in our GIA simulations, we have used fully *a–priori* ice sheets scenarios and viscosity profiles, being aware that a significant modification of the viscosity profile would amount to generate a new ice history since the Last Glacial Maximum in order to match the RSL observations (Paulson et al., 2007).

Our GIA computations, obtained by an improved version of the open source code SELEN (Spada and Stocchi, 2007), are shown in Figure 4.10. Here we account for the sea–level variations associated with the rotational feedback (Milne and Mitrovica, 1998) and, since we aim at estimating the uncertainties related with the ice sheets history

and mantle viscosity, we do not account for the horizontal migration of shorelines. In all computations, the deglaciation scenarios for North America, Eurasia, Antarctica and minor ice sheets are also included. As in our previous ERR and GER computations, rates of displacement are computed in the reference frame with origin in the center of mass of the Earth system (including surface loads). This ensures consistency with the comparisons with GPS rates of uplift data discussed below, which are expressed in the ITRF2005 reference frame (Khan et al., 2008). In Figure 4.10 we show results obtained by implementing four different scenarios in our numerical code SELEN. In Figure *a* we employ the ice sheets chronology ICE–5G (Peltier, 2004) while in Figure 4.10*b*–*d* we consider three variants (corresponding to different viscosity profiles, see below) of the ice model progressively developed at the Research School of Earth Sciences (RSES) of the National Australian University by Kurt Lambeck and co–workers (see Fleming and Lambeck 2004 and references therein). Since this model is valid as of 2005, we will refer to is as to ANU05 in the following. Its Greenland component is referred to as GREEN1 – first order Greenland ice model – by Fleming and Lambeck (2004).

Models ICE–5G and ANU05 differ in several aspects, including the mantle viscosity profile, the ice volumes distribution at the Last Glacial Maximum and the time history of Equivalent Sea Level, which represents the amount of ice water exchanged between the oceans and continental ice sheets over time. These differences are ultimately the consequence of the different sets of global relative sea–level data and modern geodetic observations used by the authors to constrain the model parameters. Here, the ice histories of ICE–5G and ANU (available from the personal web page of W. R. Peltier and kindly provided by K. Lambeck, respectively), are implemented in SELEN (Spada and Stocchi, 2007). For ICE–5G, which incorporates the Greenland ice sheet reconstruction by Tarasov and Peltier (2002), we employ an incompressible Earth model characterized by a two–layer viscosity profile that approximates the multi–layered profile VM2 (details are given in Peltier 2004) while for ANU05 we adopt the effective values for the lower, nominal and upper solutions of Fleming and Lambeck (2004) (viscosity values are shown in Table 5.2 for the four models employed here). We note that independent computations based on ICE–5G (Khan et al., 2008), show the same broad pattern of Figure 4.10*a*, but with significantly larger local values (in the range of several mm yr^{-1}) and a markedly enhanced subsidence in the Baffin Bay and in the Davis Strait. As discussed below, these differences have a significant impact on the interpretation of the GPS observations.

Table 4.3: Lithospheric thickness (LT) and mantle viscosity η for the GIA models employed in this study (labels UM and LM denote upper and lower mantle, respectively). ANU05 data are taken from Fleming and Lambeck (2004), while ICE–5G data are representative of volume–averaged VM2 viscosity values (Peltier, 2004).

GIA Parameter	ICE–5G (VM2)	ANU05 (Lower)	ANU05 (Nominal)	ANU05 (Upper)
LT (km)	90	50	80	100
η_{UM} ($\times 10^{21}$ Pa·s)	0.5	0.2	0.4	0.5
η_{LM} ($\times 10^{21}$ Pa·s)	2.7	5	10	20

Though it was not possible to unequivocally identify the origin of these differences, it is likely that they results from a combination of effects, including the time–discretization employed to compute the time–derivatives of vertical displacements and geoid variations, the different spatial resolution (i. e., the ℓ_{max} value) employed in modeling (L. Tarasov, personal communication, 2011) and finally our choice to use a coarse two–layers depth–average version of the VM2 viscosity profile. These issues are going to be addressed within a SLE benchmark program along the lines of a recent initiative of the GIA community (Spada et al., 2011b). To facilitate the inter–comparison and the validation of our results, the GIA numerical codes and input data used to obtain Figure 4.10 are available from GS.

The maps in Figure 4.10 show a significant variance that supports previous concerns about the effective accuracy of GIA computations over Greenland (Khan et al., 2007, 2008). For all solutions shown, local vertical velocity values across the GrIS are of the order of a few mm yr^{-1}, somewhat less than the background (regionally averaged) RER elastic velocities shown in Figure 4.9. Correcting the ICESat elevation change data for these GIA effects implies a mass budget correction of approximately 1 Gt yr^{-1} (Sørensen et al., 2011), a small amount if compared to the cumulative error associated with the ICESat data inversion and firn compaction corrections ($\pm$28 Gt yr^{-1} for solution M3). As it is apparent from Figure 4.10, a major difference between ICE–5G and ANU05 results is the uplift pattern in the southwest of Greenland, where the ICE–5G predictions show a marked subsidence in the surroundings of the GPS site of KELY, approximately between latitudes 62° and 72°N. As pointed out by Khan et al. (2008), this subsidence is caused by the re–advance of the ice margin in west Greenland to its current location

during the last 8,000 years. This feature appears not to be present in the ANU05 model, though the effects of more recent re–advances ("neoglacial" periods) have been considered by Fleming and Lambeck (2004). Other significant differences between the predictions based on ICE–5G and ANU05 visible in Figure 4.10 can be attributed to the characteristics of the rheological profiles employed (see Table 5.2), to the time history of the ice sheets surrounding the GrIS (especially Laurentia) or to the methods followed in the GrIS reconstruction. While Fleming and Lambeck (2004) have only employed constrains from Holocene relative sea–level (RSL) histories from sites along the coastlines of Greenland, Tarasov and Peltier (2002) have also used 3–D dynamical ice sheets models (e. g., Huybrechts 1996).

Comparison of GPS uplift with modeled estimates

As discussed below (and as pointed by Khan et al. 2010), observations of vertical movements at the GPS sites shown in Figure 4.10*a* in conjunction with elastic rebound modeling can help to discriminate between competing GIA models. However, a full understanding and interpretation of some features of the uplift patterns in Figure 4.10, such as those apparent in the northeastern portion of the GrIS will only be possible when sufficiently long series of data will become available from the GNET sites shown in Figure 4.2*b*. In Figure 4.11 we compare various model predictions with GPS observations at the GPS sites of KELY *(a)*, THUL *(b)*, SCOR *(c)*, KULU *(d)* and QAQ1 *(e)*, whose locations are reported in Figure 4.2 (the numerical data employed to draw this figure are summarized in Table 4.4). Black diamonds reproduce the results of Khan et al. (2008) in their Table 4 and only account for elastic rebound. Similarly, black triangles are results from our RER modeling based on the mass balance M3 shown in Figure 4.2*a* and on the response function of Figure 4.1*b* (with $\ell_{max} = \ell_\infty$). Using model M2 of Sørensen et al. (2011), characterized by a mass balance reduced by $\sim 20\%$ would reduce the RER results by ~ 1 mm yr^{-1} without changing the main conclusions of this work. The combination of the RER predictions with the four GIA scenarios discussed in Figure 4.10 are displayed by an open circle (ICE–5G) and squares (the three variants of ANU05). Observed secular rates of vertical uplift and their uncertainties ($\pm 1\sigma$), shown by shaded rectangles, are taken from the work of Khan et al. (2008) (see their Table 2) and are expressed in the ITRF2005 reference frame. For NUUK (a tide gauge station), the rate of vertical uplift has been obtained by Khan et al. (2008) with the aid of altimetry data. In some cases (e. g.

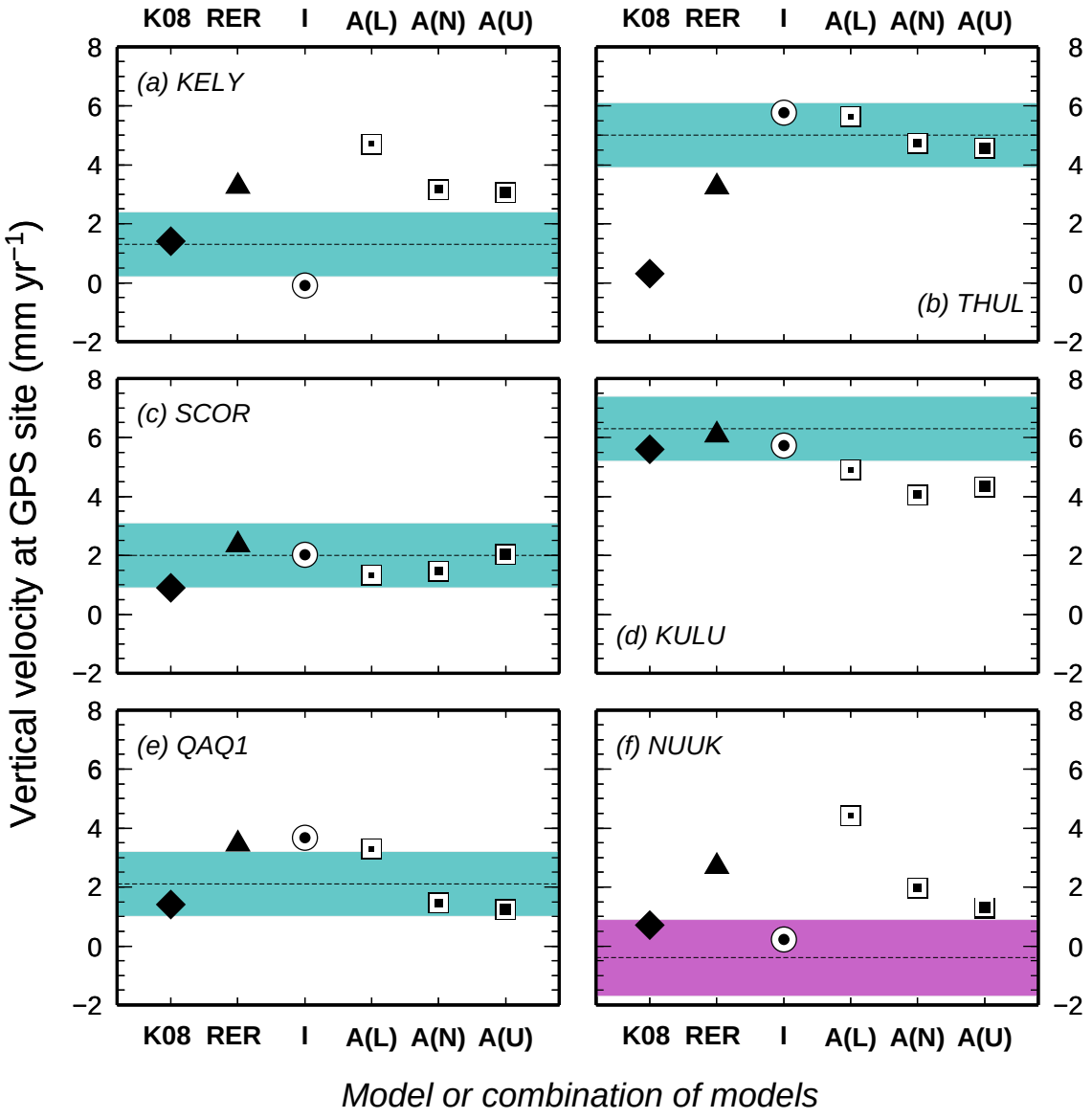

Figure 4.11: Rates of vertical uplift observed at relevant GPS sites *(a–e)* and at the NUUK tide gauge *(f)* (shaded, from Khan et al. 2008). Model predictions are as follows. K08 and RER: Elastic rebound uplift rate according to Khan et al. (2008) and this work, respectively; I: combination of RER with our GIA computations based on ICE–5G; A(L), A(N) and A(U): combination of RER with the lower, nominal and upper ANU05 solutions.

Table 4.4: Observed and predicted vertical velocity dU/dt at the GPS sites (KELY to QAQ3) and tide–gauge (NUUK) considered in this study. In agreement with Khan et al. (2008), THUL indicates the combined THU1/THU2 time series (the secular uplift rate is assumed to be the same at both locations). Predicted values for the GIA and the ER processes are separately presented. Units are mm yr^{-1} throughout.

GPS site	KELY	THUL	SCOR	KULU	QAQ3	NUUK
Longitude λ ($^\circ W$)	50.94	68.78	21.95	37.14	46.04	51.75
Latitude φ ($^\circ N$)	66.98	76.53	70.48	65.57	60.71	64.18
Observed dU/dt [a]	1.3 ± 1.1	5.0 ± 1.1	2.0 ± 1.1	6.3 ± 1.1	2.1 ± 1.1	-1.5 ± 1.3
GIA component						
ICE–5G(VM2)[a]	−3.3	−0.1	+2.0	−1.7	+1.0	−3.3
ICE–5G(VM2)[b]	−1.95	+1.86	−0.64	−0.12	+0.94	−1.57
ANU05(L)	+1.44	+2.39	−1.02	−1.16	−0.16	+1.74
ANU05(N)	−0.10	+1.50	−0.89	−2.02	−2.00	−0.72
ANU05(U)	−0.22	+1.33	−0.32	−1.74	−2.23	−1.38
ER component						
Khan et al. (2008)[a]	+1.4	+0.3	+0.9	+5.6	+1.4	+0.7
RER (M3)[c]	+1.42	+0.30	+0.64	+4.01	+0.91	+0.89
RER (M3)[d]	+3.26	+3.23	+2.34	+6.07	+3.45	+2.68
GER (M3)[e]	+3.42	+3.64	+2.82	+8.09	+4.29	+3.27

[a] Reproduced from Khan et al. (2008).

[b] Details of our numerical implementation of ICE–5G(VM2) are given in Section 4.3.4.

[c] Here $h = h^{APLO}$ and $\ell_{max} = \ell_\infty \equiv 10^5$. Only the ICESat M3 mass balance from the drainage basins n. 10, 11, 13 and 20 considered by Rignot and Kanagaratnam (2006) is taken into account.

[d] Here $h = h^{APLO}$ and $\ell_{max} = \ell_\infty$.

[e] As in *d)*, but with $\ell_{max} = 128$.

KELY and THUL), the GPS record length exceeds a decade and, in all cases, it overlaps the span of the ICESat observations considered in this study (2003–2008). Following Khan et al. (2008), we make the hypothesis that the secular trends at the sites considered in Figure 4.11 are associated with the combined effects of the elastic uplift caused by the present-day mass loss and of the (steady–state) viscoelastic uplifts associated with past changes. However, short–term effects associated with crustal heterogeneity (Ivins and Sammis, 1996) or shallow upper mantle transient components of deformation (Spada et al., 2011a) cannot be discounted, even on a decade time scale. Furthermore, inter–annual effects caused by accelerations of the mass loss of the main outlet glaciers of the GrIS (Velicogna and Wahr, 2006a; Khan et al., 2010) are not considered here, since the ICESat mass budget employed in this study represents a time average over the whole observation period (Sørensen et al., 2011).

Some trends in Figure 4.11 are worth to discuss. First, elastic rebound (black filled symbols) effectively appears to constitute the major component of total vertical deformation at most of the GPS sites considered. However, there are remarkable exceptions which will be discussed below. Second, the RER solution always exceeds (in some case very significantly, as for THUL), the Khan et al. (2008) results. We expect that the dominance of the RER uplift rates mostly reflects differences in the mass budgets employed. To test this hypothesis, we have adopted an approach similar to Khan et al. (2008), who have employed the regional mass balances published by Rignot and Kanagaratnam (2006), based on radar interferometry observations. In particular, we have performed further RER computations in which we have retained, in the ICESat mass balance M3 of Figure 4.2, only the drainage basins numbered by 10, 11, 13 and 20 in the work of Rignot and Kanagaratnam (2006), which are encompassing the glaciers KG, HG, SG and JI, respectively. The results of this consistency test, reported in Table 4.4 are found to be in good agreement with those obtained by Khan et al. (2008) (the only significant disagreement is possibly relative to KULU). This finding further confirms the consistency of the ICESat –derived mass balance M3 with independent observations, and explicitly indicates that the contribution of relatively small glaciers located in the vicinity of the GPS site (and naturally included in our RER modeling) is important and in specific cases it can dominate the one associated with larger but relatively distant sources. In this respect, a particularly interesting example is that of THUL, where the RER vertical uplift rate (Figure 4.11*b*, ~ 3 mm yr^{-1}), largely exceeds

the small value computed by Khan et al. (2008) (0.3 mm yr^{-1}), who have only included the major glaciers in their computations. It is likely that the vertical deformations at the GPS site of THUL are mostly associated with the mass loss at the nearby Gades Glacier (and at those further to the south), where uplift rates are locally as large as ~ 15 mm yr^{-1}(see Figure 4.9*f*).

According to our computations in Figure 4.11, predictions based on the combination RER+ICE–5G (open circle) fall always within the shaded ($\pm 1\sigma$) region or lies marginally outside. Considering the modeling uncertainties and the simplifying assumptions made, we find that this level of agreement between GPS observations and model predictions is acceptable. In SCOR, QAQ1 and KULU, the GIA process does not alter the already satisfactory fit between the RER solutions and the GPS observations while, remarkably, the GIA contribution helps to reconcile the RER solution with the GPS trend at the sites of THUL, NUUK and KELY. This result is clearly at variance with one of the main conclusions of Khan et al. (2008), who attributed the significant discrepancies (as large as ~ 3.7 mm yr^{-1}) between observed and predicted rates at THUL, KULU and SCOR to limitations of the GIA model (namely, ICE–5G). As a further remark, we note that the model predictions including the GIA component based on model ANU05 (squares) show a considerable scatter and, globally, a reduced performance compared to ICE–5G. The misfit can be tentatively attributed to the inhomogeneity of the spatial distribution of the RSL observations that are used to constrain the spatiotemporal features of ANU05. For example, the lack of RSL observations from the Southwest of Greenland (Fleming and Lambeck, 2004) can be invoked to motivate the relatively poor fit at KULU, but this could hardly justify the misfit at KELY, seen the large number of observations that Fleming and Lambeck have employed from the coasts facing the Baffin Bay. Though it is not our purpose to perform a rigorous statistical analysis of the results Figure 4.11, the misfit diagram shown in Figure 4.12 can help to classify the performances of the various models employed (as a rule of thumb, a misfit $M \approx 1$ would indicate a good match between data and model predictions). As expected, the misfit curve has a minimum when combinations of ER and GIA predictions are considered (central portion of the figure), and increases when ER and GIA predictions are considered separately. In agreement with the qualitative scenario in Figure 4.11, the best performing combination of models is RER+(ICE–5G) ($M \simeq 1.2$). The larger value for RER+ANU05(U) ($M \simeq 2.7$) mainly arises by the misfit of the GIA model at the GPS sites of KELY and KULU. In Figure 4.13

we show the rates of vertical uplift expected at all the GPS (GNET) sites of Figure 4.2*b*, according to different combinations of GIA and RER computations. In the absence of transient rheological effects (Spada et al., 2011a), these trends will not change over the next few centuries, provided that the melting rate of the GrIS will not change. Dotted curves only account for the elastic deformation, while the solid ones incorporate the GIA (ICE–5G) effects. Observed rates are not shown (except those at the main GPS sites of Table 4.4); due to the short record period, vertical uplifts at these GPS sites cannot still be established with an acceptable level of precision. To directly appreciate the effects of elastic mantle layering upon total vertical deformation, the computations in frame *(a)* have been performed using $h = h^{APLO}$ in Eq. (4.4) LDCs, while in (*b*) $h = h^{ALMA}$. Assuming that the rate of ice loss in Greenland will remain constant in the future and that transient rheological effects (Ivins and Sammis, 1996) can be neglected, the results shown in Figure 4.13 can provide an estimate of the rates of vertical uplift expected during the next century (Spada et al., 2011a) (to a first approximation, regional sea–level variations along the coasts surrounding the GPS sites will be mainly controlled by vertical

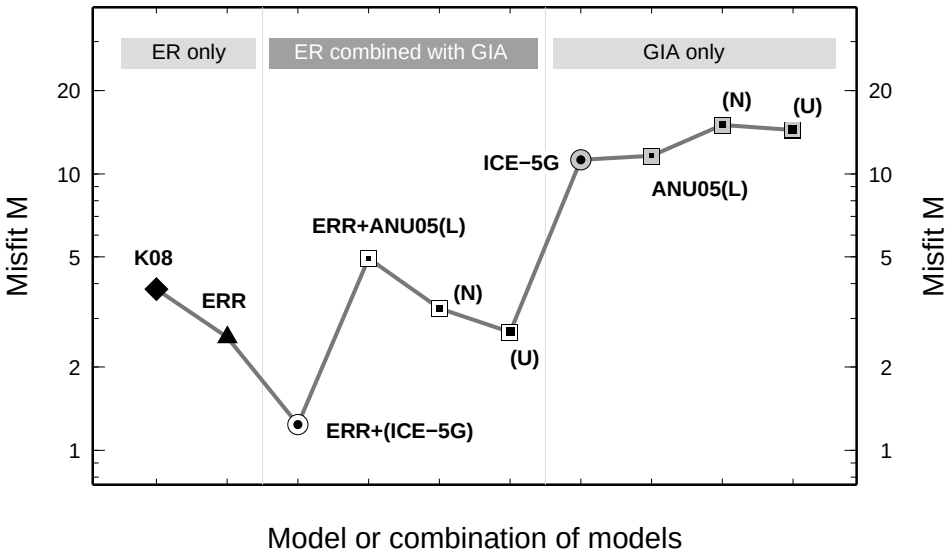

Figure 4.12: Misfit between model predictions and the GPS observations of Figure 4.11. Misfit for purely ER ("Elastic Rebound") models, for combinations of ER and GIA models and for GIA models only, is computed as $M = \frac{1}{N} \sum_{i=1}^{N} ((\mathrm{mod}_i - \mathrm{obs}_i)/\sigma_i)^2$ where N is the number of sites considered ($N = 6$), obs_i is an observed GPS uplift rate, σ_i its uncertainty (see Table 4.4) and mod_i is a modeled rate. Note that the M–axis is logarithmic. The symbols are connected by segments only for showing qualitatively the misfit trend with varying combination of models.

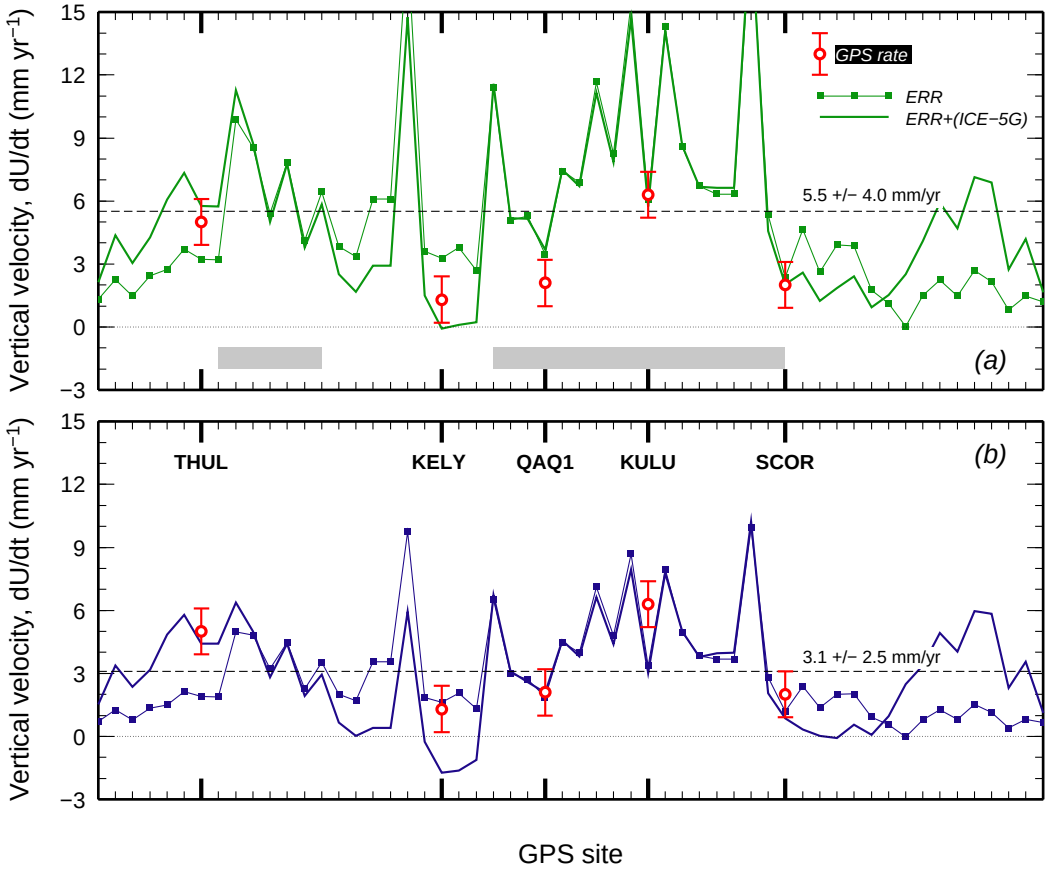

Figure 4.13: Vertical uplift rates expected at all the GPS sites shown in Figure 4.2 according to several model predictions. In frame *(a)*, the elastic component (RER) of total uplift is computed using the LDCs $h = h^{APLO}$, while in *(b)* $h = h^{ALMA}$. Dashed lines show the average trend of predicted vertical uplift and its standard deviation. Shaded rectangles indicate the range of GPS sites where vertical GIA movements are negligible compared to ER movements. These sites range between DKSG and QAAR and between UTMG and SCOR, respectively (see Figure 4.2*b*).

displacements, with an amplitude $\approx -dU/dt$). Figure 4.13 shows the relative importance of GIA compared to elastic rebound. GPS sites in the range marked by the two gray shaded rectangles in frame (a) are virtually only affected by elastic rebound. It clearly appears that among the GPS sites that currently dispose of a relatively long record period, only THUL and KELY are sensitive to the GIA component of vertical deformation. This conclusion is unaltered if the elastic deformations are computed using $h = h^{ALMA}$, as done in frame (b). However, as expected from the qualitative arguments in Section 4.2, vertical velocities in Figure 4.13*b* are reduced with respect to (a). The average reduction is significant (~ 2 mm yr^{-1}), indicating that the elastic structure of the outmost layers

plays an important role in the assessment of vertical deformations.

4.3.5 Concluding remarks

We have investigated some geophysical consequences of the recently published estimate of the annual mass loss of the GrIS (Sørensen et al., 2011), derived from surface elevations observed by ICESat observations, firn compaction and surface density modeling. In particular, we have provided new estimates for the crustal uplift rates associated with elastic and viscoelastic rebound, regional and global sea–level fingerprints, and provided a new discussion on the impact of elastic and viscoelastic rebound on geodetic GPS signals in Greenland. Our results can be summarized as follows.

i) The long–wavelength ($\ell_{max} = 128$) ER of Greenland in response to present–day mass loss shows a clearly bimodal pattern, according to the spatial pattern of the ICESat mass balance model employed in this study. While the rates of vertical uplift at the GrIS margins amount to several mm yr^{-1} with peak values of $\sim$ 10 mm yr^{-1}, in the bulk of Greenland they range between 2 and 4 mm yr^{-1}. At these wavelengths, we have found no sign of broad scale subsidence in the central portion of the GrIS in response to the mass accumulation evidenced by our preferred M3 mass budget. A direct comparison with results obtained by the GRACE mass balance published by Wouters et al. (2008), performed in the same range of wavelengths ($\ell_{max} = 60$) has revealed that the ICESat uplift rates exceed, at the GrIS spatial scale, the GRACE ones primarily as a consequence of the largest average mass balance in the time period 2003–2008. At smaller spatial scale, ICESat and GRACE–derived vertical movements mainly differ where mass loss is, according to the M3 ICESat mass balance, spatially more concentrated (this occurs especially in the SG and JI areas, where the misfit between the two uplift maps varies between 2 and 3 mm yr^{-1}). High–resolution uplift maps based on the mass balance M3 reveal fine details of the elastic uplift pattern of Greenland and of the geoidal variations, including regions that are subject to subsidence in response to local ice re–advance. While in the case of the northeastern Storstrømmen glacier subsidence is expected since the glacier is recovering from a previous surge (Reeh et al., 1994), for Flade Isblink the ICESat record elaborated by Sørensen et al. (2011) possibly constitutes the first evidence of accretion over a multi–annual time scale.

ii) The sea–level equation provides the natural means of evaluating the contribution of elastic rebound to the regional and global sea–level variations caused by the melting of

the GrIS. We have found that the regional sea–level fall along the coasts of Greenland is strongly anti–correlated with vertical movements. In this regional context, where we have confirmed that self–gravitation of the oceans is playing a minor role, the approximate equation $dS/dt \simeq -dU/dt$ can be applied (Spada et al., 2006). The eustatic (i. e., globally averaged) rate of sea–level change associated with the ICESat melting scenario M3 amounts to $\approx +0.67$ mm yr^{-1}, in good agreement with the value suggested by the GRACE mass balance recently obtained by Velicogna and Wahr (2006a) and Wouters et al. (2008) and also with previous estimates of secular sea–level variations based on classical (tide–gauge) observations (Mitrovica et al., 2001). Since approximately 2003, we note a clear acceleration of ice mass loss from the GrIS , and we underline that the IPCC AR4 (Lemke et al. 2007) with contribution to sea level of 0.21 ± 0.035 mm yr^{-1}underestimated the contribute of GrIS to present-day sea level rise. The ICESat –based global sea–level signature (fingerprint) shows the typical, non–uniform pattern of near–field sea–level fall and far–field sea–level rise (well above the eustatic value) expected as the effect of the elastic deformation of the Earth and of self–gravitation (Mitrovica et al., 2001). Except in the immediate near field of the GrIS , the spatial heterogeneity of the ICESat mass balance M3 does not produce significant deviations from the fingerprint associated with an eustatically equivalent (but spatially uniform) mass balance. We have found that the current mass loss in Greenland has a significant impact on key areas as the Mediterranean, where it can produce a sea–level rise of ~ 0.5 mm yr^{-1}, comparable with the long–term GIA contribution in the bulk of the basin (Tsimplis et al., 2011).

iii) The GIA component of present–day uplift in Greenland has been evaluated using a suite of different scenarios for the global history of melting since the Last Glacial Maximum, based on different geophysical constraints (Peltier, 2004; Fleming and Lambeck, 2004). Our findings support previous observations by Velicogna and Wahr (2006a) and Khan et al. (2007, 2008), who have emphasized the importance of the GIA component but, at the same time, have evidenced a significant spread of the GIA predictions which is ultimately associated with uncertainties in the ice melting scenarios and mantle rheological profiles. Using combined (ER+GIA) models, in the last part of this work we have addressed the problem of the interpretation of trends of vertical displacement recorded at the five GPS sites with sufficiently long records previously considered in the literature (particularly, by Khan et al. 2007 and Khan et al. 2008). We have explicitly shown that ER predictions at these GPS sites are

significantly affected by mass loss in near–field drainage basins resolved in the ICESat mass balance and previously excluded in ER modeling (in this respect, a particularly interesting case is that of THUL, where previous ER computations by Khan et al. 2008 have clearly underestimated the uplift rate). According to our computations, only data from two out of the five GPS sites considered (namely THUL and KELY) can be currently employed to constrain competing GIA models; the others (SCOR, KULU and QAQ3) are currently only responding to ER. In the absence of significant tectonic deformations at the GPS sites, we would expect that ER predictions combined with GIA could acceptably explain the observations. According to our modeling efforts, at the sites of THUL and KELY (and at the tide gauge of NUUK) the GIA (ICE–5G) component of the total rate of displacement effectively helps to reconcile ER (ICESat –based) predictions with the available GPS observations, minimizing the total misfit.

4.4 Antarctica

4.4.1 Mass Balance of Antarctica

The Antarctica Ice Sheets (AIS) covers about 98% of the Antarctic continent and is the largest single mass of ice on Earth. It covers an area of almost 14 million km^2 and contains 30 million km^3 of ice. That is, approximately 61% of all fresh water on the Earth is held in the Antarctic ice sheet, an amount equivalent to 70 m of water of oceans. Physically, Antarctica (Figure 4.14) is divided in two by Transantarctic Mountains: western Antarctica and eastern Antarctica correspond to the West Antarctic Ice Sheet (WAIS) and East Antarctic Ice Sheet (EAIS). In east Antarctica, the ice sheet rests on a major land mass, but in west Antarctica the bed can extend to more than 2500 m below sea level. Davis et al. (2005) note that there is evidence of conflicting trends in ice sheet thickness across Antarctica: the WAIS has been thinning over the past decade, while the EAIS became thicker over the period 1992 through 2003. The possibility that the WAIS could react rapidly to external forcing was first proposed in the late 1960s (Mercer, 1968). Moreover Bamber et al (2007) suggest that ice sheet-ocean interactions might yield ice-stream acceleration ultimately leading to disintegration of the WAIS. Mass gains from accumulating snow, particularly on the Antarctic Peninsula and within east Antarctica, exceed the ice dynamic mass loss from west Antarctica (Zwally and Giovinetto, 2011). The result exacerbates the difficulty

Figure 4.14: Map of Antarctica.

of explaining twentieth century sea-level rise (Wingham, 2006). Due to the recent performance of satellite gravity missions (CHAMP, GRACE, and GOCE) and satellite altimetry missions (ICESat, CRYOSAT-2), several mass balances of the AIS (and of the associated uncertainties) have been published. The overall contribution of the Antarctic ice sheet to global sea-level change thus depends on the separate balance between WAIS and EAIS (Velicogna et al., 2006b). Table 4.5 gives a review of mass balances of the WAIS, EIS, and AIS . The mass balance elaborated by Wingham (2006), based on satellite altimetry, represents an outlier from the range shown in Table 4.5. On the other hand, satellite altimetry measures height of ice (or sea)–surface height. In order to provide an estimate of volume, it is necessary to apply corrections for the elevation change. The largest elevation change correction that must be applied is the firn compaction correction. This, with GIA and bedrock movements, is an important element of uncertainty upon the estimate the mass balance (Sørensen, 2010). Estimates of recent changes in mass balance range from gains of 27 Gt yr^{-1} of ice to loss over -190 Gt yr^{-1} of ice. Because 360 Gt yr^{-1} represents an annual eustatic sea level rise of 1.0 mm yr^{-1}, recent estimates indicate a contribution of AIS to sea level rise ranging between 0.075 mm $yr^{-1}$and 0.52 mm yr^{-1}. There is of course uncertainty in the estimation methods, but with the exception

Table 4.5: GIS mass change trends from altimetry, mass-budget and gravity-change approch.

Author	Method	Period	Volume $km^3\ yr^{-}1$	Mass Gt $yr^{-}1$
Velicogna et al. (2006b)	GRACE	Apr 2002-Aug 2005	-148 ± 21	$--$
EAIS			0 ± 56	$--$
WAIS			-148 ± 21	$--$
Wingham (2006)	Altimetry	1992-2003	$--$	27 ± 29
Rignot et al. (2008a)	InSAR	1992-2008	$--$	-138 ± 92
EAIS			$--$	-4 ± 61
WAIS			$--$	-106 ± 60
Velicogna (2009)	GRACE	Apr 2002-Feb 2009	$--$	-143 ± 73
Chen et al. (2009)	GRACE	Apr 2002-Jan 2009	$--$	-190 ± 77
EAIS			$--$	-57 ± 52
WAIS			$--$	-132 ± 26
Wu et al. (2010)	GRACE	2002-2008	$--$	-87 ± 43
EAIS			$--$	-23 ± 29
WAIS			$--$	-64 ± 32
Zwally and Giovinetto (2011)	GRACE	1992-2001	$--$	-31 ± 21
EAIS			$--$	-16 ± 21
WAIS			$--$	-47 ± 21

of Wingham mass balance (Wingham, 2006), multiple different types of measurement techniques all show that Antarctica is losing land ice as a whole, and these losses are accelerating quickly (Velicogna, 2009). The time intervals covered by the published mass balance estimates varies from few decades to less than five years in some cases. This is a second factor of uncertainty. Wu et al. (2010) combine GRACE data with data of ICESat laser altimetry providing high-resolution mapping of ice topography. However, the GRACE data are contaminated by the mass redistribution in the mantle of Earth due to glacial-isostatic adjustment. Moreover, because of GIA contamination, GRACE results over Antarctica are more uncertain than over Greenland (Cazenave and William, 2010). Over Antarctica, the GIA effect is of the same order of magnitude as present-day ice mass change (Ivins and James, 2005). However, the GIA correction depends on still poorly known parameters, such as mantle viscosity of the Earth and deglaciation

history (Cazenave and William, 2010). Rignot et al. (2008a), combining InSAR data with regional climate modeling over 1992-2006, confirms a widespread ice mass loss in west Antarctica while, in comparison, east Antarctica was found in near balance.

4.4.2 Results

Global elastic deformations

To model the elastic rebound due to present-day Antarctic ice mass changes we adopt an average estimate mass loss rates elaborated in previous works (see Table 4.5). We simulate the AIS through ~ 9000 equal disc-shaped elements with angular radius $\beta \approx 0.2^{\circ}$ corresponding to an area of $\sim$ 2500 km^2. Due to limits in our knowledge of balance velocities and model resolution, we distribute the mass loss of -100 Gt yr^{-1} equally across the WAIS. Figure 4.15 shows mass variations caused by present-day WAIS ice melt, corresponding to an Equivalent Sea level of 0.256 m. The mass change field was expanded to spherical harmonic degree ℓ_{max}= 128 and, using the improved SELEN progran (Spada and Stocchi, 2007) that elaborates a rebound model solving the sea level equation for an incompressible PREM Earth, considering rotational feed-back, to produce modeled elastic rates. Figure 4.16 shows the rates of sea–level change (dS/dt), the vertical displacement (dU/dt) and the geoid elevation (dN/dt), respectively, based on the WAIS mass budget and obtained by the GER method to degree $\ell_{max} = 128$. The fields are mapped on a quasi–regular geodesic grid with spacing of $\sim$ 500 km, obtained by the icosahedron method of Tegmark (1996). In the considered range of wavelengths, the maximum rates of elastic uplift in the first frame of Figure 4.16 amount to $\sim$ 0.5 mm yr^{-1} and are concentrated in key sector of West Antarctica between the Weddell Sea and Ross Sea (Figure 4.14), were we impose mass loss according to the mass balance WAIS (see Figure 4.15). Due to the uniform melt-water relase of WAIS model, it is not possible to detect areas of local subsidence, which are however suggested by localized ice thinning event such as the collapse in 1995 of the Larsen A and Prince Gustav ice shelves (Thomas et al., 2011) but we note the differential pattern of geophysical quantity between the WAIS and EAIS. This approach follows the pioneering work of Mitrovica et al. (2001) who computed pattern of geophysical component using a trend of 1 mm/yr of present-day sea level rise originating from Antarctica. Significant differences in term of $\dot{S}$, $\dot{U}$ and $\dot{N}$ are evident in the near field between the WAIS and EAIS when we computed the elastic response of Antarctica based on WAIS mass balance. The rate of sea–level change $\dot{S}$

(Figure 4.16) reaches its largest amplitude (~ -1 mm yr^{-1}) in the proximity of Palmer Land (closed to North Antarctic Penisula). $\dot{S}$ is characterized by larger spatial variations compared with $\dot{U}$ and $\dot{N}$, which is a consequence of long wavelength of deformations pertain the geoid compared with the Earth surface (see frame dU/dt and dN/dt of Figure 4.16). The third plot of Figure 4.16) shows that the sea surface, as seen from the Earths center of mass ($\dot{N}$), collapses across the WAIS area while the EAIS shows a smoothly vertical uplift trend. In spite to the rough mass balance models the magnitude and pattern of $\dot{N}$ agree with the secular trends in geoid observed by GRACE from August 2002 until November 2009 as Chambers et al. (2010) show in Figure 1a of their article.

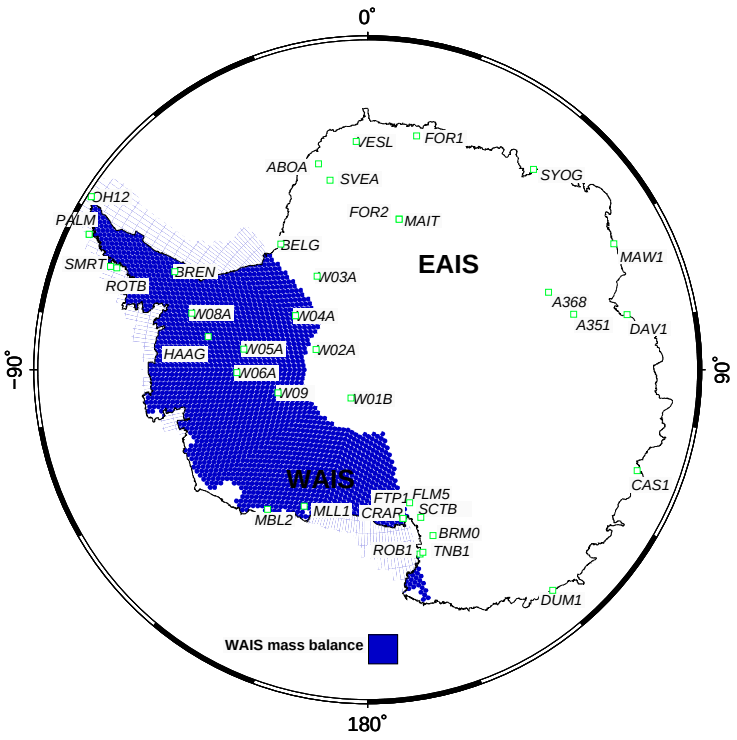

Figure 4.15: Spatial distribution of ice mass loss for the Antarctica Ice Sheets according to general agreement upon widespread ice mass loss is in West Antarctica (WAIS). The whole AIS is discretized into ~ 8865 equal disc-shaped elements with angular radius $\beta \approx 0.2°$ corresponding to an area of 500 km^2. The total mass balance of WAIS is -100 Gt yr^{-1}. The squared symbols show the GPS sites used to analyze the vertical displacement of Antarctica Ice Sheets. The GPS trend come from Thomas et al. (2011).

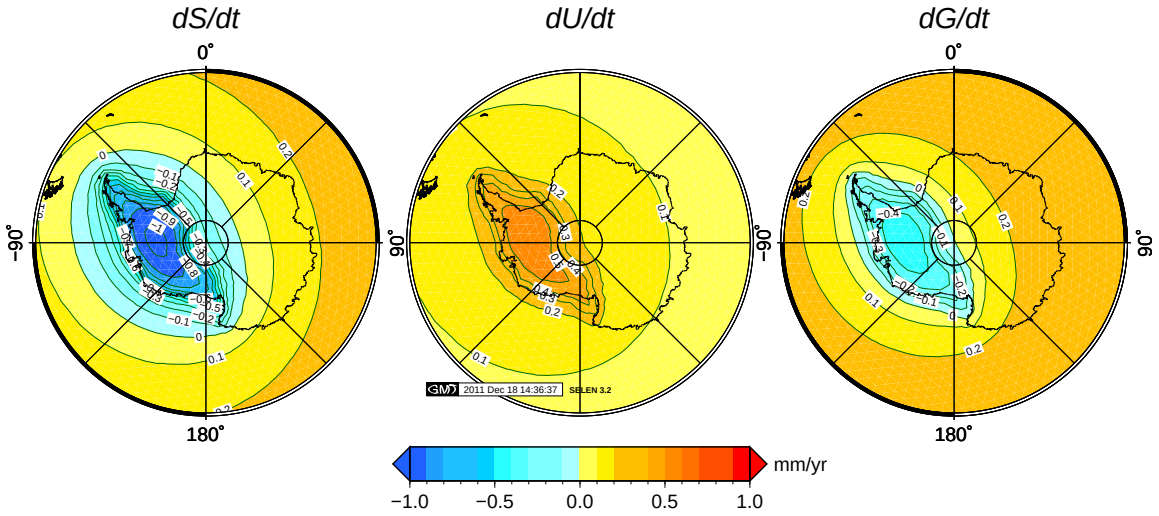

Figure 4.16: Rates of sea–level change (dS/dt), elastic vertical velocity (dU/dt) and of geoid displacement (dN/dt), computed by the GER method to degree $\ell_{max} = 128$, according to WAIS model of mass balance of Antarctica. In all frames, contour lines are spaced by 1 mm yr^{-1}.

Sea level fingerprints

The GER approach based on Eq. (4.1) allows for a "gravitationally self–consistent" evaluation of the global sea–level variations associated with the WAI mass balance model of the WAIS. The sea–level change pattern or "fingerprint" (Mitrovica et al., 2001, 2009; Riva et al., 2010) associated with this mass balance solution is shown in Figure 4.17. With a total mass budget of -100 Gt yr^{-1} according to our computations the WAIS model would provide, on a rigid and non–self–gravitating Earth, an eustatic sea–level variation at a rate of $+0.256$ mm yr^{-1}. The predictions in Figure 4.17 have been normalized by the eustatic value (total meltwater volume divided by the area of the ocean). Figure 4.17, clearly illustrates significant deviations from eustasy, with maximum $\dot{S}$ values that exceed the average eustatic value in the regions located in the far field of the WAIS (e. g., along the north western coastline of America). The departure from eustasy is due primarily to self-gravitation in the surface load, although the loading and rotational effects will also contribute. The blue contours in the vicinity of Antarctic Peninsula indicates where sea level is predicted to fall according to WAIS scenario. The remaining shades of blue denote areas where the predicted sea-level rise is closed to eustatic value but with opposite trend. Because the average change must equal the eustatic value, these areas must be balanced by zones where the sea level rise exceeds this value (red contours). Indeed, the

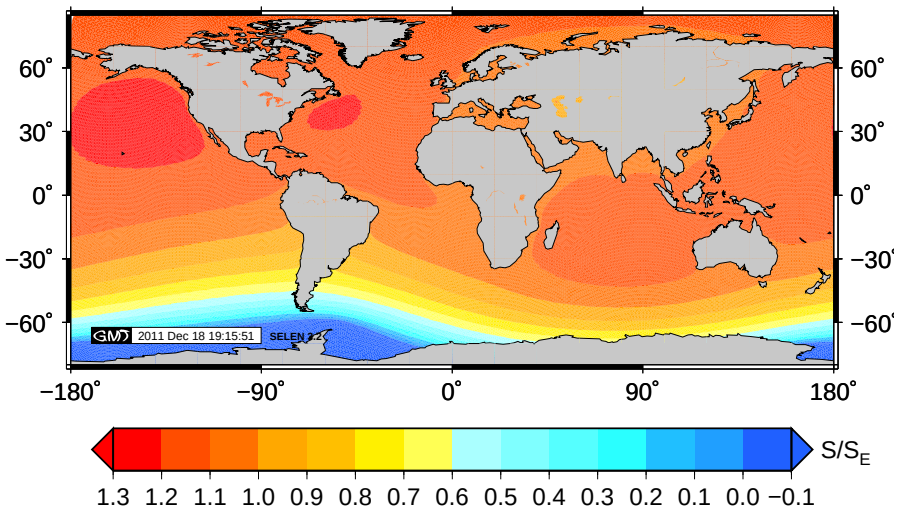

Figure 4.17: Global sea–level variation associated with the mass balance WAIS of Figure 4.15. The maximum sea-level rise for this scenario, which occurs off the western and eastern coast of north America, is 30% of the eustatic value.

maximum sea-level rise for this scenario, which occurs off the western and eastern coast of north America, is 30% of the eustatic value. This agrees with the recent results of Mitrovica et al. (2009), who estimated a highly accentuated sea-level rise in the oceans bordering North America. In the Mediterranean area melting of Antarctica contributes with 0.28 mm $yr^{-1}$to sea level rise, o equivalently 1.1 the normalized value (Figure 4.18). Recalling the contribute to sea level rise of Greenland upon the Mediterranean basin between 0.4 to 0.6 mm yr^{-1} from NW to SE, we note that in spite the Greenland proximity to Mediterranean, the net effect is roughly equal to eustatic component of each continental ice sheets (Antarctica and Greenland). These results reinforce serious concerns about the impact on Mediterranean coastal communities of a future instability in the WAIS and GrIS .

GIA of Antarctica

Estimates of present-day GIA are crucial for determining current ice mass balance estimates over Antarctica, especially when using data from the Gravity Recovery and Climate Experiment (GRACE) (Tapley et al., 2009). Traditionally, separating current ice mass change from GIA relies upon a modeled estimate of GIA Velicogna and Wahr (2006a). Current GIA models rely on a reconstruction of the ice load since the

Last Glacial Maximum (LGM), which is poorly constrained and remains uncertain (Denton and Hughes, 2002). The reconstructions are usually obtained from glaciohydro-isostatic models (Lambeck and Purcell, 2005; Peltier, 2004) and glacial geology (Ivins and James, 2005). Late Pleistocene ice models differ in mantle viscosity profile, ice volume distribution at the Last Glacial Maximum (see Figure 4.19). In our GIA computations, we predict the present-day GIA effect following the method, that has already been used for the GrIS (see Section 4.2), using an improved version of the open source program SELEN (Spada and Stocchi, 2007), which elaborates a rebound model solving the sea level equation for an incompressible PREM Earth model, considering rotational feed-back, to produce modeled viscoelastic rates. We have used three fully a-priori ice sheets scenarios and viscosity profiles. For the characteristic of rheological profiles coupled with ICE-5G (VM2) and ANU05 we refers to later section (section 4.3.4). The ice model IJ05 was proposed by Ivins and James (2005). It is a regional model because includes the ice chronologies of Antarctica ice sheets, but neglects the others important continental ice sheets of last glacial phases. Following the work of Ivins and James (2005) the model viscosity profile used with IJ05 is an average global

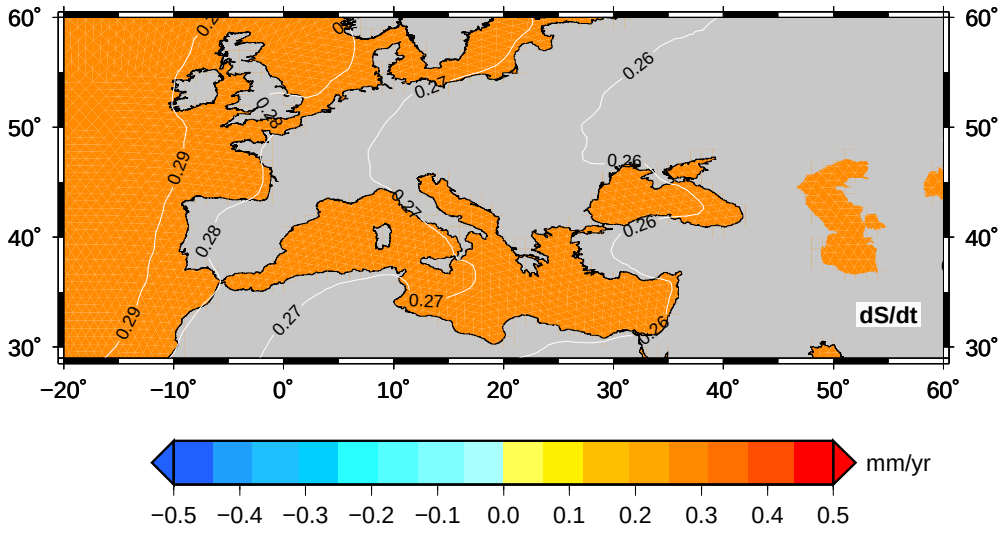

Figure 4.18: Present–day rate of sea–level change (dS/dt) across the Mediterranean associated with the WAIS melting scenario of Figure 4.15. Maximum rates (~ 0.27 mm yr^{-1}, i.e. close to the eustatic value) are predicted along the spanish peninsula. To note that the color table is limited to ± 0.5 mm yr^{-1}and that the eustatic value is 0.26 mm yr^{-1}.

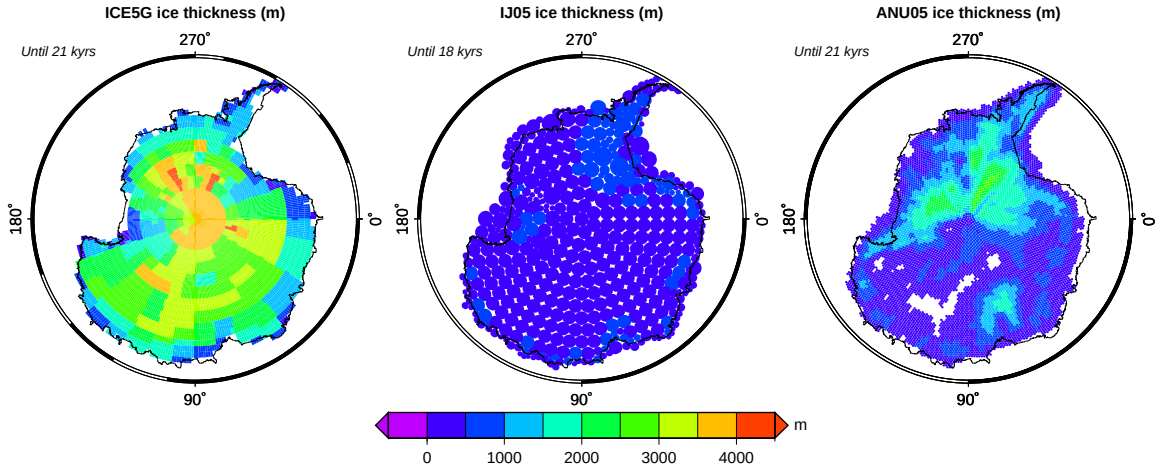

Figure 4.19: Antarctica ice thickness distribution according to ICE-5G (left frame) IJ05 (center) and ANU05 (right frame)at the Last Glacial Maximum. ICE-5G is characterized by spatial discretization with spherical quadrilaterals. IJ05 and ANU05 is characterized by spatial discretization based on discs ice element shape.

estimate for mantle viscosity computed by Mitrovica and Forte (2004) and includes a viscosity upper mantle of 4 10^{20} Pa s and a viscosity lower mantle of 6 10^{21} Pa s. However, since IJ05 is not bound to a specific Earth model, large variations in uplift rates could be generated with the use of a different viscosity layering and alternative rheologies. The maps of ice thickness distribution until LGM are shown in Figure 4.19 for all three ice models. The total amount of ice varies greatly among the models. ICE-5G store about 18 m ESL, ANU05 includes 25 m ESL while IJ05 stores only 10.34 m ESL. ICE-5G simulates the maximum ice thickness distribution, more of which occurs in the center of ice sheets. In spite the magnitude of thickness ANU05 and IJ05 agree that the significant thickness on Antarctica is relatively limited to around WAIS (see Figure 4.19). However, this is mainly a consequence of the strong control of the present topography. Significant differences have also been observed between these models. The significant degree of uncertainty in the GIA models highlights the difficulties involved in the current approach adopted to remove the GIA effect using a forward model to estimate the Antarctic ice sheet mass balance. The maps in Figure 4.20 show a significant variance that supports previous concerns about the effective accuracy of GIA computations over Antarctica (Cazenave and William, 2010). For all solutions shown, local vertical velocity field varies in the range of about $\pm$ 10 mm yr^{-1}. This range is one order of magnitude of GER elastic velocities shown in Figure 4.16.

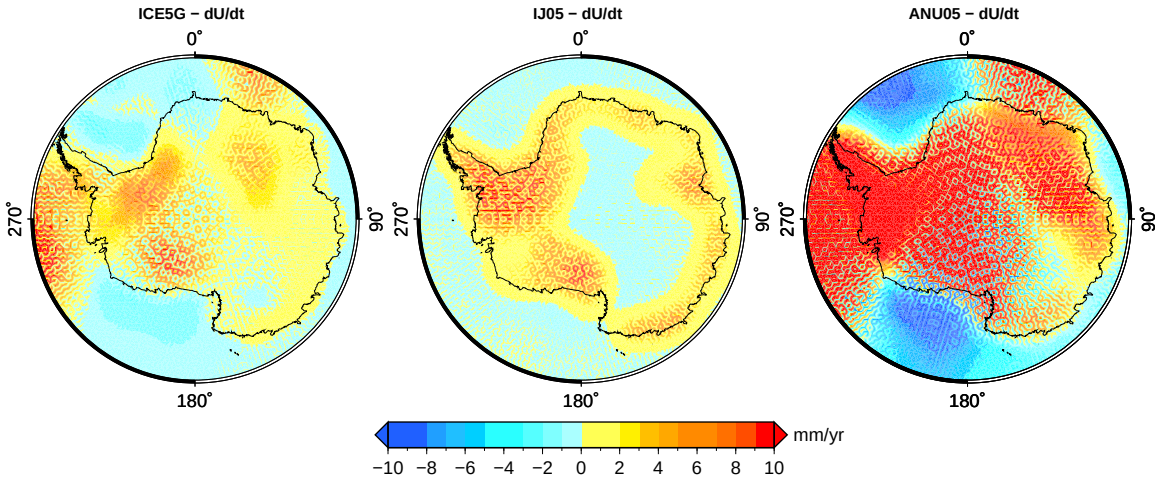

Figure 4.20: Present–day GIA uplift rates computed according to our implementation of the sea-level equation, and using the three models described in the body of this Chapter (see Section 4.4.2) and in Table 2.1 of Chapter 2. In all these GIA computations, $\ell_{max} = 128$.

As it is apparent from Figure 4.20, the rebound model predicted by ANU05 includes the stronger vertical uplift deformation across the AIS with a maximum velocity around the North Antarctic Peninsula.

This feature appears not to be present in the ICE-5G and JI05 rebound models. The offset is related to different ice chronologies. Indeed the uplift is caused by the the time-history considered by ANU05 for Antarctica that includes a gradual phase of melting up to the present with about 2-3 m of sea-level rise occurring in the past 6000 years (Lambeck and Nakada, 1990). In contrast the ICE-5G ice model set the end of melting around 4 kyrs BP. As on indirect effect, the Ross Sea and the Weddell Sea experience a differential vertical deformation as a consequence of ocean loading force (Simon et al., 2010). Consequently, with ANU05, ocean loading generates differential deformation between the continental margin and the see floor where the subsidence reaches -10 mm yr^{-1} (see frame 3 of Figure 4.20). Moreover other significant differences between the rebound models based on ICE-5G, IJ05 and ANU05 can be attributed to the characteristics of the rheological profiles employed and methods followed in the AIS reconstruction. We note that independent computations based on ICE-5G (see Figure 1 of Thomas et al. 2011) shows the same broad pattern of Figure 4.20 but with significantly

larger local values (in the range of several mm yr^{-1} and a markedly enhanced uplift in the Palmer Land and Ross sea. As discussed below (see Section 4.4.3), these differences have a significant impact on the interpretation of the GPS observations. Causes for the disagreement between our ICE-5G computations and the ICE-5G predictions computed by Thomas et al. (2011) are presumably due to the different spatial resolution employed in modeling and to the different version of ICE-5G model employed. As showed by independent computations of GIA effect across the Greenland (see Section **??**), the version of ICE-5G model available from web page (*http://www.sbl.statkart.no*) of SBL (the Special Bureau of Loading) and those available from the web page of Prof. W. R. Peltier are based on different time discretization for the last millennium that can cause important offset prediction between the two GIA models. Biases such these are investigated within the sealevel equation benchmark program along the lines of a recent initiative of the GIA community (Spada et al., 2011b) in order to facilitates the inter-comparison of GIA predictions.

4.4.3 Discussion

Observations of present-day rates of crustal motion across the Antarctica constrain both the response of Earth to surface mass changes and tectonic motions of the Antarctic plate. The response of Earth to surface mass changes includes the elastic response of the solid Earth to ongoing ice mass change and the delayed response due to the spatial evolution of the unloading ice from the Antarctica Ice Sheets since the Last Glacial Maximum. Several recent GPS campaigns have measured crustal motion in the Transantarctic Mountains (Raymond et al., 2004), Victoria Land (Zanutta et al., 2008), Marie Byrd Land adjacent to the Ross Sea (Donnellan and Luyendyk, 2004), the Antarctic Peninsula (Dietrich et al., 2004). Recently, GPS velocity field is elaborated by Thomas et al. (2011) using GPS sites placed across the Antarctica, both inland and coastal east and west Antarctica. However, a full understanding of vertical displacement of AIS will only be possible when sufficiently long series of data will become available from the west cost of the AIS, around the Embayment Amunden sea (in the shout of WAIS) where the GPS POLENET network has been placed.

In spite of the largest extensional regimes of the West Antarctic rift system (Donnellan and Luyendyk, 2004) the previous studies of geodetic GPS-based analysis (Raymond et al., 2004; Zanutta et al., 2008; Donnellan and Luyendyk, 2004) indicate no

significant present motion between East and West Antarctica larger than 1-2 mm yr^{-1}. Much of the observed crustal deformation on the continent is attributed to the GIA process (Wahr et al., 1995; Zanutta et al., 2008; Thomas et al., 2011). In Figure 4.21 we compare the GPS vertical velocity with vertical displacement predicted by WAIS regional elastic model, ICE-5G rebound model, IJ05 regional rebound model and ANU05 rebound model, from bottom to up of Figure respectively. The numerical data employed to draw this figure are summarized in Table 4.4.3.

Table 4.6: Observed and predicted vertical velocity (mm yr^{-1}). [a] Reproduced from Donnellan and Luyendyk. [b]GPS sites record a different rate between 1998-2003 and 2003-2007, (see Table by Thomas et al. 2011).

GPS site	ICE–5G(VM2)	IJ05	ANU05	GER	Osserved
MAIT	0.55	1.22	3.98	0.15	0.14 ± 0.57
FOR1	-0.07	3.08	0.11	0.12	-1.38 ± 0.76
FOR2	0.55	-1.22	3.97	0.15	2.09 ± 0.88
SYOG	0.36	3.03	0.29	0.10	2.26 ± 0.36
MAW1	2.55	3.56	0.72	0.09	0.06 ± 0.39
A368	1.97	3.76	6.55	0.12	0.39 ± 1.0
A351	1.61	5.94	5.68	0.11	0.81 ± 1.28
DAV1	1.04	6.66	1.91	0.09	-0.94 ± 0.49
CAS1	0.40	4.63	0.38	0.09	1.18 ± 0.43
DUM1	0.07	7.70	0.64	0.10	-0.79 ± 0.46
FTP1	1.99	4.20	5.59	0.28	2.14 ± 2.77
ROB1	2.12	0.17	3.89	0.25	7.54 ± 2.59
TNB1	1.99	0.23	3.87	0.26	-0.23 ± 0.81
CRAR	1.61	4.13	5.07	0.36	1.00 ± 0.65
MCM4	1.61	4.11	5.07	0.36	0.71 ± 0.37
SCTB	1.61	4.13	5.07	0.36	0.63 ± 1.10
MBL1[a]	5.31	5.32	2.44	0.45	3.28 ± 1.09
W01B	5.01	-0.52	10.47	0.26	-2.8 ± 1.17
MBL2	2.15	3.11	0.89	0.38	-0.23 ± 4.13
W09	6.63	3.28	10.04	0.53	-2.20 ± 2.42
W06A	4.63	7.77	10.01	0.55	3.54 ± 2.01
W05A	6.79	9.97	12.12	0.55	4.86 ± 1.01
HAAG	4.57	11.49	10.02	0.55	3.47 ± 0.71
W08A	4.73	12.26	8.53	0.54	1.31 ± 1.28
W02A	5.92	3.27	13.39	0.32	2.83 ± 1.18
OHI2-EL1[b]	1.46	0.64	0.46	0.35	6.78 ± 0.83
OHI2-EL1[b]	1.46	0.64	0.46	0.35	3.22 ± 1.68
PALM	1.38	2.44	1.40	0.35	0.08 ± 1.87

(continued on next page)

(continued from previous page)

PALM-EL[b]	1.38	2.44	1.40	0.35	8.75 ± 0.64
ROTB	2.01	3.82	2.59	0.43	1.50 ± 1.90
ROTB-EL[b]	2.01	3.82	2.59	0.43	6.96 ± 0.66
SMRT	2.55	4.78	3.09	0.45	-0.22 ± 1.93
SMRT/EL[b]	2.55	4.78	3.09	0.45	3.15 ± 1.94
BREN	4.61	10.43	5.93	0.51	3.85 ± 1.60
W04A	8.28	8.20	14.18	0.47	3.42 ± 0.84
BELG	2.34	6.87	5.55	0.26	2.97 ± 1.32
W03A	4.47	6.65	11.22	0.24	-2.47 ± 1.28
ABOA	0.35	5.89	1.30	0.15	1.4 ± 0.84
SVEA	0.91	5.16	3.35	0.16	2.07 ± 1.95
VESL	0.14	4.07	0.72	0.14	1.06 ± 0.45

Observed GPS rates of vertical uplift and their uncertainties, have been provided by Thomas et al. (2011) that processed vertical site velocities for 35 distinct locations using GIPSY/OASIS v5.1 provided by NASA Jet Propulsion Laboratory and expressed the GPS velocity field in the ITRF2005 reference frame. The GPS sites, with variable length of measurements in the range 1995-2010, include the permanent GPS station TNB1 (Mario Zucchelli Station), installed in 1998 at Terra Nova Bay, 13 GPS geodetic stations, located on rocky outcrops throughout the EIS, 10 GPS sites placed along the cost of Ross sea, 5 GPS sites along the North Antarctic Peninsula (NAP) and the remaining 6 GPS sites cover the center of WAIS area. The Interesting is to note (see Table S2 of auxiliary material of Thomas et al. 2011) that some GPS data experience of strong variability in uplift rates when the GPS time series move to nowadays. For example MBL1 shows a rate of 0.6 ± 1.49 mm yr^{-1} between 1998 and 2003 while between 2003 and 2007 the GPS showed a rate of 6.41 ± 1.61 mm yr^{-1}. With an opposite trend, OHI2-EL2 records a vertical displacement of 6.78 ± 0.83 mm yr^{-1} between 2002 and 2010 that decreases to 3.22 ± 1.68 mm yr^{-1} between 2009 and 2010. MBL GPS sites, located along the Ross sea, suggest that this area is particular sensitive to accelerations of the mass loss of the main outlet glaciers. Furthermore, the NAP region (OHI2-EL2r GPS site Thomas et al. (2011)) experiences large year-to-year fluctuations and exhibit no long-term trend.

In the plot placed in the bottom part of Figure 4.21 we compare the GPS vertical velocity with vertical displacement predicted by WAIS regional elastic model. The WAIS model elaborated through the GER method produced always a small amount of vertical

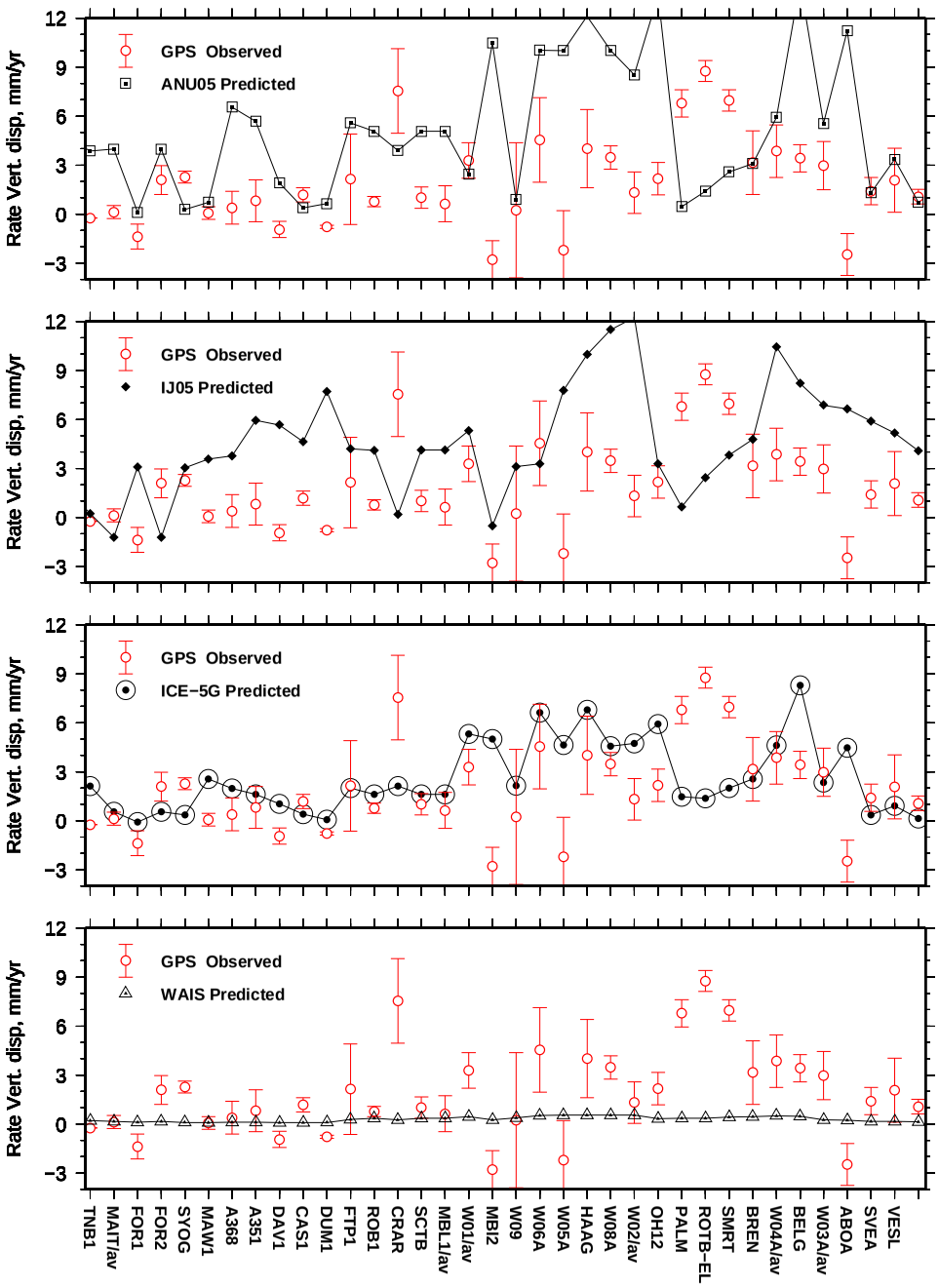

Figure 4.21: Rates of vertical uplift observed at GPS sites with their uncertainties from Thomas et al. (2011) compared with model predictions. From bottom to up: Elastic rebound uplift rate computed using GER method based on WAIS mass balance, GIA computations based on ICE-5G in the second frame, GIA computations based on IJ05 in the third frame), GIA computations based on ANU05 in the upper frame.

displacement of about 0.2 mm yr^{-1}, value that underestimates the localized variable trend shown by GPS sites. We therefore found unsatisfactory the elastic rebound inferred by

WAIS, and we believe that new developments of present day ice sheet model inferred by ICESat and or GRACE will allow to constrain the real trends of ice loss nowadays. A overview of all plots of Figure 4.21 suggests, with the exception of he North Antarctic Peninsula, that GIA effect represents the major cause of vertical deformation in the area. The vertical rates predicted by viscoelastic models enable to fit the GPS uplifts around the NAP (PALM, ROTB, SMRT GPS sites) with the values always lower of GPS trends. This indicates that the contribution of present day ice melting dominates the vertical displacement in this specific area. The Antarctic Peninsula drains much ice (Rignot et al., 2008a) but mass loss magnitude and pattern is not completely known. In the Nap region the elastic model elaborated by Thomas et al. (2011) who have employed the regional mass balances published by Rignot et al. (2008a) fails to reproduces the vertical velocities in the NAP region. Recalling the Greenland results we know that the detailed surface load variations of small glaciers may have the potential of affecting vertical movements (and consequently regional sea–level variations) on a much smaller spatial scale. Thus, is likely that the vertical deformations at the GPS sites OH12 and PALM are mostly associated with a presumed ice mass loss trend of about 2 m yr^{-1} from the local ice shelves occurred around the tip of NAP. In the EIS area, GPS velocities are in agreement with ICE-5G in showing small or negligible uplift. This finding suggests that GIA explains almost the GPS signal in the EAI area and further confirms the consistency of mass in balance of EAI at decades scale. However, the strong spatial ice loss estimates by IJ05 and ANU05 in the East Antarctica since the LGM exasperate the vertical deformations. Around the Ross sea the model predictions are in general agreement with the GPS observations. Among the upward vertical motions so far published (Donnellan and Luyendyk, 2004; Wahr et al., 1995; Thomas et al., 2011) the MBL region (MBL1 and MBL3 GPS stations) estimate an average uplift between 10 mm yr^{-1} (Wahr et al., 1995) and 3.28 mm yr^{-1} (Thomas et al., 2011). All three GIA models predicted an uplift rate around 5 mm yr^{-1} quite consistent with Thomas et al. (2011) prediction. The central area of the WAIS experiences a vertical uplift substantially lower than prediction models. In spite the small offset between observation and ICE-5G prediction, ANU05 and IJ05 shows a higher offset. The delayed melting mostly of which occurs after 6 kyrs included within IJ05 and ANU05 Antarctica regional models inferred high rates of uplift. This allows us to suggest that the offset between the prediction models is likely predominantly due to error in detailed chronology of ice melting. We suggest that the deglaciation phase was

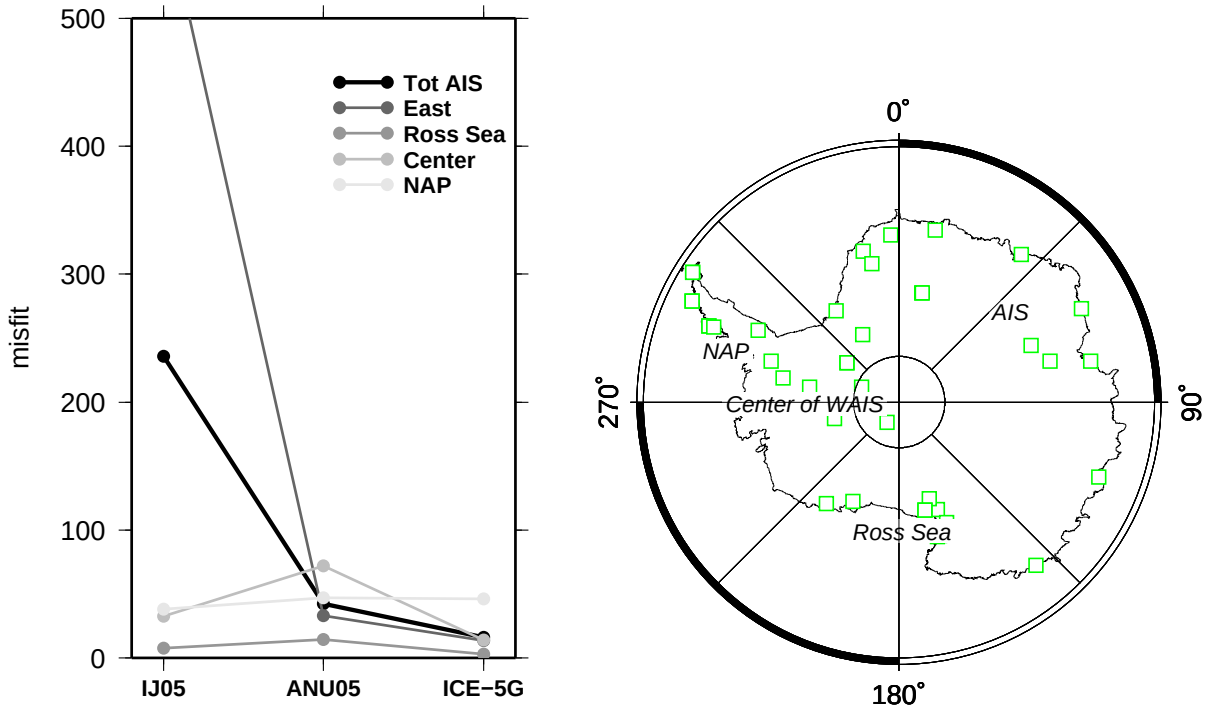

Figure 4.22: Misfit between predicted and observed vertical rate displacement for the GPS data set (Thomas et al., 2011) as a function of Antarctic sub-region for each ice model used in this work. The map on the right, shows the sub-regions that include the GPS sites (square symbols).

completed before 6 kyrs, between 8 and 7 kyrs BP (see e. g. Ingolfsson and Hjort 1999) (this issue will be taken up in the Chapter 6). However Thomas et al. (2011), explain the disagreement of vertical velocity between observations and predictions due to large thickness included within the ICE5G models. As a further remark, we note that predictions based on the ANU05 and the IJ05 ice models show a considerable scatter and a reduced performance compared with the ICE-5G ice model. We summarized the degree of agreement between observations and predictions in Figure 4.22. As expected, the misfit curve has a minimum when GIA predictions based on ICE-5G are considered and increase when IJ05 are considered. In agreement with the qualitative scenario in Figure 4.21 the larger value for IJ05 mainly arises by the misfit of GIA model at GPS sites occurred in the East area while predictions based on ANU05 model shows the worst fit at GPS sites placed in the center area of WAIS in Figure 4.22.

4.4.4 Conclusion

We have provided new estimates for the crustal uplift rates associated with elastic and viscoelastic rebound, and global sea-level fingerprints, and provided a new discussion on the impact of elastic and viscoelastic rebound on geodetic GPS signals in Antarctica. Our results can be summarized as follows.

i) We simulated the present-day ice melting of Antarctic Ice Sheets through ~ 9000 equal disc-shaped elements with angular radius $\beta \approx 0.2^{\circ}$ that losses 100 Gt yr^{-1} of ice from the West Antarctic only, corresponding to a ESL rise of 0.26 mm yr^{-1}. The maximum rates of elastic uplift are $\sim$ 0.5 mm yr^{-1} and are concentrated in key sector of West Antarctica between the Weddell Sea and Ross Sea. Due to the uniform melting of WAIS model it is not possible to detect areas of local uplift, which are however suggested by localized ice thinning event but we note the differential pattern of geophysical quantity between the WAIS and EAIS.

ii) The WAIS based global sea–level signature (fingerprint) shows the typical, non–uniform pattern. The departure from eustasy is due primarily to self-gravitation in the surface load, although loading and rotational effects will also contribute. The maximum sea level trend (dS/dt) value that exceed the average eustatic value of about 30%, occurs in the regions located in the far field of the WAIS, in particular off the western and eastern coast of north America, in agreement with recent results of Mitrovica et al. (2009); Bamber et al. (2009). In the Mediterranean area the Antarctica contributes with 0.28 mm yr^{-1} to sea level rise that match 1.1 of normalized value. Recalling the contribute to sea level rise of Greenland upon the Mediterranean basin between 0.4 to 0.6 mm yr^{-1} from NW to SE, we note that in spite the off set of about 40 Gt yr^{-1} between the mass balances between Greenland and Antarctica, the net effect is roughly equal to eustatic component of each continental ice sheets (Antarctica and Greenland).

iii) The GIA component of present–day uplift in Antarctica has been evaluated using three fully a-priori ice sheets scenarios and viscosity profiles: ICE-5G (VM2) (Peltier, 2004), ANU05 (Lambeck and Purcell, 2005) and the regional Antarctic models IJ05 by Ivins and James (2005) characterized by about 18 m ESL, 25 m of ESL and 10.34 m ESL respectively. Our findings support previous observations by Wahr et al. (1995); Velicogna (2009); Thomas et al. (2011) who have emphasized the importance of the GIA component across the Antarctica and at the same time, have evidenced a significant spread of the GIA predictions which is ultimately associated with uncertainties

in the ice melting scenarios and mantle rheological profiles. In the last part of this work we have addressed the problem of the interpretation of trends of vertical displacement recorded at 36 GPS sites with sufficiently long records provided by Thomas et al. (2011). With a 0.2 mm yr^{-1} of vertical displacement inferred by WAIS model we found the WAIS elastic rebound unsatisfactory and we believe that new developments of present day ice sheet model inferred by ICESat and or GRACE will allow to constrain the real trends of ice loss nowadays. With the exception of the North Antarctic Peninsula, the GIA effect represents the major cause of vertical deformation in the area. In order to reproduce the vertical velocities recorded by GPS sites placed along the NAP region we can assume a prominent mass loss from local ice shelves with a trend of about -2 m yr^{-1}. This is a future challenge. According to our computations, GPS data can be currently employed to constrain competing GIA models. The GIA rebound model based on ICE-5G represent the models minimizing the total misfit. Finally we conclude suggesting that any robust assessment of the sea-level hazard associated with the loss of major ice reservoirs must, of course, account for the most important potential sources of melt-water, namely Greenland, the East Antarctic. Nevertheless, future projections should avoid simple, eustatic estimates and be based on a suitably realistic ice sheets mass balance.

Chapter 5

Sea level change during the Roman Period

5.1 Introduction

Two thousand years ago the ice sheets in North America and Eurasia were completely disappeared and the rates of melting of other continental ice masses were small. The transition from the middle to the end of interglacial conditions is clearly critical issue. A large number of reconstructions, since the Last Glacial Maximum have been elaborated through global ice models. With regard to the end of ice melting Lambeck and Purcell (2005) documente a rapid melt between 6 and 4 kyrs BP and underline that a smaller amount of ice continued to disappear after this time as a consequence of a delayed melting of the Antarctic ice sheets (Nakada and Lambeck, 1989; Lambeck, 1993). However, Milne et al. (2005) put the ending of polar sheets ablation between 7 and 4 kyrs BP while Tarasov and Peltier (2002) suggest a re-advance of the Greenland Ice Sheets during the Late Holocene. This latter is corroborated by regional sea level change analysis using in pairs Glacial Isostatic Adjustment models (hereafter GIA) and ICESat and GPS observations (Spada et al., 2010, subm.). Constraining the Late Holocene melt contribution to global sea level rise is important to establish the baseline contributions to 20^{th} and 21^{st} century sea–level rise (Gehrels, 2009). The sea level change community agrees with a rapid sea level rise since the 19^{th} century, while the timing of sea level stabilization during the Late Holocene is poorly constrained.

Relative sea level observations around the word for the last 2000 years (Kemp et al., 2011) show a regional signal that depart from eustatic value as a consequence of perturbations in Earth gravity field, solid surface and polar motion. Previously glaciated

areas are experiencing post glacial uplift, thus sea level records a relative sea level fall. Surrounding these regions are the so called peripheral bulges. These bulges subside and the sea level rises at rates higher then eustatic value. that reduced this signal even fall in areas close to the ablating ice sheets and amplified it with a rise sea level in areas far from the melt source, or a reduced sea level rise for the subsidence of sea floor. Kemp et al. (2011) compared late Holocene relative sea level observations (hereafter RSL) after glacial isostatic correction. They showed that along the east coast of United States from at least BC 100 until AD 950 sea level was stable while the Cook Island (South Pacific Ocean) recorded a falling sea level over the last 2000 years. Relative sea level (hereafter RSL) in New Zealand have remained relatively stable throughout the past 7000 years and was rising slowly from AD 1500 to AD 1900 (Gehrels et al., 2008).

In the Mediterranean area the spreading of Roman archaeological sites contribute to constrain the sea level change for the last 2000 years (Flemming, 1999). Previous research indicates that the ocean volume appears to have remained constant for much of the past 2000 years (Sivan et al., 2004). Around the costs of northern Tunisia and western of Libya (Anzidei et al., 2010) the Punic-Roman archaeological sites indicate that at local scale, RSL change increased 0.2 - 0.5 m since the last 2 kyrs. Along the Lazio coastline Lambeck et al. (2004b) observed a RSL at Roman age of -1.22 $\pm$ 0.06 m and estimated that the paleo-sea level was at -0.13 $\pm$ 0.009 m after the contribution of GIA is removed from their observations. Around Marseille, archaeological, geological and biological field evidence suggest a relative sea level rise of 0.5 m between 2000 years BP and the present (Morhange et al., 2001) in agreement with Lambeck and Bard (2000).

Within the European project ECOST Action ES0701 "*Improved constraints on models of Glacial Isostatic Adjustment*" a first field trip was been organized in order to reassess the importance of archaeological sea level indicators along the Tyrrhenian coasts of Italy (Figure 5.1). The COST group supervised by Prof. Pirazzoli P. and Evelpidou N., included Ruggieri G., Spada G., Picchi C., Vassilopoulos A. Because many fish tanks occurs within military zones they were not accessible at the time of the first field trip. To overcame to these logistic problems, a second field trip was been organized and supervised by Ruggieri G., in order to include others four fish tanks, three located along the Tyrrhenian coasts of Italy (Figure 5.1) and one along the italian side of Adriatic coastline (closed to Ancona city).

In this chapter we estimate the sea level change during the Roman period from the

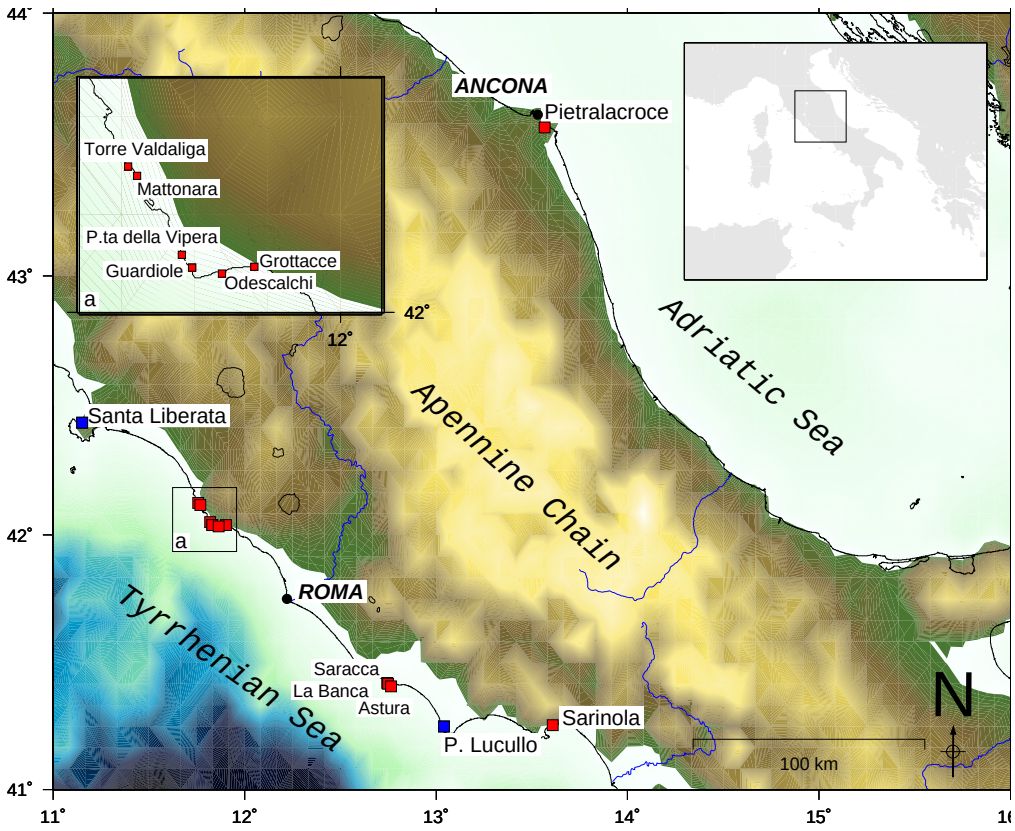

Figure 5.1: Location map of the Roman fish tanks along the Italian coast lines mentioned in this work. The sites marked by blu squares have been considered in previous studies.

archaeological Relative Sea Level (RSL) observations collected along Lazio and Marche coastlines and we compare it with RSL predicted by global GIA models. A correct GIA analysis can not ignore the sensitivity upon the ice history and rheological parameters. For this purpose we test two different global ice models and several rheological profiles.

The practice of separating relative sea level into an isostatic and a eustatic component (Kemp et al., 2011; Lambeck et al., 2004b) allows to quantify the amount of equivalent sea level (ESL) as water exchange between ice and ocean. In the same way Milne and Mitrovica (2008) tackle this issue searching the sites less sensitive to uncertainty in model parameters and hydro-isostasy deformation, and thus more suitable for obtaining a more precise measure of eustatic sea level variations. Following this idea we quantify how much the RSL predictions depart from the global eustatic signal. In addition we have attempt to recognize the hydro-isostatic contribution against the glacio-isostatic contribution. Some of the results presented in this chapter have been published in Geoarchaeology (2011) with a title: *Sea level variations during the Late Holocene from*

revised observations of Roman fish tanks on the Tyrrhenian coast of Italy, by Evelpidou N., Pirazzoli P., Vassilopoulos A., Spada G., Ruggieri G., Tomasin A..

5.2 Study area

The geodynamic setting of Lazio and Ancona area represents the back-arc basin and the foreland basin respectively of the Appenninic chain-foredeep system. Following the main orogenic phases of the Appenninc chain the coastal area of central Italy was subjected to general uplift until the Plio-Pleistocene. In the Lazio area, the later extension processes related to the Tyrrhenian back-arc basin caused crustal thinning and the ongoing alkali-potassic explosive volcanism. Here relative sea level changes linked to glacial/interglacial stage with regional tectonics induced three transgressive/regressive cycles (Barbieri et al., 1994). The elevations of the terraces indicates that the coastal area rose at rate of 0.1 - 0.2 mm/yr during the Late Pleistocene (Bordoni and Valensise, 1998). The morphology of the studied area of Lazio is a linear low coast, often rocky, extending towards the sea with long cliffy, generally of small height constituted by aeolian deposits. In the most sheltered inlets, or near the mouth of small rivers, flintly or sandy beaches mixed with pebbles are found. The rock is often made of Pietraforte, capped by thin layers of panchina, always plunging towards the sea, with characteristic erosion features: honeycomb decomposition, lithophaga holes, or globous features often under the control of diaclase networks. It is in this kind of rock formations that have often been cut the fish tanks basins. The connection between the shore and the low flat panchina is often made by a low cliff (generally less than 3 meters high) on which can be distinguished paleosoils, the archaeological layer, and the present soil. The foreland basin undergoes a progressive North-Estern migration in pairs with the Appenninic chain-foredeep system (Calamita and Deiana, 1988). Within the foreland basin Ancona area, belong to the periadriatic basin, occurred in the eastern side of the thrust Appenninic chain, where a minor overthrust allow to outcropping of carbonate sequence. During the Last Glacial Maximum the Adriatic sea was almost completely in subaerial conditions. The maximum marine ingression was reached 5 kyrs BP. The morphology of the Ancona coastline is a indented rocky coast with high cliff with off-shore platform almost flat until the -20 m contour line bathymetry after which the slope increase sea-ward (Curzi, 1986). The cliff is constituted by clay limestone and chalk stratified and Pietralacroce fish tank is carved into these deposits.

5.3 Methods

The study of Glacial Isostatic Adjustment effect is based on three input components: the global ice models, the Earth models, and a program to compute the sea level change. The majority of global ice models use ice histories that cover the whole of last glacial cycle. Ice margin positions prior to the LGM are in these models often poorly constrained. To take into account the effects of the differences in ice chronology reconstructions, we use two distinct ice global models: ICE-5G (VM2) (Peltier, 2004) and ANU05 (Lambeck et al., 2004b). Figure 5.2 shows the the time steps of ice melting for each global ice model. ICE-5G constitutes our reference model. With 22720 disk of 1 degree of half-amplitude It defines the time-dependent loads of ice since the Last Glacial Maximum (LGM). In particular ICE-5G is characterized by 127.15 m of ESL at LGM to occur 21 kyr BP. Most of it is stored in the Laurentide ice sheet (Tarasov and Peltier, 2002) (Figure 5.2). In

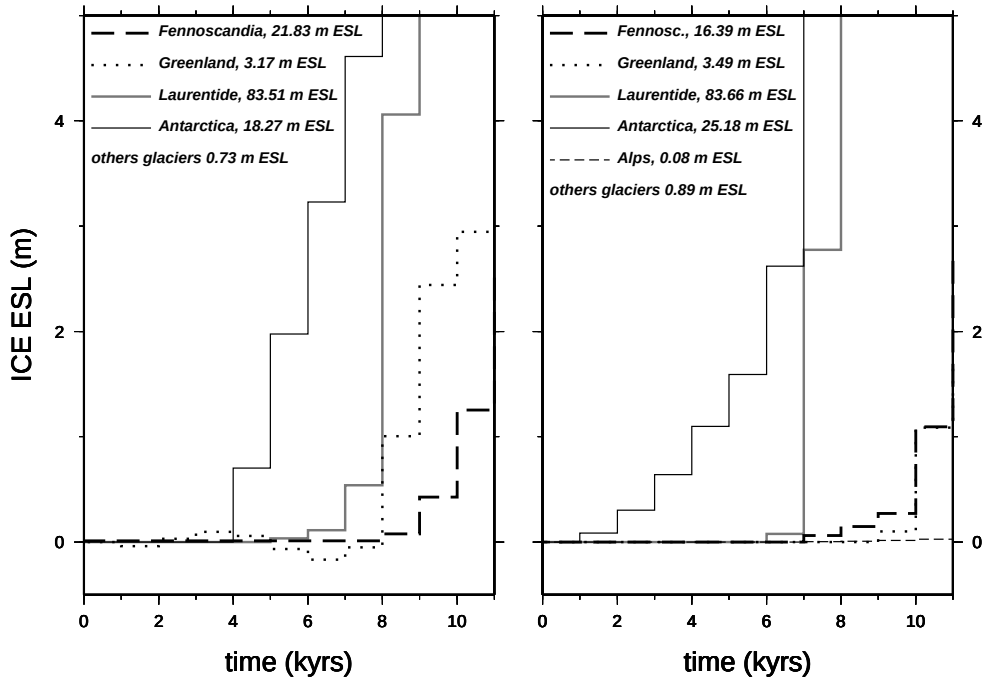

Figure 5.2: The ESL as a function of time of the major land-ice source, constituents of the global ice models. ICE-5G in the left frame and ANU05 in the right frame.

addition to ICE-5G, here we also consider the global ice model ANU05 (Lambeck et al.,

2004b) based on the inversion of geological sea level and shoreline data supplemented by observational evidence of ice margin locations and, in a few instances, by limiting ice thickness estimates. With 29813 ice elements, it describes a melting rates different from ICE-5G (Figure 5.2) and characterized by ESL of 129 m since the LGM set to 21 kyr BP (Fleming et al., 1998).

Here the Earth response is computed using a spherically symmetric, self-gravitating Maxwell visco-elastic Earth model where the elastic structure of the Earth is based on the seismic model PREM (Dziewonski and Anderson, 1981) and the viscous structure is in agreement with that proposed by previous authors. VM2 is the mantle viscosity profile related to ICE-5G which well fits many hundred Holocene relative sea level histories in North America, Europe and worldwide (Argus and Peltier, 2010). VM2 is the mantle viscosity profile having an elastic lithosphere thickness of 90 km, a mean upper mantle viscosity of $0.5{\cdot}10^{21}$ Pa s and a mean lower mantle viscosity of $2.7{\cdot}10^{21}$Pa s. A second set of computations has been made according to the ANU05 model, characterized by three-layer visco-elastic profiles with a lithosphere thickness in the range 50 and 100 km, upper mantle in the range between 0.2 and 0.5 $\cdot 10^{21}$ Pa s, a lower mantle in the range between 5 and 20 $\cdot 10^{21}$ Pa s . The public domain program SELEN (Spada and Stocchi, 2007) allows to solve the Sea Level Equation (Farrell and Clark, 1976) and to decompose the paleo sea level into contributions from the eustatic term and the glacio-hydro-isostatic term. The eustatic term S_E is the sea level variation S that would be observed completely neglecting the gravity variations and assuming a rigid Earth, considering the only transfer of water from a continental source of ice to the ocean and vice versa. S_E can be expressed quantitatively as:

$$S_E = -\frac{m_i}{\rho_w A_0}\,, \tag{5.1}$$

where symbol m_i is the ice mass variation, ρ_w is the density of water and A_0 is the area of the surface of the oceans, which is assumed constant.

The glacio-hydro-isostatic term represent the vertical displacement (U) and the change in geoid surface (N) due to the combined action of the ice and ocean load variations. If we consider a melting event that occur very far away from the area of study, the ice load can be neglected and the vertical displacement of solid Earth and geoid depends on water load variations across the oceans that we refer to ocean load (L_o):

$$L_o(\theta, \lambda, t) = \rho_w S_E(\theta, \lambda, t)\mathcal{O}(\theta, \lambda)\,, \tag{5.2}$$

where the $\mathcal{O}_\omega$ is the ocean function, θ is colatitude, λ is longitude, t is time. In this case we solve the Sea Level Equation through a ice-free approach where the term I (see Chapter 2), the ice thickness variation is set to zero and the response to the ocean load is:

$$S_o(\theta, \lambda, t) = \frac{\rho_w}{\gamma} G_s \otimes_o S + S_E - \frac{\rho_w}{\gamma} \overline{G_s \otimes_o S}, \tag{5.3}$$

where S_o is sea level change based on this ice-free approach, $\rho_w = 1000$ kg m^{-3} are the densities of water, γ is the reference surface gravity, $G_s = G_s(h, k)$ is the sea–level Green 's function (dependent upon the h and k viscoelastic load–deformation coefficients – LDCs), S^E represents the eustatic term, $\otimes_o$ denote spatio–temporal convolutions over the ocean–covered regions, and the over-bar indicates an average over the surface of the oceans that ensures mass conservation (Farrell and Clark, 1976; Spada and Stocchi, 2006).

In this work we test the different ice chronologies solving the Sea Level Equation at maximum harmonic degree $l_{max} = 128$ as compromise between accuracy and efficiency in computation (Stocchi and Spada, 2009). Following the equations 5.2 and 5.3, the ice-free approach allows to estimate relative sea level due to the hydro-isostatic contribution affected mid latitude sites enclosed the Mediterranean (Mitrovica and Milne, 2002; Stocchi and Spada, 2009). Our recent surveys of Roman fish tanks within the European project COST Action ES0701 "*Improved constraints on models of Glacial Isostatic Adjustment*" reassess the importance of archaeological sea level indicators along the coasts of Italy (Lazio, Marche). Using RSL indicators collected during the field works (see Section 5.5 and Appendix A) we compare the field observations with the predictions obtained by numerical simulations of Glacial Isostatic Adjustment. The relative sea level (RSL) predicted by models is relative to the present sea level according to:

$$RSL(\omega, t_{BP}) = S(\omega, t_{BP}) - S(\omega, t_P)\,, \tag{5.4}$$

where ω denote the colatitude (θ) and longitude (λ) of sites , t_{BP} denotes a given time before present and t_P is the present time. To focus on the effect of hydro-isostatic component of GIA we solve the Sea Level Equation (in the simplified form S=N-U) taking into account the deformation due to ocean load L_o 5.2 in term of geoid surface variations (N_o) and Earth surface variations (U_o). We refer to the Appendix A to details of archaeological sea level indicators. The Appendix A includes the description of each fish tank surveyed during the two field works, supplied by measurements collected from the fish tanks and maps of fish tanks.

5.3.1 Archaeological survey

During autumn 2010 and the summer 2011 two field trips were been organized in order to reassess the importance of archaeological sea level indicators along the Tyrrhenian coasts and Adriatic coast of Italy (Figure 5.1). Along the Lazio coastline we surveyed Torre Valdaliga and Mattonara, closed to Civitavecchia town, Punta della Vipera, Guardiole with rectangular shape and Guardiole with apse shape, Grottacce and Odescalchi around S. Marinella city, Saracca, La Banca, and Astura to south of Nettuno, Sarinola closed to Formia Harbour (all sites in Figure 5.1). The only fish tank found along the italian coastline of Adriatic sea is Pietralacroce (south of Ancona, see Figure 5.1). This fish tank was investigated in collaboration with Superintendence of Archaeological Heritage of Marche region, that first surveyed the structure of the fish tank. The twelve fish tanks were systematically surveyed in detail (see Appendix A) and their submerged parts were studied by snorkeling. During field works, mapping of the fish tanks took place along with measuring their most significant morphological characteristics. Several measurements were performed on each location and the accuracy was improved by multiple measurements. The methodology includes correction of measurements for tide and atmospheric pressure values at the exact time of the measurements and finally the evaluation of the height and functional depth to the average sea level, which differs depending on the typology of the evidence, its use and the local tide amplitudes. Hourly astronomical tide predictions, deduced from harmonic constants were used at the moment of field measurements. However, corrections deduced from real tide records at Civitavecchia, Gaeta, Naples and Ancona tidal gauges, available from ISPRA web page (*http://www.mareografico.it/*), were subsequently applied.The Civitavecchia tide gauge is used to correct the measurement of fish tanks occurred between Civitavecchia and S. Marinella. Naples tide gauge is used to Sarinola, Ancona to Pietralacroce fish tank while the measurements made within the three fish tanks around Nettuno was corrected using the average between Civitavecchia and Gaeta tide gauges. The uncertainty of 0.05 m is introduced to consider the total amount of errors due the sea surface bias and survey method.

5.4 Archaeological sea level indicators

Submerged Roman fish tanks occurs along the coastline of Tyrrhenian sea with an exception of one surveyed in Adriatic sea closed to Ancona. Fish culture spread between the I sec. BC and II sec. AD; in particular Tacito wrote that the highest diffusion of fish tanks was between 31 BC and AD 69. Usually rich families used to build moles and fish tanks near their coastal villas. At the beginning, the fish culture was linked to religious ceremony, since the fish symbolized the fertility. Later, fish culture became the privilege of the rich (Giacopini, Marchesini, Rustico, 1997). The use of the fish tanks underlined the economic power of the owner through the sumptuous installations along the coastline that allowed them to eat fresh fish during banquets. In the Mediterranean area the spreading of Roman archaeological sites contribute to constrain the sea level change for the last 2000 years (Flemming, 1999). Within the archaeological sites, the fish tanks may be considered as palaeo-sea level markers that allow accurate evaluation of relative sea level variations during the last two millennia (Schmiedt, 1972; Lambeck et al., 2004b). Different architectural features provide to estimate palae-sea level when the relationship with sea level at time of construction is identified. They exhibit hydraulic works with different characteristics according to the coastal and submarine geomorphology, the coastal circulation and the kind of breeding fish. Roman piscinae are either cut in shore platforms, partly built, or wholly built. The understanding of hydraulic functions of these features is required for a successful interpretation of main sea level indicators. Roman piscinae dated by the nearby Roman structures, clearly define the upper and lower limits of sea level at the time of their construction.

One of the main characteristics of fish tanks is an outer protection breakwater (mole) constructed all around the basins, that should exceed the basin levels *Mox praeiaciuntur in gyrum moles, ita ut complectantur sinu suo et tamen excedant stagni modum* (Columella, XVII) meaning *In addition moles are constructed all around in order to surround the basins and exceed their level.* Channels (Figure 5.3 a) connected the tank with the open sea to ensure water renewal. Channel direction ranges according to the individual morphological and dynamic coastal characteristics of the area, trying to take advantage of wave power in order to let fresh water pass into a fishpond. The basins were delimited by walls over which foot-walks (*crepidini*) remained emerged. In some cases (Piscina di Lucullo, Formia, Astura, Punta della Vipera) lower levels of foot-walks are found used for maintenance, oyster culture, etc. Several basins were connected

!t

Figure 5.3: Field photographs of key sites showing archaeological sea level indicators. a) Channel of Odescalchi fish tank, divided into two vertical parts by a block. b) Tanks opening where occurred the sluite gate at Pietralacroce fish tank. c) Sluice gate of Grottacce fish tank, kept at the Santa Marinella Museum. d) Upper foot-walks and lower foot-walks at Pietralacroce fish tank (*crepidini*). e) Carvings (arrow) for overflow situated at the top of the dividing wall.

through submerged arched openings (Piscina di Lucullo, La Banca, Punta della Vipera), or through fixed gates (*cataractae*) with holes, permitting the passage of water but not of fish (Ventotene) and depressions cut at the top of the walls (Piscina di Lucullo, Fosso Guardiole, La Mattonara). Sluice gates along the channels or between the basins were operated along sliding grooves cut into stones (examples: Piscina di Lucullo, Formia, Astura, Odescalchi) (Figure 5.3 b, c); their marks may be especially useful, if well interpreted, to estimate the past sea level.

In order to reconstruct the former MSL it is essential to interpret all fieldwork measurements and choose the best sea level indicator for each fish tank (Figure 5.3). Some criteria have been proposed below. Accordingly to Columella *Spissi deinde clatri marginibus infiguntur, qui super aquam semper emineant, etiam cum maris aestus intumuerit* the *upper foot-walk* (Figure 5.3 d) was always at a higher level of high tide. Considering that in the Tyrrhenian sea the tide average estimated by Pirazzoli and Tomasin (2008) is between - 25 cm and +35 cm, the upper foot walk was at a +35 cm from mean sea level. Such an estimation has, however, the drawback to lower the ancient MSL when the crepidine is eroded. It is therefore necessary to specify that the former MSL was not lower than the top of the crepidine at +35 cm.
The *sluice gate* (Figure 5.3 c) from Grottacce fish tank, kept in the Museum of Mare e della Navigazione Antica, Santa Marinella, is 60 cm high. From comparison with the distribution of recent hourly sea level heights at the Civitavecchia tide-gauge station Pirazzoli and Tomasin (2008), it seems logical that the top of the sluice gate (as the foot walks), were constructed 35 cm above MSL with the base of the sluice gate at -25 cm in order to perform a tide control during the day. The latter is valid only assuming that there were no other gates of different size in the fish tank. However, a position at +35 cm would not be convenient, for basins only 0.6 m deep intended for flat fish, that tends to stay near the sea bottom, because if the top of the grid were at +35 cm the lowest holes of the grid would be situated at -18 cm, and there would not be influx of sea water during 440 hours per year (i.e. during 5% of the time) in a basin in which the water, at low tide, would have remained about only 40 cm deep. However, fresh-water supply from the nearby Guardiole river, could have been sufficient in this case. Assuming that the sluice gate would have been of the same type of that preserved in the Santa Marinella Museum, it would have been more convenient, for flat fish tanks, to set the sluice gate located at the top of a foot walk in a position between +30 cm and -30 cm. In conclusion, it seems more useful

Table 5.1: Measurements of hydraulic features used ad archaeological sea level indicators. The measurements written in column five represents the distance from mean sea level at time of survey after tide and atmospheric pressure corrections.

Lon	**Lat**	**Site**	**Tide Gauge**	**Measurements**
deg	**deg**	**fish tank**		**m**
42.124	11.758	Torre Valdaliga	Civitavecchia	−0.05
42.116	11.768	Mattonara	Civitavecchia	−0.01
42.049	11.819	P.ta della Vipera	Civitavecchia	−0.12
42.038	11.831	Guardiole rett.	Civitavecchia	−0.21
42.038	11.831	Guardiole abs.	Civitavecchia	−0.22
42.039	11.902	Grottacce	Civitavecchia	−0.38
42.033	11.865	Odescalchi	Civitavecchia	−0.01
41.421	12.745	Saracca	Average Civit. and Gaeta	0.01
41.417	12.749	La Banca	Average Civit. and Gaeta	−0.01
41.408	12.765	Astura	Average Civit. and Gaeta	−0.05
41.255	13.609	Sarinola	Naples	−0.23
41.255	13.609	Pietralacroce	Ancona	−0.45

for the fish tanks of 1.22 m depth, the top of the foot walk should be estimated rather at 35 cm above the former MSL, while for fish tanks of the 0.6 m depth the top of the foot walk could hardly exceed 30 cm above MSL, assuming that the depth of the basins at the time of construction was not deeper than present. *Carvings for overflow* (Figure 5.3 e) were situated at the top of the dividing walls. According to Auriemma and Solinas (2009) they had to be near the average sea level or a few cm above, in order to be put in action only during high tide. It seems likely that overflow only occurred above high tide, in the case of a surge (e.g. at MSL + 15 cm). The *grooves* along the channels allow the vertical movement of the sluice gate. It were situated between the basin and the channel (Astura, Saracca). The base of grooves (threshold) some times occurred at the same depth of the lower foot-walk (Pietralacroce, Sarinola) (Figure 5.3 d) meaning that the lower crepidine could not remain dry. Some time it is deeper (Odescalchi), in this case the function of lower foot-walk remains uncertain. In general the top of groove is the same level of upper foot-walk and it is interpret in the same way of sluice gate.

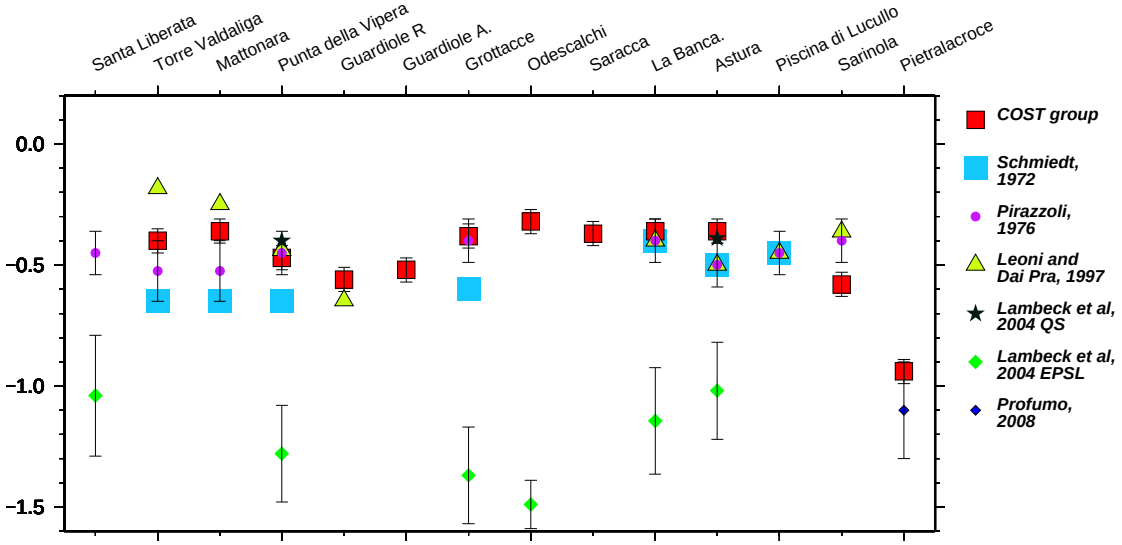

Figure 5.4: RSL observations for Tyrrhenian coast according to various authors. All most data indicate a relative sea level between -0.65 m and -0.30 m below msl at 2000 kyrs, while (Lambeck et al., 2004b) suggest a relative sea level around -1.20 m below msl.

5.5 Results

Table 5.1 summarizes the measurements of the best preserved features for each fish tank before tide and pressure corrections.To obtain the Archaeological sea level Indicators we combine the measurements with the interpretation of the relative positions of the hydraulic features described in Section 5.3.1. The mean relative sea level obtained from the twelve archaeological sea level indicators within a time widow of 113 years since 2048 years BP is -0.45 $\pm$ 0.08 m below msl. In agreement with most of the previous works (Schmiedt, 1972; Pirazzoli, 1976; Leoni and Dai Pra, 1997; Lambeck et al., 2004a) our observations indicate that sea level rose of about 50 cm during the last 2000 years with a constant rate of 0.225 mm/yrs. Since the 70^{th} several authors provides to interpret this archaeological markers (Figure 5.4). Most of them (Schmiedt, 1972; Pirazzoli, 1976; Leoni and Dai Pra, 1997; Lambeck et al., 2004a) have suggested a sea level rise that does not exceed 0.65 m. Lambeck et al. (2004b) have recently suggested a sea level rise of approximately 1.28 m from observations conducted at the fish tanks of Santa Liberata, Punta della Vipera, Grottacce, Odescalchi, La Banca, Astura in contrast with the previous literature. The critical issues to be sought in the different interpretation of hydraulic position of

features, errors of measurements, the span of time during which the sea level could be rise. Following the method employed by Evelpidou et al. (2011, in press), the upper foot-walk, the overflow carving and, the channels with the groove for the sluice gate are the best indicators of paleosea level, when, of course, they are preserved from wave erosion.

The upper foot-walks, as underlined by latin writers (Columella, XVII) are always higher then high tide level, considering that in the Tyrrhenian sea the tide average estimated by Pirazzoli and Tomasin (2008) is between - 25 cm and +35 cm, we put the upper foot walk at +35 cm from mean sea level. However Lambeck et al. (2004b) use a lower foot-walks as sea level indicators that occur at a general distance of 30 cm from the upper foot-walks. Moreover Lambeck et al. (2004b) suggested a tidal range of 45 cm with a difference of tide correction of about 15 cm between the two methods. These difference allow us to explain almost the the gap in measurements between our results (or the results of Lambeck et al. (2004a)) and the results of Lambeck et al. (2004b). Pietralacroce fish tank (the last one of Figure 5.4) indicates a deeper sea level during the Roman period with a difference of about 50 cm respect the sites placed along the Tyrrhenian sea. If we can assume a marginal effect of tectonic movement for the last 2 kyrs for the Lazio area, we can not do it for the Adriatic area and the possibility for slow tectonic subsidence should not be ignored. The prediction of the RSL at time 2 kyrs BP was generated using SELEN program (Spada and Stocchi, 2007) tuning the Earth model and the Late Pleistocene ice history reconstructed by ICE-5G (VM2) describe in Section 5.3. Each RSL prediction is plotted as a square in Figure 5.5 and the vertical line describe the estimated uncertainties of GIA prediction. Estimates of the accuracy of the isostatic calculations are based on the accuracy of the Earth parameter and include the poor-known visco-elastic property of the mantle. In agreement with previous works (Stocchi and Spada, 2009; Tsimplis et al., 2011) that testified a large average uncertainty both for the RSL (Stocchi and Spada, 2009) and tide gauges (Tsimplis et al., 2011) when the Earth model parameters beneath the 670 km depth discontinuity are perturbed, we test different lower-mantle viscosity with one order of magnitude of uncertainties. The adopted perturbative method for the isostatic calculation determines an error of $\pm$ 0.2 m upon the RSL predictions. As shown Figure 5.5, the predictions explain almost the observations.This agreement suggests that the long wavelength component of Glacial Isostatic Adjustment is the principal causes of sea level change for the last 2 kyrs in the Lazio coastline. Considering the preferred ICE-5G (VM2) model, the residual between the observations and the predictions of RSL

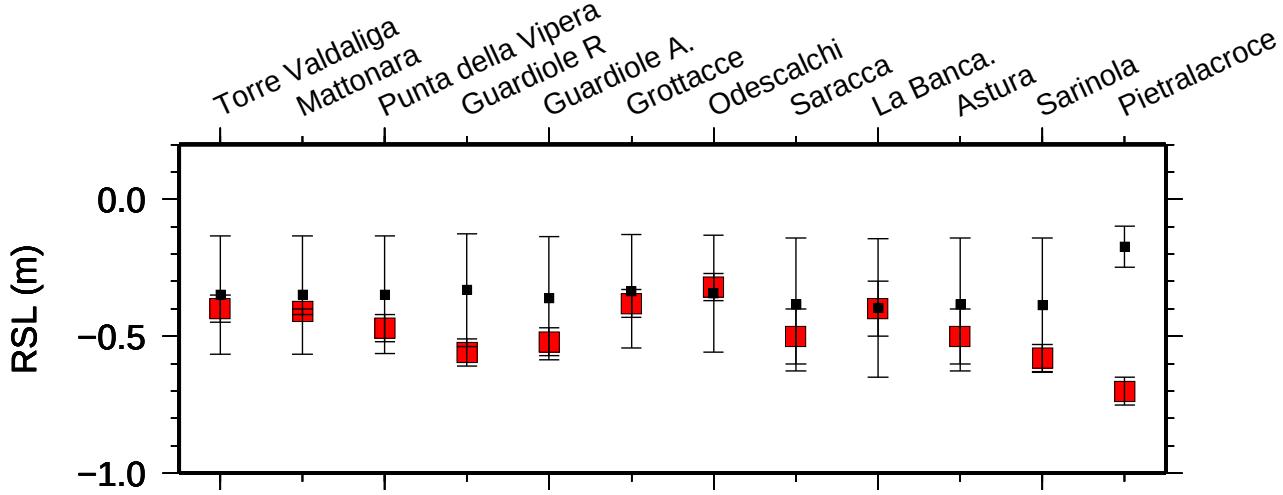

Figure 5.5: Comparison between RSL observed (red square symbols) and RSL predicted (black circle symbols, model ICE-5G (VM2 L90), for all fish tanks considered in this study. The error bars show GIA model uncertainties evaluated according to the perturbative approach obtained for different lower mantle viscosity.

is bout 0.1 m. This leaves some room for a contribution of recent sea level variations driven by climate change, which according to IPCC estimates amount to ~ 20 cm during the last century when globally averaged (IPCC, 2007) or 13 ± 0.01 cm if we consider the Trieste tide gauge as reference of secular sea level trends of whole Mediterranean basin. As we discussed in the introduction (Section 5.1) Milne et al. (2005) and Tarasov and Peltier (2002) put the ending of polar sheets ablation between 7 and 4 kyrs BP. Hence after 2 kyrs BP the contribution of eustatic component to sea level change is ~ 0 and the combination of glacio and hydro-isostatic effect rules the sea level variations.

These latter two effects have a complex geographical pattern that is also determined by the time-dependent ocean-continents distribution (Milne and Mitrovica, 1998). The amplitude of glacio and hydro-isostatic contributions to RSL depends on the location of the site with respect to the former ice sheets. In the near-field sites, the glacio-isostatic component directly associated with ice loading and unloading is dominant, while far field sites are mostly affected by deformations associated with hydro-isostasy (Milne and Mitrovica, 2008). The Mediterranean is far to the polar ice sheets, however Lambeck and Purcell (2005) suggest that Italy and much of Mediterranean, due the proximity with the former Northern Europe ice sheets, is located on their bulge and RSL here rise during the Holocene even after ice volumes have stabilized. In particular

direct glacio-isostatic effects play a significant role in the northern Adriatic region (Stocchi and Spada, 2009) and in southern France (Lambeck and Purcell, 2005). To illustrate the pattern of RSL across Italy during the late post-glacial period, we show the contour lines of RSL in Figure 5.6. Figure 5.6 shows a wide subsidence in the bulk

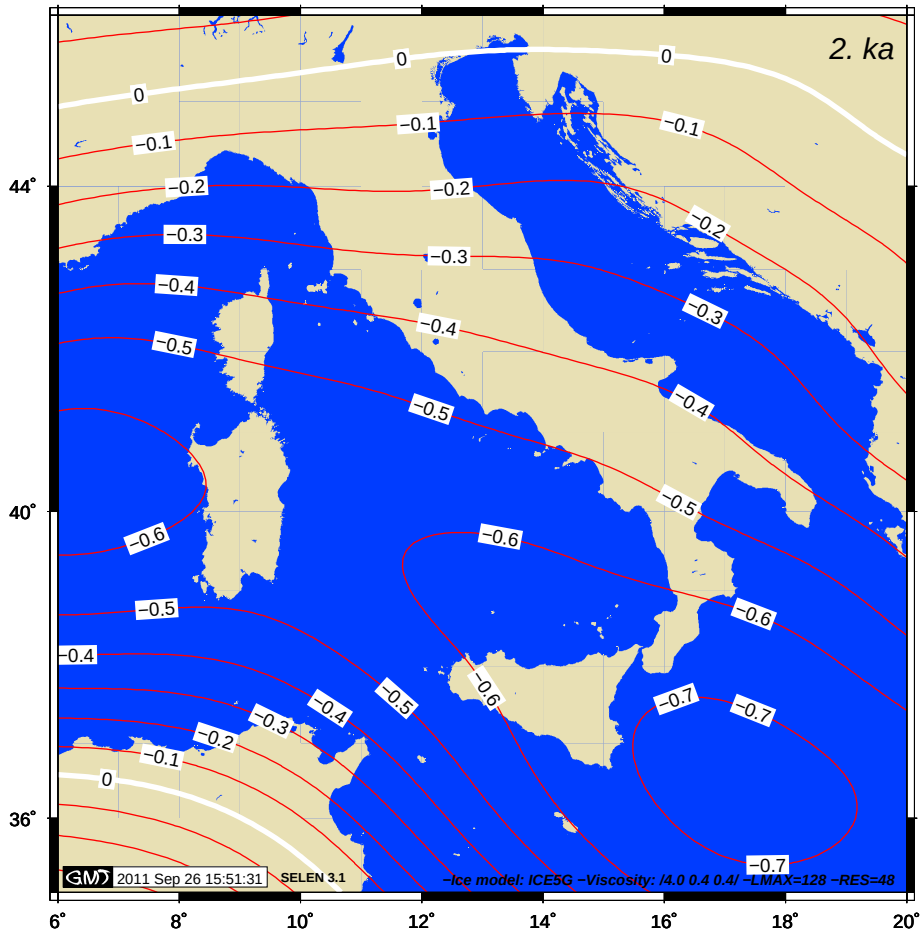

Figure 5.6: Contour lines of RSL (m) at 2 kyrs BP across the Italy according to model ICE-5G (VM2). The red line indicates the contour lines are spaced 0.1 m. The white line represent the RSL as nowadays.

of basin, along the Sicily channel where the contour line indicates a RSL of 0.7 m below the present while close to the coastlines, the RSL is around -0.2 m and the contour-lines are arranged parallel to the coastline, indicative of water loading contributing a major role to the spatial variability of the overall isostatic signal. By decomposing the sea level signal in eustatic, hydro-isostatics and self gravitational signals, we can describe in a quantitative way the weight of each contribution to sea level change (table 5.2).

Table 5.2: Sea Level observed and ICE-5G (VM2) for all sites. S_E denote the Eustatic signal, S_O represents the hydro isostatic component of GIA deformation, S_{GSC} is the sea level predicted for the self gravitational consistent methods.

Site	**time**	σ **time**	**RSL Obs**	σ **RSL**	S_E	S_O	S_{GSC}
fish tank	**kyrs**	**kyrs**	**m**	**m**	**m**	**m**	**m**
Torre Valdaliga	2048	13.0	−0.4	±0.05	0.03	0.216	−0.35
Mattonara	2048	13.0	−0.36	±0.05	0.03	0.216	−0.35
P.ta della Vipera	2016	21.0	−0.47	±0.05	0.03	0.207	−0.34
Guardiole rett.	1930	50.0	−0.56	±0.05	0.03	0.197	−0.33
Guardiole abs.	1930	50.0	−0.52	±0.05	0.03	0.208	−0.36
Grottacce	1960	10.0	−0.38	±0.05	0.03	0.202	−0.33
Odescalchi	2000	50.0	−0.32	±0.05	0.03	0.206	−0.34
Saracca	2016	21.0	−0.51	±0.05	0.03	0.150	−0.38
La Banca	2060	50.0	−0.35	±0.05	0.03	0.149	−0.39
Astura	2016	21.0	−0.35	±0.05	0.03	0.149	−0.38
Sarinola	2060	50.0	−0.58	±0.05	0.03	0.147	−0.38
Pietralacroce	2000	50.0	−0.94	±0.05	0.03	0.147	−0.17

When we compare the observations with the eustatic predictions we note that the eustatic signal is significantly smaller in the range of 0.03 m as we would expect for a late post glacial phases. The S_o correspond to the "hypothetical sea level" signal S^h_{OCEAN} used by Mitrovica and Milne (2002) to inspect the relative sea level when the ice loading is neglected. The method to predict the hydro-isostatic effect, mentioned in Section 5.3 reconstructs a extreme scenario in the absence of gravitational (N) and bedrock (U) deformation effects associated with the Late Pleistocene ice land cover. In this point of view the positive relative sea level obtained with S_o method indicates a sea level fall and as suggest by Figure 5.7, the phenomenon of sea level drop starts 4000 years ago when the amplitude of N_o and U_o deformations exceeds the eustatic signal and continue until today. In spite the dominant role of hydro-isostatic component at Mediterranean scale, along the Lazio coastline no Holocene high-stand was been surveyed (Lambeck et al., 2004a) suggesting a important control of glacio-isostatic contribution before 4 kyrs BP in agreement with Lambeck and Purcell (2005). The relatively nearby Fennoscandian component caused glacio-isostatic deformation that resulted in vertical movement of the crust of Earth and geoid surface throughout Europe. Melting of the Fennoscandian ice

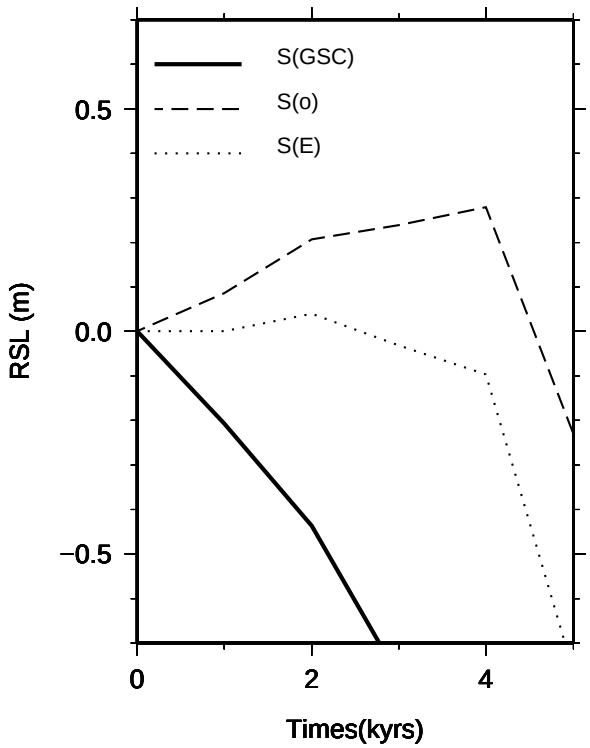

Figure 5.7: The predicted RSL curves during the last 5 kyrs for the sites occurred along the Tyrrhenian coastal area (see Figure 5.1). Self-gravitational-consistent (S_{SGC}): RSL curve obtained solving the Sea Level Equation; S_E: RSL curve obtained considering the eustatic component (Eq. 5.1); S_O: RSL curve obtained considering the Ocean load component (Eq.5.3); All the RSL curves are based on ICE-5G (VM2).

sheets removed the load from the previous glaciated continental area and allowed the crust to rebound here and leading to a subsidence of the crust around the ice sheet periphery (forebulge). The resulting vertical land movement is controlled by the viscosity of the mantle. The viscous effect is spatially wide ranging and responds on relatively long time scales. The material within the mantle returns from the forebulge to the area that was depressed by the ice-sheet. In the case of Lazio coastline, the pattern of sea level curve until 4 kyrs BP depends on the collapse of Fennoscandian forebulge while for the last 4 kyrs the hydro-isostatic component controls the RSL curves of Tyrrhenian sites.

5.6 Discussion

5.6.1 RSL indicators and tectonic implications

The coastal archaeological sites of Roman age located along the coasts of Lazio and Marche regions show that locally sea level has risen between 0.36 m and 0.94 m during the last 2 kyrs. As noted above, the only site with a strong difference between the observed and predicted value occurs for Pietralacroce fish tank, on the Southern part of Ancona city (see Figure 5.1). Relative sea level here was -94 cm msl while the isostatic predictions that are consistent with the results for the Tyrrhenian sites indicate that relative sea level was not lower of -0.17 m. The comparison between model prediction and observation is indicative of a subsidence characterized by an average constant rate of -0.38 mm/yr for the last 2000 years. Ancona belong to the sismogenetic area of Coastal-Adriatic Province that is characterized by a relatively deep (10 to 30 km) seismicity occurred in the last 2000 thousand years (Lavecchia et al., 2007). As recorded over the past 27 years (1983-2009) by the Istituto Nazionale di Geofisica e Vulcanologia's (INGV) seismic network, it is characterized by low- to medium-magnitude ($M \leq 5.0$) (Santini et al., 2011). The small tectonic activity is ascribed to the flexure-hinge retreat of a lithospheric slab of Adria microplate (Meletti et al., 2000) that setting a subsidence of 1mm/yr on times scales of the order 10^6 years around Venice related to the subduction of the Adria plate (Doglioni, 1993; Carminati et al., 2007).

On much shorter time scales, (less then one decade) using the focal mechanism associated with the seismic events occurred between 2003 and 2009 in the central-northern part of Marche region, Santini et al. (2011) analyses the stress patterns in this region. Consistently with the above studies (Meletti et al., 2000; Doglioni, 1993; Carminati et al., 2007), Santini et al. (2011) suggests that the extensional domain clearly works to chain and indicates a dominant NW-SE to N-S oriented compression in the Adriatic onshore in recent times. In this geodynamic framework the low subsidence can be explained considering that the area have experienced in the same long term low subsidence recorded at Venice area. For Ancona area, available observations of this predicted rate came from analysis of regional and local networks of continuously operating GPS made by Baldi et al (2009) that shows very low velocities of less than 1 mm/yr at the limit of the resolution of the GPS technique or below. This range is higher then that found by the GIA model and probably the prediction fells below GPS resolution.

5.6.2 GIA Models comparison

In the previous Section (Section 5.5), the local response of VM2 viscoelastic Earth model associated with ICE-5G global ice model has been investigated. To quantified the sensitivity of GIA to assumptions about the ice history we perform the same analysis described in Section 5.5 for ANU05 and than we compare the results with those obtained using ICE-5G. Firstly we reconstruct the RSL curves using VM2 viscosity profile and in second instance we employed the referred viscosity profile related to ANU05 that presents a range of viscosity between 0.3 and 0.5 $\cdot 10^{21}$ Pa s for upper mantle and between 10 and 20 $\cdot 10^{21}$ Pa s for lower mantle. Figures 5.8 and 5.9 show the RSL curves predicted for the all sites of the table 5.2 since 5 kyrs BP. The black lines are representative of RSL curves predicted for rheological profile ICE-5G (VM2) while the green dashed lines are representative of RSL curves predicted for ANU based on VM2 rheological profile. The reconstructed RSL curves vary smoothly from site to site occurred at Lazio coastline for both models. Instead the Adriatic area shows a different GIA history characterized by a knee at 4 kyrs BP caused by the end of melting assumed by ICE-5G model at this epoch, after which the sea level rose very slow until nowadays. In contrast the ANU05-VM2 curve predicts a small sea level highstands (above present MSL) between 4 and 2 kyrs ago followed by shallow negative sea level change in an area where such features are not geologically documented. When we analyzed the RSL at 2 kyrs BP (Figures 5.8 and 5.9), the predictions from two models are approximately shifted by 0.2 m and the offset between ICE-5G and ANU05 reflects differences in the time-history and ice melting (see Figure 5.2). The misfit can be tentatively attributed to the melting of the Wurm Alpine glacier considered in ANU05 but neglected by ICE-5G. Deeper investigations reveals that the small ESL stored (ESL of 0.8 m) and successively released by Wurm Alpine glacier does not produce RSL variation enough to explain the offset cited above but only a couple of centimeters that it is not enough to explain the offset cited above. It is more plausible that the misfit reflects the difference of equivalent sea level of Antarctic ice sheets for the last 6 kyrs (Figure 5.2).

5.6.3 Effects of mantle rheology

Figures 5.8 and 5.9 clearly show preference for the tuning employed VM2 with ICE-5G ice model (Peltier, 2004) for these sites. Although, the predictions of RSL curve indicated by green lines in Figures 5.8 and 5.9 are based on ANU05 and two end-member of Earth

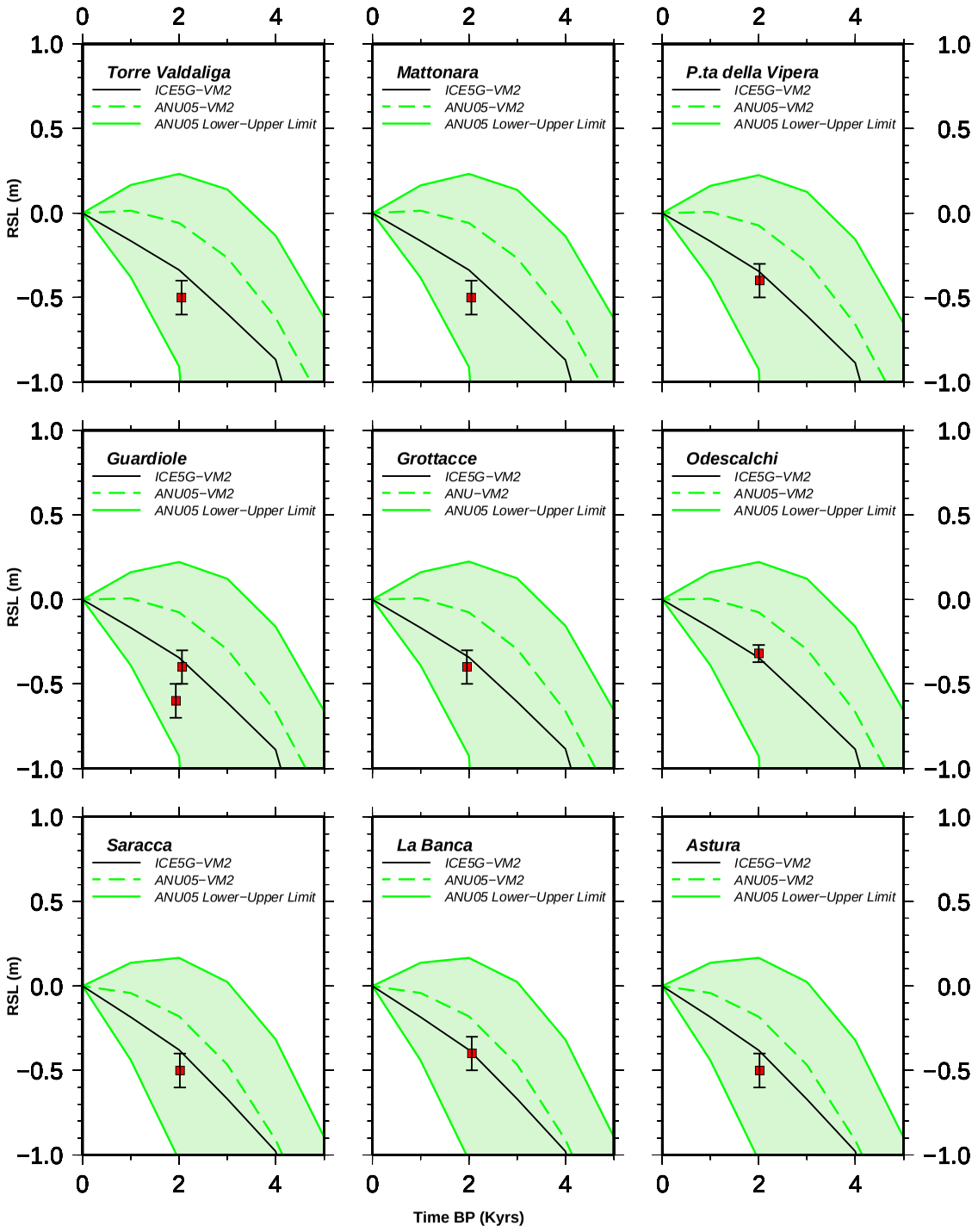

Figure 5.8: Sea level curve predictions for the last 5 kyrs, based on the reference Earth model VM2 and two ice global models: ICE-5G (black line) and ANU05 (dashed green line). ANU05 model was tuned to analyze different sea level curves (green shadows)based on the range parameters of Earth model elaborated by Lambeck and Purcell (2005) . The red squares with error bars show the sea level observations at the eleven sites shown in Figure 5.1.

models for a three-layered mantle. The two green lines enclose the green shadow areas that indicate predictions of RSL curved based on parameters in the range of upper mantle between 0.2 and 0.5 $\cdot 10^{21}$ Pa s and ower mantle in the range between 5 and 20 $\cdot 10^{21}$ Pa s . The range of model viscosity profile was employed by Lambeck and Purcell (2005) that have elaborated a number of regional solutions for the Mediterranean sites consistent with observations. In the case of Lazio and Marche archaeological sites the Earth-model dependence of the predictions for this parameter range is more sensitive and substantially larger than the observational uncertainties. When we analyzed the RSL offset between the ice models, it increased when we perturb the isostatic model with viscosity parameters. To support this guess, we show in Figure 5.10 isolines of paleo sea level obtained by varying upper mantle (η between 10^{20} and 10^{24}) and lower mantle (η between 10^{21} and 10^{25}) at time of 2 kyrs BP. The various authors generally agree that the viscosity increases by 1-2 orders of magnitudes throughout the mantle (e.g. Lithgow- Bertelloni and Richards, 1998). Steinberger and Calderwood (2001), however, found a gradual increase by almost a factor of 1000. Whether the increase is predominately gradual or stepwise from the upper to the lower mantle is still debated. Misfits to the data of greatest magnitude (≥ 2 m) occur when we consider a stiff lower mantle in pairs with a upper mantle of one order of magnitude smaller. Figure 5.10 is a further crucial contribution on this comparison since it fully explains the difference between the ICE-5G and ANU05 models in terms of

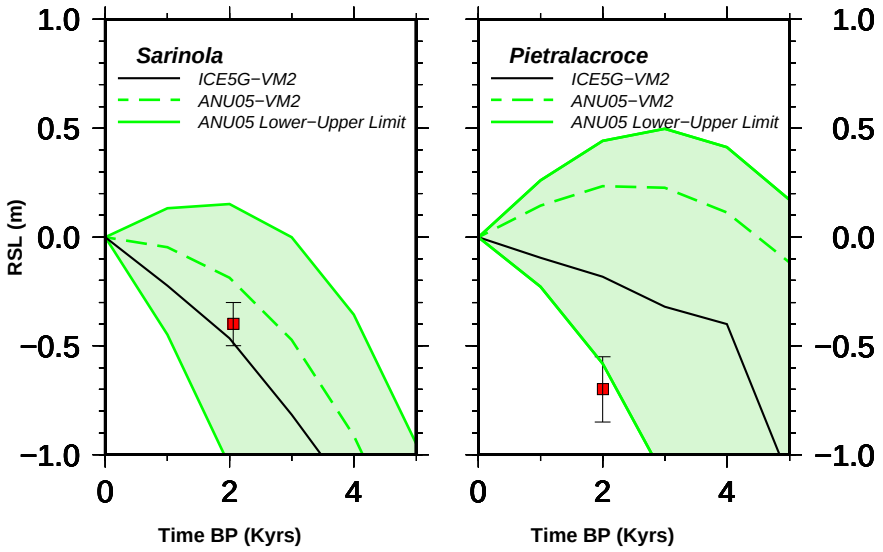

Figure 5.9: Continued.

RSL predictions. The pattern of isolines reveals that below 10^{21} Pa s viscosity for the upper mantle, the ice models respond in the same way to viscosity perturbation with a large average uncertainty for RSL when we test several lower mantle viscosity but ICE-5G is less sensitive compare with ANU05 predictions. Sea level below the present is always predicted in Lazio coastline with a range of value comparable with the observations when we use ICE-5G. Inspection of the diagram b of Figure 5.10 reveals that the predictions of ANU05 are not unique. The viscosity parameters determine a range of RSL between +2 m and -2 m msl that can be choose to obtain results similar to the observations. In particular using a traditional upper mantle with viscosity below 10^{21} Pa s the ANU predictions is sensitive to lower mantle only, with a wide RSL range predictions between +2 and -2 m.

In an attempt to reproduce the Lazio RSL during 2 kyrs ago GIA correction for ANU05 model is computed using a lower mantle viscosity around 20 10^{21} Pa s. Otherwise we can reproduce the GIA-RSL Lambeck et al. (2004b) value of -1.37 m using a stiff lower mantle around 10^{23} Pa s viscosity. However the poorly knowledge of mantle viscosity profile enables to constrain the GIA correction. In order to determine the GIA spatial variation over which this prediction would continue to apply will require

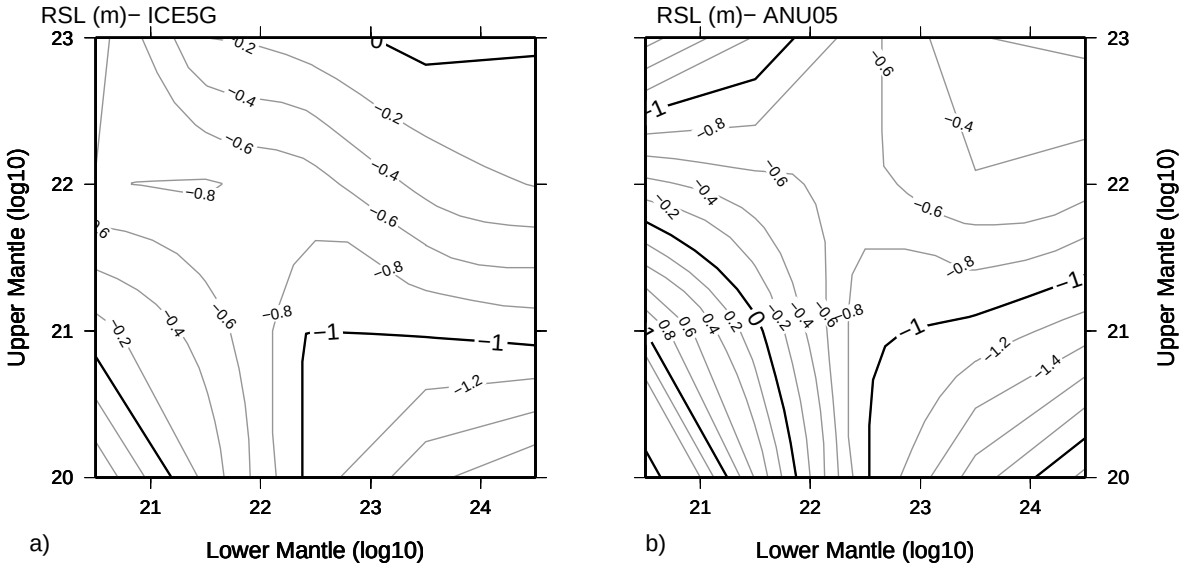

Figure 5.10: Predicted RSL at 2 kyrs BP along Lazio fish tank sites using ICE-5G (a) and ANU05 (b) ice models for upper and lower mantle viscosity values in the range $10^{20} \leq \eta \leq 10^{24}$ Pas. In both these computations lithospheric thickness is set to 90 km.

explicit comparisons with additional relative sea level data from the Mediterranean region. For example in the next chapter we focus on the RSL along the southern Tunisia coast that allows to better constrain the GIA predictions. Nevertheless, with Figure 5.11 we

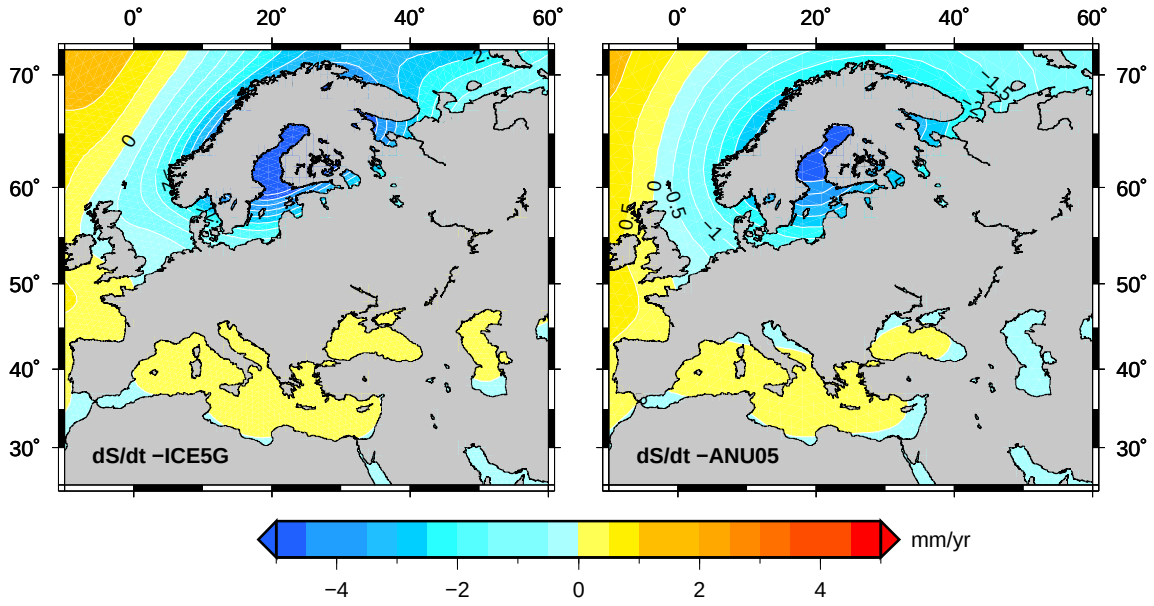

Figure 5.11: Numerically predicted present sea level (dS/dt) due to the drainage of Pleistocene ice sheets reconstructed by ICE-5G (left frame) and ANU05 (right frame). The computations adopt the rheological profile to reproduce the Lazio RSL. ICE-5G is associated with VM2 radial profile (Peltier, 2004). The rheological profile related to ANU05 presents a η upper mantle 3^{20} Pa s and η lower mantle 10^{22} Pa s. In both these computations lithospheric thickness is set to 90 km. The blue contours show the zone of predicted sea level fall, the remaining contours, from yellow to orange are regions of progressively higher sea level rise.

choose to investigate the implications of rheological profile of GIA contribution upon the present sea level change. Setting the GIA models consistent with the results for the Tyrrhenian and Adriatic sites we computed the present-day trend of sea level change (dS/dt) in Figure 5.11. In spite the difference on ice melting chronologies of models (see Figure 5.2) the predictions of ICE-5G and ANU05 share a similar trend around the sites of Lazio coastline. This is the result to force agreement between observations and ANU05 predictions through modification of the Earth rheology. In this case the nominal Earth model is largely compatible to the our RSL observations. For both the ice models, the rates of present sea level change run in NW-SE trending band with a range of -8 and -6 mm/yr around the centre of Fennoscandian ice sheets disintegration. As one moves progressively farther from the location of the Fennoscandian ice centre, the predicted sea

level rises. At the field sites in the Tyrrhenian and Adriatic sea the sea level predicted by ANU05 has a value between -0.1 and +0.1 mm/yr suggesting, as showed in Figure 5.11 the vicinity to the forebulge region. In contrast all the Mediterranean area present a positive dS/dt predictions when ICE-5G (VM2) is used. On the other hand, the range of Earth models related to ANU05 and explored in Figures 5.8 and 5.9 have the capability of explaining the observations by Lambeck et al. (2004b) with an increase in lower mantle viscosity. The stiff lower mantle viscosity increases the rate of present sea level rise in the Lazio area and predicts a sea level fall trend in the Ancona area.

5.7 Conclusion

We have investigated the relative sea level changes for the last 2 kyrs along the coast of central Italy. We have used archaeological sea level indicators derived from observations of the best preserved hydraulic features within eleven fish tanks. In particular we have provided the estimates for the former sea level during the Roman period and we have elaborated a quantitative analysis on the GIA contribution upon the RSL sites located along the coast of central Italy. Our findings can be summarized as follows.

i) In order to reconstruct the former MSL we have interpreted all fieldwork measurements and chosen the best preserved sea level indicator for each fish tank (Figure 5.3). Within the hydraulic features, the sluice gate, the upper foot-walk, the overflow carving and, the channels with the groove for the sluice gate are the most important features that record the palae-sea level at the time of fish tank construction, when, of course, they are preserved from wave erosion. The mean relative sea level obtained from the eleven archaeological sea level indicators of Lazio coastline is -0.45 $\pm$ 0.08 below msl during the Roman Period. Our observations indicate that sea level rose of about 50 cm during the last 2000 years with a constant rate of 0.225 mm/yrs. The relative sea level at Ancona site occurred at -0.94 $\pm$ 0.05 m msl, about half deeper of Lazio sites.

ii) The glacio glacio-hydro-isostasy is the cause of sea level change of central Italy. This process is the responses of planet to glacial and ocean loading/unloading relate to Late Pleistocene ice sheets at rates that are functions of the ice chronology and rheology of the mantle. By decomposing the sea level signal in eustatic, hydro-isostatic and glacio-isostatic signal, we quantified that during the Roman Period the eustatic contribution is 0.03 m, the hydro-isostatic signal is about 0.27 m that combined with the glacio-sisostatic

effects produced a RSL of - 0.35 m. Analyzing the misfit between our observations and a suite of plausible predictions we have noted that ICE-5G (VM2) represents the best model to explain the sea level change for the last 2000 years. Moreover the study supports a ice chronology characterized by a ending of rapid melt between 6 kyrs and 4 kyrs in agreement with Tarasov and Peltier (2002) and Milne et al. (2005) rather then a delayed ice melting during the last 2 kyrs proposed by Lambeck and Purcell (2005). Comparisons between observations and RSL predictions within the investigated area may allow the identification of Pietralacroce outlier sea level site, which provides important information on local effects such as tectonic subsidence around Ancona area with a rates of -0.38 mm/yr for the last 2000 years. Considering the preferred ICE-5G (VM2) model, the residual of 0.1 m between the observations and the predictions of RSL leaves some room for a contribution of recent sea level variations driven by climate change, which according to IPCC estimates amount to $\sim$ 20 cm during the last century when globally averaged (IPCC, 2007) or 13 ± 0.01 cm if we consider the Trieste tide gauge as reference of secular sea level trends of whole Mediterranean basin. The sensitivity of the Tyrrhenian and Adriatic RSL to the ice sheets chronology present an offset of 0.2 m at time of 2 kyrs ago. Predictions based on ANU05 model are elaborated with a wide range of viscosity profile that lead to substantially different GIA corrections. The perturbative method reveals that the prediction of ANU05 are not unique and the viscosity parameters determines a range of RSL that can be choose to obtain results similar to the observations. We have quantified the contribution of ocean and ice load upon the RSL curves of sites located in the coastal sector of central Italy. In the case of Lazio coastline, the pattern of sea level curve until 4 kyrs BP depends on combined effect of idro-isostasy and glacio-isostasy. In particular here, the idro-isostatic effect predicted a sea level fall for the last 2000 years. However the glacio-isostatic effect counteracts this signal thus, resulting in a monotonous sea level rise. Amongst the late Pleistocene ice sheets, obviously Fennoscandian ice sheets plays a important role in shaping the RSL curve of glacio-isostatic effect which in turn depends on viscosity profile of the mantle.

iii) Finally we have computed the rates of sea level change across the Europe, using the preferred rheological profile for both ice models. We have shown that both ice models assume that the central Italy, as the almost part of Mediterranean, is located within the Fennoscandian forebulge. In spite the difference on ice melting chronologies of models (see Figure 5.2) the predictions of ICE-5G and ANU05 share a similar trend around the

sites of Lazio coastline.

Chapter 6

Mid-Holocene highstand in the Gulf of Gabes

6.1 Introduction

In contrast with the well recognized middle to late Holocene highstand in equatorial ocean basins (Lambeck and Nakada, 1990), mid-Holocene highstands seem not to exist in the Mediterranean as a whole (Edwards, 2006). However field scientists (Paskoff and Sanlaville, 1983; Jedoui et al., 1998; Morhange and Pirazzoli, 2005) identify evidence for relative sea level (here after RSL) situated above modern sea level on theTunisian coast, that do not match with the results of existing geophysical models (Lambeck et al., 2004a).

Following the advice of Pirazzoli (2005) we increase the collaboration between modelers and field scientist through the study of traces of ancient shorelines in SE Tunisia. In this chapter we present new data on the morphological, biological and sedimentary record of paleo sea-levels at El Grine area (SE Tunisia). The field campaigns at El Grine area (SE Tunisia) occurred in November 2009 and was been partially funded by Ecole Nationale d'Ingenieurs de Sfax and supervised by Barbara Mauz, University of Liverpool.

We explain the palaeo sea-level observations in term of glacial isostatic adjustment. We have accomplished this goal through a suite of computations based on a spherically layered incompressible Earth model and two different available ice chronologies (Peltier, 2004; Lambeck and Purcell, 2005). Because the improved SELEN 3.2 GIA code, takes into account the shoreline migrations, it is appropriate code to be used to asses the sea-level curve predictions on sites placed along the Gabes Gulf, characterized by a large and shallow continental shelf.

In 1998 Jedoui et al., have a good correspondence between the zone VI of Clark et al. (1978) and their observations in the southestern Tunisia. Stocchi et al. (2005) studied the relative sea-level curves in terms of Clarks zones and interpreted the mid-Holocene of SE Tunisia high-stands (Jedoui et al., 1998; Morhange and Pirazzoli, 2005) as the effect of continental levering caused by the catastrophic event CRE3 deriving by Antarctica ice source (Stocchi et al., 2009). Continuing the work of Stocchi et al. (2009) we evaluate the SE Tunisia coast regarding its potential sensitivity to the melting history of Antarctic ice sheet. Moreover we evaluate what happens in the area of study if we modified the ice chronology model in order to reproduce the 8.2 kyrs climate event (Kendall and Mitrovica, 2008).

6.2 Origin of Holocene highstand

The sea-level change in response to rapid melting is the target of sea-level fingerprinting methods to infer melt distribution from sea-level observations (Clark et al., 2002; Mitrovica et al., 2001). The sea-level fingerprint is the not uniform global pattern of sea-level change associated with the melting of continental ice masses. In particular sea-level in the vicinity of a melting ice sheet will fall as a consequence of uplift crust underneath the region of ice loss. In addition the gravitational attraction of the ice sheet on the water also decreases due to ice mass loss. Both effects combine to cause a relatively large relative sea-level fall when compared to the globally averaged rise. Of course, given that sea-level in areas near the melting ice sheets is dropping, sea-level in other areas must increase at a rate greater than the global average in order to conserve mass.

Clark et al. (1978) separated the global sea-level variation into six geographical zones which they argued would be characterized by broadly similar post glacial sea-level histories as northern hemisphere ice sheets melt: I) a monotonic sea-level fall associated with previously glaciated regions; II) a sea-level rise at the periphery of these areas due the collapsing forebulge; III) a relatively far field region where a slight emergence of beaches are expected but it is time-dependent; IV) a sea-level rise slower then zone II; V) a far field region of low amplitude late Holocene sea-level fall occurring subsequent to the cessation of deglaciation and leading to a sea-level highstand; VI) a late Holocene highstand of varying amplitude far-field continental shorelines. These latter geographical zones relative to a specific ice-sheet melting histories have been the subject of study during the last thirteen years by several authors (Lambeck and Nakada, 1990; Mitrovica and Milne, 2002;

Peltier and Fairbanks, 2006) who explained more in detail the regional variations of sea-level change and the departure from eustatic signal through two important mechanism labelled collectively as 'ocean syphoning' (Mitrovica and Peltier, 1991) and 'levering' effects (Mitrovica and Milne, 2002).

Ocean syphoning refers to the transfer of water from equatorial regions to high latitudes, where it fills the space left by the subsidence of glacial forebulges (Mitrovica and Peltier, 1991). The levering effect is the uplift of continental margins caused by water loading offshore. The water load in the middle of the ocean produces a hydro-isostatic subsidence of the sea floor and active a syphon water from the coastline to the bulk of the basin that amplifies the sea-level fall. The glaciological community recognizes several unstable periods responsible of ablating continental ice sheets since the Last Glacial Maximum. The Bølling warm period at approximately 14.2 kyrs ago corresponds to a first well-known rapid melt event called Melt Water Pulse 1a. At the end of the Younger-Dryas cold period, the Melt Water Pulse 1b occurred, centered at 12 cal kyrs. The climatologists (see e.g. Zoller and Heinrich 1960) recognized a sudden drop of global temperatures occurred approximately 8.2 kyrs before the present that may have been caused by a small meltwater pulse from the final collapse of the Laurentide ice sheet of northeastern North America, hence called the 8.2 kyrs climate event (Alley et al., 1997; Barber et al, 1999). There is also a fourth rapid injection of meltwater event approximately 7600 years ago called MWP2 that is characterized by about 5 m of global equivalent sea-level (Blanchon and Shaw, 1995; Bird et al., 2007). The most extreme of these events (MWP1a) was firstly identified in the coral based record of RSL from Barbados island (Fairbanks, 1989). To complement the record from Barbados, the Tahiti record shows a synchronous hiatus corresponding MWP1a, and the latter two catastrophic rise events. The precise ice source of melt water pulses is still open to debate (Bassett et al., 2005; Peltier, 2005). No consensus on the source of the MWP1a has been reached yet and a contribution from North America, Scandinavia and the Barents Sea (Blanchon and Shaw, 1995; Clark et al., 1996) rather than Antarctica (Clark et al., 2002) has been proposed

Revising climate proxy $\delta^{18}O$ Peltier (2005) underlined that GRIP and GISP2 deep ice-cores from Summit Greenland record a northern hemisphere warm period in the range of time that is conventionally identified in Heinrich event 1 as well as the range of time corresponding to MWP1a. No expression of warm period is recorded in the

Vostok Antarctica ice core in the southern hemisphere. Otherwise Peltier (2005) proposed Antarctica ice sheets as the principal source of MWP 1b (Figure 6.1). Fairbridge (1961)

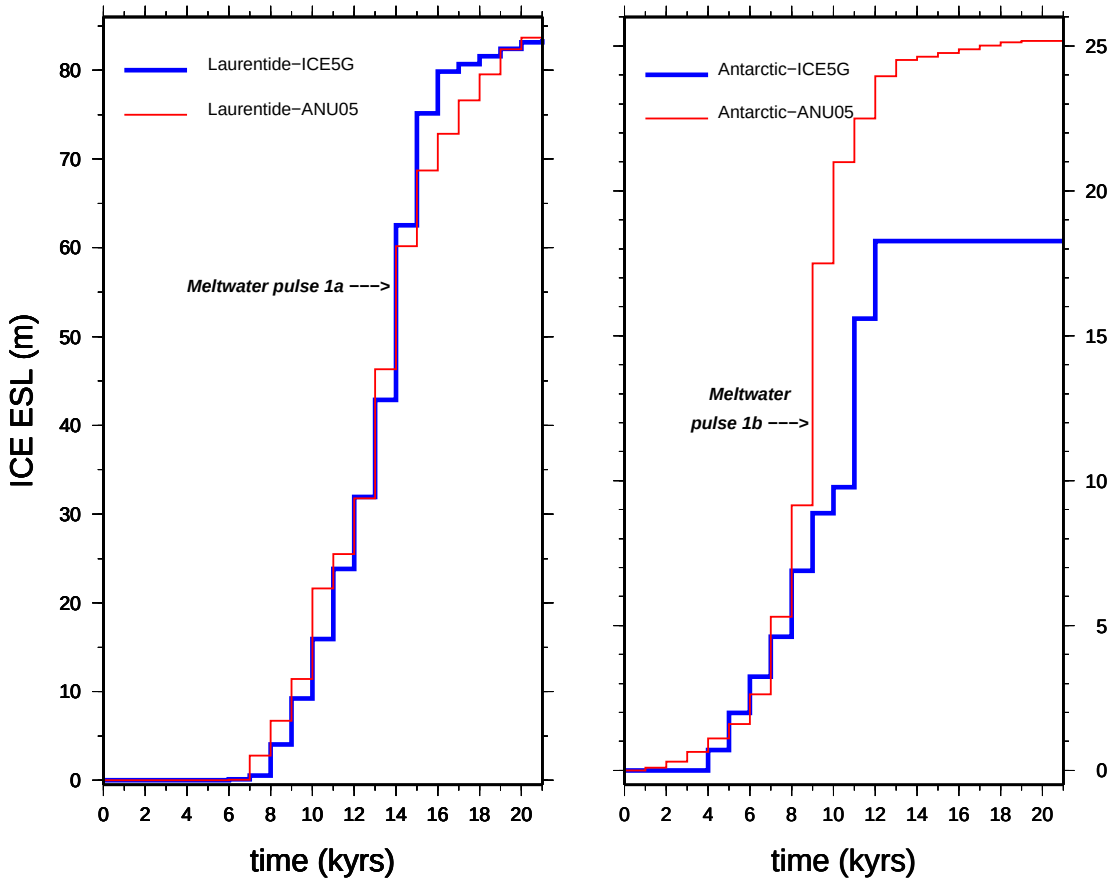

Figure 6.1: The Equivalent sea-level (ESL) as a function of time of the two major land-ice potential sources of MWP: Laurentide and Antarctica. According to ICE-5G (Peltier, 2004) Laurentide is the principal source of MWP 1a while Antarctica is the principal source of MWP 1b (Peltier, 2005). No explicit reference we find about the MWP sources included in ANU05 (Lambeck and Purcell, 2005). However in agreement with ICE-5G, the diagrams show that ANU05 put a MWP event around 14 kyrs from Laurentide ice sheets and a second MWP event from Antarctica around 9 kyrs.

identified a Late Holocene high-stand in the Western Australian coastline and established a sea-level curve that depart from the eustatic curve as a consequence of two collapse

events of the Laurentide ice sheet (Fairbanks, 1989). In contrast with the uncertain source of the two MWP events, most climatologist agree that the 8.2 kyrs cooling event was likely initiated by a catastrophic outflow of proglacial Lakes Agassiz and Ojibway with subsequent weakening of the Atlantic meridional overturning circulation. However, the total freshwater discharge and its duration remain uncertain. The ice volume loss is about 1-2 10^{14} m^3 (Barber et al, 1999; Clarke et al., 2004) to 5 10^{14} m^3 (von Grafenstein et al, 1998). Whether or not there was a further meltwater pulse (MWP2) is subject of debate (Church et al, 2011). Several Caribbean reefs appeared not to have been able to keep pace with rapid rates of sea-level rise around 7600 years ago (Blanchon and Shaw, 1995). Moreover observations from Singapore (Bird et al., 2007) from the Baltic Sea (Yu et al, 2007) and Indo-Pacific region (Woodroffe and Horton, 2005) add further evidence for a rapid rise prior to reaching present-day level around 7500 years ago.

Careful work by a number of geomorphologists in the past decade have evidenced a distinct pattern of middle Holocene highstands along the Gabes Gulf (Jedoui et al., 1998; Morhange and Pirazzoli, 2005) and in other sites along the coastal area of Mediterranean basin (Pirazzoli, 1991; Aloisi et al., 1978). However, field data of south Tunisia are in debate and, for example, questioned by (Lambeck et al., 2004a) who suspect that the deposits situated above modern sea level along the coast of SE Tunisia are storm-induced and do not provide evidence for the highstand of the sea level. Hence, it is of great importance a full validation of these observations.

6.3 Previous works

Evidences of mid-Holocene emergence around the south-eastern Tunisian coast was found around Jerba Island (Paskoff and Sanlaville, 1983), next to the town of Zarzis (Paskoff and Sanlaville, 1979), in the lagoon Bahiret el Biban (Strasser et al., 1989), close to the city of Gabes (Dalongeville et al., 1980) and at the Sebkhet el Melah (Fontes and Perthuisot, 1971) (see Figure 6.2). To understand the height-age relationship between the paleoshorelines described by previous works, Jedoui et al. (1998) carried out a geological survey and provided more radiocarbon dates derived from lamellibranchiata species. A well preserved outcrop at Sidi Jmour allowed them to recognize a transgressive succession composed of paleosol unit, littoral dune unit and beach deposits unit dated to mid Holocene highstand characterized by a sea-level at 0.40 and 1 m above the present msl. They found a second paleoshorelines at 0 m and dated to 1846 yrs BP. This latter coincides

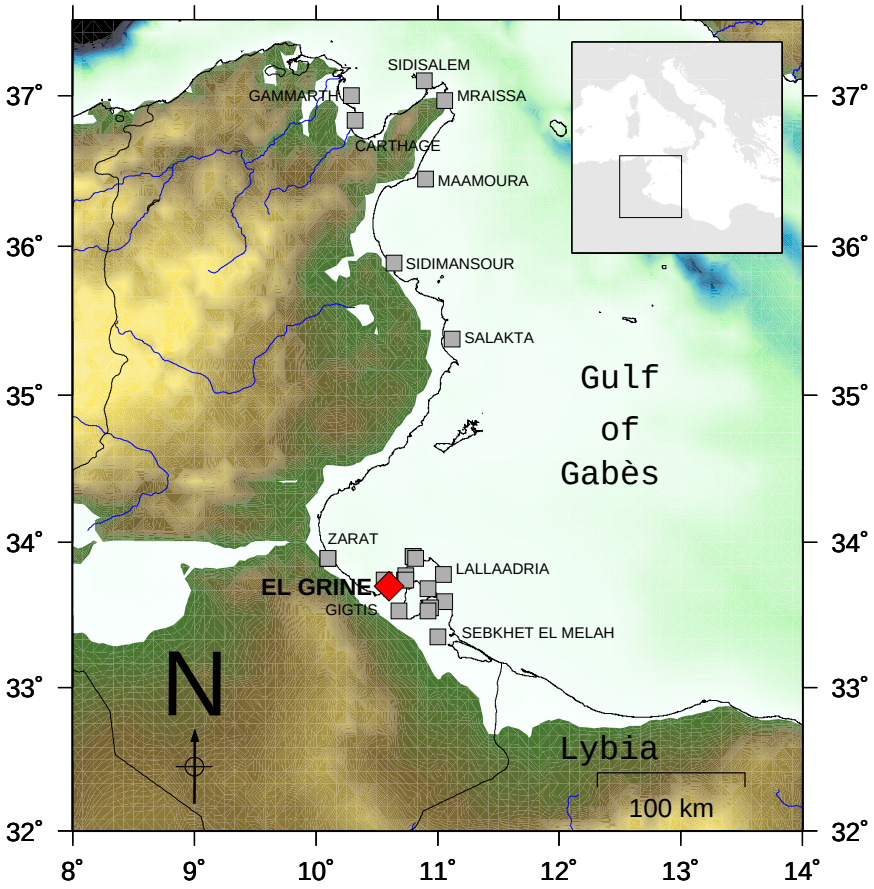

Figure 6.2: Location map of the RSL sites along the Tunisian coast mentioned in this work. The red square site has been revised and analyzed in this study. The gray square sites inferred from previous measurements.

with the present-day shoreline and is assigned to modern sea-level. The age obtained by Jedoui et al. (1998) for the El Grine zone, the key area of this study, is 5735±60 ^{14}C years BP or 6495 – 6028 years BP in caleander ages. This date agrees with those obtained in the same area by Morhange and Pirazzoli (2005) and Anzidei et al. (2010) (see Table 6.1). Morhange and Pirazzoli (2005) collected Petricola Lithophaga, Vermetus triqueter, Cerithium vulgatum still in growth position, from which they obtained an ^{14}C age of 5210 ±35 years BP, 5065 ±30 years BP and 6810 ±40 years BP respectively. In fact, in Morhange and Pirazzoli (2005), the elevation of sea-level indicators was referred to the

upper biological limits of living infralittoral populations and subsequently corrected using tidal predictions provided by the SHOM (Service Hydrographyque et Oceanographique de la Marine) model at the time of the surveys

Anzidei et al. (2010) date a Lithophaga still in situ to 5846-5700 years cal BP collected at 0.3 m above to the local mean sea-level. They interpret this paleontological proxy as lower limit of paleoshorelines since the lithophaga lives only underwater even during the lowest tides. Moreover, Fabricius (1970) produced a detailed study in radiocarbon ages of the ooids[1] within the limestone that laying a marine terrace at northeastern part of Jerba Island, and northern coastal sector of Zarzis and at Akara coast. They showed that the older ooids belong to the landward side of the terraceswhich occurs between 2 and 7 m at Jerba, Zarzis and Akara presented an age of about 21-27 kyrs. The ooids within the seaward side of terrace were analyzed more in detailed by Fabricius (1970) with the aim to confirm the hypothesis of a present time origin of ooids occurred in modern littoral sands (Lucas, 1955). Dating the different coating of ooids he found that outermost layers of the ooids is dated at 6000 years BP while layers nearer to the nucleus of the ooids had 7.770 years. The authors reject the hypothesis of a present-day origin of ooids and conclude that they were formed during the Holocene climatic optimum stage.

6.4 Geological setting

The study area (Figure 6.2) is located along the southeastern cost of Tunisia and comprises the Gulf of Gabes and Djerba Island. The Gulf of Gabes is one of the few Mediterranean regions where the tidal range is morphologically significant. Tides are semi-diurnal and can reach a range of 1.8 to 2.0 m at spring tides (Sammari et al., 2006). Morhange and Pirazzoli (2005) using the SHOM model, predicted a tidal range for El Grine of ± 0.4 m for November 2002. Morphologically, the area includes a general low relief on land and large shallow continental shelf on sea. The general flat topography corresponds to the coastal plain of Jeffara basin, bounded by the Atlas system to N-NW (Burollet, 1991) and Jeffara escarpment to S-SW (Bodin et al., 2010). The Jeffara basin has undergone a complex and polyphase structural history since the Carboniferous. Subsidence began during the Permian and later culminated with the Triassic rifting event marked by the deposition of a thick marine sequence (Gabtni et al.,

[1]Ooids are more or less spherical, sand-sized grains with a concentrically or radially layered, mainly calcareous coating around a nucleus of various origin.

2009). A general NW-SE oriented coastal depression of tectonic origin characterized the entire Cretaceous as evidenced by faults-related features in southern Gulf of Gabes (Bouaziz et al, 2003). The Early to Middle Cretaceous sedimentary succession shows an initial silicolclastic deposition followed by a carbonate sequence as a consequence of the transition from a mainly continental to fully marine environment. Further to the south the Cretaceous deposition changed from intercalations of marno-chalk and sandstones to dolomites, gypsum-clay and carbonate sediments (Ammara et al., 2010). The Neogene European/African plate collision imposed a compressional regime that resulted in the formation of the Maghrebidan mountain to the North (Pena and Abdelsalam, 2006) and subsidence along the eastern part of Tunisia, where the Gabes Basin was formed.

Later on, during the Miocene, a transgressive phase resulted in open sea deposition. The latter was then covered by continental and fluvio-lacustrine deposits as a consequence of the general relative sea-level fall that characterized the Villafranchien period (Plio-Pleistocene) (Frebourg et al., 2010). In the studied area the Quaternary deposits are dominant and overly in discordance early Pleistocene marine deposits (Bouaziz et al, 2003). Jedoui et al. (2002) distinguished two different sediment units, one characterized by siliciclastic and one by carbonate deposits (subtidal to backshore facies). The siliciclastic unit lacks of S. Bubonius fossil but contains other marine microfauna. It is truncated by the overlying carbonate unit which consists of oolitic and bioclastic sands with Senegalese fauna Jedoui et al. (2002). This unit is characterized by a depositional sequence from marine to aeolian facies. Based on paleontological ad sedimentological analysis the two units have been attributed to the MIS 5e relative sea-level higstand Jedoui et al. (2002). The elevations of these paleo sea-levels range between 3 m to 6 m above msl, comparable to those of marine littoral deposits found in other tectonically stable areas (Bouaziz et al, 2003). Recent research demonstrates that the southern Tunisian coastal area has remained relatively stable, with no significant tectonic activity for at least the last 130,000 years (Paskoff and Sanlaville, 1979; Bouaziz et al, 2003; Jedoui et al., 2002).

6.5 Materials and methods

6.5.1 Relative sea level indicators

Geological transects of deposits (Figure 6.3) was carried out during the field campaign at

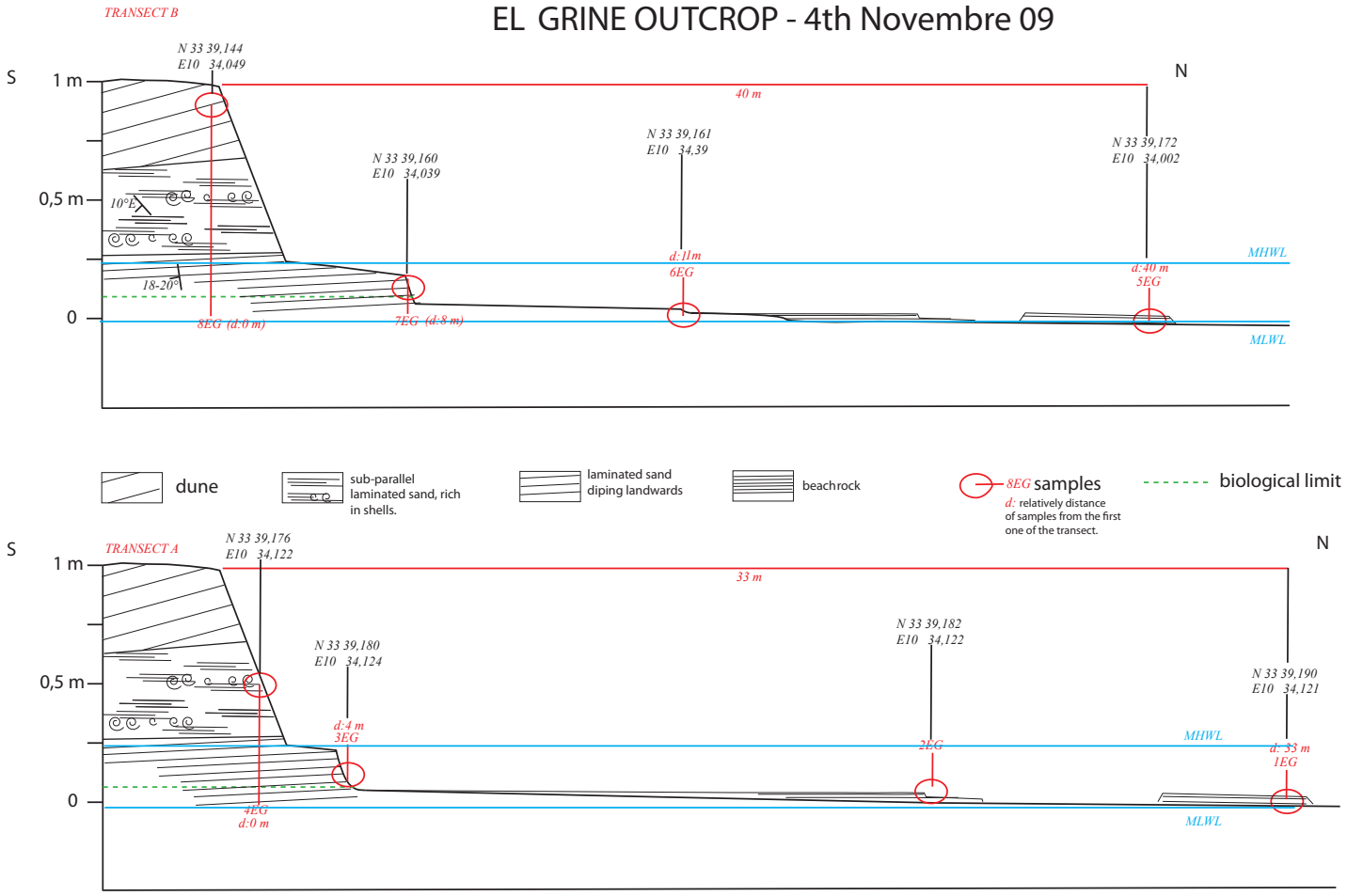

Figure 6.3: Geological transect A and B in the El Grine area.

El Grine area in November 2009 (Figure 6.4). The fieldtrip was funded by Ecole Nationale

Figure 6.4: Location of the two transects A and B in the frames b and a respectively located in El Grine area (see Figure 6.2). In c the arrows indicate the locations of samples used to date. In d we show with dashed green line the biological limit. Frame e shows the microfacies EGb.

d'Ingenieurs de Sfax and supervised by Dr. Barbara Mauz, University of Liverpool. Beachrock samples were collected from the intertidal zone, between the supra and sub littoral zone. The samples were taken from the different beds of deposits exposed in the transverse sections, from the beach to the sea and belong to two perpendicular transects spacing about 30 m: the samples 1EG, 2EG, 3EG, 4EG are representative of transect A and 5EG, 6EG, 7EG, 8EG are representative of transect B. sea-level broadly corresponds to the upper biological limits of living infralittoral populations (e. g. Lithophaga or

Table 6.1: Summary of the radiocarbon ages and observations of RSL data obtained for Holocene coastal deposits at El Grine area, in southeastern Tunisia from previous works: Morhange and Pirazzoli (2005) (M); Jedoui et al. (1998) (J); Anzidei et al. (2010) (A). The Site n in the first column refers simply to the reference number include within the list of sample used by each author. The calibrated ages in the fifth column are obtained using CALIB 6.0 (Stuiver et al., 2005).

Site n El Grine	lat	lon	age (yrs) C^{14}	age (yrs) Calibrated	obs. rsl (m)	Material	Ref.
7	33.74	10.73	5210 ± 35	5210 ± 39	$\geq 1.72 \pm 0.11$	Petricola s.	M
7	33.74	10.73	5065 ± 30	5828 ± 56	$\geq 1.72 \pm 0.11$	Vermetous. t. s.	M
7	33.74	10.73	6810 ± 40	7649 ± 32	$\geq 1.12 \pm 0.74$	Cerethium v.	M
Gif-09922	33.64	10.55	5735 ± 60	6277 ± 249	0.65 ± 0.35	Lamellibran.	J
9 (20)	33.65	10.56		5873 ± 27	$\geq 0.31 \pm 0.05$	Lithophaga	A

Vermetids). The elevations were measured, with reference to the sea surface at the time of survey (mean lower water level) by means of a folding ruler. These measurements were then corrected by tides according to the algorithm of the PMSLS (*http://www.pol.ac.uk*), and compared with the nearest tide gauges. The stratigraphic reconstruction of the area bases on standard rules of stratigraphic classification (ISSC, 1994) is used. The eight carbonate samples allow to investigate the evolution of microfacies and constrain the depositional environments of rocks. The interpretation of depositional environments is based on Flugel (2004). Standard thin sections of 8 rock samples were examined for their petrography characteristic under optical microscope Nikon Eclipse 6400POL petrographic according to (Dhunam, 1962; Folk, 1962; Krumbein and Sloss, 1951; Zuffa, 1979; Tucker, 1981). In addition, we analyzed polished rock slabs within cathodoluminescence method (CL) for elemental chemistry of cement at the School of Environmental Sciences (Liverpool University) using a Technosyn 8200 Mk operating at 20 kV and 40 mA with an unfocused electron beam under He atmosphere at 0.2 Torr vacuum pressure. This latter, helps to observe and interpret the diagenetic setting but also to identify stages of cementation. The radiocarbon ages (Table 6.1) obtained by Jedoui et al. (1998); Morhange and Pirazzoli (2005) were been calibrated using CALIB 6.0 (Stuiver et al., 2005) with the aims to homogenise the methods of calibrations. As first step we use the age obtained by previous authors considering that the outcrop of beach rocks in El Grine area is small enough to obtain a good stratigraphic correlation with the deposits recognized by the previous authors. However this method needs to be validated dating our samples. The School of

Environmental Sciences (Liverpool University) employ the OSL technique to obtain the age of our sample. We highlight that the ages are preliminarily (Mauz pers. comm.).

6.5.2 Glacial Isostatic Adjustment Theory

Models of glaciation-induced sea-level change have improved dramatically in the past few decades. The original sea-level theory derived by Farrell and Clark (1976) has been extended to incorporate a variety of effects, such as: lateral shifts in shoreline position associated with local changes in sea-level (e.g. Johnston, 1993; Peltier, 1994; Milne et al., 1999); the growth and retreat of marine-based ice sheets (Milne, 1998; Peltier, 1998; Milne et al., 1999) and the feedback of glaciation-induced perturbations in Earth rotation (e.g. Milne and Mitrovica, 1996, Mitrovica and Milne 2003). The recent version of code SELEN 3.2 include some of this effects in particular the later shifts in shoreline position and perturbation in Earth rotation. In this Chapter we focus on implications upon sea-level change when we consider the shorelines migrations inside the Sea-Level Equation (Farrell and Clark, 1976). In the simplified form the sea-level equation namely:

$$S(\omega) = [N(\omega, t) - U(\omega, t)]\, \mathcal{O}(\omega, t)\,, \tag{6.1}$$

where N is the sea surface variations relative to the Earth centre of mass, U is the position of the solid surface. $(\mathcal{O})$ (Munk and MacDonald, 1960) is the function that determines the shape of oceans. Since we assume fixed shorelines, the "ocean function" $\mathcal{O}$ at sites (ω) is:

$$\mathcal{O}(\omega) = \begin{cases} 1, & \omega \in \text{oceans} \\ 0, & \omega \notin \text{oceans} \end{cases}\,. \tag{6.2}$$

Where the ocean function is equal to unit the water-loading is applied (Eq.5.3). If we include the shift of shorelines, the altitude of the element that constitutes the oceans around the Earth is put in relationship with the present topography (T_p). Following the method proposed by Peltier (2004), we may infer the topography with respect to sea-level at any time in the past by computing:

$$PT(\omega, t) = S(\omega, t) + [T_p(\omega) - S(\omega, t_p)]\,, \tag{6.3}$$

where $S(\omega, t)$ is the relative sea-level predicted solving the sea-level Equation (Farrell and Clark, 1976) and the ocean function is redefined considering the paleo topography (PT):

$$\mathcal{O}^1(\omega) = \begin{cases} 1, & PT(\omega) > 0 \\ 0, & PT(\omega) < 0 \end{cases} \tag{6.4}$$

At any point in space (ω) and at any instant of time t for which $PT > 0$ we may assume that we have ocean. A consequence of these processes is that the areal extent of the Earth surface which is subjected to loading by the ocean varies over time. As tested by (Peltier, 1999) this procedure converges in few iterations because the impact of the time dependence of the ocean function on sea-level is a second order effect since this involves a smaller number of points. To reconstruct the regional palaeotopography, we made use of the ETOPO 5 topographic dataset of the National Center for Atmospheric Research and we assume that this topography has not changed during the past.

In order to describe how the glacio-hydro isostatic factors contribute to the spatial variability of sea-level change in Tunisia region, we adopt the ICE-5G deglaciation model (Peltier, 2004) and the ANU05 ice model (Lambeck and Purcell, 2005). This method allows investigating the sensitivity of relative sea level upon the history of ice sheet melting. The viscosity profiles used here and in the later chapter is the average VM2 model characterized by a elastic lithosphere with 90 km thickness, and two viscosity mantle layers respectively of $0.5 \cdot 10^{21}$ Pa s for upper mantle and $2.7 \cdot 10^{21}$Pa s for lower mantle. As proposed by Lambeck and Purcell (2005) we adopt for ANU05 the nominal viscosity profile characterized by a lithosphere thickness of 65 km, upper mantle of 0.3 $\cdot 10^{21}$ Pa s, a lower mantle of 10 $\cdot 10^{21}$ Pa s.

6.6 Results

The coasts of the El Grine area (Gulf of Gabes), shown in Figure 6.4 with an average elevation of 1-2 m allows observing the following result. From field work we have identified four lithostratigraphic units. The lithostratigraphic unit 1 forms the lowermost part of the cliff and and includes laminated grainstone dipping 18-20 degree West. The thickness of their front (seaward) is between 10-25 cm, while landward the thickness is between 25-30 cm. At ten cm from the mean lower water level the biological limits occurs along the outcrop. The angular unconformity (U1) separates the Lithostratigraphic unit 1 from Lithostratigraphic unit 2. It is well developed and occurs at constant elevation of 25 cm above the mean lower water level. Seaward were the Lithostratigraphic unit 2 does not overly the Lithostratigraphic unit 1 the angular unconformity passes into a erosional surface. The overlying Lithostratigraphic unit 2 is a grainstone yielded abundance of organic-rich layers where shells characterized buy large size ($\sim$ 1 cm) are strongly oriented. The thickness of deposit is in general constant and about of 70 cm. The

Lithostratigraphic unit 3 constitutes the upper unit and the basal erosional contact occurs (U2) occurs at elevation of 70 cm above the mean lower sea level. It is characterized by laminated bioclastic sand. Seaward, several beachrock emerges at the basic level of mean lower water level, is Lithostratigraphic unit 4. Lithostratigraphic unit 4 overlying the Lithostratigraphic unit 1 but the nature of contact is not clearly observable . The length of beachrock varies from half meter to three meters, its width reaches 30 cm. The lack of extension and of lateral continuity of deposits prevents the recognition of facies but a detailed sedimentary and petrographic laboratory analyses of two transect, gives clues to the environment of deposition. All analytical data established in this study are shown in Table 6.2.

6.6.1 Microfacies analysis of the carbonated deposits

Detailed sedimentary and petrographic analysis of transect at El Grine, based on the approach described in Section 6.5, reveals fourth distinctive microfacies, which are referred as EGa, EGb, EGc, EGd (Figure 6.5). The microfacies allow to describe at small scale the lithostratigraphic units. Lithostratigraphic unit 1 includes EGa microfacies, Lithostratigraphic unit 2 includes EGb microfacies, Lithostratigraphic unit 3 includes EGd microfacies, Lithostratigraphic unit 4 includes EGc microfacies.

6.6.2 EGa (samples 2EG, 3EG, 6EG, 7EG)

Sandy grainstone, moderately sorted, dominant components are ooids (64%) and skeletal grains (30%) as shown in Figure 6.5 a. The ooids are superficial and normal ooids showing one or more concentric layers as coating around the nucleus which exhibit a tangential orientation of aragonite crystal. The nucleus is dominantly bio- or siliciclastic grain. The skeletal grains are constituted by red algae (Halimeda, Melobesiae), foraminifera (Miliolidi and Elphidium) and mollusc shell remains (bivalves, echinoderm and gasteropodes). The primary porosity is quite obscured by cement. The cements include marine isopachous bladed high Magnesium calcite (HMC) cement, scalenohedral dogtooth cement, gravitational fabric calcite cement, interparticle bridge of microcrystalline or granular calcite cement.

6.6.3 EGb (sample 4EG)

Sandy grainstone, moderately to poorly sorted, part of the grains is aligned in a preferred grain orientation (Figures6.4(d) and 6.5 (b)), dominant components are ooids (57%),

Table 6.2: Results from field and sedimentological analysis

Sample	Elev. cm	Descriptions	Matrix	Microfacies	Litho. Units	Dep. Environ.
1EG	0 ± 5	Litarenite well sorted with dominant micritized ooids and silicoclast components.	Coarsely dogtooth rim cement, circumgranular calcite.	EGc	4	Foreshore
2EG	0 ± 5	Oolitic sand grainstone moderate sorted.	Circumgranular bladed cement, interparticle bridge microcrystalline granular calcite.	EGa	1	Shoreface
3EG	15 ± 5	Oolitic sand grainstone moderate sorted.	Microcrystalline dogtooth cement with circumgranular fabric.	EGa	1	Shoreface
4EG	40 ± 10	Oolitic grainstone poorly laminated layers rich in bioclasts.	Microcrystalline scalenohedral dogtooth cement with circumgranular and gravitational fabric.	EGb	2	Foreshore
5EG	0 ± 5	Litarenite well sorted with micritized ooids and silicoclast components.	Coarsely dogtooth rim cement, circumgranular calcite.	EGc	4	Foreshore
6EG	0 ± 5	Oolitic sand grainstone moderate sorted.	Circumgranular bladed calcite cement.	EGa	1	Shoreface
7EG	15 ± 5	Oolitic sand grainstone moderate sorted.	Circumgranular bladed calcite cement, coarsely dogtooth with irregular rim or gravitational fabric.	EGa	1	Shoreface
8EG	65 ± 15	Bioclastic sand poorly sorted, poorly cemented.	Cement almost absent, evidence for dissolution.	EGd	3	Backshore

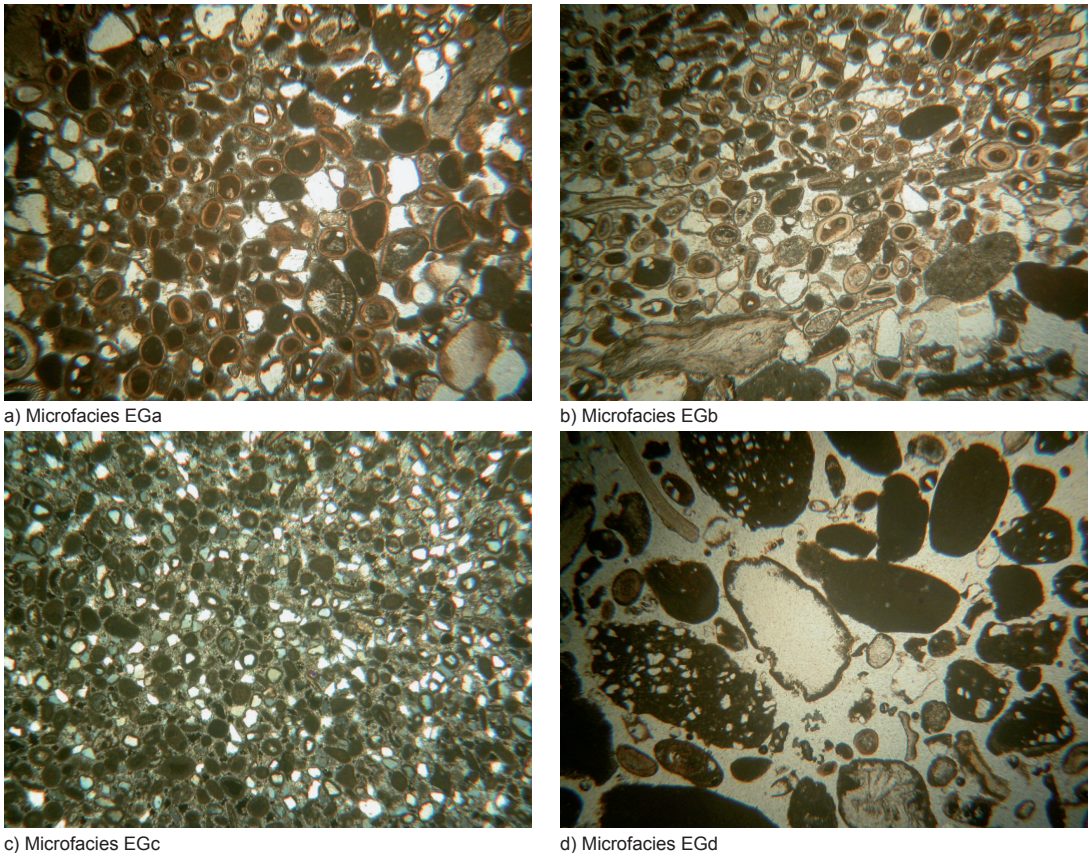

Figure 6.5: Microphotographs of the encountered microfacies. All the images are in normal light. The scale is the same for all pictures. a) 6EG thin section representative of EGa microfacies characterized by sandy grainstone, moderately sorted where the main components are ooids. b) 4EG thin section rapresentative of EGb microfacies characterized by sandy grainstone, moderately to poorly sorted, part of the grains is aligned in a preferred grain orientation, dominant components are ooids. c) 1EG thin section representative of EGc microfacies characterized by litharenite bearing carbonate detrital components, well-sorted, composition is dominated by non-skeletal grains. d) 8EG thin section representative of EGd microfacies characterized by coarse bioclastic sand, very poorly sorted and poorly cemented.

bivalve shells (10%) and sub-angular siliciclastic grains (5%). Most ooids are superficial ooids and present a circular shape with tangential fabric of carbonate crystals. The nucleus is bioclast or siliciclastic grain. In the Figure 6.5 b is possible to note that the bivalve shell exhibit elongate shape (most of them are conus cerithes) favouring fabric orientation. Others skeletal grains are: foraminifera (Miliolidi), coralline red algae (Halimeda, Melobesiae), echinoderma. The cement occurs as an irregular rim around the grains with bladed or radiaxial fibrous type cement with gravitational fabric. The major

thickness of cement occurs as gravitational fabric in the intergranular space.

6.6.4 EGc (sample 1EG)

Litharenite bearing carbonate detrital components, well-sorted, composition is dominated by non-skeletal grains (95%) which are ooids and siliciclastic grains (Figure 6.5 c). The ooids are superficial in structure with concentric layers showing relics of original tangential fabric due to micritisation. The coating shows ruptures indicating a reworked origin of the ooids. Quartz and feldspars with sub-angular shape are the dominant constituents of the siliciclastic component. Few foraminifera and echinoderma are present exhibiting recrystallised shells filled with micrite. The cement shows a coarsely crystalline rim of dogtooth type cement with irregular thickness and circumgranular calcite that fills almost all the voids.

6.6.5 EGd (sample 8EG)

Coarse bioclastic sand, very poorly sorted and poorly cemented. Coralline red algae (10%) (Melobesiae, Halimeda), foraminifera (20%) (Miliolidi, Ammonia) and shell fragments (10%) of gastropods and bivalve are abundant. Coarse sand lithoclasts (30%) dominate the non-skeletal grain fraction. The Figure 6.5 highlights the near-absence of cement: a very thin rim of microcrystal calcite around the grains.

6.6.6 Calcite cements description

The beachrock samples under examination show various diagenetic features, fabrics and texture of cements. From the petrographic analysis it was hypothesised that High-Mg calcite and (low-Mg) calcite is the dominant carbonate cement. High-Mg calcite occurs as isopachous bladed rim cements, micritic neomorphic cements and microsparite. Calcite occurs as scalenohedral dogtooth, microsparite and circum-granular cement. Figure 6.6 shows the different colors of cement under cathodoluminescence analysis. Isopachous microcrystalline fabric forms a rim around the grains (Figure 6.6 B1 and B2). The shape of this cement is bladed in 6EG and 7EG (size $< 25\mu$mm) samples and dogtooth within 2EG, 3EG, 4EG (size $< 10\mu$mm). Under cathode excitation the isopachous rim cement emit a very dull blue color. Scalenohedral dog-tooth crystals (Figure 6.6 C) with irregular and broken rim occur around grains. Moreover, the irregular rim of dogtooth crystals are also observed overlying isopachous microcrystalline bladed cement. In this case the growth

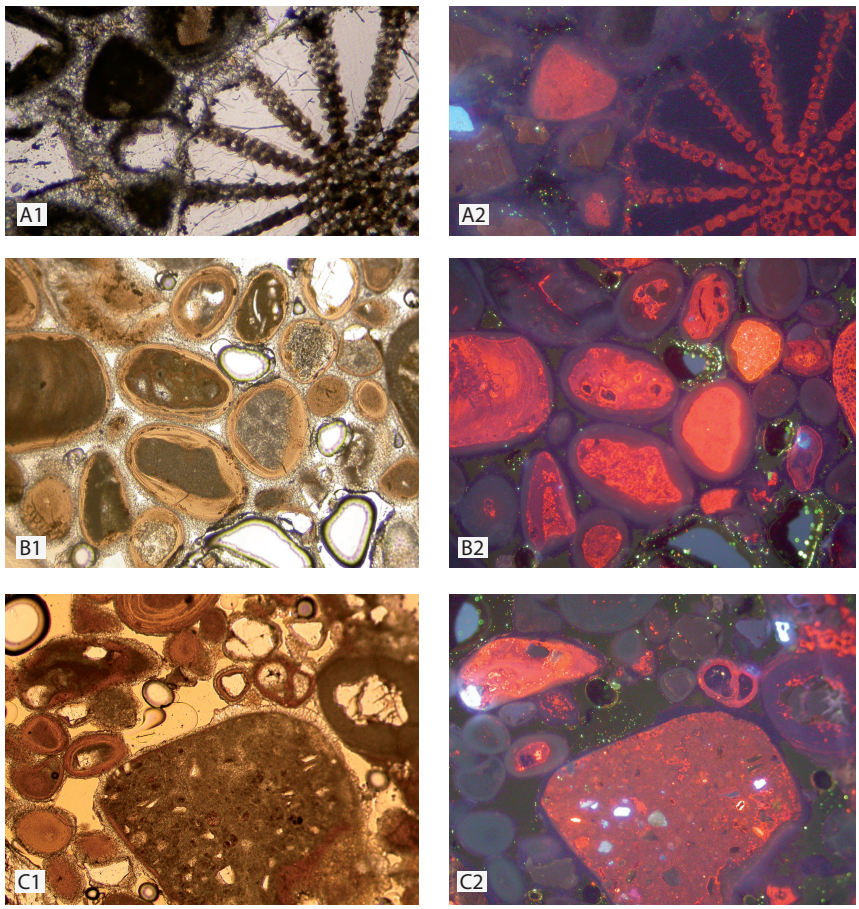

Figure 6.6: Microphotographs of microfacies images from transmitting light (A1, B1, C1) and cathode luminescence (A2, B2, C2). A: 5EG thin section representative of EGc microfacies is characterized by scalenoedral dogtooth cement (A1); under cathodoluminescence it evidences a violet color cement (A2). B: the 6EG sample, shown in B1, present a very well developed isopachous rim cements; under cathodoluminescence It evidences a very dull blue color (B2). The fabrics, size and CL of cements are the typical characteristics associated with marine phreatic diagenesis. C: within the 4EG sample the lithoclasts are bordered by dogtooth cements with gravitation and bridge fabrics. Under cathodluminescence (C3) the irregular and coarse dogtooth cements exhibits a very dull blue color with a thin layer of bright red color in the outermost part of the large lithoclast occurred in middle of the figure. The range from blu to red color evidenced within cements by CL analysis testifies a meteoric phreatic diagenetic environment.

axes of dogtooth crystals and bladed crystal is parallel. The size of dogtooth crystals is about 1 mm where they form a meniscus or gravitational fabric cement (4EG, 7EG). Under the cathode the dogtooth cement exhibits a dull blue color with an outer margin of bright luminescent CL. Microsparite cements fill most of the inter-particles primary porosity with bridge fabric cement. Under CL it exhibits a non-luminescent or blue color. Biotic voids are filled by microsparite showing bright yellow-orange bands under CL.

Pellets, ooids and shell remains experience neomorphic transformation to micrite. Under CL this micrite exhibits a variable color as a function of its elemental composition. If the micrite is a diagenetic product of red algae, the CL color is red or violet/red. If the micrite is a diagenetic result of ooids, its CL color is violet. When shell remains are micritized, the CL is red or yellow-orange. Circum-granular calcite fills almost completely the voids in 1EG1 and 5EG. Under CL it exhibits a blue colour with an outer band being of brighter colour.

6.6.7 Diagenetic setting

The Figure 6.7 encapsulates the principal type and pattern of cements recognized in beachrocks. In particular EGa, EGb microfacies, exhibit the typical characteristics associated with marine phreatic diagenesis: isopachous microcrystalline fabric. CL shows that this cement is characterized by very dull blue or violet cement. This colour is described by Aimieux (1989) to be the intrinsic colour of carbonate. The faint Mn as CL activator and the isopachous fabric indicate precipitation from oxidising water under shallow marine condition. Moreover, qualitative petrographic analysis shows that the cement is relatively reach in Mg. The high-Mg calcite composition of the cement suggests a significant influence of sea-water in their precipitation (Flugel at al., 2004). Non luminescent (violet) scalenohedral cement differs from circum-granular isopachous rim cement in crystal shape and size indicating precipitation under conditions of reduced sea-water agitation and reduced availability of Mg^{2+} ions. Moreover, the outer margin of dogtooth crystals exhibiting bright luminescent CL is generally interpreted as being caused by a decrease in redox potential (Eh) which results in reduction of Mn4+ to Mn2+ where Mn2+goes into solution and is subsequently incorporated in calcite lattice. Decreasing Eh is expected to occur alongside progressive marine burial diagenesis (Kaufmann, 2007), or in a stagnant marine phreatic zone at near-suface temperature and pressure conditions interpreted as a sign of fresh-water flooding by Aimieux (1989). The growth of dogtooth crystals starts on the surface of components or syntaxially on isopachous rim. The growth of dogtooth crystals on very thin rim cement probably indicates partial neomorphism replacement of bladed isopachous rim cement. The pore filling proceeds toward the central area of the pore through circum-granular fabric calcite cement. Both types of cement are interpreted to reflect a progressive shift from marine to meteoric diagenesis environment. The corrosion surface of bladed rim cement, the neomorphic replacement with dogtooth

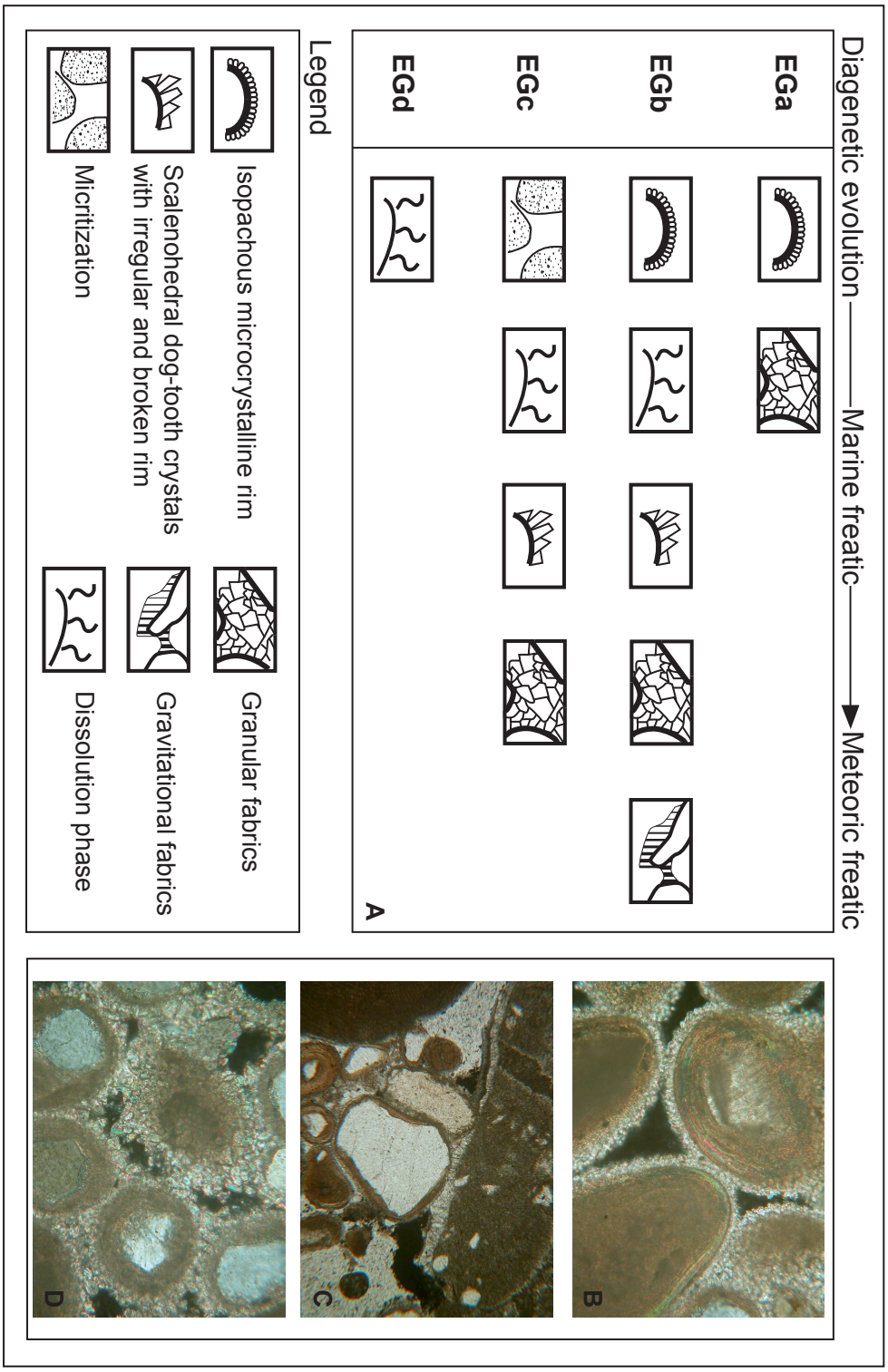

Figure 6.7: Schematic diagenetic evolution of beachrock samples analyzed in this study. A) Cement type and cement fabric recognized in each microfacies. B) Isopachous microcrystalline rim found in 6EG thin section belong to EGa microfacies. B) Scalenohedral dog-tooth crystals with irregular rim or gravitational fabric found in 4EG thinsection belong to EGb microfacies. C) Ooids micritized bordered by scalenohedral dog-thooth crystals with granular fabric founded in 1EG thin section belong to EGc.

cement and the irregular rim with meniscus and gravitational fabric are evidence for fresh water influence during the early diagenesis.

6.6.8 Interpretation of Microfacies

The petrographic and textural analysis of thin sections indicate that the sediments were deposited in shallow marine subtidal to supratidal environment. Microfacies EGa and EGb exhibit a vertical shallowing upward succession. The absence of sedimentary structure within the microfacies EGa suggests a massive deposition or a reworking of sediment by biotic components. This could be interpreted as deposit of low energy subtidal or deeper intertidal environment. Within the microfacies EGb the shell orientation are typical of the intertidal environment because of transported shell by sea water during low and high tide. This feature could be associated with a persistent laminar sea current within the intertidal environment. Within the microfacies EGb the shell orientation are typical of the intertidal environment because of transported shell by sea water during low and high tide. This feature could be associated with a persistent laminar sea current of the intertidal environment. The isopachous rim fabric and HMC composition of cement support the hypothesis of a marine environmental depositions and a marine-phreatic diagenetic environment.

The micritization of the ooids cortex within EGc suggests that the ooids are not of autochtonous origin. Neomorphic replacement of aragonite by calcite is the first diagenetic phase occurring in the microfacies EGc. Moreover, the smaller grain size and the well sorting of grain testify sustained water agitation. However, the well sorting could be inherited in which case the sorting cannot be associated with the energy of the sea water. The EGc is characterized by enrichment of the siliciclastic component. The possible explanation for this major shift in composition is an influx of terrigenous sediment from a proximal river caused by a seaward shift of the shoreline due to lowering of the relative sea-level. In this case microfacies EGa and EGb would correspond to sea-level highstand and the EGc would record a transition toward the fall in sea-level.

More information about the environmental setting of the microfacies is obtained from the cement: arrangement and fabrics of dog-tooth cement indicating meteoric environment is common within EGc, EGb and EGa suggesting a seaward shift of the shoreline due to relative sea-level fall. Moreover, the range of CL color exhibited by dog tooth cement from blue to red, emphasizes the transition from marine phreatic to meteoric

diagenetic processes. Finally the EGd microfacies represent the supratidal deposits still today under formation.

6.7 Discussion

6.7.1 Relative sea level Indicators at El Grine area

The microfacies and stratigraphic analysis allow to obtain a picture of the stratigraphy of El Grine area (Figure 6.8). The well exposed unconformity divides the shoreface deposits

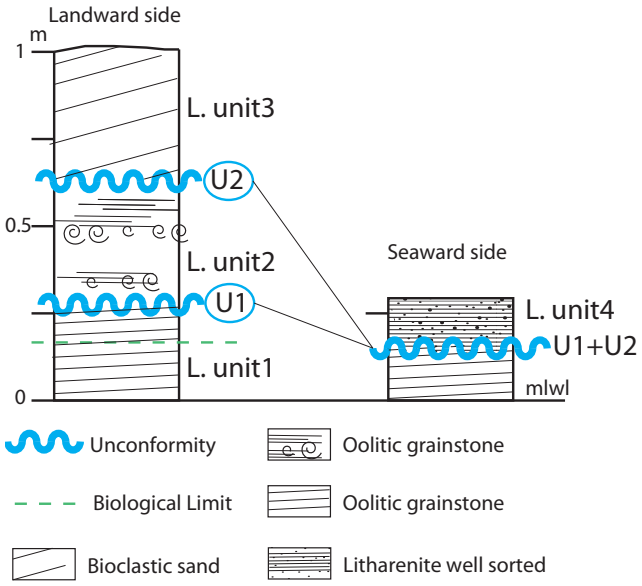

Figure 6.8: Stratigraphy of El Grine area. U1 and U2 refer to Unconformity. L. refers to Lithostratigraphic unit.

(Lithostratigraphic unit 1 and EGa microfacies) from the overlying foreshore deposits (Lithostratigraphic unit 2 and EGb microfacies). A erosive surface (unconformity) limits the foreshore deposits (Lithostratigraphic unit 2 and EGb microfacies) by the overlying backshore deposits (Lithostratigraphic unit 3 and EGd microfacies). Seawards the Lithostratigraphic unit 4 (characterized by EGc microfacies) occur above the shoreface deposits (Lithostratigraphic unit 1 and EGa microfacies). The preliminary ages obtained by the School of Environmental Sciences (Liverpool University) allow to obtain a picture of the chronostratigraphy of El Grine area. Based on preliminary age the Lithostratigraphic unit 1 presents an age of 100 kyrs and Lithostratigraphic unit 4 is around 4 kyrs old. This means that Lithostratigraphic unit 2 and Lithostratigraphic unit 3 have been deposited during the times window between 100 kyrs and 4 kyrs. This chronostratigraphic

reconstruction is in agreement with the reconstruction recognized by Jedoui et al. (1998) at Sidi Jimour site (Jerba Island, SE Tunisia). Figure 6.9 shows the stratigraphic

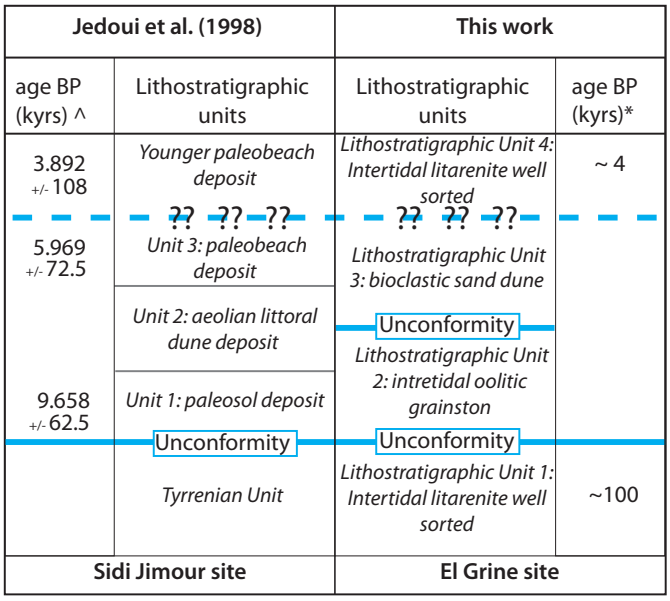

Figure 6.9: Stratigraphic correlations between our works (elaborated at El Grine site)and the one of Jedoui et al. (1998) at SIdi Jimour site (Jerba Island, SE Tunisia). ˆcalibrate ages obtained using CALIB 6.0 (Stuiver et al., 2005); ∗ preliminarily ages by School of Environmental Sciences (Liverpool University), based on OSL technique.

correlation between our works and the one of Jedoui et al. (1998). The well exposed unconformity separates the Tyrrhenian shoreface deposits (Lithostratigraphic unit 1 and EGa microfacies with an age of around 100 kyrs) from the overlying foreshore deposit (Lithostratigraphic unit 2 and EGb microfacies) and backshore deposit (Lithostratigraphic unit 3 and EGd microfacies). Seawards the Lithostratigraphic unit 4 (characterized by EGc microfacies) occur above the Tyrrhenian deposits. Stratigraphic correlation allows to relate the Litostratigraphic unit 2 and 3 to units 1, 2, 3 of Jedoui et al. (1998) that have an age between 5.969 ± 72.5 kyrs and 9.658 ± 62.5 kyrs. Based on the stratigraphic correlations of Figure 6.9, Lithostratigraphic unit 2 corresponds to the relative sea-level observations of palaeoshoreline formed during the middle Holocene time.

Biological limit (Figure 6.3), found for the Lithophaga boring along the Lithostratigraphic unit 1, is situated at at 0.10 m above the minimum low tide and represents a precise indicator of present former mean sea-level. The Lithostratigraphic unit 2 represents a former foreshore environments which today occurs 0.4 ± 0.1 m below this level. Hence it allows us to recognize a relative sea-level indicators uplifted of about

0.4 ± 0.1 m above the modern mean sea-level. Moreover, the diagenetic setting of calcite cements (Figure 6.7) suggests a seaward shift of the shoreline after lithifications process, interpreted as due to relative fall of sea-level.

The beachrock representing Lithostratigraphic unit 4 indicates a second former of intertidal zone located near to mean lower water level. The estimated age for this beachrock is around 4 kyrs, The observation and the age show that sea level has risen to its present level around 4400 years ago in this area.

A clear stratigraphic contact is not evident between Lithostratigraphic unit 4 and Lithostratigraphic unit 2 and 3. The lack of overlapping between the Lithostratigraphic units 2-3 and Lithostratigraphic unit 4 enables to clarify the stratigraphic relationship on field work. However the interpretation of the unconformities suggest that U1 is related to a subaerial and subsequent marine erosion relate to the relative sea-level fall and rise of sea-level during the last 100 kyrs. The U2 characterized by contact between foreshore and backshore is related to a subaerial erosion occurred after the middle Holocene time. Seaward the U1 and U2 have come together in one unconformity evidenced by the overlap of foreshore (Lithostratographic units 4) on shoreface (Lithostratigraphic units 1). In this case the unconformity evidences a stratigraphic gap.

6.7.2 RSL predictions

As underlined in Section 6.3, most of the evidence of sea-level variations during Holocene time in Tunisia occur in southeastern coastal border (Figure 6.2) and around the northern tip of Tunisia. We obtained proxies of two relative sea level from El Grine area. First relative sea-level was at least $+0.4 \pm 0.1$ m msl higher than present at the time between 5 kyrs and 7 kyrs BP. We note that independent observations (Jedoui et al., 1998; Morhange and Pirazzoli, 2005) based on palaeontological and sedimentological analysis show the same range of age (see Table 6.1) but at significant higher altitude (more than 1 m above the mean sea level). Though it was not possible to unequivocally identify the origin of this offset, it is likely that it results from the different methods of estimation used to measure the position of RSL indicators in the field. The second and early relative sea-level having reached its modern level about 4000 yr BP. A schematic curve that reproduces our observations is illustrated in Figure 6.10 where in an interval t_1 and t_2 sea-level rise rapidly such that the dominant contribution to the change is the equivalent sea-level rise (ESL). At time t_2 melting ceases. After that (at time t_3) the sea floor undergoes a

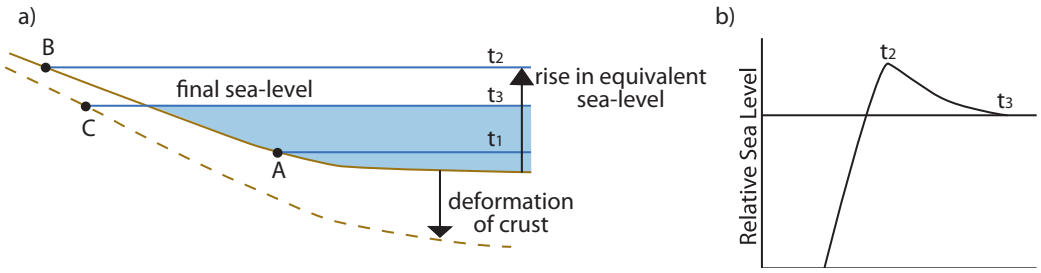

Figure 6.10: Schematic illustration of sea-level change relative to the a continental margin. At time t_1 sea-level begins to rise rapidly up to time t_2 and the shorelines moves from A to B. When no further meltwater is added into the ocean the contributions to further sea-level are the consequence of the deformation of Earth. Under the weight of the additional meltwater the sea floor subsides and the sea-level appears to fall relative to the shoreline to a point C at time t_3.

deformations by un amount that is a function of the water column above. The bulk of basin subsides by an amount that is different to the coast (see dashed line in Figure 6.10). This effect produces a water siphoning and a continental levering (Mitrovica and Milne, 2002) leaving behind a coastal highstand that marks the time at which meltwater injection into the oceans ceased (Lambeck and Nakada, 1990; Mitrovica and Milne, 2002).

To illustrate this point we show the form and magnitude of the GIA signals in the El Grine area in Figure 6.11. The black line of Figure 6.11 is obtained by solving the sea-level Equation (Eq. 6.1) for the ICE-5G (VM2) model. The pattern of the ICE-5G sea-level curve is characterized by knee a 4 kyrs associated with a abrupt change in gradient of sea-level change. Since 4 kyrs BP the sea-level rose with a rate of 3.2 mm/yr, after 4 kyrs BP the sea-level fell with a rate of -0.14 mm/yr reaching its present position at recent time. Based on different SE Tunisia sites (Jerba Island) Stocchi and Spada (2007) also predicted a sea-level highstand during the middle Holocene using ICE-5G-VM1. Difference observed with respect to the sea-level pattern of Figure 8 of Stocchi and Spada (2007) can be attributed to the different rheological profile (VM1) associated with the ICE-5G ice global model.

The shape of RSL curve modeled with ICE-5G of Figure 6.11, reproduces quite well the concept outlined in Figure 6.10. This means that the ICE-5G ice scenario predicts that the levering effect is the dominant contributor to the shape of RSL curve at the El Grine site. The grey line in Figure 6.11 is the RSL curve obtained by the ANU05-nominal Earth

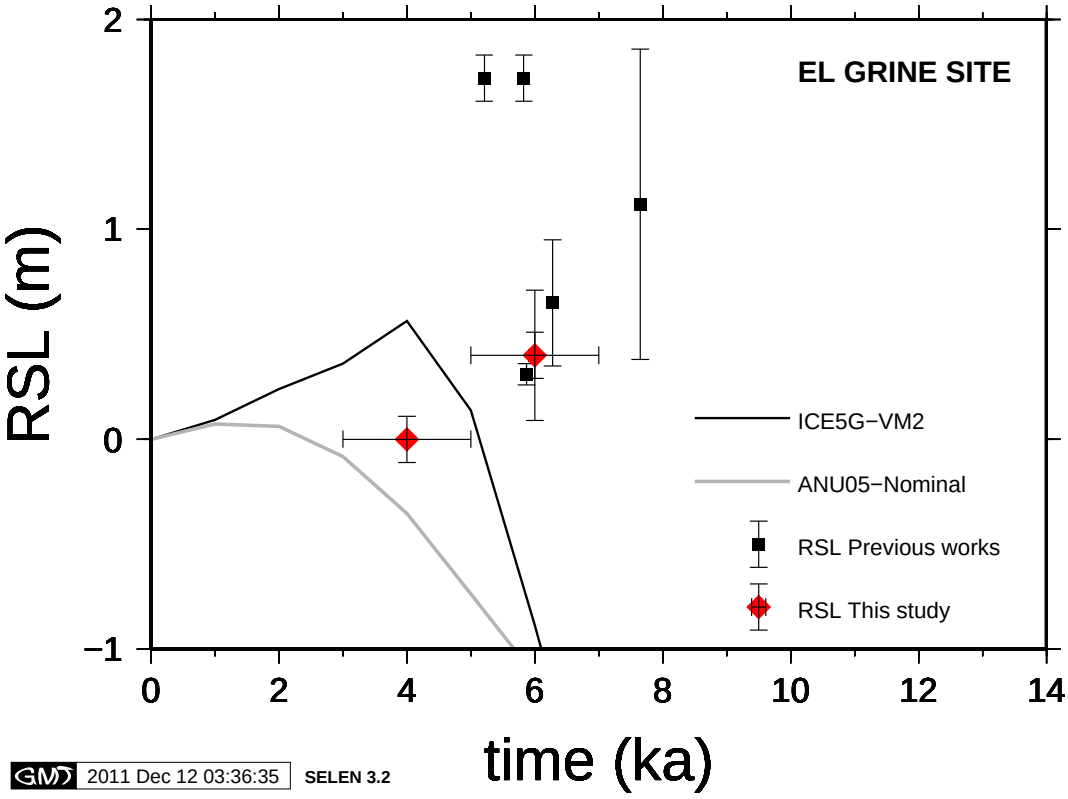

Figure 6.11: Predicted RSL at El Grine sites, for Earth model VM2 and ice model ICE-5G and ANU05. The highstand predicted for ICE-5G appears closed to 4 kyrs, while those relative to ANU05 is predicted around 5 kyrs.

model. By inspection of Figure 6.11 it is evident that, according to ANU05, sea level has never been higher than today. The ANU05 scenario is worthy of discussion. The reduced sea-level rise predicted by ANU05 in comparison with ICE-5G is predominantly due to a weak levering effect. The mechanism of levering effect is evident when two conditions are verified. First a meltwater pulse event or an adequate amount of melt water wast released from continental ice source, and second the mantle viscosity must be appropriate to allow for a differential deformation between the centre of the basin and its margin.

According to the Figure 6.1 (right frame) for the ANU05 model, the Antarctica ice sheets releases an amount of water of ten m of ESL during the time step 10-9 kyrs corresponding to an abrupt rise event occurring 9 kyrs ago. Hence the first condition is valid. However the nominal rheological profile, the rheological profile associated with ANU05, provides a lower mantle of 10^{22} Pa s. In this case the magnitude of viscosity

of lower mantle produces a long wavelength deformations that causes a homogeneous and uniform subsidence throughout the basin that prevents the levering effect. Moreover the Antarctic history included in ANU05 is characterized by a continued melting of ice between 6 kyrs and 2 kyrs for an amount of 2 m ESL. As consequence, during this time windows the ocean floor subsides at the same rate as the ocean volume continues to expand.

The comparison of observations and predictions inferred by ice models (Figure 6.11), indicate that the predictions are quite inconsistent with the observations, and hence other variables, such as shorelines migrations or modification of ice chronologies should be taken into account in order to elaborate RSL curves in agreement with the observations.However the ICE-5G model predicts a highstand at 4 kyrs BP with a amplitude (~ 0.5) comparable with the RSL observed but shifted in time of 2 kyrs earlier.

Recalling the first condition necessary for a highstand to occur as mentioned above, this observation suggest that an important catastrophic rise event could have occurred close to 6 kyrs BP.

6.7.3 RSL predictions using shorelines migrations

Considering the low relief of the land and the large shallow continental shelf on sea that characterizes the Gulf of Gabes, a local rise or fall of sea-level as shown in the sea-level curve predictions of Figure 6.11 could produces an onlap or offlap, respectively, at the ocean-continent interface and thus a significant migration of the shoreline. To test the sensitivity of the SE Tunisia RSL curves upon the shorelines migrations we analyze the GIA effect at regional scale, using the RSL observations of Tunisia coast inferred by previous works (Anzidei et al., 2010).

The spatial distribution of RSL indicators is shown in Figure 6.2. These includes the sites examined by Anzidei et al. (2010) along the Northern portion of Tunisia where archaeological remains such as pools and fish tanks indicate that 2000 years ago the sea-level was about -0.4 m msl. In the Gulf of Gabes a middle Holocene highstands was observed by Morhange and Pirazzoli (2005) (1.72 ± 0.11), by Jedoui et al. (1998) (0.65 ± 0.35 m), Anzidei et al. (2010) (0.3 ± 0.11 m). Our recent observations suggest that a well-developed highstand existed along the El Grine zone reaching an amplitude of at least 0.4 $\pm$ 0.1 m. Despite the consistency with the predicted highstands the observations around Gigtis, Rass Segala and Erseif Anzidei et al. (2010) indicate the absence of a sea-level

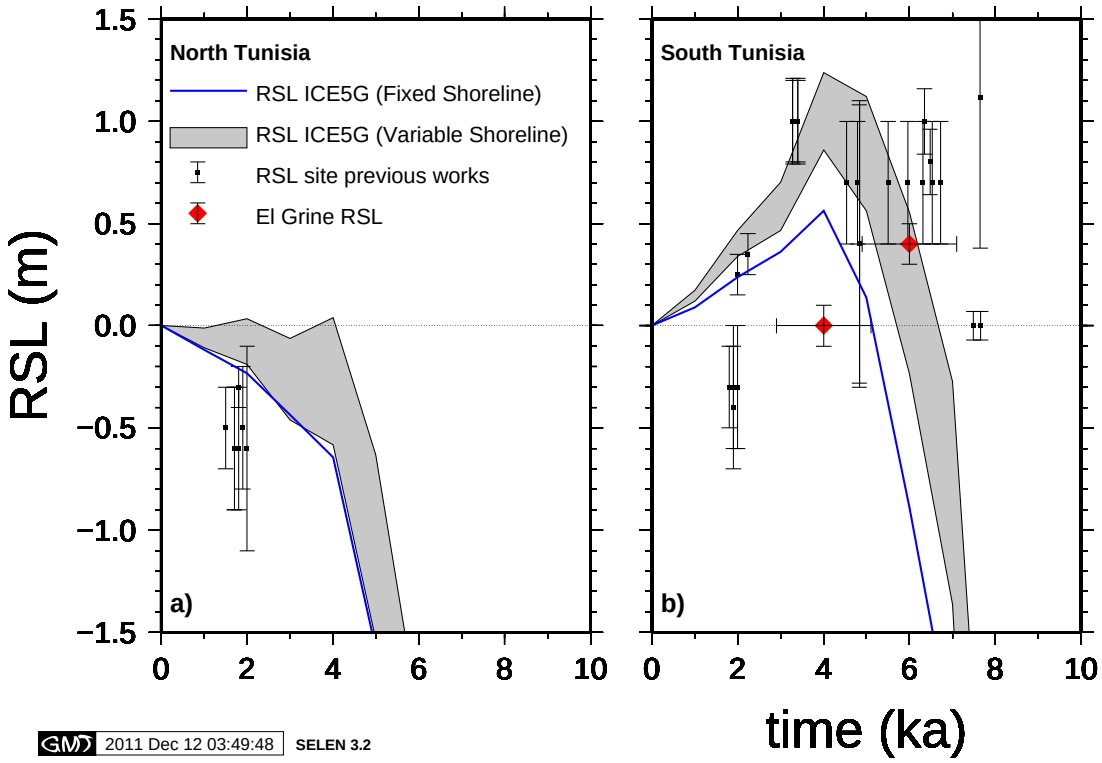

Figure 6.12: Predicted RSL curves at Tunisia sites (as shown the Figure 6.2) for Earth model VM2 and ICE-5G ice model. In the frame b) the black points occurred below the present sea-level, represent the RSL observations around Gigtis, Rass Segala and Ersifet obtained by Anzidei et al. (2010). The red diamonds represents our Observations.

higher then today in this three sites . However the indicators here not have the intrinsic accuracy of fish tanks Anzidei et al. (2010) and probably these recent relative sea-level changes have not yet been adequately constrained. Figures 6.12 and 6.13 show the RSL curves modeled using ICE-5G and ANU05 both including (gray shadow) and excluding (simple line) the influence of variable coastlines. Merging together the curves obtained at each site solving the sea level equation for variable coastline, we note a large spatial variability of the curves compared with the pattern obtained assuming fixed shorelines. We show this spatial pattern variations with a shadow area in both frames of Figures 6.12 and 6.13. Even a cursory inspection of Figures 6.12 and 6.13 reveals that ICE-5G-variable shoreline provides a better fit to the RSL observations at El Grine compared with RSL predicted using fixed shoreline.

Consistently with the computations of Figure 6.11, RSL variations driven by the

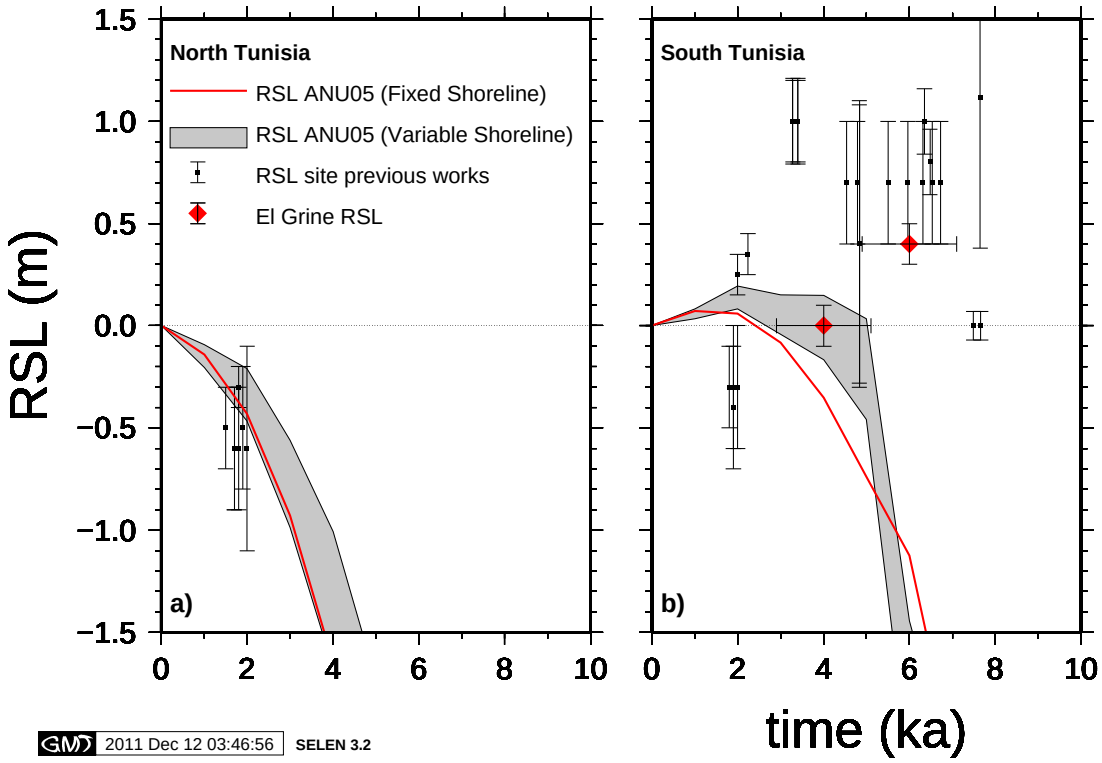

Figure 6.13: Predicted RSL curves at Tunisia sites (as shown the Figure 6.2) for nominal Earth model and ANU05 ice model. See the text for explanations.

melting of ICE-5G (b) show a clear highstand at 4 kyrs BP around the Southern Tunisia with a peak amplitude varying between +1.23 m at Zarat and +0.86 m at Lalla Adria. The offset between Zarat and Lalla Adria reflect the relative location to the centre of the basin as the Figure 6.2 shown (a more detailed discussion will be presented below).

Moreover the offset between fixed and variable coastline predictions reflect the difference in the time-dependent ocean loading at global and hence at local scale. For the same incremental change in equivalent sea-level the migration of shorelines across the low gradient continental shelf of Gulf of Gabes causes a rise in sea-level higher then those predicted by fixed shoreline computation at El Grine area. We note that shorelines migration requires a change of the areal extent of the Earth surface which is subjected to load and hence exert a control on the levering effect. In this case the shoreline migration increases the process of continental levering.

Comparing frames (a) and (b) of Figure 6.12 it is interesting to note that the pattern of sea-level curve predictions have a strong spatial variations moving from north

to south. In the frame (a) of Figure 6.12 sea-level reaches present sea-level at 4 kyrs BP with local variation depending on the latitude coordinate of sites. The results suggest that the GIA effects through the glacio-isostatic and hidro-isostatic components, predicted by ICE-5G (VM2) scenario, result in effects of different spatial scale along the coast of Tunisia region. In particular the ocean load produces a signal that that decreases from south to north, moving to north weakening the levering effect, thus decreasing the offset of sea-floor surface positions between the centre of basin and the continental margin.

According to Lambeck et al. (1996) within a distance of typically 40^0 to 60^0 latitude from the ice centres, the glacio-isostatic term is important in shaping the overall pattern of apparent land subsidence. With respect to the Fennoscandia ice sheets centre, part of the Tunisia region lies within this latitudinal range. The results is that the ice load acts differently in the north than in the south Mediterranean: the north area is related to the Fennoscandian forebulge collapse, the south region is far enough away from the centre of Fennoscandian ice sheets not to be involved. However tuning of rheological profiles can amplify the ocean loading at the expense of the ice loading thus shaping the highstand around the coast of the north Tunisia. In contrast with spatial variations of sea-level curve reconstruct by ICE-5G (VM2), a slight conciliation between fixed and variable shoreline predictions is shown when RSL curves are computed using ANU05 ice model (Figure 6.13). The RSL curves predicted when we include the variable shorelines in the ANU05 ice model reproduce almost the pattern of RSL curves predicted for the fixed shoreline. Exception in Frame (b) is the smooth signal of sea-level higher than today of about +0.2 m at 2 kyrs ago. It represent at local scale, the levering effect that act at the time at which the ice model ANU05 assumes the end of melting.

These results, shown in Figures 6.12 and 6.13, demonstrate that the impacts of shoreline migration on relative sea-level history of El Grine area by amplify the signal of middle Holocene highstand using ICE-5G, and a substantial improvement emerge in sea-level curve predictions when we include the shorelines migrations on the computations of the sea-level equations using ANU05-nominal Earth model.

6.7.4 Ocean and Ice load induced RSL variations

Figure 6.10 illustrates conceptually how middle Holocene highstands can develop along continental margins because of the adjustment of the Earth to water load after the ending of melting phase. Figures 6.12 and 6.13 reproduce the sea-level history obtained for the

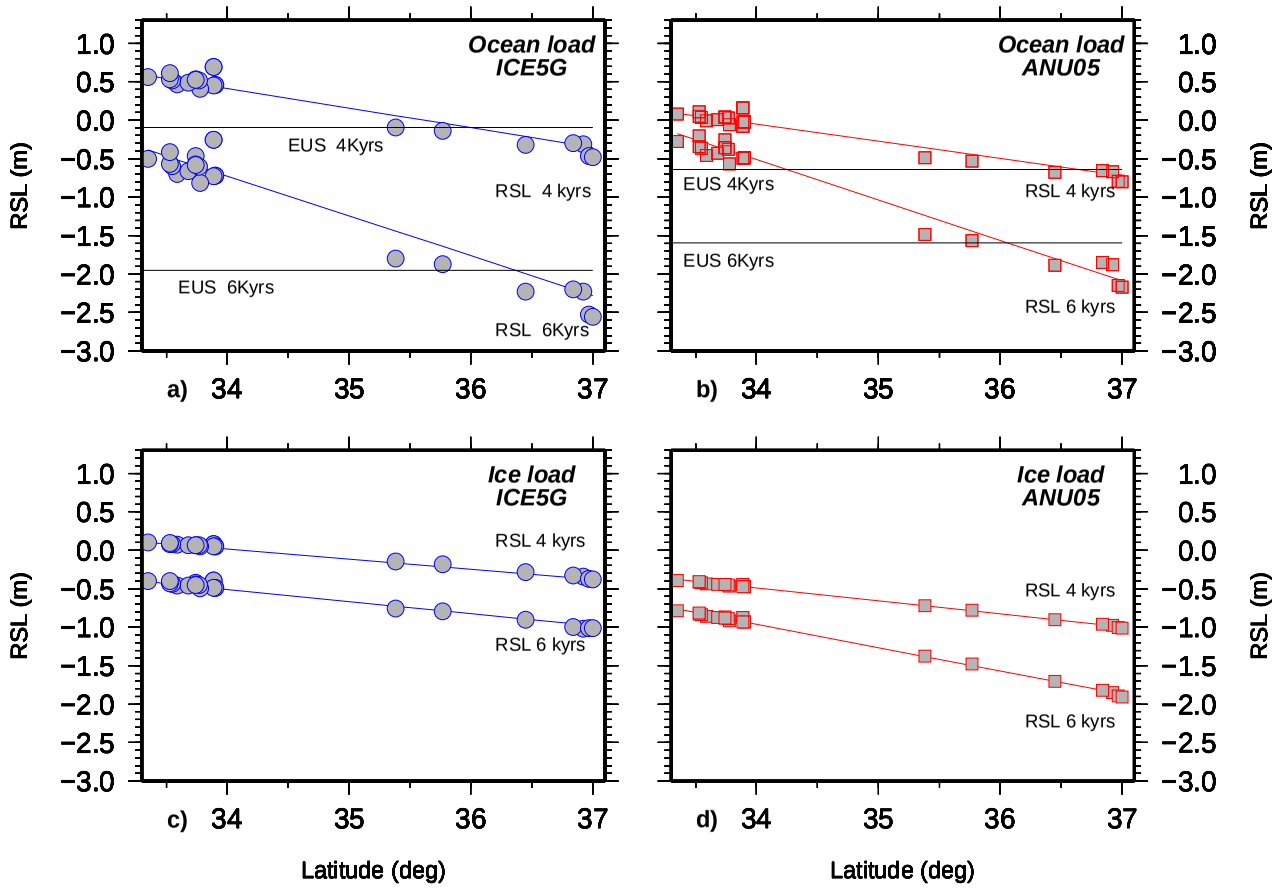

Figure 6.14: Predicted RSL of sites along the Tunisia coastal region at 6 kyrs BP and 4 kyrs BP. Each frame include the ice load and or water load components of ICE-5G and ANU05 model respectively. The horizontal lines represent the eustatic contributions predicted for each ice models.

total surface load. Otherwise, the results in Section 6.7.3 suggest that the GIA effects (the glacio-isostatic and hidro-isostatic components), act in different manner at spatial scale along the coast of Tunisia region, especially for RSL predicted by ICE-5G (VM2) scenario. The following analysis allows to show the sensitivity of Tunisia sites upon the latitude variations. To address this point in Figure 6.14 we plot the separate contribution to RSL variations along the Tunisia coast due to glacio-isostatic (S_I) component and hydro-isostatic (S_O)component. According to our simulations the Sea Level equation can be schematically rewritten as:

$$S(\omega, t_{BP}) = S_I(\omega, t_{BP}) + S_O(\omega, t_{BP}) + S_E(t_{BP})\,, \tag{6.5}$$

where the RSL variations ($S(\omega, t_{BP})$) at location ω and time t BP, represents the sum of glacio–isostatic component ($S_I(\omega, t_{BP})$), hydro–isostatic component ($S_O(\omega, t_{BP})$) and the eustatic value. The distribution of RSL Tunisia field sites allows to analyze the RSL variations through a transect north-south between Sebkhet El Melah site on the south and Gammarth on the north, in the interval of latitude between $\sim 33^o$ and 37^o degree. According to Figure 6.14 we obtain that the effect of ocean load on RSL variations is a negative trend both for ICE5G model and ANU05 model. Major gradients are predicted for RSL at 6 kyrs as shown in Table 6.3. Also from the results of Figure 6.14 the water load component, referred as the continental levering effect, is largely responsible for the departure of RSL from the eustatic signal. Important to note the latitude at which the regression lines of ocean loads cross the eustatic value. At 4 kyrs the sites located south of 36^o latitude experience sea-level higher than the eustatic value while those north of 36^o latitude experienced a RSL lower than the eustatic signal. We explain this difference in RSL amplitude with the distance of sites from the centre of the water load, hence the centre of the basin.

As expected, the ICE-G5 computation shows a strong latitudinal sensitivity to the water load, whose amplitude vary quite quickly from north to south with a negative trend of -0.52 m/deg (at 6 kyrs BP) and -0.35 m/deg (at 4 kyrs BP) in the latitude range of about hundred kilometres in length. ANU05 predictions show a steeper gradient compared with ICE-5G RSL profile at 6 kyrs BP despite a low latitudinal sensitivity shown in Figure 6.13. However, the offset of ESL between 6 kyrs and 4 kyrs assumed by ANU05, is around 1 m, thereby insufficient to obtain a RSL spatial variations and a middle Holocene highstand in the south Tunisia. If the levering effect is excluded from the relative sea-level computation, the low gradient shown by ice load frames (c and d of Figure 6.14) produces steeper RSL curves in south Tunisia while the relative sea-level curves of NE Tunisia remains the same. Finally, we estimate that the levering effect process contributes to an ongoing sea-level change of +1.5 m during the middle Holocene and +0.5 m at 4 kyrs BP for the ICE-5G model.

6.7.5 RSL variations induced by coast geometries

A third factor that could affect the sea-level in SE Tunisia is the shape of coastlines. The shape of the coastlines alters the predicted RSL curves at local scale since this factor tunes the amplitude of the continental levering effect. Lambeck and Nakada (1990)

Table 6.3: Calculation of RSL trend from relative sea-level data for site along the Tunisia coast. The trend lines are shown in Figure 6.14.

Ice Model	Load Surface	Time kyrs	Trend a	σ
ICE-5G	Ocean Load	4	−0.353	0.02
		6	−0.518	0.01
	Ice Load	4	−0.353	0.3
		6	−0.353	0.58
ANU04	Ocean Load	4	−0.221	0.70
		6	−0.524	0.80
	Ice Load	4	−0.169	0.30
		6	−0.304	0.47

demonstrated that because of the irregular shape of coastlines and because of the existence of shallow coastal shelves, the loading of the sea floor by the rising sea during deglaciation is regionally quite variable and capable of producing different RSL highstand amplitudes. For example they found at Karumba, in the southeast corner of the Gulf of Carpentaria (Australia), a highstand much enhanced compared to Rockingham Bay (north-east coast) due to the gulf geometry. However the sensitivity of coastal sector upon the morphologie-induced RSL variations was not investigated and as Lambeck and Nakada (1990) conclude, this issue is poorly understood.

To estimate upper and lower bounds of the El Grine site GIA response to the gulf geometry, we have solved the sea-level Equation for various " virtual" sites across the the Gulf of Gabes. The " virtual" sites are placed along two transects (Figure 6.15) oriented north-south and west-east respectively, between the continent and off shore of Gabes Gulf. In the following computations the ice model and rheological profile related to ICE-5G model are included and fixed shorelines were taken into account. As shown in Figure 6.16, both north-south and west-east transects show the same pattern of RSL curve characterized by a knee at 4 kyrs BP that marks the end of deglaciation, or rather the end of Antarctica ice melting. As shown in Figure 6.16, the GIA response reveals a clear patterns of RSL change across two transects that strongly depend upon the relatively locations of " virtual" sites to the centre of basin. In particular, the colour shade of curves from black to gray indicates the tendency to reduce the emergence of relative sea-level, vanishing with the shift of the " virtual" site to seaward were the site responds to ocean

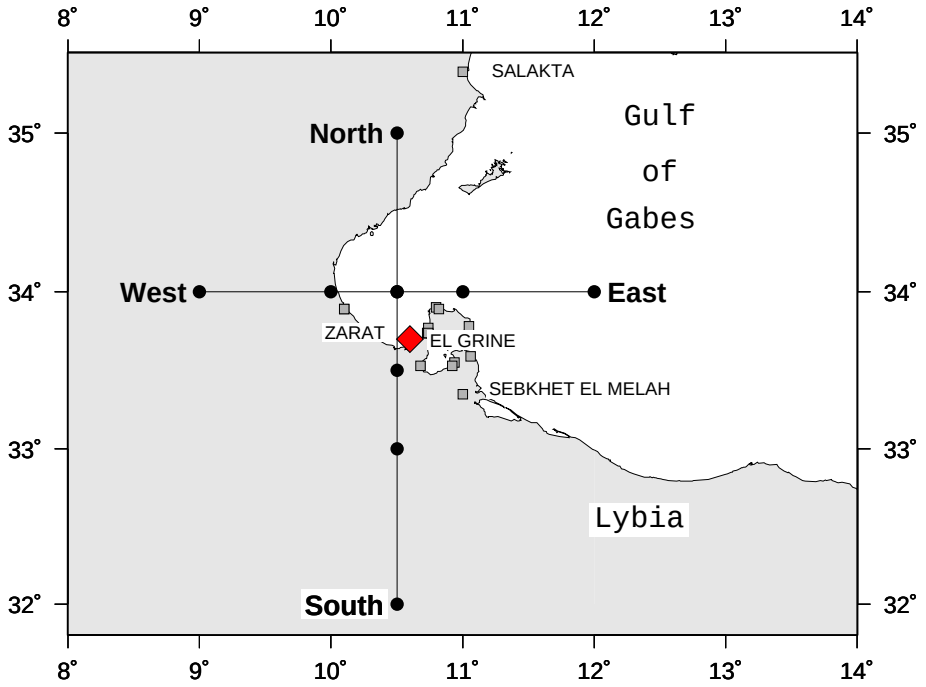

Figure 6.15: Location map of the " virtual" sites placed along the north-south and west-east transects across the Gabes Gulf.

loading like an island. The predicted highstand in Gabes Gulf is within a range between 1.3 and 0.3 m. The largest highstands is found in westward and southward land observers with in excess of about one meter, while submergence is predicted in the area located at high latitude or eastward. The regions of emergence and submergence are separated by transition zones in which the sea-level nearly follows the eustatic curve.

Our finding support previous observations by Stocchi and Spada (2007) who have emphasized the importance of spatial variations of GIA component in the Mediterranean area. In agreement with their computation, we find that hydro–isostatic component of GIA determines the submergence of central Mediterranean sea and a significant change of highstand amplitude when coastline geometry is concave. Moreover the inspection of Figure 6.16 shows that onshore with distance from the coast the amplitude of highstand tends to increase and the virtual sites respond to ocean loading like a continent. In the case of El Grine site the pattern of RSL curve suggests that the cost of SE Tunisia respond to ocean loading like a continent. In the case of El Grine site the pattern of

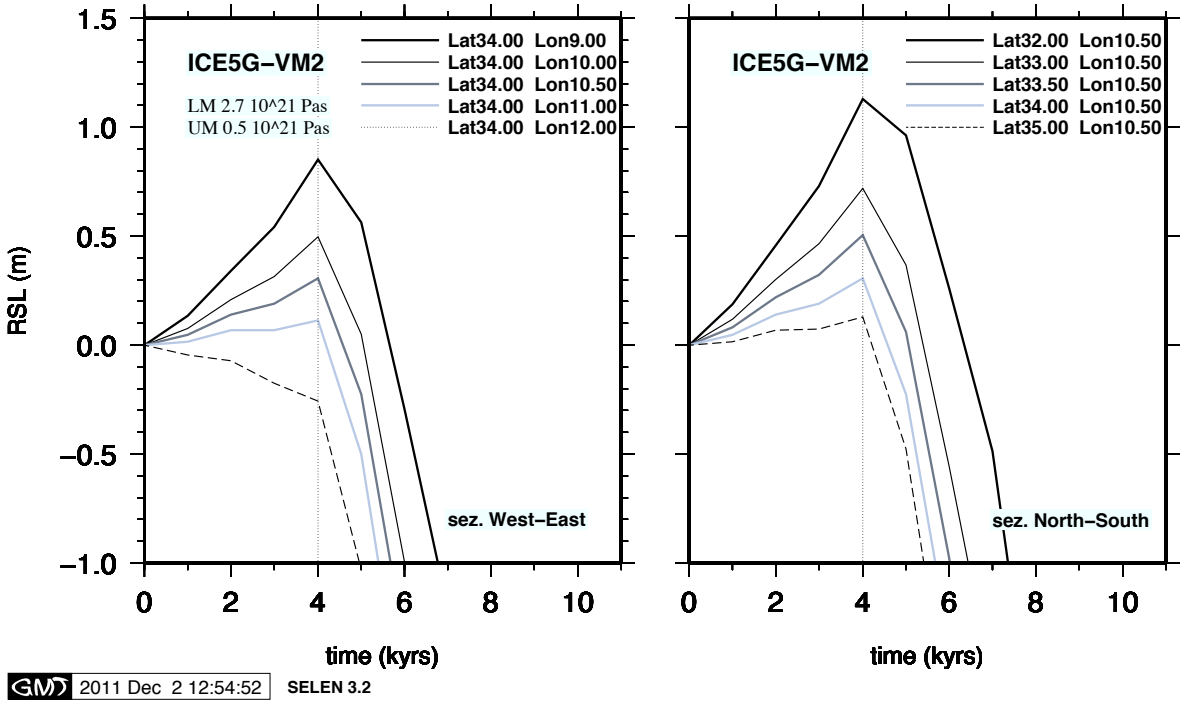

Figure 6.16: RSL curve of " virtual" sites placed along the north-south and west-east transects. Both north-south and west-east transects show the same pattern of RSL curve characterized by a knee at 4 kyrs BP that marks the end of deglaciation.

RSL curve suggests that the cost of SE Tunisia response as a continent as well. We explain this pattern because gulf geometries such as the one of the Gabes gulf increases the distance between the centre of the basin and the continental margin, thus causing a differential deformation between the bulk of basin and its margin. However, this differential deformation should be closely linked to the viscosity of the lower mantle. In the closed basin like the Mediterranean the basin orientation is extremely important as morphological control on the performance of the levering effect. In particular, the gulf of Gabes investigation demonstrates that the sites showing significant emergence of sea level are those located approximately normal to the axis of the basin inside the bay.

6.7.6 Sensitivity to the melting history of late Pleistocene ice sheets

The SE Tunisia sites lie within far field with respect to the ice sheets of the LGM (Lambeck and Purcell, 2005). Within this location, sea-level change is dominated by

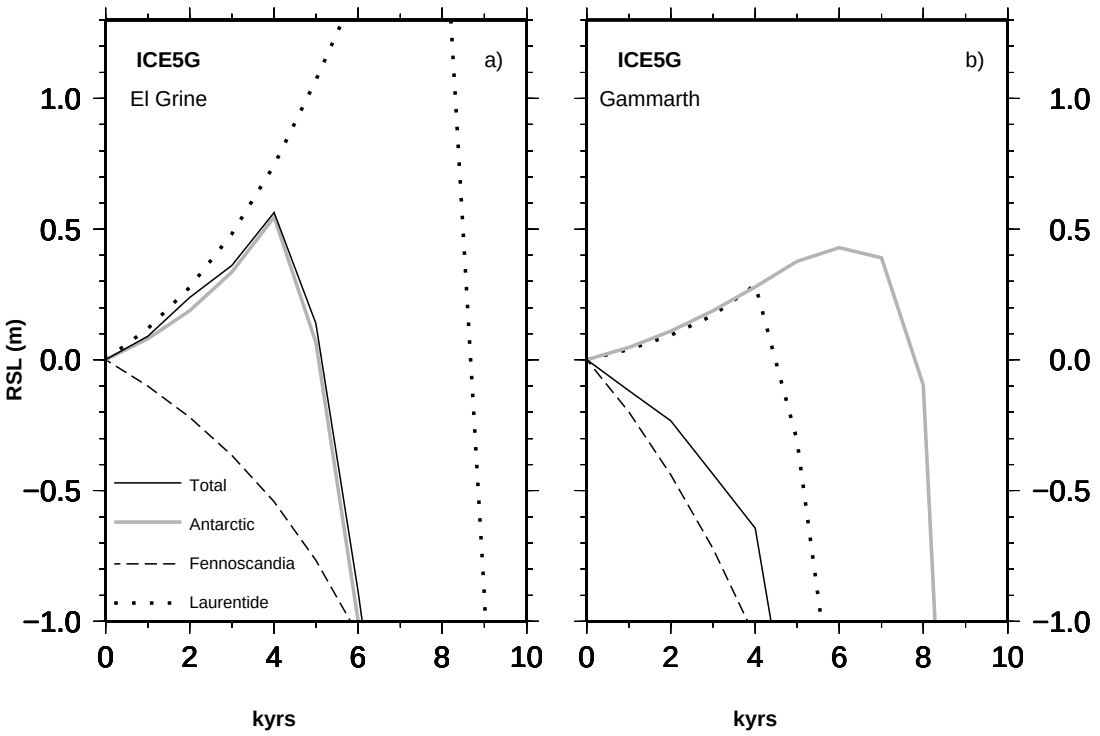

Figure 6.17: Contributions to RSL change due to the most important individual components of the ICE-5G global ice model at El Grine (SE Tunisia) and Gammarth (NE Tunisia)sites, see Figure 6.2

water loading due to the addition of meltwater to the ocean basins. The raised beaches evidenced along the SE Tunisia are mainly sensitive to temporal variations of the total volume of late Pleistocene meltwater and of melting history of each ice sheet source. In order to examine the sensitivity of the SE Tunisia sea-level predictions to the different ice sources we compare sea-level curves based on the two available ice global models that take into account the history of each ice source component of last glacial period. Here we consider individual contributions from the major late Pleistocene ice sheets: Laurentide, Fennoscandian, Antarctica, and ignore other minor constituents. In particular we employ the Laurentide, Fennoscandian and Antarctica components of the ICE-5G and ANU05 global ice models and the results obtained are shown by the dotted, dash and solid lines in Figures 6.17. and 6.18.

The diagrams in Figure 6.17 reveal that, for the last 6 kyrs, Antarctica ice component is responsible for the knee behaviour of the RSL curves both at El Grine and Gammarth sites. Two features are noticeable. First, the pattern of RSL curve based on Antarctica ice component reproduces the shape of RSL curve based on the

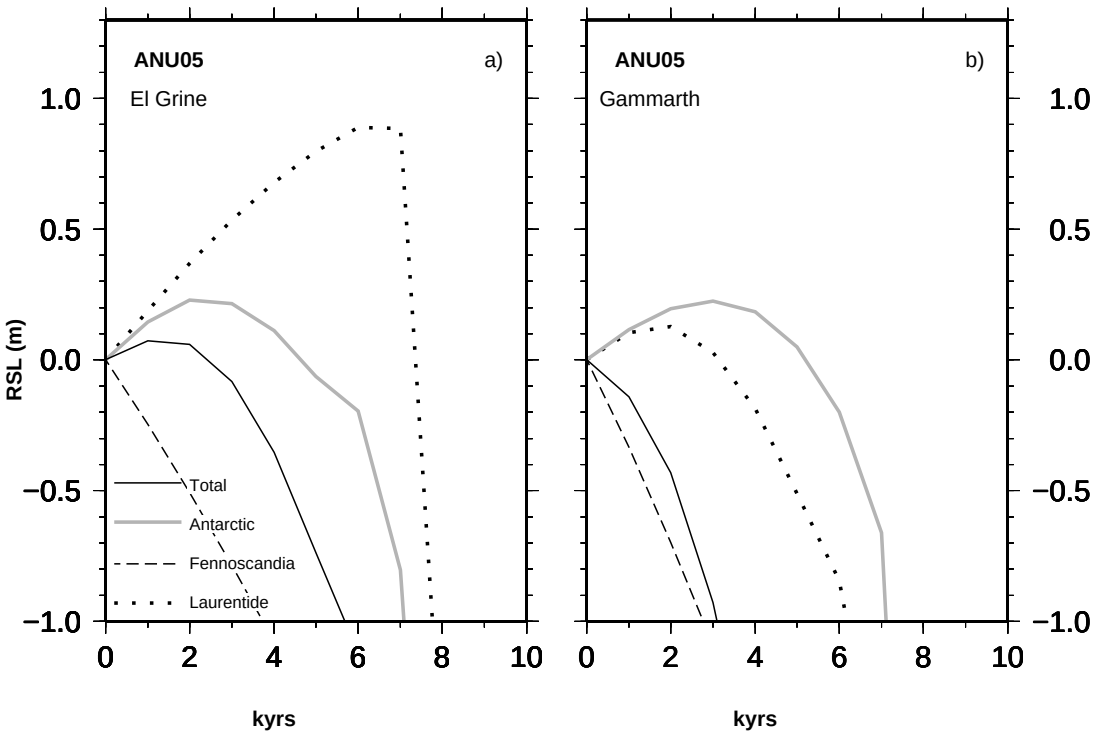

Figure 6.18: Contributions to RSL change due to the most important individual components of the ANU05 global ice model at El Grine (SE Tunisia) and Gammarth (NE Tunisia) sites, see Figure 6.2

total ice model ICE-5G at El Grine site. Second, for the Gammarth site, Antarctica ice component increases the amplitudes of RSL curve and thus fails to reproduce the slow and monotonous sea level rise produced by the total ice model ICE-5G. Third, the pattern of RSL curve based on Fennoscandian ice component reconciles more than two others ice components the RSL , based on the total ice model ICE-5G at Gammarth site. These observations indicate that the RSL curves at Tunisia sites are mostly determined by the chronology of the individual ice source deglaciation model. In particular, the El Grine site and in general the SE Tunisia are located at a distance such that Laurentide and Fennoscandian RSL predictions cancel each other with the result that SE Tunisia is sensitive to melting history of the only Antarctica ice sheet. This agrees with the recent results of Stocchi et al. (2009) who estimated a Tunisia RSL change driven apparently by Antarctica ice sheet during the middle Holocene. They still observed a substantial cancellation of the effects of North America and Fennoscandia using models ICE3G (Stocchi and Spada, 2007) or ICE1G+A3 (Stocchi et al., 2009). Instead the Gammarth site and in general, the NE Tunisia is more sensitivity to melting history of Fennoscandian

ice sheet. The peculiar character of Tunisia potentially provides information for testing the isostatic models and allows us to reassess their use as RSL far field site to constrain the history ice sheet of Antarctica and Fennoscandia respectively for the last 6 kyrs.

When the ANU05 is considered instead (Figure 6.18), the curves based on each ice sheet component clearly show the same broad pattern of RSL curves based on ice-sheet components of the ICE-5G ice model ANU05 at El Grine site but with significantly smaller amplitude. In Gammarth the offset between ANU05 and ICE-5G predictions reflect differences in the chronology of the each ice sheet component. For the El Grine site, the RSL variations seems to be sensitive to the ice sheets timehistories of relatively nearby Fennoscandian component also that causes a smoothing of the final RSL curve (dotted line). However there is quite an agreement between the pattern of RSL curve based on Antarctica ice component and RSL curve based on the total ice model ANU05 at El Grine site. When recalling Figure 6.14, the peculiarity of the two sites considered in Figures 6.17 and 6.18, allows to establish, a latitudinal limit located around the 36^o degree of latitude, to the north of which the RSL predictions are affect by Fennoscandian ice sheets and to the south of which which the Antarctic ice sheet becomes the predominant component of the RSL predictions.

6.7.7 Two modified Antarctic ice sheets models

In the previous section we have noticed that the observed middle Holocene sharp highstand in SE Tunisia could be dominated by the history of melting of the Antarctic ice sheet, since contributions to relative sea-level from the two major northern hemisphere ice sheets (Laurentide and Fennoscandia) have have similar magnitudes but opposite signs. Moreover we have grounds to believe that the that the middle Holocene highstand along the SE Tunisia coast records an impulsive melting event.

In order to test the hypothesis of a delayed and rapid deglaciation of the Antarctic ice sheet, we compare predictions based on two plausible scenarios of Antarctic ice sheet chronologies component with the sea-level observations described in Section 6.5.1. The original Antarctic component comes from ICE-5G and ANU05 respectively. To examine the pattern of the RSL curve at El Grine and others Tunisia sites we alter the original scenario by forcing the end of Antarctic deglaciation to 6 kyrs ago. Evidence that supports this choice comes from the debate about a second meltwater pulse (MWP2). Blanchon and Shaw (1995)note that several Caribbean reefs appeared not to have been

able to keep pace with rapid rates of sea-level rise around 7600 years ago and interpret this as rapid and abrupt RSL rise due to a meltwater pulse. Moreover observations from Singapore (Bird et al., 2007) from the Baltic Sea (Yu et al, 2007) and Indo-Pacific region (Woodroffe and Horton, 2005) add further evidence for a rapid rise prior to reaching present level around 7500 years ago. In the original computation of ICE-5G the maximum extent of the Antarctic ice sheet is attained around LGM and remains constant until 12 kyrs. The major deglaciation occurs occurs around 11 kyrs and end at 4 kyrs contributing to a total equivalent sea-level (ESL) of 18.27 m (Figure 6.1).

ANU05 assumes a 25.18 m ESL contribution of the Antarctic between 30 kyrs and 2kyrs. The 7 m difference of ESL represents the ESL contribution released by ANU05 between 25 kyrs and 18 kyrs (Figure 6.1). The time-history considered by ANU05 for Antarctica component is characterized by a strong event of melting between 12 kyrs and 10 kyrs (like window time of MWP 1a) and next gradual phased of melting up to the present with about 2-3 m of sea-level rise occurring in the past 6000 years. In the previous chapter (Chapter 5) we showed that an eustatic sea-level rise more than 1-2 m during the last 6 kyrs alters the predicted RSL curves of Lazio and Marche RSL sites. Moreover here we note that this scenario, reduces the dominance of ocean syphoning at El Grine site in a manner such that isostatic adjustment predictions become incompatible with the observational data. In the following the modified Antarctica component of ICE-5G is denoted by A1IS (Antarctica 1 Ice Sheet) and the modified Antarctica component of ANU05 is denoted by A2IS. The ice element distribution is the same of the originals ice models. The sea-level predictions associated with these two MWP2 scenarios coupled to the viscosity profiles VM2 and nominal models. Note that predictions are shown only for the past 10 kyr. As shown in Figure 6.19 and Table 6.4 different results are obtained when the two Antarctic chronologies (A1IS, A2IS) are implemented in ICE-5G and ANU05. To explain amplitude and timing of SE Tunisia sea-level highstand, the Antarctic ice sheets must have melted abruptly and not continuously over the past 6 kyrs as Lambeck and Nakada (1990) and Lambeck and Purcell (2005) proposed. The local sea-level curves at the EL Grine site reflect the end of a catastrophic event. In particular the A1IS scenario predicts a sudden melting between 7 and 6 kyrs of 3 m of ESL which is responsible for the rise of the RSL above modern sea level at 6 kyrs BP at the El Grine site The A2IS, modified Antarctic chronology of ANU05, is characterized by a sudden melting between 7 and 6 kyrs of 4 m of ESL that is responsible for the highstand of 1.3 m at El Grine site.

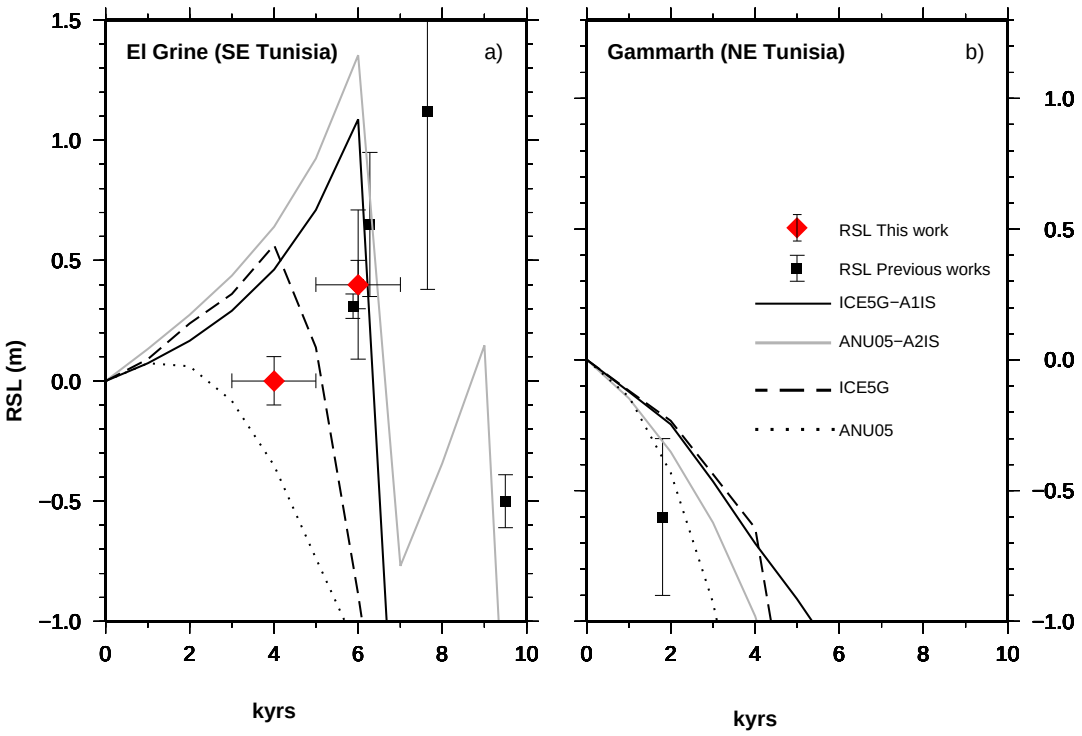

Figure 6.19: Contributions to RSL change due to the most important individual components of the ICE-5G global ice model at El Grine (SE Tunisia) and Gammarth (NE Tunisia)sites, see Figure 6.2

When ANU05+A2IS ice chronology (gray lines in Figure 6.19 is considered the predicted middle Holocene curve shows a highstand one magnitude higher then the original ANU05 chronology. As we expected, the impact of the modified Antarctic ice chronology is barely appreciated around the NE Tunisia (e.s. Gammarth in Figure 6.19) fot both models. In qualitative agreement with the result obtained for the middle Holocene highstands, chronologies ICE-5G+A2IS (black lines) and ANU05+A2IS (gray lines) do not improve the fit with the late Holocene stationary sea-level and with the site placed in the NE side of Tunisia. This revised melting history for Antarctica is not consistent with the observations of paleo shorelines at 0 m msl that points to sea-level having reached its modern level around 4kyrs BP. However the rate of sea-level fall between 6 kyrs and the present suggest to shift the catastrophic event before 7 kyrs.

The same issue has been discussed by Stocchi and Spada (2007) who acknowledged the potential contribute of the RSL indicators on the coast of Tunisia to constrain the time history of Antarctica in the last 6 kyrs. Using the available RSL indicators of Jerba Island they tested ICE-1G, ICE-3G and and ICE-5G ice global models coupled with VM1

Table 6.4: Observed RSL at the El Grine sites (elaborated in this study) and Gammarth site obtained by (Anzidei et al., 2010), compared with predicted RSL based on GIA models considered in this study. Units are m throughout.

			El Grine1	El Grine2	Gammarth
RSL Indicators			$0.4 \pm 0.1m$	$0 \pm 0.1m$	$-0.58 \pm 0.3m$
age (kyrs) BP			6 ± 0.5	4 ± 0.5	1.8 ± 0.05
Ice Models	ICE-5G-VM2	FS	-0.88	-0.167	0.21
		VS	0.27	1.22	-0.075
		A	-0.99	0.58	0.083
		A1 IS	1.086	0.49	0.072
	ICE-5G+A1IS		1.08	0.46	-0.24
	ANU05-nominal	FS	-1.12	-0.80	-0.37
		VS	-1.70	-0.46	-0.34
		A	-0.19	0.147	0.123
		A2IS	1.52	0.76	0.18
	ANU05+A2IS		+0.40	-0.04	-0.19
	8.2E	SGC-FS	0.04	-0.03	0.0
	ICE-5G+8.2E	FS	-0.84	-0.164	0.21
	ANU05+8.2E	FS	-1.08	-0.77	-0.37

rheological profile. They found that ICE-3G and ICE-5G reproduced the field observations better than ICE-1G but not well, although ICE-1G includes only the Northern hemisphere ice sheets. However, ICE-3G includes an Antarctic ESL contribution of 25 m since 18 kyrs, unlike ANU05 which assumes this to happen already after 30 kyrs.

However, ICE3G includes an Antarctic ESL contribution of 25 m since 18 kyrs, unlike ANU05 which assumes this to happen already after 30 kyrs. Moreover Stocchi and Spada (2007) tested a suite of plausible scenario for the melting of Antarctica, incorporating this within ICE-3G. They conclude that a sensibly reduced ESL at the LGM (ESL 14m at 21 kyrs BP) and a time-history characterized by a constant rate between 12 and 5 kyrs allow to produce the highstand observed at Jerba island. However the off set of ESL (4 m) between the ESL suggested by Stocchi and Spada (2007) and the ESL included within ICE-5G (Peltier, 2004) for the Antarctica ice sheets remain a weakness. In agreement with our work Stocchi and Spada (2007) reject the idea of a delayed a delayed melting phase of the Antarctica ice sheets, a hypothesis that was supported by Lambeck and Nakada (1990) due to systematically overestimates of RSL observations on

the Tyrrhenian and Adriatic coast.

6.7.8 The 8.2 kyrs event

Peltier (2005) believes on the basis of ICE-5G model results that the Laurentide ice sheet and other northern hemisphere continental ice components are the source for MWP-1a while the melting of the Antarctic ice sheet triggered MWP-1b. As show in the Figure 6.11 the melting chronologies of ICE-5G model allow to predicted the highstands in El Grine zone but the peak is shifted from 6 kyrs by 2 kyrs to 4kyrs. In contrast we find no explicit reference about the inclusion of others catastrophic sea-level rise events such as the 8.2 kyrs event or the MWP2 events into ICE-5G model. For this reason in this section we modified the ice model chronology to include the melting chronologies of lakes Agassiz and Ojibwai that should have been responsible for the 8.2 kyrs event. We compute the sea-level pattern or fingerprints associated with the the 8.2 kyrs event by solving the Sea-Level Equation. The predictions are based on the reference Earth viscosity model mentioned in Section 6.5.2. Considering the distance of the Mediterranean from the margins of the lakes Agassiz and Ojibwai, the GIA process associated with ice unload should not affect the RSL predictions fo our far field sites. We have modelled this ice sheet using a single element with disc shape of circular crosssection having an half–amplitude of 10^o and a variable thickness between 27 m and 128.5 m. This simplification implies a range of error within 0.1 m as suggest by Spada et al. (2010, subm.) analyzing the fingerprints in the remote far-field site comparing different spatial ice-mass distribution of Greenland Ice Sheets. Evidence in support of the chosen ESL for melting chronologies of lakes Agassiz and Ojibwai comes from Kendall and Mitrovica (2008). The geographical coordinate of centre of disc corresponds to colatitude 31.81 and longitude 280.00 respectively. Moreover the size of disc allows to border the paleo margin of the combined proglacial Lake Agassiz-Ojibway. The ice-lakes stored the total amount of water between the LGM (18 kyrs) age and 9 kyrs. After this, the ice model that we call 8.2E injects all the water stored within the within the time frame of 9-8 kyrs.

Figure 6.20 shows the extreme scenario of the sea-level fingerprint associated with the drainage of 8.2E ice model characterized by the maximum melting water volumes (5 m ESL) at 6 kyrs BP.

In the near field the negative sea-level signal is a results of the geophysical components of GIA: the gravitational attraction of mass (ice and water) decrease until it

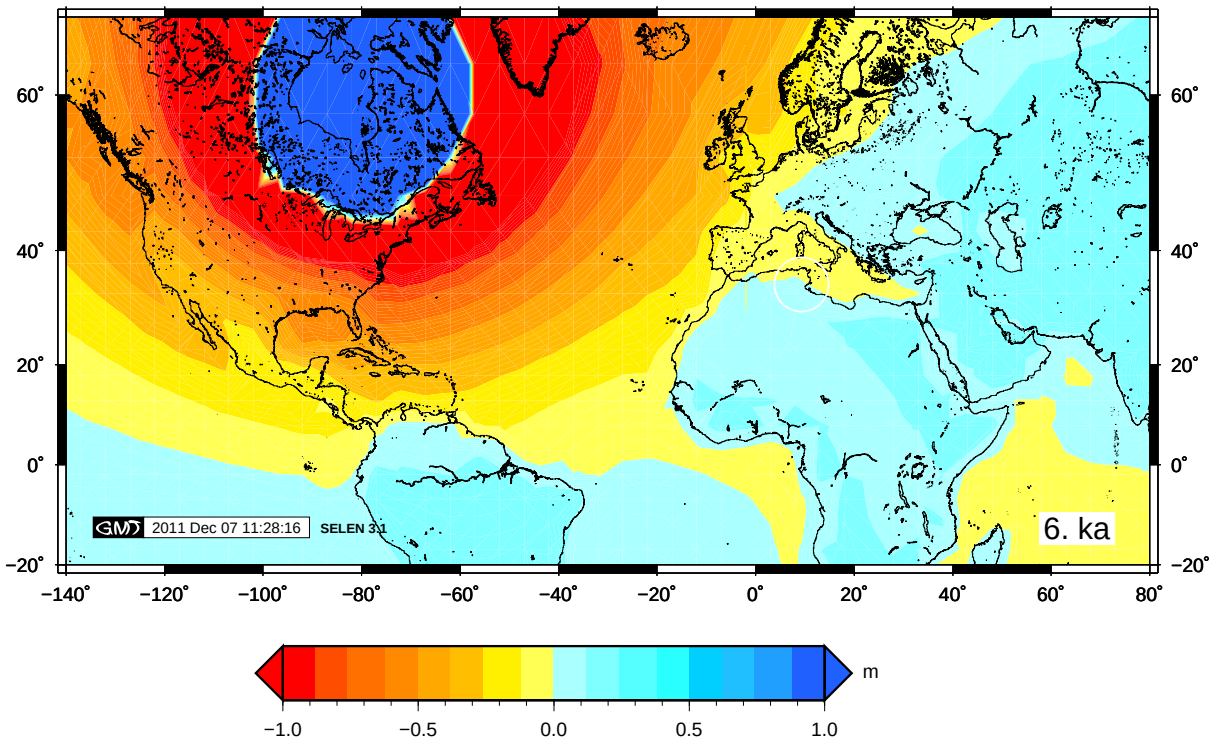

Figure 6.20: Relative sea-level fingerprint across the America, Europe, North Africa associated with the 8.2E melting scenario at 6 kyrs BP. The white circle marks the southern Tunisia sites where the blu color shows the peculiar zone of predicted sea-level rise.

disappear and the Earth surface tilt in order to reach a new isostatic equilibrium. As one move progressively further away from the the lakes, the predicted sea-level rise increase, eventually exceeding the eustatic value. At the El Grine field site the sea-level fingerprints related to 6 kyrs BP has a value of 0.04 $\pm$0.01 m. The sea-level error came from the prediction obtained testing several melting water volumes. Thus the RSL predictions related to the 8.2 kyrs event is one order of magnitude lower than the RSL predictions obtained with ICE-5G-VM2.

This investigations reveals that the small ESL change induced by the 8.2 kyrs event does not produce high enough RSL variation enough to explain the middle Holocene highstands at El Grine area. It is more plausible that the misfit between ICE-5G predictions and RSL observations evidence within the Section 6.7.2 reflects the poorly constrained ice chronology and of the total amount of equivalent sea-level stored within Antarctic ice sheets for the last 6 kyrs.

We note also that the Gabes Gulf remain a peculiar area to constrain the levering effect mechanism. as shown by the blu zone along the SE Tunisia in Figure 6.20.

6.8 Conclusion

We have investigated the deposits outcropping along the coast of Gabes Gulf (SE Tunisa). In particular, we have provided new evidence of middle Holocene highstands and and provided a discussion on the impact of viscoelastic rebound onTunisia sites. Our results can be summarized as follows.

i) The sedimentological, morphological, microfacies and chronological analysis allow to recognize two different formers of paleo sea-level along the coast of Gabes Gulf, in particular in El Grine area. First relative sea-level was at least $+0.4 \pm 0.1$ m msl higher than present at the time between 5 kyrs and 7 kyrs BP. The second and early relative sea-level having reached the modern sea level about 4000 yr BP. The second paleo sea-level testified that sea level reached its present position (and maintained it) around 4000 years ago. These indicators provide for the first time evidence for a RSL fall and hence complete the Holocene RSL history of this coast. The two paleo -sea-level indicated that the postglacial rise of sea level took place in one phase of rapid rise until ∼6000 BP and a second phase of near stability with minor oscillations of sea level.

ii) The emergence that took place between about 7000 and 5000 years BP it cannot be ascribed to tectonics but is related to GIA effect.The magnitudes and patterns of GIA models results, suggested that hydro-isostatic effect through the continental levering mechanism, is the dominant contributor to the shape of RSL curves. The GIA effect based on ICE-5G (VM2) indicated an RSL above the present around 4 kyrs while the observations recorded an highstand shifted back of about two thousand years at around 6 kyrs BP. In contrast no sea-levels higher then present are predicted by ANU05. Substantial improvement of sea-level curve predictions it is obtained when we include the shorelines migrations on the computations of the Sea-Level Equations using ICE-5G (VM2) and ANU05-nominal Earth model.

iii) GIA effects through the glacio-isostatic and hydro-isostatic components, act in different manner at spatial scale along the coast of Tunisia region, especially for RSL predicted by ICE-5G (VM2) scenario. The sites situated south of 36^o degree latitude experience a sea level higher than the eustatic value while at sites north of 36^o degree of latitude, the sea-level change underwent a RSL signal lower than eustatic signal. The

peculiarity of the two sites, representative of north and south area of Tunisia coast, allowed to establish a latitudinal limits located around 36^o, a limit within which the RSL predictions are affect by Fennoscandian ice sheets and beyond which the Antarctic ice sheet becomes the predominant component of the RSL predictions. If the levering effect is extracted from the relative sea-level curves of theTunisia sites, the RSL curves in SE Tunisia flatten while the RSL curves of NE Tunisia remain the same. In the case of the El Grine site the pattern of RSL curve suggests that the coast of SE Tunisia responds as a continent as well. We explain this trend emphasising that the basin orientation is extremely important as morphological control on performance of well-developed highstand during the middle Holocene. The pattern of the sea-level curve at El Grine site produced by the Fennoscandian ice component is nearly identical but with opposite trend to the RSL prediction of Laurentide ice component. This means that SE Tunisia sites are located at a distance such that Laurentide and Fennoscandian RSL predictions cancel each other out, and that SE Tunisia sites is sensitive to melting history of Antarctica ice sheet. We find that to explain amplitude and timing of SE Tunisia sea-level highstand, the melting of theAntarctic ice sheet may be characterized by a catastrophic melt pulse event and not by a constant increase of ocean volume for the past 6 kyrs as proposed (Lambeck and Nakada, 1990; Lambeck and Purcell, 2005).

iv) We elaborated two plausible models for the melting of Antarctica during the last 6 kyrs: A1IS and A2IS. This models are modified models (for the last 6 kyrs) of Antarctica ice chronologies included within ICE-5G and ANU05 respectively. Both models are characterized by a catastrophic rise event between 7 and 6 kyrs, while differ in ESL. A1IS assumes 18 m ESL and A2IS assumes 25 m ESL. In qualitative agreement with the result obtained for the middle Holocene highstands, these models reconcile with our first RSL proxy. However the two plausible ice model chronologies, are not consistent with the observations of paleo shorelines at 0 m msl (our second RSL proxy).

vi) An assessment of a north hemisphere catastrophic event upon RSL curves of Mediterranean basin, reveals that the small ESL includes within the 8.2 kyrs event does not produce RSL variation enough to explain the middle Holocene highstands at El Grine area. Thus strengthens the hypothesis about the SE Tunisia as field sites to constrain the melting history of Antarctic ice sheet for the last 6 kyrs BP.

Chapter 7

Conclusion and final remarks

In the composition of this Thesis, we have followed the development of our investigations on sea level change processes during these three years. In particular, we have examined some geophysical consequences of melting of present and past ice sheets. All these analyses were based on the implementation of the sea level equation and on the analyses of the vertical displacement of surface of the Earth. The improved version SELEN program has been an important tool to solve the sea level equation. The sea level change process is controlled by several parameters. In Chapter 3 we focused on the analysis of the rheological ones. We have presented how a set of linear rheological models responses to the accretion of an ice sheet with simple geometry. Using ALMA program, we have illustrated the vertical and horizontal displacement field obtained by a set of rheological models, through the spectral and the spatial domain analyses. Spectral domain analysis, demonstrated that, at decadal and century scale, the presence of a low viscosity layer cause the largest departure from the purely elastic solution amongst rheological models taken into account. We have found, within analysis in spatial domain, that significant departures from the elastic solution are expected for many of the rheological models considered, at all the spatial scales. However we have found that the sensitivity of vertical deformation to shallow upper mantle rheology is considerably more complex at the ice sheet margin. In the context of global climate change, these results are relevant to regional sea level variations in response to present and future ice fluctuations.

In Chapter 4 we focused on some geophysical consequences of melting of present ice sheets. We have used together recently signals acquired by satellite mission and GPS, to provide indipend cross validation checks of model of ice melting at decades and millennia time scales. With regard to GrIS we have used the M3 mass balance (-240$\pm$28 Gt yr^{-1})

based on ICESat data in order to determine the regional and global fingerprint of sea level variations, vertical deformations of the solid surface of the Earth and variations of shape of the geoid. We have demonstrated that GrIS contributes with $\sim$+0.67 mm yr^{-1} to global sea level rise. At Mediterranean scale, we found that the current GrIS mass loss produces a sea–level rise of $\sim$ 0.5 mm yr^{-1}. We have developed a Fortran code that made us able to elaborate high-resolution regional elastic rebound model (RER), in response to current ice mass changes derived from ICESat mission. The RER model has been described in Chapter 4. We have demonstrated that improved estimates may have an impact on the interpretation of GPS data from stations located close to glaciers associated with rapid mass loss. This is well illustrated by the case study in Greenland (Section **??**) where the RER vertical uplift rate, based on ICESat data (M3 mass balance), predicts rates of vertical displacement locally as large as $\sim$ 15 mm yr^{-1}. We have combined the elastic component of vertical uplift with estimates of the viscoelastic displacement fields associated with glacial-isostatic adjustment (GIA), according to a set of published ice chronologies and associated mantle rheological profiles. Then we have compared the total deformation field with GPS observations. In notable contrast with past reports, we have shown that vertical velocities obtained by GPS data from five stations with sufficiently long records and from one tide gauge at the GrIS margins can be reconciled with model predictions based on the ICE-5G deglaciation model (Peltier, 2004) and the elastic rebound associated with the new ICESat-derived mass balance.

With regard to Antarctica we have elaborated a plausible mass balance in order to determine the regional and global fingerprint of sea level variations, vertical deformations of the solid surface of the Earth and variations of shape of the geoid. Assuming -100 Gt yr $^{-1}$, WAIS contributed with $\sim$+0.26 mm yr^{-1} to global sea level rise. At Mediterranean scale, we found that the current WAIS mass loss produces a sea–level rise of $\sim$ 0.3 mm yr^{-1}. Hence, based on our predictions, the total contribution of polar ice sheets to present-day sea level rise is about $\sim$1mm $^{-1}$ in agreement with previous results. We therefore found unsatisfactory the elastic rebound inferred by WAIS, and we believe that new developments of present day ice sheet model inferred by ICESat and or GRACE will allow to constrain the real trends of ice loss nowadays. The vertical velocity field derived from WAIS model produced a small amount of vertical displacement across the Antarctica, of about 0.2 mm yr^{-1}, value that underestimates the localized variable trend

shown by GPS sites. Observations of present-day rates of crustal motion across the Antarctica constrain both the response of Earth to surface mass changes and tectonic motions of the Antarctic plate. Considering the small component predicted by WAIS mass balance, we have compared vertical deformations based on competing GIA models with vertical velocities obtained by GPS sites located along the AIS. In agreement with previous results we have demonstrated that GIA effect represents the major cause of vertical deformation recorded by GPS. The NAP zone is an exception, and here, elastic deformation plays a important role. With the statistical analysis we have shown that in spite the best performing models ICE-5G, the misfit has a large value in the range of 10-50 that misrepresented the observations.

Spatial and temporal variations of the Holocene sea levels studied in this thesis provided important constraints on the melting history of the major ice sheets, and in particular on the melting of Antarctic ice sheet. In this study, we have examined the sea-level variations along the center of Italy (Chapter 5) and Tunisian region (Chapter 6).

Roman fish tanks were analyzed in term of archaeological sea level indicators for sea level change for the last 2000 years. The mean relative sea level obtained from the eleven archaeological sea level indicators of Lazio coastline is -0.45 $\pm$ 0.08 msl during the Roman Period. Sea-level observations also indicate a slow subsidence around Marche region with a rates of 0.38 mm yr^{-1}. Based on GIA analysis, we have shown that the pattern of sea level change across the Mediterranean, exhibits a relatively large water-load component which, at specific sites, might exceed the water-volume component. The interplay between these two components shapes the deformation pattern across the Mediterranean basin resulting in a Mediterranean sea level which deviates from the global eustatic sea level in both time and space. Sea-level comparison between observations and predictions based on a suite of *a priori* ice models, suggested that Pleistocene ice ended to melt at least around 4 kyrs BP in agreement with ICE-5G ice model scenario. Moreover we examined the sensitivity analyses of RSL to GIA effect using competing and available ice models. ANU05 models computed large range of predicted value because of unknown viscosity property of mantle within the area of interest. This approach failed to constrain the local GIA effect in the center of Italy. Reduce uncertainty required knowledge of regional rheological models. It will be possible when new knowledge of mantle viscosity will be obtained.

The sudy of coastal deposit of SE Tunisia have confirmed the existence of a sea-level highstand during the middle Holocene. The method used to investigate

beachrocks deposits included sedimentological analyses, diagenetic characterization of cement, stratigraphical reconstruction and chronostratigraphic analysis using OSL to date the sampling. Thus, these more accurate investigations allowed to indicate a former sea level at 0.4 $\pm$ 0.1 m above the present sea level dated $\sim$ 6000 years BP and a second former sea level at 0. 0 $\pm$ 0.1 m dated $\sim$ 4000 years BP. The emergence that took place between about 7000 and 5000 years BP it cannot be ascribed to tectonics but is related to GIA effect.The magnitudes and patterns of GIA models results, suggested that hydro-isostatic effect through the continental levering mechanism, is the dominant contributor to the shape of RSL curves. GIA analysis indicated that the highstand resulted by levering effect of continental margin. Moreover, in agreement with previous works we found that SE Tunisia sites are sensitive to melting history of Antarctica ice sheet. We have shown also that to explain the pattern and timing of SE Tunisia sea-level highstand, the history of Antarctic ice sheets may be characterized by catastrophic rise event between 7 and 6 kyrs. Including this rise event within ICE-5G and ANU05 we have found good agreement with the observed highstand. In contrast, any ice model reproduces that sea-level reached about its present position 4000 years ago as. With regard to the debate about the source of middle Holocene highstand, we have revealed that catastrophic events driven by north hemisphere until the middle Holocene, such as the 8.2a event, failed to reproduce the highstand in Mediterranean area and at local scale, failed to reproduce the highstand at El Grine site. Some interesting future work would be to use observable vertical velocity obtained by GPS and far-field RSL observations, such as the SE Tunisa sites, in combination, in order to constrain the Antarctica ice chronology.

Appendix A

Fish tanks measurements

A.1 Sarinola

Sarinola fish tank is located at Formia town, between the modern harbor and the seafront street. It has a rectangular shape with a length of 60 m and width of 30 m. There are three main basins subdividing the fish tank. The rhombus ponds are located inside the two later basins respectively. A third of the tank is now covered by the new seafront street. Remains of a thick outer protection mole, which must originally have been higher than the inner basin walls, has now been leveled at a height similar to that of the crepidini.

At this fish tank (Figure A.1), the most important of the measurements taken refer to the two *cataractae* (sliding grooves for sluice gates) and foot-walks (*crepidini*). Both *cataractae* show a double sliding groove and Sarinola is, with Odescalchi, the only fish tanks in Italy where both of them have been preserved. The first sluice gate was probably solid, to stop the incoming water. The second was probably a net or a sluice with small holes to allow the water and small fish to enter, but with holes not large enough for bigger fish to go out. These *cataractae* used to be at the upper part of the fish tank, especially at the levels of the tidal range. The part of the upper foot-walk best preserved from erosion (site F), is situated at -23 cm, while it was at -12 cm according to the measurements published by Schmiedt (1972) and at -12.6 cm according to Leoni and Dai Pra (1997). The best preserved part of the lower foot-walk (site Y) has been found at - 57 cm, consistent with the level published by Schmiedt (1972) (-60 cm). Such differences in elevation can be partly explained by very recent changes in the relative sea level. Leoni and Dai Pra (1997) specify that point M, a rectangular block of travertine, which has its upper surface at the same level of the lower foot-walk, is facing the eastern opening of the tank and is cut by two parallel grooves; point M is interpreted as the threshold of a

double sluice gate. A similar threshold may exist at N (-56 cm) and N' (-66 cm), which is an inclined block, with grooves. As it is facing an opening of the tank and at about the same depth of the lower foot-walk, it can be interpreted as the threshold of a sluice gate, meaning that the lower foot-walk could not remain dry. According to Leoni and Dai Pra (1997), from sites M and N-N sliding gates were going up, probably to the level of the outer wall or to that of the upper foot-walk, permitting to install small gates about 45 cm high.

At Sarinola there is an outer mole, thicker than the peripheral basin walls, that does not seem to have been mentioned in any previous map, which must have been built to limit the impact of wave action. Its presence also limited the impact of erosion. Its present elevation is often similar to that of the upper foot-walk, though exceeding it locally. It is possible that the levels of both the outer mole and the *crepidini* have been lowered to an unknown amount by erosion. The thresholds, being below the direct reach of waves have probably been less lowered by erosion than the foot-walk from where the top of the cataracta was worked. At the time of Jacono (1913) the top of the protected mole remained emerged slightly more than 30 cm at low tide, while the lower foot-walk along the walls of the two

The upper foot-walk parallel to the quay is 95 cm wide and its best preserved top was measured at about -20 cm, while the top of the best preserved part of other subdivision walls was measured at -12 cm. Morphological characteristics of the fish tank that give a precise measure of sea-level are: the walls of outer protection quay rising above present sea level representing the highest level of foot walks; the inner walls of 3 basins; the arches connecting the basins and the arches for producing shade. The bottom channels were usually built at the same depth of the tank. Around and outside the external walls, a lower step may be observed which is nowadays eroded by wave activity. Arches connecting the basins may also have been used to provide some shadow to fish. This kind of lozenge basins was almost at sea level at low tide. Assuming that the tide and the climate (wind, air pressure) in Roman times were similar to the present ones, cataracta at least 60 cm high would have been useful for an acceptable working of this fish tank, while a cataracta only 45 cm high, corresponding to the difference in level between the upper and the lower foot-walk, e.g. from -20 to +24 cm in relation to the former MSL, would have been exceeded by the tide levels by almost 200 hours per year and would have prevented influx of fresh sea water during 366 hours per year. For a 45 cm

high cataracta, the outer perimetric wall near N-N should have been lowered by erosion, like the surface of the outer protection mole, by at least 10 to 20 cm since Roman times. If this reconstruction is correct, the upper foot-walk has been affected by a similar lowering. On the other hand, with a 60 cm high, cataracta working e.g. between -25 and +35 cm, the frequency of flooding of the basins and of interruption of the sea-water influx would have been much more limited and acceptable, possibly implying a stronger erosion of the top of the basin walls with the top of the *crepidini* even slightly higher than the present sea level.

Nevertheless, there were as many as 15 openings between the basins and the sea, according to the map by Jacono (1913). If there was a gate at most of them (to be noted that the sites of sliding grooves mentioned by Schmiedt (1972) are different from those observed by Leoni and Dai Pra (1997), the number of gates may have counterbalanced a smaller height for each gate. At this point it should be taken into account that while the bottom depth was measured at about 1 m (Table 1), measurements approximately 40 years ago (Schmiedt, 1972) provide a depth of about 1.2 m, while at the time of Jacono (1913) it was about three meters deep, thus little above the average depth reported by Columella for this type of fish tank (i.e. 2.13 to 2.74 m). The thresholds with two parallel grooves exist at -56 to -66 cm at site N-N, facing the south eastern opening of the tank, and possibly the top of a 45 cm high gate had to be located near the present sea level. It seems that the wind direction fetch that could mostly affect the Sarinola fish tank corresponds to directions between 120o and 270o. These winds, that are the most capable to cause strong waves and surges at Formia, are clearly not predominant (about only one third of wind occurrences). Therefore, Sarinola fish tank is not normally affected by especially frequent strong wave and surge effects. In addition the Sarinola fish tank was not facing the open sea, but was relatively sheltered inside the dock of a Roman harbor (Ciccone, 1992). The threshold of site N, measured at -56 cm, indicates that sea level should be higher than this level. Assuming that the best preserved upper foot-walk (-23 cm) was constructed 35 cm above mean sea level, the former MSL could be estimated at about -58 $\pm$ 5 cm.

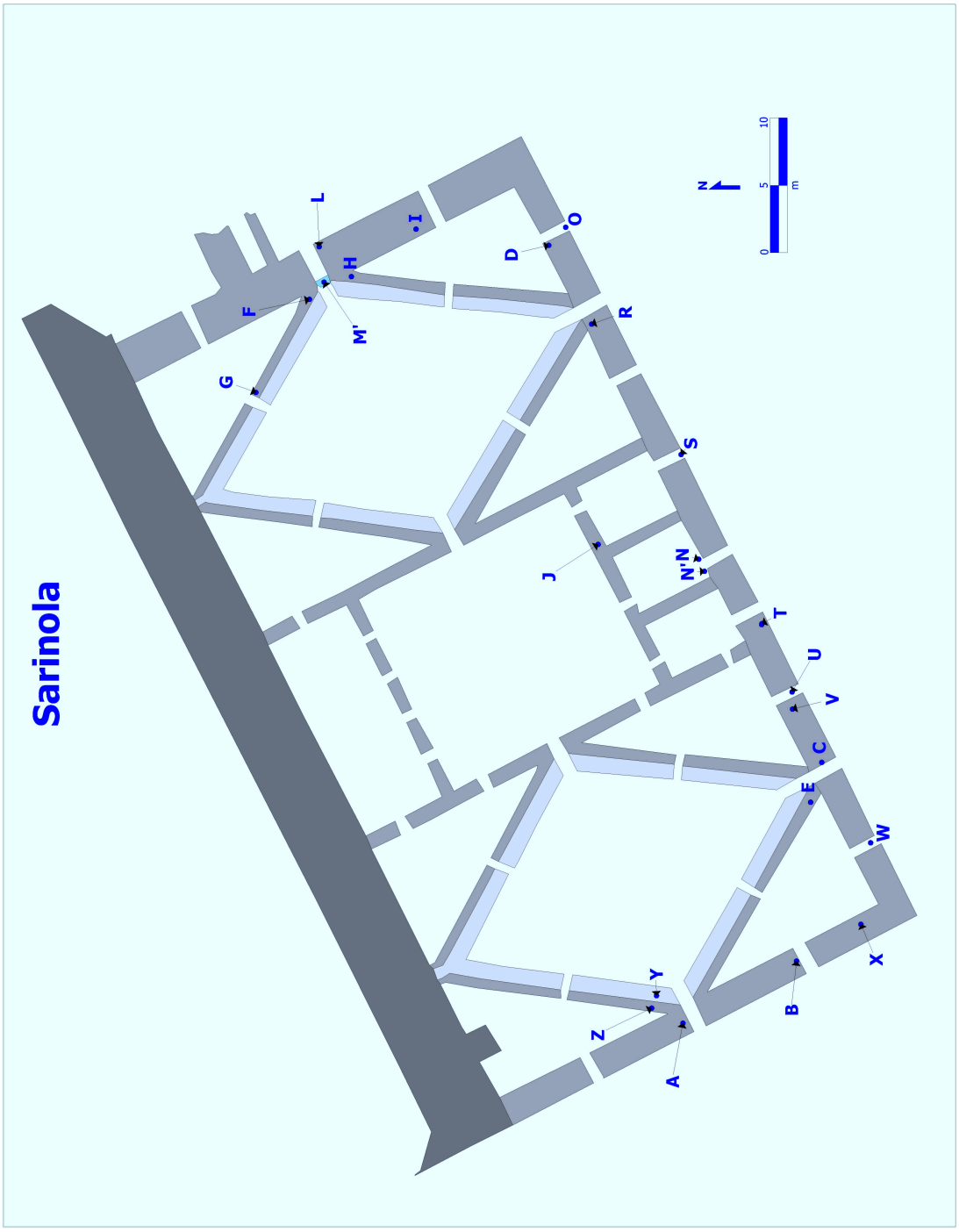

Figure A.1: Map of Sarinola fish tank. The letters refers to the measurements. See text for explanations.

A.2 Punta della Vipera

Punta della Vipera fish tank (Figure A.2) is located near Civitavecchia town, close to the ruins of a Roman villa. The shape is rectangular with dimensions of 48 m of length, 30 m of width and apparent present depth 1.77 m. The fish tank is protected on three sides by a quay 2-3 m wide, which may emerge 0.9 m in its best preserved parts, and includes a circular and many rectangular basins. Water comes through three covered channels, which arrive at -20 cm to the western quay (Schmiedt, 1972). At the outer breaker many rectangular small basins exist, probably used for the breeding of certain fish types or for mollusca culture. Such basins exist at site R and O and the depth of the basin is measured at -60 cm. The upper foot-walk parallel to the quay is 95 cm wide and its best preserved top was measured at about -20 cm, while the top of the best preserved part of other subdivision walls was measured at -12 cm. Morphological characteristics of the fish tank that give a precise measure of sea-level are: the walls of outer protection quay rising above present sea level representing the highest level of foot walks; the inner walls of 3 basins; the arches connecting the basins and the arches for producing shade. The bottom channels were usually built at the same depth of the tank. Around and outside the external walls, a lower step may be observed which is nowadays eroded by wave activity. Arches connecting the basins may also have been used to provide some shadow to fish. This kind of arched channels have been measured at site B (-24 cm) and M (-19.5 cm) for the top-foot-walk of the arch and at site A for the internal part of the arch (-69 cm). According to Schmiedt (1972) the top of the channels should have remained emerged during the highest tides. In fact, he assumes that the top of the channels should be at a level of 40 cm above the former MSL in order to allow the fish tanks maintainers to reach the entrance of the outer channels into the fish tank basins also during storms. The upper foot-walk was measured at various sites and it seems that for the outer part of the fish the best preserved one is site C at -20 cm, while the circular foot-walk is higher (e.g. site J, at -12 cm) because it is less exposed to erosion by wave activity. Assuming that the upper foot-walk was at 20 21 the same position related to MSL along the site, then the difference between the best preserved upper foot-walk of the outer and circular part, suggest that has been eroded by at least 8 cm since its construction.

The lower foot-walk (e.g. site K) is located at -79 cm. Along the wall between sites N and N there is a lower step at 40 cm below sea level, from which another arch, arched channels have been measured at site B (-24 cm) and M (-19.5 cm) for the top-foot-walk of

the arch and at site A for the internal part of the arch (-69 cm). According to Schmiedt (1972) the top of the channels should have remained emerged during the highest tides. In fact, he assumes that the top of the channels should be at a level of 40 cm above the former MSL in order to allow the fish tanks maintainers to reach the entrance of the outer channels into the fish tank basins also during storms. The upper foot-walk was measured at various sites and it seems that for the outer part of the fish now covered by sand, of 35 cm height was used to bring water to the nearby basin. Different papers propose a different sea level rise which ranges from 0.4 m to 1.28 m. According to Schmiedt (1972) RSL was estimated at -0.65 m based on the observed level of sluice gate (-0.25 m) and the 0.40 m estimated to let walking on, while according to Pirazzoli (1976 a, b) the RSL has been estimated at -0.45 m assuming that the slab covering the channels was emerged at high tide. Leoni and Dai Pra (1997) deduced from the elevation of the top of the arched channels (that they measured at -64 cm) a RSL of at least -44 cm and from the circular foot-walk (that they measured at -12 cm) a RSL of maximum 32 cm. Lambeck et al. (2004a) estimated RSL at -0.40 m according to previous works while Lambeck et al. (2004b) estimated RSL at -1.280.20 m according to the range between the bottom and upper level of an unspecified sluice gate. The internal part of the top of the arch could be considered as a threshold. The top of the arch i.e. at -19.5 cm is coinciding with the upper foot-walk so it should be slightly above the sea level. With the best preserved foot-walk at -12 cm, assuming it was constructed 35 cm above MSL, one may deduce a former MSL at about -47$\pm$5 cm.

Figure A.2: Map of Punta della Vipera fish tank. The letters refers to the measurements. See text for explanations.

A.3 Torre Valdaliga

The Torre Valdaliga fish tank (Figure A.3) is located along the Aurelia Street, near a power station where the Valdaliga tower still exists, built in 1616 by Paolo V. The fish tank of Torre Valdaliga, cut into the rock, is located in front of a Roman villa (republic age; Augustan age, 50-27 BC) which is destroyed nowadays. The Torre Valdaliga fish tank has a rectangular shape with dimensions of 39 by 19 m. The fish tank is connected to the sea through three channels that are now sunk by 0.5 m of water near the tank and 0.6 m and 0.7 m moving toward the sea. Several small basins exist along the west side of the fish tank. Close to the channels, are situated cataracts used for fishing.

Morphological characteristics giving a precise estimation of palaeo sea-level are the grooves, the foot-walk and the wave cut platform. Many measurements have taken place along the fish tank and it seems that the best preserved foot-walk is located at site I (-5 cm), while the best preserved wave cut platform is located at -9 cm. Schmiedt (1972) noted that this is a rare example of fish tank completely cut into the rock because, according to Columella (R.R. VIII, 17: *vel exciditur in petra cuius rarissima est occasio....*), it was necessary to find an abrasion platform easy to cut and located at a good position. He measured the lowest point (-63 cm) of the platform surface, in which the outer part of channels for water supply has been cut, and assumed that this had to be the sea-level position at the time of construction. Authors measured the lowest point of the platform at -52 cm (G site) although the bottom of the adduction channels had been often encumbered with rock debris and the surface of the platform being developed at irregular heights making necessary the cleaning before measuring. In addition, as noted by Pirazzoli (1976b) twenty centuries of marine abrasion have certainly contributed to the lowering of the platform surface. Schmiedt (1972) also reported that remnants of sluice gates and sliding grooves could be observed at sites E, F, G and H. Leoni and Dai Pra (1997) estimated the RSL rise to about 18 cm from the site I, at the top of the best preserved foot-walk level. By measurements taken during the fieldwork, we verified that the platform surface is ranging from - 9 cm to -20 cm. Specifically, according to site G, bottom is at -52 cm, while platform at -20 cm. The depth of the channel is fluctuating depending on the site of the measurement. Channels are inclined towards open sea. The deepest point of the channel towards the fish tank is at site C (-80 cm). Sites B and D should correspond to the *crepidini* chosen by Leoni and Dai Pra (1997) as best preserved, but we verified that what is mentioned as *crepidini* all around B measurements i.e. B,

B^I, B^{II}, B_i, B_i^I corresponds to the wave cut platform. Those measurements are ranging between -9 and -19 cm, which also fit with the rest measurements of the platform, at different sites of this fish tank. The top of the *crepidini* is also measured in different sites. foot-walk at site D is located at -32 cm. Site F may also correspond to a foot-walk and it has been measured at -17 cm, while the bottom below the foot-walk is at -40 cm. The platform was possibly also used as an upper foot-walk and when it was not possible, an artificial one was constructed. For example at site L a foot-walk was constructed but possibly at site I, a platform was used. At sites E, F and G grooves exist that may be used as a threshold. Site E is the best preserved, where the different constructed steps are clearly visible. It also includes a step that is probably part of the lower and upper foot-walk at -26 cm and -36 cm accordingly, as it occurs almost all around the fish tank. Assuming that the upper foot-walk was situated at +35 cm and taking into account the best preserved one, we suggest a former MSL at -40± 5 cm.

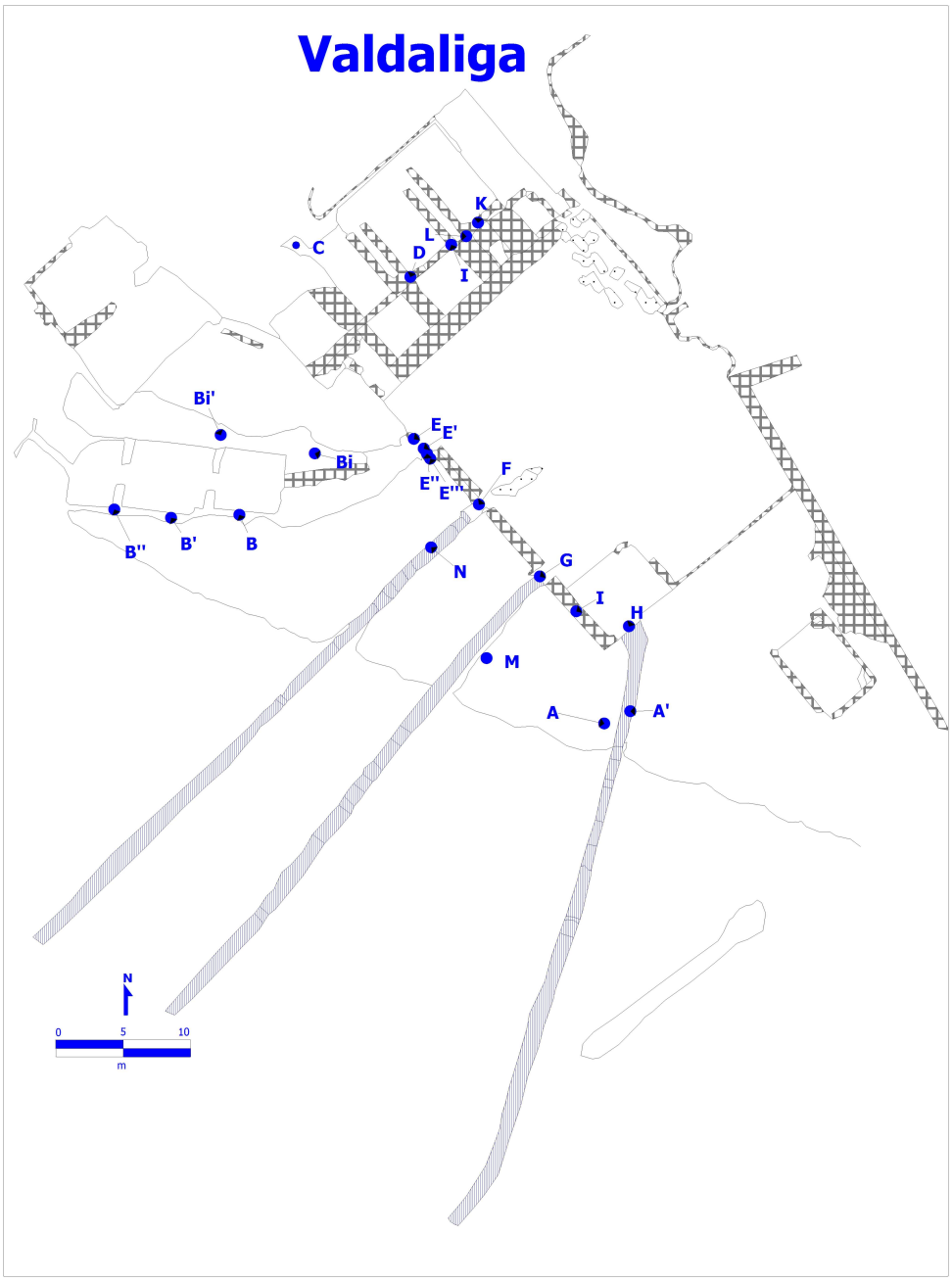

Figure A.3: Map of Torre Valdaliga fish tank. The letters refers to the measurements. See text for explanations.

A.4 Mattonara

The Mattonara fish tank (Figure A.4) is located between the Valdaliga power station and the modern harbor of Civitavecchia, near the ruins of an Etruscan necropolis. The fish tank belongs to a coastal complex comprising a Roman villa (republic age 50-27 BC), located at the east side of the tank, a dock and a circular tank called Buca di Nerone. The architecture is similar to the Torre Valdaliga fish tank but no published article describes the structure and its geometric characteristics.

The survey allowed us to redefine the structure of Mattonara fish tank and develop an updated map. The rectangular shaped tank presents a length of 28 m and a width of 11 m. There are two main channels connecting the fish tank with the open sea. Six small ponds of different size, but all rectangular exist at the north side of the tank. The depth inside the ponds varies from -1 to -1.5 m. The different ponds are connected to each other by a surface channel situated at 26 cm below sea level. At the southern part of the fish tank there are also ponds but less in number and larger in size than those at the northern part. Close to the channels a wall subdivided the tank, is making a corridor opening in the middle of the tank in front of the northern channel.

The upper foot-walk, the top of the walls subdividing the tank into smaller basins, measured at different sites (e.g. W, X, S), is nowadays situated at about -16 cm. This fish tank is situated in a very protective area for wave erosion and we assume that the erosion is small with respect to the rest of visited fish tanks. Site L corresponds to an arched channel the top of which is situated 3 cm below sea level. Site N is situated at -26 cm and it is the bottom of a small carving for the "trop plein" used during overflow, which, in order to assure its functionality, should be at about 15 cm above MSL. Crepidinae around the main channels is situated at about -36 cm (site R). Schmiedt (1972) estimated palaeo-sea level at -0.63 m based on an observed cut along the platform. Pirazzoli (1976a, b) estimated the sea level between -65 cm and -40 cm like at Torre Valdaliga, while Leoni and Dai Pra (1997) estimated the RSL rise between 17 cm based on the foot-walk and 25 cm based on the top of a channel. The upper foot-walk suggest a former MSL at -36$\pm$ 5 cm, while the overflow carving a slightly lower MSL at -41$\pm$ 5 cm.

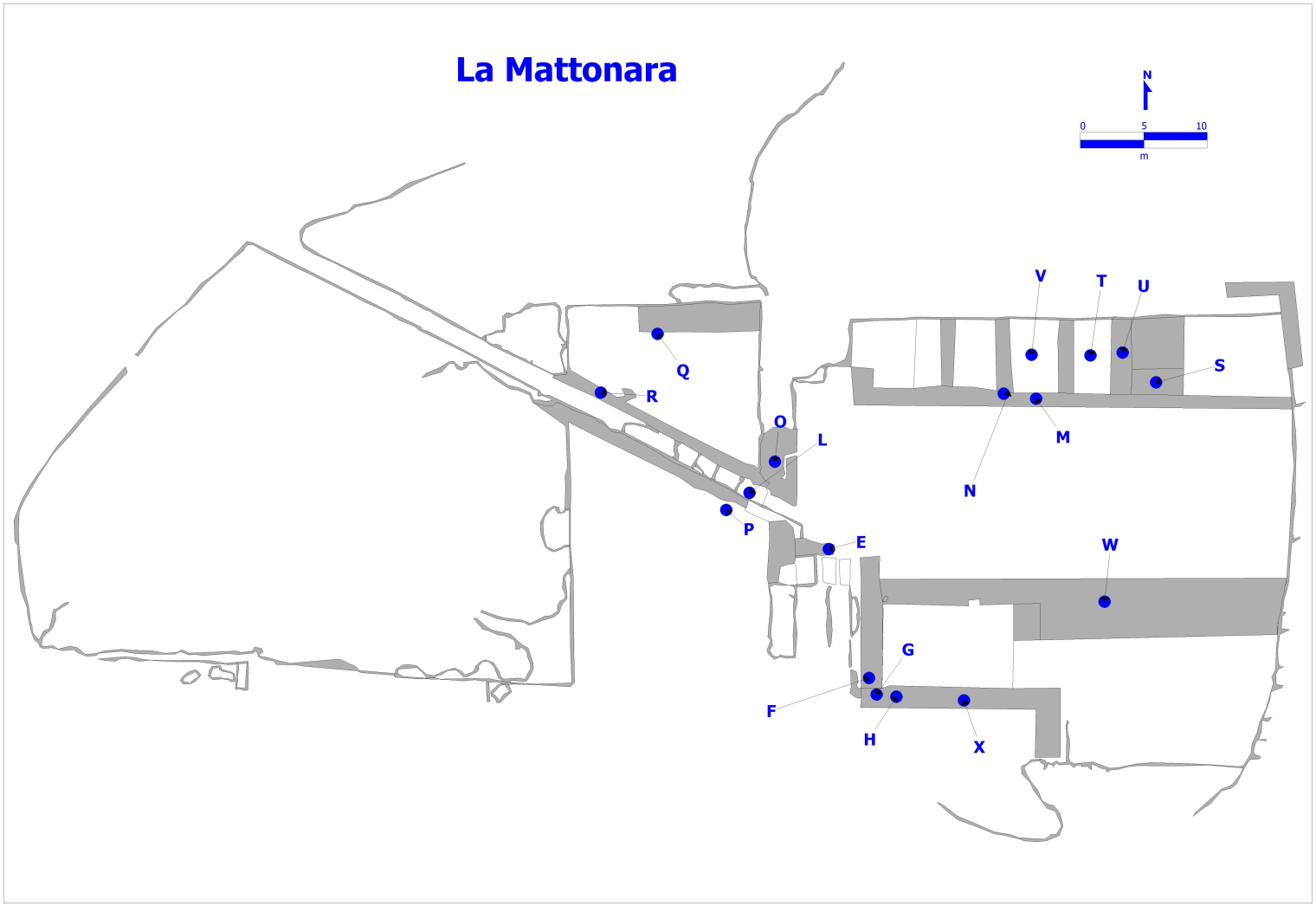

Figure A.4: Map of Mattonara fish tank. The letters refers to the measurements. See text for explanations.

A.5 Fosso Guardiole A and B

Two fish tanks may be observed near the mouth of Fosso Guardiole one is rectangular (Guardiole A), consisting of five basins protected by an outer quay, while the other (Guardiole B), apsidal, is made of a single basin about 0.6 m deep.

A.5.1 Fosso Guardiole A

Guardiole A (Figure A.5) presents a concrete ground mole seawards and it is subdivided into ten fish tanks of different length. Some of these smaller tanks comprise double walls used for the fresh water passage. In the outer quay different kinds of channels exist in order to permit water renewal.

Upper foot-walk is measured at many different sites along the Guardiole A fish tank and the best preserved seems to be site P (-37 cm). At many sites along the outer breaker small circular tanks exist probably for breading different kinds of fish. Site T is one of them, very well preserved, at -4 cm. At Guardiole A sites S, A, Q and R correspond to different types of channels that should have always been submerged. Site E nowadays measured at -39 cm and is interpreted by Leoni and Dai Pra (1997) as a possible *sfioratoio* (carving for discharging the excess of water), was situated at the former high tide level. This, according to Pirazzoli and Tomasin (2008), would bring the former MSL about 11 cm below the taken measurement at -39 cm if the astronomical high tide has to be considered, or at a slightly lower level if moderate surges have to be taken into account.

Based on the construction characteristics (blocks placed the one beside the other with many wide channels) and the site position (further away from the coastline and less protected than other sites around the area), along with the field observations showing that the whole site is less preserved than Punta della Vipera, we assume that erosion has lowered at least 16 cm the best preserved upper foot-walk. Based on the above assumption, site P (best preserved upper foot-walk) should have been found at -21 cm. Assuming that the upper foot-walk was relative to the former sea level +35 cm, this would bring the former MSL at less than -56± 5 cm.

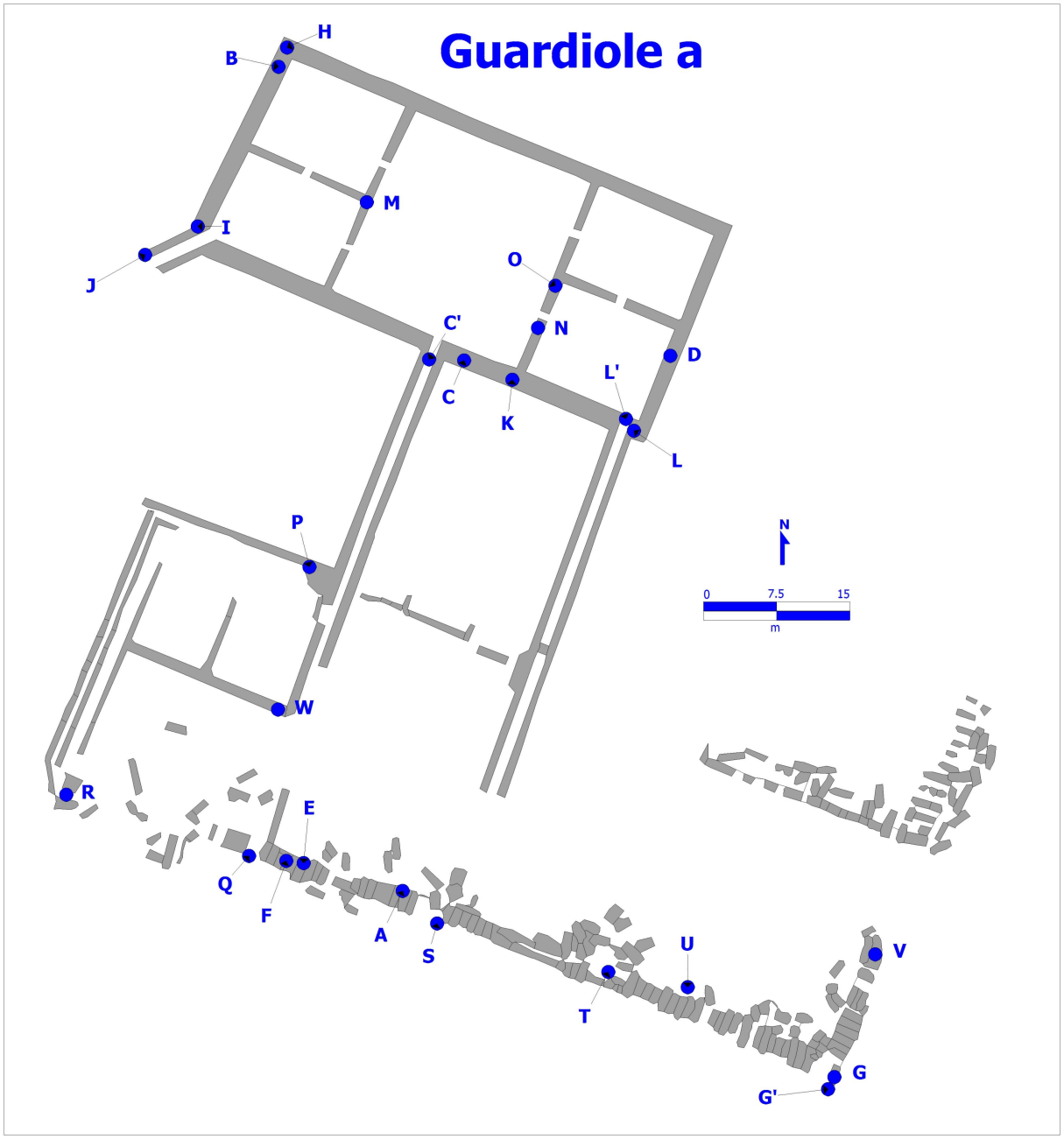

Figure A.5: Map of Guardiole A fish tank. The letters refers to the measurements. See text for explanations.

A.5.2 Fosso Guardiole B

Guardiole B (Figure A.6) is characterized by an apse shape, is composed of one basin and two *crepidini* exist along the border of this tank. Inside it, additional walls exist with also *crepidini* but their use is uncertain.

The outer perimetric mole may be expected to have been built slightly higher than the basin walls, to protect them against waves. This concerns many of the measurements (Figure A.6) indicated (e.g. B^I, C, D, E, F, H, I), which show that the top of the mole was at around -27.5 cm. It has to be noted that the top of the mole may have been often wet. The top of the best preserved foot-walk of the basins (foot-walk) can be expected to have been built to remain most of the time dry. Points e.g. A, A^I, P and possibly G suggest that this dry foot-walk is nowadays at about -40 cm. If the bottom of the basins was at -82 cm, and the bottom of channels at about -80 cm (J) or -90 cm (D^I), the low tide at the time of construction could hardly have been below these levels.

Leoni and Dai Pra (1997) mention a lower step on the inner part of the western wall, about 17 cm below the central foot-walk level, but they do not deduce any clear estimate from it. Schmiedt (1972) deduced a RSL rise of 72 cm from the submergence at -37 cm of the top of the structures, while the estimation of Leoni and Dai Pra (1997) is of a RSL rise between 60 and 65 cm. At Guardiole B, no threshold has been observed while the best preserved remaining top of upper foot-walk (site A^I) has been measured at -38 cm. We assume the same amount of erosion to have lowered Guardiole B as the one assumed for Guardiole A. Thus, site A should have been measured at less than -22 cm suggesting an ancient MSL level at -52$\pm$ 5 cm.

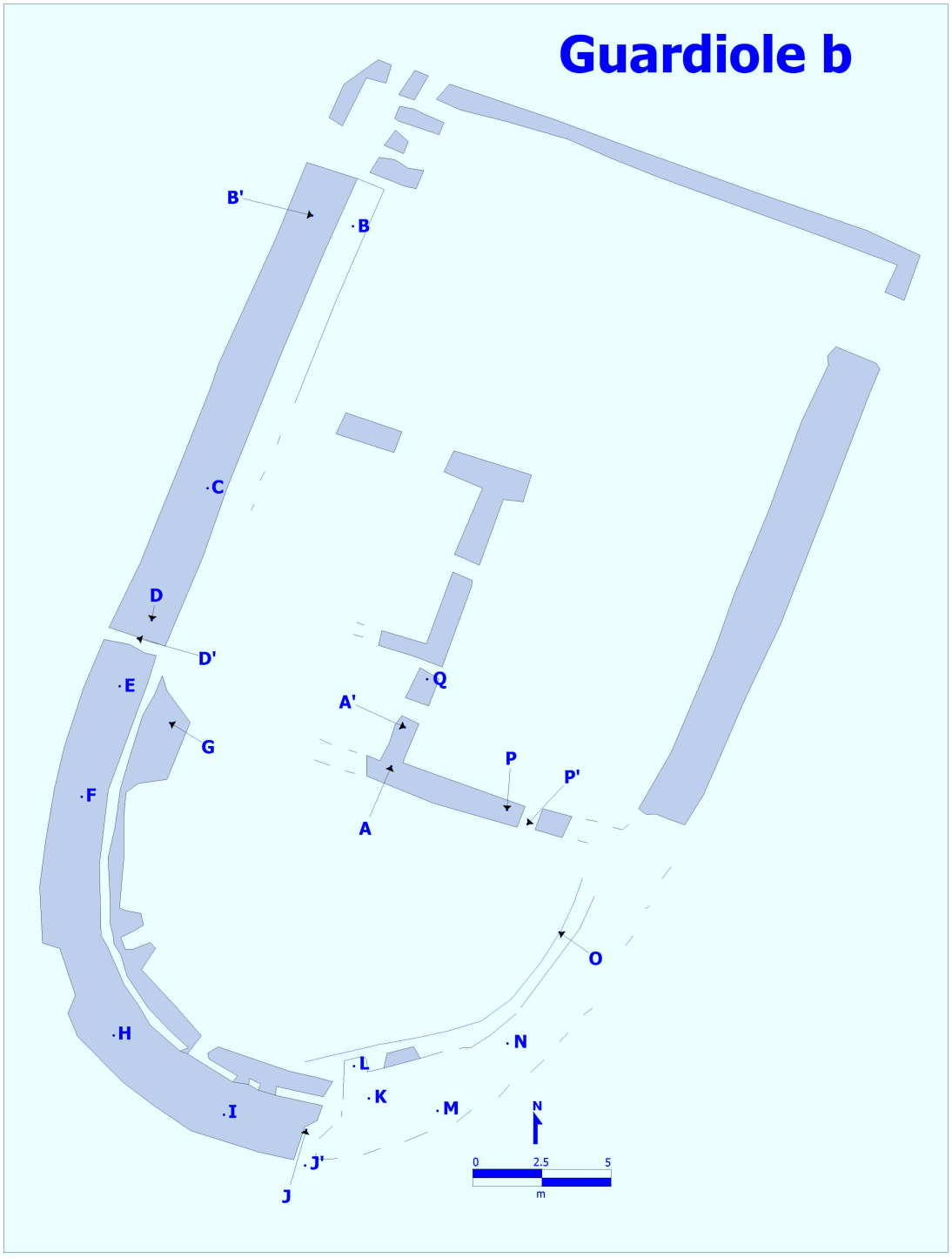

Figure A.6: Map of Guardiole B fish tank. The letters refers to the measurements. See text for explanations.

A.6 Odescalchi

The Odescalchi fish tank (Figure A.7) is situated near the modern harbor, close to the ruin of villa DUlpiano (I sec. A.C.). The eastern side of the tank is constituted of three sectors of blocks. A large natural block of marine platform occurs on the southern side of the fish tank. Ruins of walls occurs in the middle of the tank that Pellandra (1997) supposed is the partition remains of smaller basins inside the tank. Floor ruins in the bottom side of the tank occur at depths of -1.80 m. Between the second and third sector Pellandra (1997) discovered two sluice gates used in pair (catractae binatae). The base of the sluice gate is 2 m deep. The most internal gate presented the groove cutting into the travertine such as the sluice gate. The holes, between 6 and 4 cm in diameter, sorting in regular position characterized the most internal sluice gate. The external sluice gate was blind and its role was to regulate the water flow in the discharge zone between the tank and the sea in correspondence with the tanks opening. A second binary system of sluice gates occurred in the south western corner of the tank. In this part of the tank six flagstones were laid in the bottom of the tank with the aim to make a horizontal groove for the gates.

Odescalchi fish tank is less preserved than the previously discussed fish tanks. Measurements (Figure A.7) taken at the outer breaker are varying a lot depending on the erosion each site has been subjected to. The best preserved site is H (-1 cm). At site B and F a channel of 68 cm width exists, nowadays filled by of debris. Channel F is very well preserved and is divided into two vertical parts by a block at -36 cm. Below the block the existing pass, full of debris nowadays, may have been used as a cataracta. At site J clear marks of drainage system exist at -37 cm assuring the water excess of the basin. In order to ensure the functionality during overflowing events, site J should be located at about 15 cm above former MSL. For Odescalchi fish tank Pellandra (1997) underlines that Columella advised to build surface tank four feet high for fish such as Moray Ell or Soles; so he calculated from a well sheltered shallower part of the basin that the sea level rise had to have been about 50-70 cm. Also, Pellandra (1997) measured and photographed, near sites G and K, the base of sliding grooves at about -1.8 m and -2.0 m respectively, while Lambeck et al. (2004b) situate this at -1.69 m. In this case the base of the sluice gates seems clearly unrelated to the tidal range and only the level of the top of the sliding grooves could eventually be used as a sea-level indicator. Based on the best preserved outer breaker which should be also used in this fish tank as an upper foot-walk,

the former MSL should be less than -36 5 cm, while the existing drainage system suggests a former MSL at least at -32 $\pm$ 5 cm.

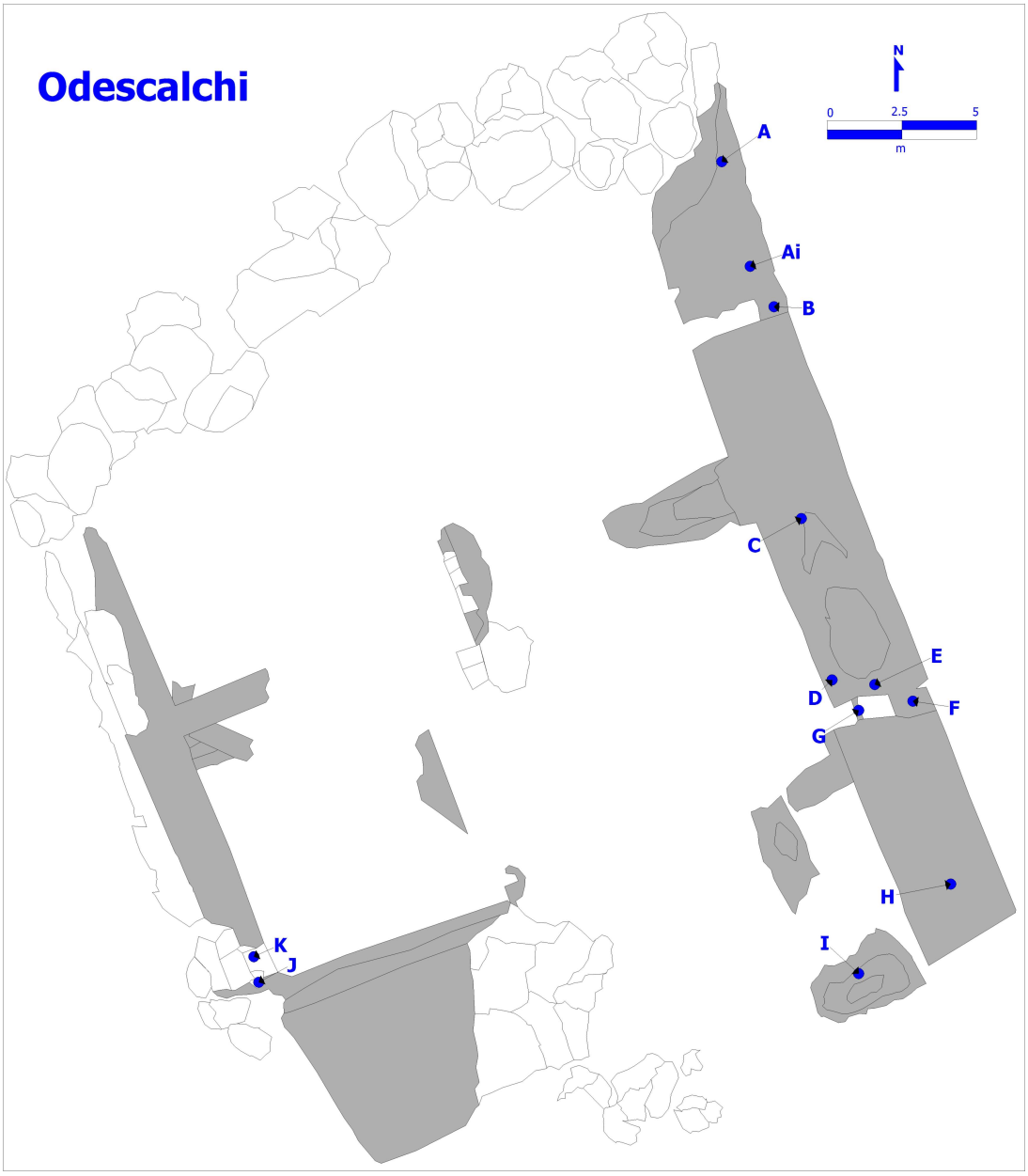

Figure A.7: Map of Odescalchi fish tank. The letters refers to the measurements. See text for explanations.

A.7 Grottacce

Grottacce fish tank (Figure A.8) is located along the Aurelia Street at 58.2 km, near a promontory where the ruins of a Roman villa (approx. AD 50) exist. In general the tank is badly conserved. It is made up of sandstones (-0.5 m bsl) and it has a semicircular shape. Two series of outer break walls, made of large blocks, protected the fish tank from storms. In the inner part of the fish tank a semicircular wall exists with two different levels of crepidinae. A lead sluice gate was found in this fish tank, which is kept at the Museo del Mare e della Navigazione Antica of Santa Marinella. It was constructed by a sluice with small holes, to allow water and small fish to come in, but with holes not large enough for bigger fish to go out.

Erosion has important influence on Grottacce fish tank and that is why measurements around this fish tank are ranging a lot. The best preserved lower foot-walk (B) is located at -111 cm, while the best preserved upper foot-walk (I) at -3 cm. Taking into account Grottacce fish tank, Schmiedt (1972) and Pirazzoli (1976 a, b) estimated the RSL at -0.4 m based on the fact that the top of the walls of the inner basins was measured at -0.2 m. Lambeck et al (2004b) use the width of sluice gate for the estimation of RSL. They have measured the upper part of the sluice gate in an unspecified location at -1.17 m and they supposed that this kind of structure is tide controlled. So, taking into account tide $\pm$ 40 cm, they estimated the bottom level of the sluice gate at -1.57 m. At Grottacce, no indication was found about the place where the sluice gate seen in the Santa Marinella Museum could be located, mainly because the fish tank is highly eroded. The fish-tanks sluice gate (*cataracta*) of the Santa Marinella Museum is the only example available in the Civitavecchia area. It is 60 cm high (in its best preserved parts). The holes start at 7 cm from the base and from the top, i.e. it permits exchange of water over a height of 46 cm. The range of hourly sea level heights during the period 1998-2006 extends over 93 cm (from -42 to +51 cm in relation to MSL). Assuming that the present tidal range and climate are similar to those at Roman times, a correct interpretation of the sea-level indicators should answer the following question: what would be the best altimetric position of the sluice gate in order to optimize the functionality of a fish tank? Varrone Reatino (De Re Rustica, III;17.9) mentions that Hortensius disdained the fish-tanks of a certain M. Lucullus *quod aestiuaria idonea non haberet, ac reside aqua in locis pestilentibus habitarent pisces eius* (because not provided by adequate exchange of water and his fishes were left in stagnant water and in pestilential sites). According to Auriemma and Solinas (2009), ss*the sea*

level could not go over the top of the grid (to avoid the leakage of water and loss of fish), nor underneath the base of the grid, to guarantee an uninterrupted influx of water. These criteria are clearly impossible to be satisfied in the Civitavecchia area with a *cataracta* 60 cm high, permitting exchange of water only over a height of 46 cm. From this point of view, we agree with Leoni and Dai Pra (1997) when they claim that the measurements deduced from fish tanks should not indicate precise levels, but rather upper or lower limits consistent with an acceptable functionality of the system, possibly also in slightly unfavorable conditions. On the other hand, there cannot be an assurance of acceptable functioning at the time of extreme tides and surges, which are exceptional and should not be considered as more dangerous and risky than a wild sea or a great storm. Tidal heights exceeding the level of the *cataracta* e and/or of the foot walks (*crepidini*) that permitted the fish to escape, must have been feared more than a temporary interruption in the influx of water for a few hours in relatively shallow basins, especially if there was possibility to add some fresh water. From the different measurements at Grottacce, site I seems the best possible sea-level indicator. According to the elevation of the foot-walk of site I, the submergence of this fish tank seems comparable to that of other sites visited during the field work. Lower foot-walk e.g. at site B should not be used as sea level indicator because it is very close to the bottom of the tank, and if it should have remained always emerged, the depth of the water in the basin would have been insufficient for a fish tank. The top of the upper foot-walk at site I (-3 cm), assuming it was emerged by 35 cm, suggests a former MSL at -38$\pm$ 5 cm.

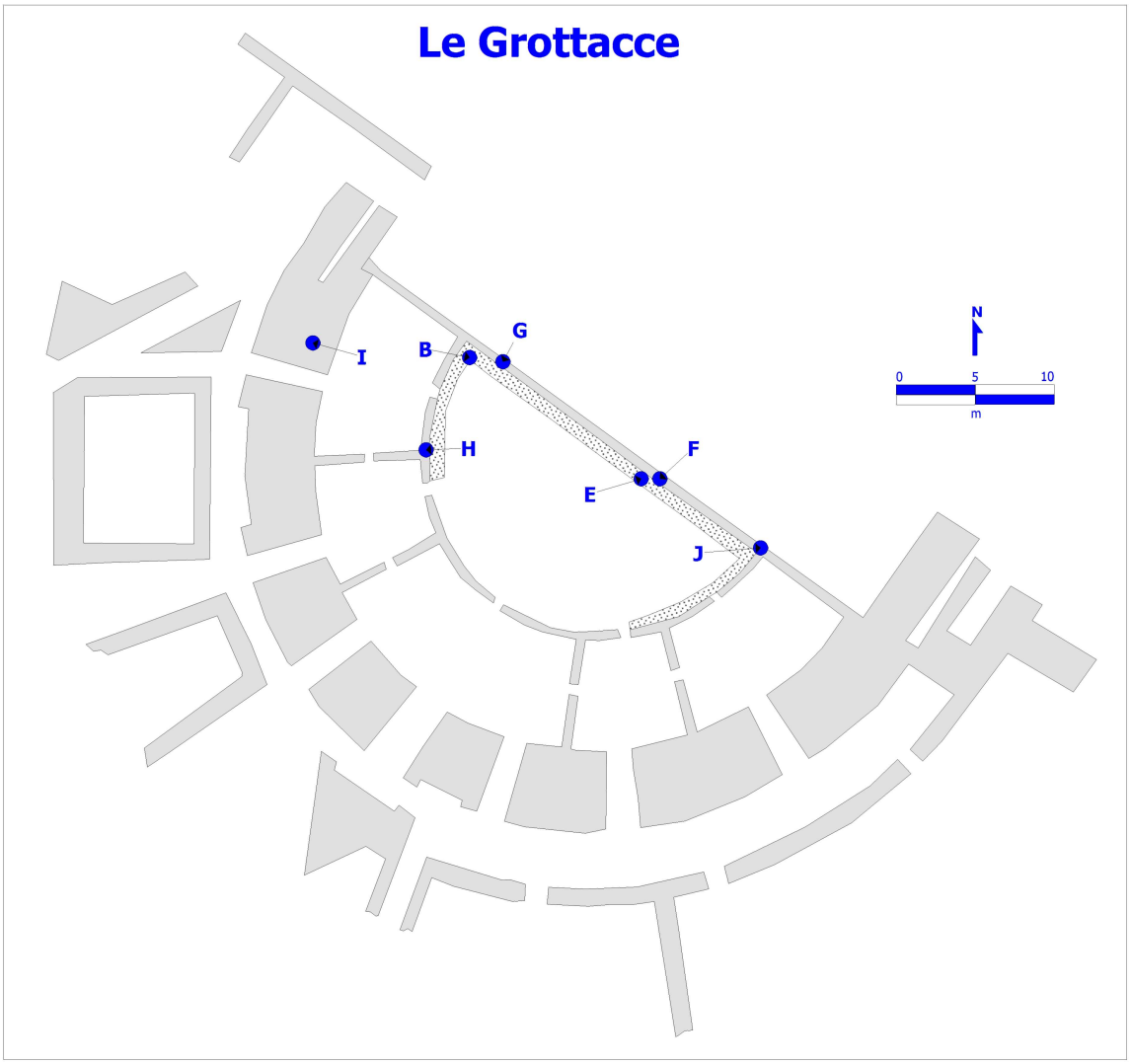

Figure A.8: Map of Grottacce fish tank. The letters refers to the measurements. See text for explanations.

A.8 Pietralacroce

Pietralacroce fish tank is located near Ancona city, below the promontory where the town of Pietralacroce occurs. This ish tank has rectangular shape in plan and measures 8.80 m by 4.20 m and lies at a depth of 2.05 m. It is completely cut into the rock. A channel, 4.60 m long occurs in the seaward west corner of the tank, It permits adequate exchange of water with open sea. Two other channels put in communication the tank A, tank B and C, while a third opening allowed the influx of water from compartment D, obtained at a lower level. The tank B, being at a height of -2.35 m is the deepest of the five, even here a channel put in communication the tank with the sea. From the different measurements at Pietralacroce site 6, seems the best possible sea-level indicator. According to the elevation of the foot-walk of site 6, the submergence of this fish tank seems larger that that of other sites visited during the field work. Lower foot-walk, parallel to the quay is 0.45 m wide and its best preserved top was measured at about 1.53 m at site 5. For the firs time we surveyed a fence where are located the tracks that guides the movement of sluite gate. It occurs at the middle of thank between tank A and tank B. The base of tracks (the threshold) matches the lower foot walk and the top was measured at about -1.35 m (site 2). However the top of the upper foot walk at site 2 is eroded and we should not be used as sea level indicator. The top of the upper foot-walk at site 6 (-59 cm), assuming it was emerged by 35 cm, suggests a former MSL at -94$\pm$ 5 cm.

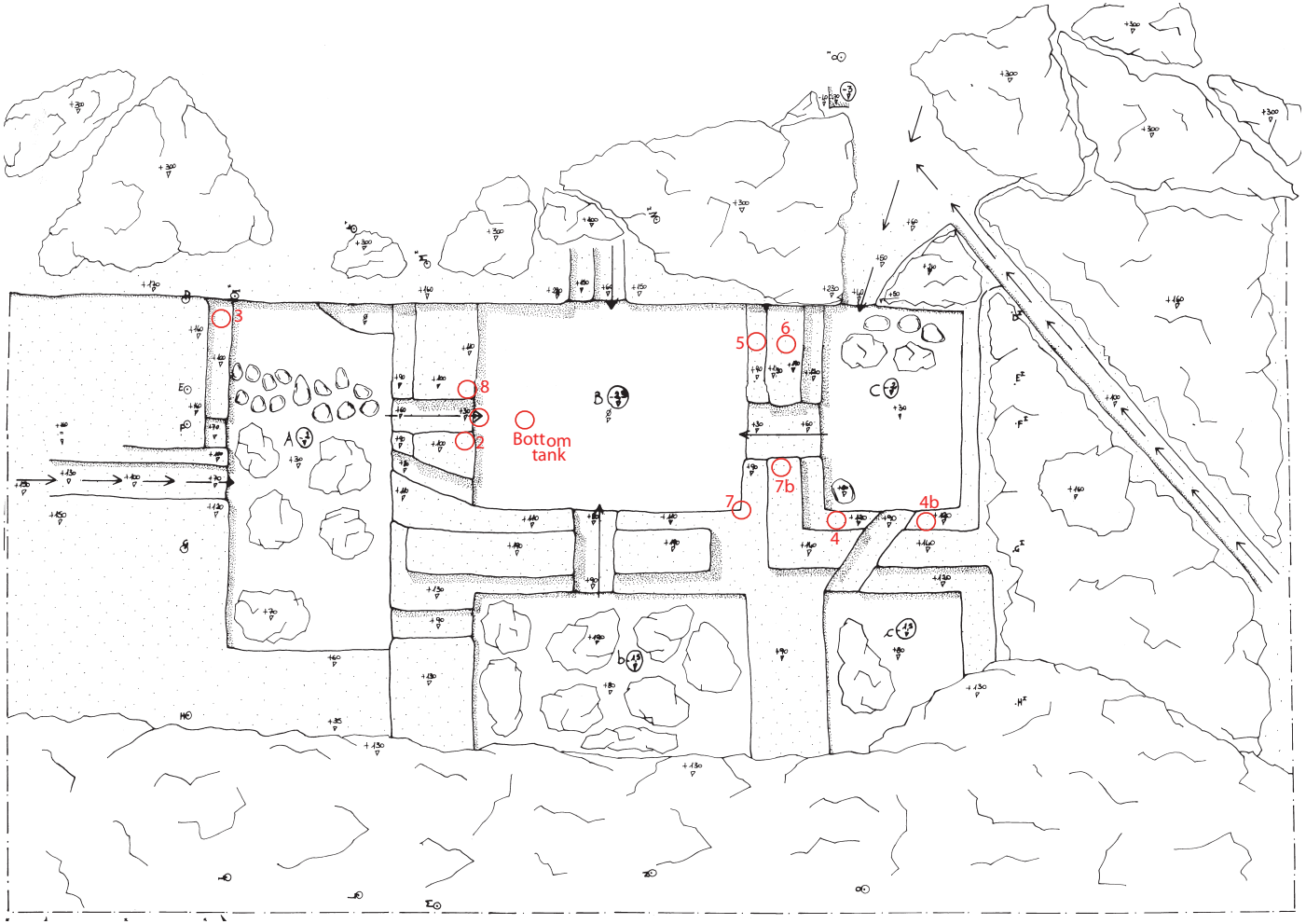

Figure A.9: Map of Pietralacroce fish tank. The letters refers to the measurements. See text for explanations.

A.9 La Banca

La Banca fish tank (Figure A.10) is located 1.6 km north-west of Torre Astura. The fish tank is positioned at the end of a small point founded on a rock shelf that extends beyond the point.The fish tank is rectangular in plan (33.2 by 20.3 m) and was subdivided into at least two roughly square tanks). Seawater probably entered the fish tank through an opening in the southern or seaward mole. The exact location of this aperture is impossible to fix due to the eroded condition of this portion of the enclosure. The long lateral walls includes four walls that would have abutted the original pier and continued to shore.It appears that all four walls were constructed rapidly, one after the other, in a single building phase. Three of these walls were one meter wide while the fourth outer wall were 44 centimetres. The part of the upper foot-walk best preserved from erosion is shown by measurement number 6. It is situated closed to mean sea level. Below this well preserved upper foot-walk we found the lower foot-walk at -35 cm from the upper foot-walk. This off set agrees with the tradition distance furnished by the Latin writers. The upper foot-walk of site 6, measured at -0.01 m, indicates that sea level should be higher than this level. Assuming that the best preserved upper foot-walk (-0.01 m at site 6) was constructed 35 cm above mean sea level, the former MSL could be estimated at about -0.35 $\pm$ 5 cm.

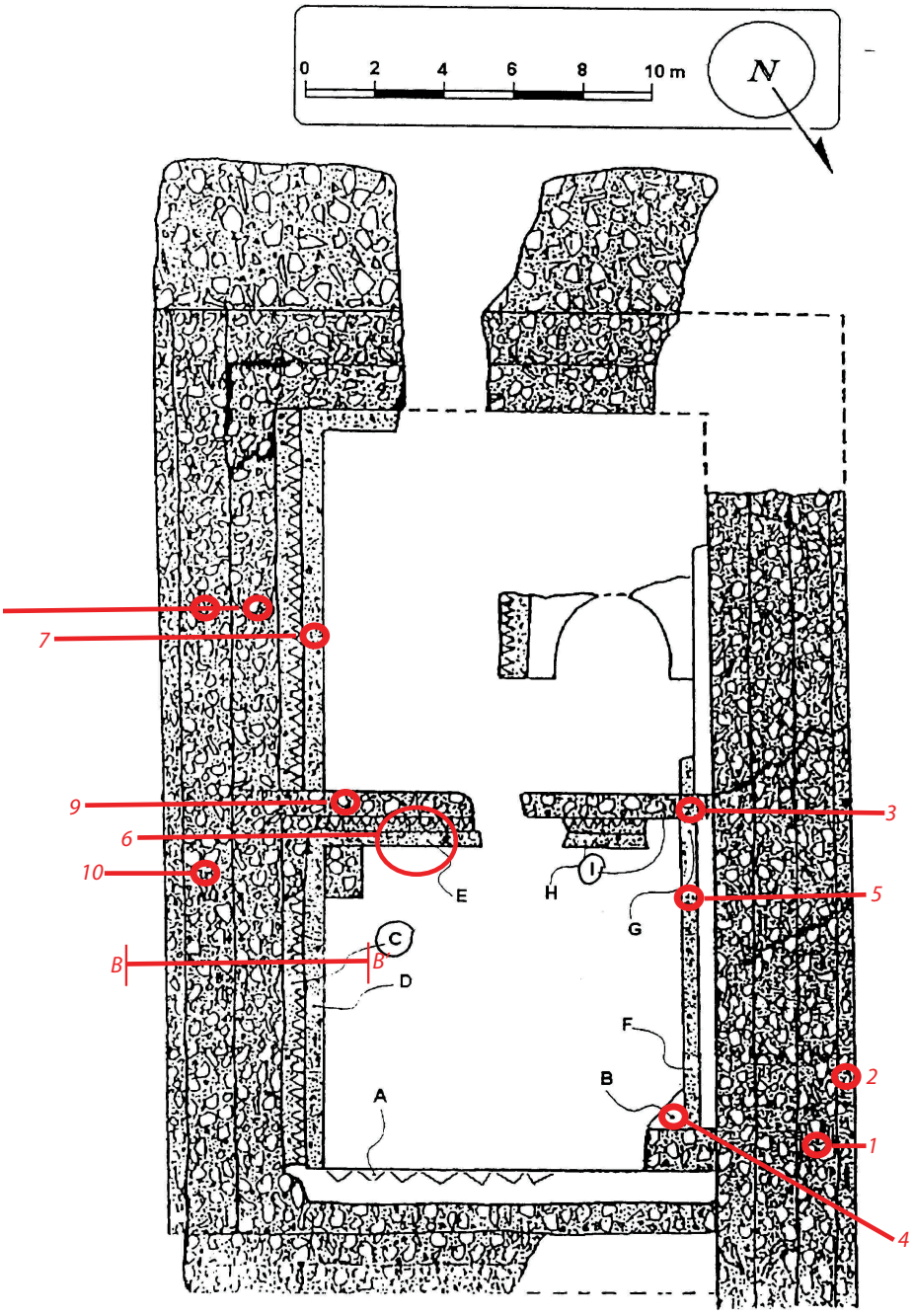

Figure A.10: Map of La Banca fish tank. The letters refers to the measurements. See text for explanations.

A.10 Astura

The Torre Astura (Figure A.11) is the most interesting site among the fish tanks occurred along Nettuno coastline. It is located around a isle where are located a roman ville (augustea age) connected to promontory by a bridge (100 m of length). The fish thank has rectangular shape and Around the border there are others rectangular tanks and ruin of harbour that becomes visible during the low tide. The partition inside the tank sunk in a range between 0.10 m and 0.20. Landward, several small tank are almost covered by sand. Here occurs a fence where are located the track that guides the movement of sluite gate. Schimdt doest give a depth of this structure but give a depth of border thank at -0.2 m. We measured the base of sliding grooves at about -50. 9 cm. This length reconciles with a sluice gate of about 60 cm of leght were the offset of 10 cm can be used to trigger the movement, such as the the lead sluice gate kept in S. Marinella museum. Assuming that the best preserved upper foot-walk (+0.1 m at site Q) was constructed 35 cm above mean sea level, the former MSL could be estimated at about -0.34 $\pm$ 5 cm.

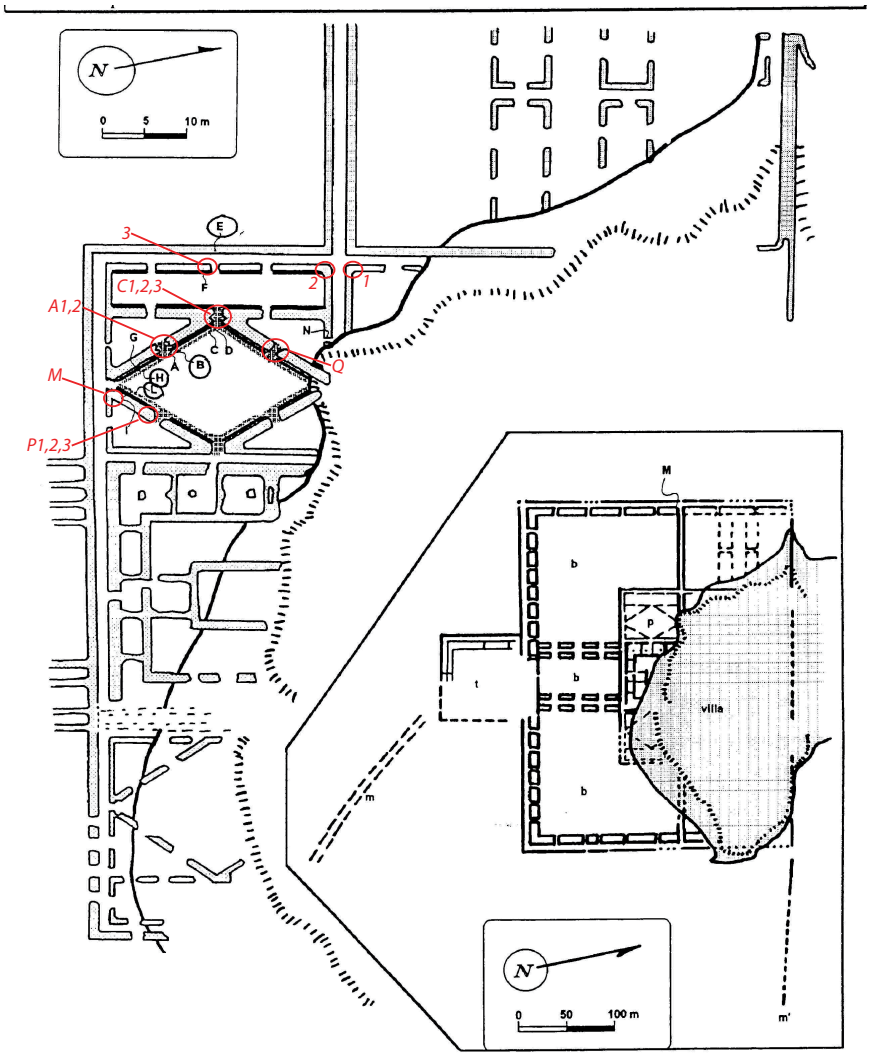

Figure A.11: Map of Astura fish tank. The letters refers to the measurements. See text for explanations.

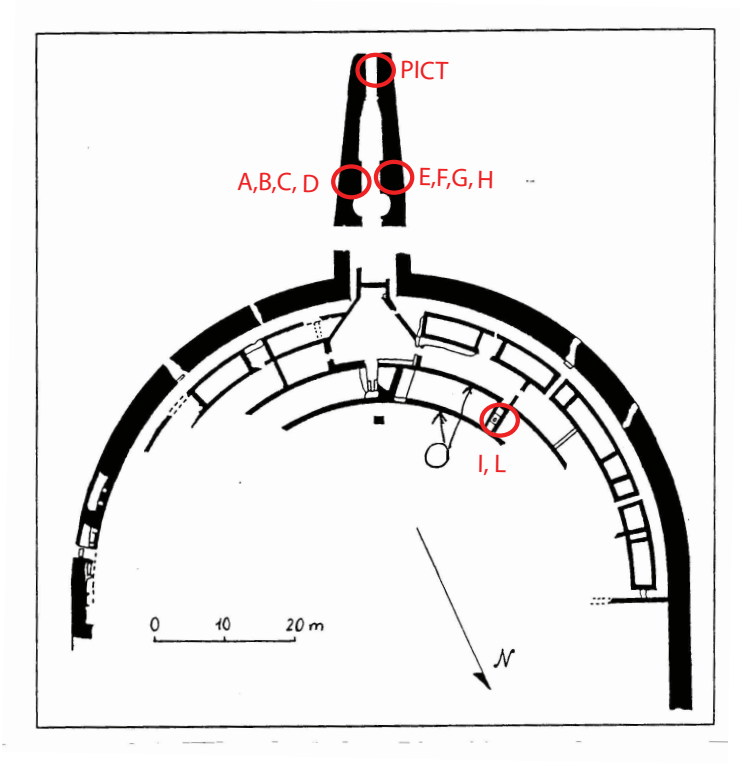

Figure A.12: Map of Saracca fish tank. The letters refers to the measurements. See text for explanations.

A.11 Saracca

The site of Saracca (Figure A.12) lies at the mouth of the river of the same name along the Tyrrhenian coast, 11.5 km east-southeast of Anzio and 54 km south-east of Rome. Along the shore there are the remains of three villae maritimae which posses fishponds. Nowadays sand dunes cover most of the villae. The fish tank was constructed on a rock shelf with projects the shore. The fish tank is semicircular in plan the perimeter of which was protected by a concrete mole of 3-5 m wide and based on a circle 90 m in diameter. The mole was pierced by at least openings (four small and one large) which allowed sea water to circulate within the enclosure. The most interesting feature of this fish tank is the group of structures that dominates the left side of the fish tank where sliding grooves for sluice gates occurs. The thresholds with two parallel grooves exist at -56 to -66 cm at site I, L, facing the south-western part opening of the tank, and possibly the top of a 45 cm high gate had to be located at near the present sea level. The upper foot-walk suggest a former MSL at -51$\pm$ 5 cm,

Bibliography

Agassiz L., 1840. Etudes sur les glaciers, *Neuchatel.*

Alexandersson, T., 1969. Recent littoral and sublittoral high- magnesium calcite lith if ication in the Mediterranean, *Sedimentology*, 12, 47-61.

Alley, R.B., Mayewski, P.A., Sowers, T., Stuiver, M., Taylor, K.C., and Clark, P.U., 1997 Holocene climatic instability; a prominent, widespread event 8,200 yr ago, *Geology*, 25, 6, 483–6. doi:10.1130/0091-7613.

Alley, R. B., and 13 others, 2010. History of the Greenland Ice Sheet: paleoclimatic insights, *Quaternary Sci. Rev.* 29, 1728–1756.

Altamimi, Z., X. Collilieux, and L. Mtivier. 2011. ITRF2008: An improved solution of the international terrestrial reference frame, *J. Geodesy* , doi:10.1007/ s00190-00011-00444-00194.

Ammara, F. H., Chkir, N., Zouari, K., Azzouz-Berriche Z., 2010. Uranium isotopes in groundwater from the "Jeffara coastal aquifer" (southeastern Tunisia), *J. Environ. Radioact.*, 101, 681-691.

Aloisi, J.C., Monaco, A., Planchais, N., Thommeret, J., Thom- meret, Y., 1978. The Holocene transgression in the Gulf du lion, south-western France: paleogeographic and paleobotanical evolution, *Geogr. Phys. Quat.*, 32, 1455162.

Amieux P., Bernier P., Dalongeville R, Medwecki V., 1989. Cathodoluminescence of carbonate-cemented Holocene beachrock from the Togo coastline (West Africa): an approach to early diagenesis, *Sed. Geol.*, 65, 261–272.

Anzidei, M., Antonioli, F., Lambeck, K., Benini, A., Soussi, M., Lakhdar, R., 2010. New insights on the relative sea level change during Holocene along the coasts of Tunisia, *Quaternary Int.* doi:10.1016/j.quaint.2010.03.018

Anzidei, M., Antonioli, F., Lambeck, K., Benini, A., Soussi, M., Lakhdar, R. (2011). New insights on the relative sea level change during Holocene along the coasts of Tunisia and western Libya from archaeological and geomorphological markers, *Quaternary Int.* , 232, 5-12.

Argus, D. F., Peltier, W. R., 2010 Constraining models of postglacial rebound using space geodesy: a detailed assessment of model ICE-5G (VM2) and its relatives, *J. Geophys. Int.* , 181, 2, 697–723, 10.1111/j.1365-246X.2010.04562.x.

Argus, D. F., Peltier, W. R., Watkins, M. M., 1999. Glacial isostatic adjustment observed using very long baseline interferometry and satellite laser ranging geodesy, J. Geophys. Res., 104, B12, 29077-29093.

Auriemma R. and Solinas E., 2009. Archaeological remains as sea level change markers: a review, *Quaternary Int.* 206, 134–146.

Baldi, P., Casula, G., Cenni, N., Loddo, F., Pesci A., 2009. GPS-based monitoring of land subsidence in the Po Plain (Northern Italy), *EPSL*, 288, 204212. doi:10.1016/j.epsl.2009.09.023

Bamber, J. L., Layberry, R. L., Gogineni, S. P., 2001. A new ice thickness and bed dataset for the Greenland Ice Sheet 1 e measurement, data reduction, and errors, *J. Geophys. Res.*, 106, 33, 773-780.

Bamber, D.C., Alley R. B., Joughin, I., 2007 Rapid response of modern day ice sheets to external forcing, *Earth Plan. Sci. Lett.*, 257, 1-13

Bamber, J. L., Riva, R. E. M., Vermeersen, L. L. A., LeBrocq, A. M., 2009. Reassessment of the Potential Sea-Level Rise from a Collapse of the West Antarctic Ice Sheet, *Science* 324, doi:10.1126/science.1169335.

Barber, D.C., Dyke, A., Hillaire-Marcel, C., Jennings, A.E., Andrews, J.T., Kerwin, M.W., Bilodeau, G., McNeely, R., Southon, J., Morehead, M.D., and Gagnon, J.-M., 1999. Forcing of the cold event of 8200 years ago by catastrophic drainage of Laurentide lakes, *nature* , 400, 344–348, doi: 10.1038/22504.

Barberi, F., Buonasorte, G., Cioni, R., Fiordelisi, A., Foresi, L., Iaccarino, S., Laurenzi, M.A., Sbrana, A., Vernia, L., Villa, I.M., 1994. Plio-Pleistocene geological evolution of

the geothermal area of Tuscany and Latium, *Mem. Desc. Carta Geologica dItalia* 49, 77134.

Barletta V. R., Ferrari, C., Diolaiuti, G., Carnielli, T., Sabadini, R., Smiraglia, C., 2006. Glacier shrinkage and modeled uplift of the Alps, Geophys. Res. Lett., 33, L14307, doi:10.1029/2006GL026490.

Bassett, S. E., G. A. Milne, J. X. Mitrovica, and P. U. Clark, 2005. Ice sheet and solid Earth influences on farfield sealevel histories, *Science* , 309, 925928.

Bills, B. G., James, T. S., 1997. Polar motion of a viscoelastic Earth due to glacial cycle mass loading, J. Geophys. Res., 102, 7579–7602.

Bird M.I., L.K. Fifield, T.S. , Teh, Chang, C.H., Shirlaw N., Lambeck N., 2007. An inflection in the rate of early mid-Holocene eustatic sea-level rise: A new sea-level curve from Singapore, *Estu. Coast. Shelf Sci.*, 71, 523–536.

Blanchon, P., and J. Shaw, 1995. Reef drowning during the last deglaciation: evidence for catastrophic sealevel rise and ice sheet collapse, *Geology*, 23, 1, 4-8.

Bodin, S., Petitpierre, L., Wooda, J., Elkanouni, I., Redfern, J., 2010. Timing of early to mid-cretaceous tectonic phases along North Africa: New insights from the Jeffara escarpment (LibyaTunisia), *J. African Earth Sci.*, 58, 489-506.

Bøggild, C. E., Reeh, N., Oerter, H., 1994. Modelling ablation and mass–balance sensitivity to climate change of Storstrmmen, Northeast Greenland, *Global Planet. Change* 9, 79–90, doi:10.1016/0921-8181(94)90009-4.

Bordoni, P., and Valensise, G., 1998. Deformation of the 125 ka marine terrace in Italy: tectonic implications. Special Publication. In: Stewart, I.S., Vita-Finzi, C. (Eds.), *C*oastal Tectonics, 146. Geol. Soc., London, 71110.

Bouaziz S., Barrier E., Soussi M., Turki M. M., , Zouari H., 2003. Tectonic evolution of the northern African margin in Tunisia from paleostress data and sedimentary record, *Tectonophysics* , 357, 227-253

Broeke, van der M., Bamber, J., Ettema, J., Rignot, E., Schrama, E., van de Berg, W. J., van Meijgaard, E., Velicogna, I., Wouters, B., 2009. Partitioning recent Greenland mass loss, *Science* 326, 984-986, doi:10.1126/science.1178176.

Burgers, J. M., 1935. *Mechanical considerations, model systems, phenomenological theories of relaxation and of viscosity*, Verh. K. Akad. Wet. Amsterdam 1, 15(3), 5–72.

Burollet P. F., 1991. Structures and tectonics of Tunisia, *Tectonophysics* , 195, 359-369.

Burov, E., Podladchkov, Y., Grandjean, G., Burg, J. P., 1999. Thermo–mechanical approach to validation of deep crustal and lithospheric structures inferred from multidisciplinary data: Application to the Western and northern Alps, *Terra Nova*, 11, 2–3, 124–131.

Calamita, E. and Deiana, G., 1988. The arcuate shape of the UmbroMarchean-Sabina Apennines (central Italy), *Tectonophysics* , 146, 139147.

Caputo, M., 1967. Linear models of dissipation whose Q is almost frequency independent, Geoph. J. Royal Astr. Soc., 13, 529–539.

Carminati, E., Silvia, E., Camuffo, D., 2007. A study on the effects of seismicity on subsidence in foreland basins: An application to the Venice area, doi:10.1016/j.gloplacha.2006.03.003.

Cathles, L. M., 1975. *The viscosity of the Earth's mantle*, Princeton University Press, N. J., 386 pp.

Cazenave, A., Dominh, K., Guienhut, S., Berthier, E., Llovel, W., Ramillien, G., Ablain, M., Larnicol, G., 2009. Sea level budget over 2003–2008: A reevaluation from GRACE space gravimetry, satellite altimetry and Argo, *Global Planet. Change* , 65, 1-2, 83-88, doi:10.1016/j.gloplacha.2008.10.004.

Cazenave A, Llovel W., 2010. Contemporary sea level rise, *Ann. Rev. Mar. Sci.* 2, 145-73. doi:10.1146/annurev-marine-120308-081105.

Cazenave A., and William L., 2010. Contemporary Sea Level Rise, *Annu. Rev. Mar. Sci.*, 2, 145-73.

Chambers, D. P., Wahr, J.,Tamisiea, M. E., Nerem R. S., 2010 Ocean mass from GRACE and glacial isostatic adjustment, J. Geophys. Res., 115, B11415, doi:10.1029/2010JB007530.

Chen, J. L., Wilson, C. R. , Blankenship, D., Tapley, B. D., 2009. Accelerated Antarctic ice loss from satellite gravity measurements, *Nat. Geosci.*, 2, 12, 859862, doi:10.1038/ngeo694.

Chen, J. L., Wilson, C. R., Tapley, B. D., 2006. Satellite gravity measurements confirm accelerated melting of Greenland ice sheet, *science* 313, 1958-1960, doi:10.1126/science.1129007.

Christensen, R. M., 1982. *Theory of Viscoelasticity*, Academic Press, NY, 364 pp.

Chung, W–Y., and Gao, H., 1997. The Greenland earthquake of 11 July 1987 and postglacial reactivation along a passive margin, *BSSA* 87, 1058–1068.

Chung, W–Y., 2002. Earthquakes along the passive margin of Greenland: evidence of postglacial rebound control, *Pageoph* 159, 2567–2584.

Church, J., Gregory, J., Huybrechts, P., Kuhn, M., Lambeck, K., Nhun, M., Qin, D., Woodworth, P., 26 others, 2001. *Change in Sea Level, Intergovernmental Panel for Climate Change (IPCC) Working Group 1, Third Assessment Report*, Cambridge University Press, Cambridge, pp. 639-694.

Church, J. A., and White N. J., 2011 Sea-Level Rise from the Late 19th to the Early 21st Century, *Surv. Geophys.*, 32, 585-602 doi10.1007/s10712-011-9119-1

Church, J. A., Woodworth, P. L., Aaruo, T., Wilson, W., S., 2011 *Understanding Sea-Level Rise and variability*, John Wiley & Sons.

Clark, P. U., Alley, R. A., Keigwin, L. D., Licciardi, J. M., Johnsen, S. J., Wang, H.,1996. Origin of the first meltwater pulse following the last glacial maximum, *Palaeoceanography* 11, 563–577.

Clark, J.A., Farrell, W.E., Peltier, W.R., 1978. Global changes in postglacial sea level: a numerical calculation, *Quat. Res.* , 9, 265–287.

Clark, P. U., Mitrovica, J. X., Milne, G. A., Tamisiea, M. E., 2002. P. U. Clark1, J. X. Mitrovica2,*, G. A. Milne3 and M. E. Tamisiea2 Sea-Level Fingerprinting as a Direct Test for the Source of Global Meltwater Pulse IA, *Science* , 295, 5564, 2438-2441, doi: 10.1126/science.1068797.

Clarke, G.K.C., Leverington, D.W., Taylor, J.T., and Dyke, A.S., 2004. Paleohydraulics of the last outburst flood from glacial Lake Agassiz and the 8200 BP cold event, *Quaternary Sci. Rev.* , 23, 389407, doi: 10.1016/ j.quascirev.2003.06.004.

Columella (XVII). De Re Rustica.

Center for Remote Sensing of Ice Sheets (CReSIS), 2006. The Icebreaker, *Quarterly Newsletter* 4, 4pp.

Croll, J., 1867. On the change in the obliquity of the ecliptic; its influence on climate of the Polar region, and level of the sea, *Geol. Soc. Glasgow*, 1866-1867, LVII.

Dalongeville, R., Paskoff, R., Sanlaville, P., Thommeret, Y., 1980. Temoins d'un niveau marin holocene superieur a l'actuel en Tunisie meridionale, *C. R. Acad. Sel, Paris*, 290, 303-306.

Daly, J. L., 2002. Testing theWaters; A report on Sea Levels, *Greening Earth Society Science Advisor*, http://www.greeningearthsociety.org/Articles/2000/sea.htm.

Davis, C.H., Li, Y. McConnell, J. R., Frey, M. M., Hanna, E. 2005. Snowfall-driven growth in East Antarctic Ice Sheet mitigates recent sea-level rise, *Science* , 308, 1898-1901.

Denton, G.H., Hughes, T.J., 2002. Reconstructing the Antarctic ice sheet at the Last Glacial Maximum, *Quaternary Sci. Rev.* , 21, 193-202.

Dietrich, R., Rlke, A., Ihde, J., Lindner, K., Miller, H., Niemeier, W., Schenke, H.-W., Seeber, G., 2004. Plate kinematics and deformation status of the Antarctic Peninsula based on GPS, *Global Planet. Change* , 42, 1-4, 313321.

Di Donato, G., Mitrovica, J. X., Sabadini, R. Vermeersen, L. L. A., 2000. The influence of a ductile crustal zone on glacial isostatic adjustment; geodetic observables along the U.S. East Coast, Geophys. Res. Lett., 27, 3017–3020.

Doglioni, C., 1993. Some remarks of the origin of foredeeps, *Tectonophysics* , 228, 120.

Donnellan, A., Luyendyk, B.P., 2004. GPS evidence for a coherent Antarctic plate and for postglacial rebound in Marie Byrd Land, *Global Planet. Change* , 42, 305-311.

Douglas, B. C., 1997. Global Sea Rise: A Redetermination, *Surv. Geophys.* 18, 2-3, 279-292. doi:10.1023/A:1006544227856

Douglas, B., C., 2001. Sea level change in the era of the recording tide gauge, *Sea Level Rise, History and Consequences*, BC Douglas, MS Kearney, SP Leatherman, San Diego, Academic Press.

Dunham R. J., 1962. Classification of carbonate rocks according todepositional texture. In: Classification of Carbonate Rock, Ed. By W. E. Ham. *Mem. Am. Ass. Petrol. Geol.* 1, 108-121.

Duff, D., 1998 Holmes Principles of Physical Geology, *Stanley Thornes*, Cheltenham.

Dyurgerov, M. B., and Meier, M.,F., 2005. Glaciers and the changing Earth system: A 2004 snapshot, *Occasional Paper* 58, 116 p, INSTAAR/OP-58, ISSN 0069-6145.

Dziewonski, A. M., Anderson, D. L., 1981. Preliminary reference Earth model, *Phys. Earth Planet. Inter.* 25, 297–356.

Edwards, R.J., 2006, Sea levels: change and variability during warm intervals, *Progress in Physical Geography* 30, 6, 785-796, doi:10.1177/0309133306071959.

Evelpidou N., Pirazzoli P., Vassilopoulos A., Spada G., Ruggieri G., Tomasin A., in press. Sea level variations during the Late Holocene from revised observations of Roman fish tanks on the Tyrrhenian coast of Italy, *Geoarchaeology* inpress.

Ewert H., Groh, A., Dietrich, R., 2011. Volume and mass changes of the Greenland ice sheet inferred from ICESat and GRACE, *J. Geodyn.* , doi:10.1016/j.jog.2011.06.003

Fabricius, F. H., 1970. Early Holocene Ooids in Modern Littoral Sands Reworked from a Coastal Terrace, Southern Tunisia, *Science* , 169, 757-760.

Fairbanks, R. G., 1989. A 17,000 year glacioeustatic sealevel record: influence of glacial melting rates on the Younger Dryas event and deep ocean circulation, *nature* , 342, 637642.

Fairbridge, R. W., 1961. Eustatic changes in sea level, *Phys. Chem. Earth* 4, 99- 185.

Farrell, W. E., 1972. Deformation of the Earth by surface loads, *Rev. Geophys. Space Phys.*, 10, 3, 761-797.

Farrell, W. E. and Clark, J. A., 1976. On postglacial sea–level, *Geophys. J. R. astr. Soc.* 46, 647–667.

Fjeldskaar, W., 1994. Viscosity and thickness of the asthenosphere detected from the Fennoscandian uplift, *Earth Planet. Sc. Lett.* 126, 399–341.

Fleming, K., and Lambeck, K., 2004. Constraints on the Greenland Ice Sheet since the Last Glacial Maximum from sea–level observations and glacial–rebound models, *Quaternary Sci. Rev.* 23, 9-10, 1053-1077.

Fleming, K., Johnston, P., Zwartz, D., Yokoyama, Y., Lambeck, K., Chappell, J., 1998. Rening the eustatic sea-level curve since the Last Glacial Maximum using far- and intermediate-eld sites, *Earth Planet. Sc. Lett.* , 163, 327-342.

Flemming, N. C., 1999 Archaeological evidence for vertical movement on the continental shelf during the Palaeolithic, Neolithic and Bronze Age periods, *Geol. Soc. London, Special Publications* 146, 129-146. doi: 10.1144/GSL.SP.1999.146.01.07

Flugel E.,2004. Microfacies of Carbonate Rocks, *Springer*, Stutz, Wurzburg, 976 pp.

Folk R. L. 1962. Spectral subdivision of limeston types. In: Classification of Carbonate Rock, Ed. By W. E. Ham. *Mem. Am. Ass. Petrol. Geol.* 1, 62–84.

Fontes J., C., and Perthuisot, J., P., 1971. Facies mineralogiques et isotopiques des carbonates de la Sebkha el Melah (Zarzis Tunisie): les variations du niveau de la Mediterranee orientale depuis 40000 ans, *Review Geographic, Physic and Geologic Dynamic*, 13, 299-314.

Frebourg, G., Hasler, C. A., Davaud, E., 2010. Catastrophic event recorded among Holocene eolianites (Sidi Salem Formation, SE Tunisia), *Sedimentary Geol.*, 224, 38-48.

Fung, Y. C., 1965. *Fundation of solid mechanics*, PrenticeHall, Englewood, Cliffs, N. J., 525 pp.

Gabtni, H., Jallouli, C., Mickus, K.L. , Zouarid, H., Turki, M.M., 2009. Deep structure and crustal configuration of the Jeffara basin (Southern Tunisia) based on regional gravity, seismic reflection and borehole data: How to explain a gravity maximum within a large sedimentary basin?, *J. Geodyn.* 47, 142-152.

Gaver, D. P., 1966. Observing stochastic processes and approximate transform inversion, *Operative Res.*, 14, 444–459.

Gehrels, W. R., 2010. Late Holocene land- and sea-level changes in the British Isles: implications for future sea-level predictions, *Quaternary Sci. Rev.* , 29, 16481660.

Gehrels, W. R., 2009. Sea-level changes since the Last Glacial maximum: an appraisal of theIPCCFourth assessment report, *J. Quaternary Sci.* 226–236.

Gehrels, W. R., Hayward, B., Newnham R. M., Southall K. E., 2008. A 20th century acceleration of sea-level rise in New Zealand, Geophys. Res. Lett.35, L02717.

Geophysic Study Committee, 1990. Sea-Level Change, *National Accademy press*, United States of America, 233. ISBN 0-309-04039-6.

Giacopini L., Marchesini B., Rustico L., 1997. L Itticultura nellantichit, Enel, Roma.

Gommenginger, C., Thibaut, P., Fenoglio M, L., Deng, X., Gomez, E., J., and Gao, Y., 2009. Retracking altimeter waveforms near the coasts, in *Coastal altimetry*, by S. Vignudelli, A. Kostianoy and P. Cipollini, Springer-Verlag, Berlin.

Gunter, B. C., Urban, T., Riva, R. E. M., Helsen, M., Harpold, R., Poole, S., Nagel, P., Schutz, B., Tapley, B., 2010. A comparison of coincident GRACE and ICESat data over Antarctica, *J. Geodesy* 83 (11), 1051–1060, doi:10.1007/s00190-009-0323-4.

Hanyk, L., 1999. *Viscoelastic response of the Earth: Initial–value approach*, Ph. D. Dissertation, Charles University, Prague, 137 pp.

Hanyk, L., Matyska, C., Yuen, D. A., 1999. Secular gravitational instability of a compressible viscoelastic sphere, Geophys. Res. Lett., 26, 557–560.

Haskell, N.A., 1935. The motion of a fluid under a surface load 1, *Physics*, 6, 265-269.

Huybrechts, P., 1996, Basal temperature conditions of the Greenland ice sheet during the glacial cycles, *Ann. Glaciol.* 23, 226–236.

Houghton, J.T. , Jenkins G.J., Ephraums J.J., 1990. IPCC first assessment report-Working Group I. Cambridge University Press, Cambridge, Great Britain, New York, NY, USA and Melbourne, Australia 410 pp.

Ingolfsson, O. and Hjort, C. 1999. The Antarctic contribution to Holocene global sea-level rise, *Polar Res.*, 18, 323-330.

IPCC, Climate Change 2007: *The Physical Science Basis*, Cambridge University Press, Cambridge.

International Subcommission on Stratigraphic Classification (ISSC), 1994. International Stratigraphic Guide -A guide to stratigraphic classification, terminology, and procedure (Amos Salvador, ed.). *The International Union of Geological Sciences and The Geological Society of America*, 2nd edition., 214 p.

Ivins, E.R., James, T.S., 2005. Antarctic glacial isostatic adjustment: a new assessment. *Ant. Sci.*, 17, 4, 537549.

Ivins, E. R., and Sammis, C. G., 1996. Transient creep of a composite lower crust. 1. Constitutive theory. J. Geophys. Res.101 (12), 27,981–28004.

Ivins, E. R., andWolf, D., 2008. Glacial isostatic adjustment: New developments from advanced observing systems and modeling, *J. Geodyn.* . 46 69–77, doi:10.1016/j.jog.2008.06.002.

James, T. S., Morgan, W. J., 1990. Horizontal motions due to post-glacial rebound, Geophys. Res. Lett., 17, 957–960.

Jedoui, Y., Kallel, N., Fontugne, M., Ben Ismail, H., M Rabet, A., Montacer, M., 1998. A high relative sea-level stand in the middle Holocene of south-eastern Tunisia, *Marine Geol.*, 147, 123–130.

Jedoui, Y., Reyss, J.L. , Kallel, N., Montacer, M., Isma, H., Davaud, E., 2002. U-series evidence for two high Last Interglacial sea levels in southeastern Tunisia, *Quaternary Sci. Rev.* , 22, 343-351.

Johnsen, S. J., Dahl-Jensen, D., Dansgaard, W., and Gundestrup, N., 1995. Greenland palaeotemperatures derived from GRIP bore hole temperature and ice core isotope profiles, *Tellus B*, 47, 5, 624-629.

Kaufmann B., 2007. Diagenesis of Middle Devonian Carbonate Mounds of the Mader Basin (eastern Antiatlas, Marocco), *J. of Sed. Res.*, 67, 5, 945–956.

Kearney M., S., 2001. Late Holocene sea-level variation. In: Douglas, B., C., Kearney M., S. , Leatherman, S., P., 2001. *Sea Level Rise, History and Consequences*, San Diego, Academic Press.

Kelly, M. A., and Lowell, T. V., 2009. Fluctuations of local glaciers in Greenland during latest Pleistocene and Holocene time, *Quat. Sci. Rev.,* 28, doi:10.1016/j.quascirev.2008.12.008.

Kendall, R. A., and Mitrovica J. X, 2008 The sea-level fingerprint of the 8.2 ka climate event, *Geology*, 36, 5, 423426, doi: 10.1130/G24550A.1.

Kendall, R., Mitrovica, J. X., Sabadini, R., 2003. Lithospheric thickness inferred from Australian post-glacial sea-level change: The influence of a ductile crustal zone, Geophys. Res. Lett.30, 1461–1464.

Kemp, C. A., Horton B. P., Donnelly, J. P., Mannd, M. E., Vermeere, M., Rahmstorff, S., 2011. *pnas.org* doi: 10.1073/pnas.1015619108.

Khan, S. A., Wahr, J., Stearns, L. A., Hamiltin, G. S., van Dam, T., Larson, K. M., Francis, O., 2007. Elasic uplift in southeast Greenland due to rapid ice mass loss, Geophys. Res. Lett.34, L21701, doi:10.129/2007GL031468.

Khan, S. A., Wahr, J., Leuliette, E., van Dam, T., Larson, K. M., Francis, O., 2008. Geodetic measurements of postglacial adjustments in Greenland, J. Geophys. Res.,113, B02402, doi:10.1029/2007JB004956.

Khan, S. A., Wahr, J., Bevis, M., Velicogna, I., Kendrick, E., 2010. Spread of ice mass loss into northwest Greenland observed by GRACE and GPS, Geophys. Res. Lett., 37, L06501, doi:10.1029/2010GL042460.

King, M. A., and 16 others, 2010. Improved Constraints on Models of Glacial Isostatic Adjustment: A Review of the Contribution of Ground–based Geodetic Observations, *Surv. Geophys.* 31, 465–507, doi: 10.1007/s10712-010-9100-4.

Klemann, V., Wolf, D., 1999. Implications of a ductile crustal layer for the deformation caused by the Fennoscandian ice sheet, *J. Geophys. Int.* , 139, 216–226.

Klemann, V., Wu, P., Wolf, D., 2003. Compressible viscoelasticity: stability of solutions for homogeneous plane–Earth models, *J. Geophys. Int.* , 153, 569–585.

Körnig, M., Müller, G., 1989. Rheological models and interpretation of postglacial uplift, *J. Geophys. Int.* , 98, 243–253.

Krabill, W., Abdalati, W., Frederick, E., Manizade, S., Martin, C., Sonntag, J., Swift, R., Thomas, R., Wright, W., Yungel, J., 2000. Greenland ice sheet: high-elevation balance and peripheral thinning, *Science* 289, 428430.

Krumbein W. C. and Sloss L.L, 1951. Stratigraphy and Sedimentation, San Francisco, W. H. Freemen and Co., 497pp.

Lambeck, K., 1980. *The Earth's Variable Rotation, Geophysical Causes and Consequences*, Cambridge University Press, Cambridge, 449 pp.

Lambeck, K., 1990. Late Pleistocene, Holocene and present sea-levels: constraints on future change, *Palaeogeography, Palaeoclimatology, Palaeoecology*, 89, 205–217

Lambeck, K., 1993. Glacial rebound of the British IslesII. A high resolution, high precision model, *Geophys. J. Int.*, 24, 19691988.

Lambeck, K., 1995. Constraints on the Late Weichselian ice-sheet over the Barents Sea from observations of raised shorelines, *Quaternary Sci. Rev.* , 14, 1, 1-16.

Lambeck, K., Johnston, P., Smither, C., Nakada, M., Glacial rebound of the British Isles-III. Constraints on mantle viscosity, *Geophys. J. Int.*, 125, 340-354.

Lambeck K., Antonioli F., Purcell A., Silenzi S., 2004a. Sea Level Change along the Italian Coast for the past 10,000 years, *Quaternary Science Reviews* 23, 203-222.

Lambeck K., Anzidei M., Antonioli F., Benini A., Esposito A., 2004b. Sea Level in Roman time in the Central Mediterranean and Implications for recent change, *Earth Plan. Sci. Lett.* 224, 563-575.

Lambeck, K., Bard, E., 2000. Mediterranean coast for the past 30,000 years, *Science Letter*, 175, 203222.

Lambeck, K., Chappel,l J., 2001. Sea level change through the last glacial cycle, *Science* , 292, 5517, 679-686.

Lambeck, K., Esat, T., Potter, E., 2002. Links between climate and sea level for the past three million years, *nature* 419, 199-207.

Lambeck, K., Nakada, M., 1990. Late Pleistocene and Holocene sea- level change along the Australian coast. Palaeogeography, Palaeoclimatology,Palaeoceology, *Global and Plan. Chan.* 89, 143–176.

Lambeck, K. and Purcell, A., 2005. Sea-level change in the Mediterranean Sea since the LGM: model predictions for tectonically stable areas, *Quaternary Science Reviews* 24, 19691988.

Lambeck, K., Antonioli, F., Anzidei, M., Ferranti, L., Leoni, G., Scicchitano, G., Silenzi, S., 2011. Sea level change along the Italian coasts during the Holocene and projections for the future, *Quaternary Int.* , 232, 250–257.

Lavecchia, G., De Nardis R., Visini F., Ferrarini F., Barbano, M. S., 2007 Seismogenic evidence of ongoing compression in eastern-central Italy and mainland Sicily: a comparison, *Boll.Soc.Geol.It.*, 126, 2, 209-222.

Lemke, P., Ren, J., Alley, R. B., Allison, I., Carrasco, J., Flato, G., Fujii, Y., Kaser, G., Mote, P., Thomas, R.H., Zhang, T., 2007. Observations: changes in snow, ice and frozen ground. In: Solomon, S., Qin, D., Manning, M., Chen, Z., Marquis, M., Averyt, K. B., Tignor, M., Miller, H. L. (Eds.). *Climate Change 2007: The Physical Science Basis. Contribution of Working Group I to the Fourth Assessment Report of the Intergovernmental Panel on Climate Change*, Cambridge University Press, Cambridge and New York, 996 pp.

Leoni G., Dai Pra G., 1997. Variazioni del livello del mare nel tardo Olocene (ultimi 2500 ann) lungo la costa del Lazio in base as indicatori geo-archeologici, *ENEA* 110 p, ISSN71120-5555.

Levitus S, Antonov J. L, Boyer T. P., Locarnini R. A., Garcia H. E., Mishonov A., V., 2009. Global Ocean heat content 1955-2008 in light of recently revealed instrumentation, Geophys. Res. Lett.36, doi:10.1029/2008GL037155.

Longman, M., 1962a. A Green's function for determining the deformation of the Earth under surface mass loads. 1. Theory, J. Geophys. Res., 67, 845–850.

Longman, M., 1962b. A Green's function for determining the deformation of the Earth under surface mass loads. 2. Computations and numerical results, J. Geophys. Res., 68, 485–496.

Love, A. E. H., 1909. The yielding of the Earth to disturbing forces, *Proceedings of the Royal Society* A, 82, 73–88.

Lucas, G., 1955. Oolithes marines actuelles et Calcaires oolithiques rcents sur le rivage africain de la Mditerrane Orientale (gypte et Sud Tunisien), *Bull. Station Oceanogr. Salammbo*, 52,1938.

Luthcke, S. B., Zwally, H. J., Abdalati, W., Rowlands, D. D., Ray, R. D., Nerem, R. S., Lemoine, F. G., McCarthy, J. J., Chinn, D. S., 2006. Recent Greenland ice mass loss by drainage system from satellite gravity observations, *Science* 314, 1286–1289, doi:10.1126/Science.1130776.

Luthcke, S., Rowlands, D., McCarthy, J., Arendt, A. Sabaka, T. Boy, J.–P., Lemoine, F., 2010. Observing changes in land ice from GRACE and future spaceborne multi–beam laser altimeter missions, EGU conference paper EGU2010–5576, Vienna, Austria.

Mainardi, F., 2010. *Fractional Calculus And Waves in Linear Viscoelasticity*. Introduction to Mathematical Models, Monograph, Imperial College Press, London, UK (A Branch of World Scientific, Singapore), , pp 340, ISBN:978-1-84816-329-4.

Meier, M. F., Dyurgerov, M. B., Rick, U. K., O'Neel, S., Pfeffer, W. T., Anderson, R. S., Anderson1, S. P., and Glazovsky, A. F., 2007. Glaciers Dominate Eustatic Sea–Level Rise in the 21st Century, *Science* 317, 1064–1067, DOI: 10.1126/science.1143906.

Meletti C., Patacca E., Scandone, P., 2000. Construction of a Seismotectonic model: the case of Italy, *Pure App. Geophys.*, 157, 11-35.

Melini, D., Cannelli, V., Piersanti, A., Spada, G., 2008. Post-seismic rebound of a spherical Earth: new insights from the application of the Post–Widder inversion formula, *J. Geophys. Int.* , 174, 672–695, doi: 10.1111/j.1365-246X.2008.03847.x.

Mercer, J. H., 1968. Antarctic Ice and Sangamon Sea Level, *IAHS*, 79, 217225.

Milne, G. A. and Mitrovica, J. X., 1998. Postglacial sea–level change on a rotating Earth, *J. Geophys. Int.* 133, 1–10.

Milne, G. A. and Mitrovica, J. X., 1998. Searching for eustasy in deglacial sea-level histories.Earth, *Quaternary Sci. Rev.* 27, 22922302.

Milne, G.A., Long, A.J., Bassett, S.E., 2005. Modelling Holocene relative sea-level observations from the Caribbean and SouthAmerica, *Quaternary Sci. Rev.* 24,11831202.

Mitrovica, J.X. and Forte, A.M., 2004. A New Inference of Mantle Viscosity Based Upon a Joint Inversion of Convection and Glacial Isostatic Adjustment Data, *Earth Planet. Sc. Lett.* , 225, 177-189.

Mitrovica, J. X., Gomez, N., Clark, P. U., 2009. The sea–level fingerprint of West Antarctic collapse, *Science* 323, 753.

Mitrovica, J.X. and Milne, G.A. 2002. On the Origin of Late Holocene Highstands Within Equatorial Ocean Basins, *Quaternary Sci. Rev.* 21, 2179–2190.

Mitrovica, J. X. and Peltier, W. R., 1989. Pleistocene deglaciation and the global gravity field, J. Geophys. Res.94, 13,651–13,671.

Mitrovica, J. X., and Peltier, W. R., 1991. On post–glacial geoid subsidence over the equatorial ocean, J. Geophys. Res.96, 20,053–20,071.

Mitrovica, J. X., Tamisiea, M. E., Davis, J. L., Milne, G. A., 2001. Recent mass balance of polar ice sheets inferred from patterns of global sea–level change, *nature* 409, 1026–1029.

Morhange, C., Laborel, J., Hesnard, A., 2001. Changes of relative sea level during the past 5000 years in the ancient harbor of Marseilles, Southern France, *Palaeogeography, Palaeoclimatology, Palaeoecology*,166, 319329.

Morhange, C. and Pirazzoli P.A., 2005. Mid-Holocene emergence of southern Tunisian coasts, *Marine Geol.*, 220, 205–213.

Munk W. H., MacDonald G. J. F., 1960. *The Rotation of the Earth*, Cambridge University Press, Cambridge, 323 pp.

Nakada, M. andLambeck, K., 1988. The melting history of the Late Pleistocene Antarctic ice-sheet, *nature* , 333, 6168, 36-40.

Nakada, M. andLambeck, K., 1989. Late Pleistocene and Holocene sea-level change in the Australian region and mantle rheology, *Geophys. J.* 96, 497517.

Nerem R., S.,1995. Measuring global mean sea level variations using TOPEX/POSEIDON altimeter data, J. Geophys. Res., 100, 25135-25151.

Paskoff, R., Sanlaville, P., 1979. Le Quaternaire rcent de Jerba et de la presqu $\hat{i}$le de Zarzis, *Rev. Tunis. Gogr.* 3, 43-69.

Paskoff, R. and Sanlaville, P., 1983. Les Cotes de la Tunisie. Variations du Niveau Marin depuis le Tyrrhnien, *Maison del Orient Mediterraneen*, Lyon, pp.192.

Paulson, A., Zhong, S., Wahr, J., 2007. Inference of mantle viscosity from GRACE and relative sea level data, *J. Geophys. Int.* , 171, 497–508, doi: 10.1111/j.1365-246X.2007.03556.x.

Peltier, W. R., Drummond, R. A., Tushingham, A. M., 1986. Post–glacial rebound and transient lower mantle rheology, *Geoph. J. Royal Astr. Soc.*, 87, 79–116.

Peltier WR. 1999. Global sea level rise and glacial isostatic adjustment, *Global Planet. Change* , 20, 93-123

Peltier W. R., 2004. Global glacial isostasy and the surface of the Ice–Age Earth: the ICE–5G(VM2) model and GRACE, *Annu. Rev. Earth Pl. Sc.* 32, 111–149.

Peltier W. R., 2005. On the hemispheric origins of meltwater pulse 1a, *Quat. Sci. Rew* 24, 1655-1671.

Peltier, W.R. and Fairbanks, R.G., 2006. Global glacial ice volume and Last Glacial Maximum duration from an extended Barbados sea level record, *Quaternary Sci. Rev.* , 25, 3322–3337.

Peltier, W., R., Shennan, I., Drummond, R., Horton, B., 2002. On the postglacial isostatic adjustment of the British Isles and the shallow viscoelastic structure of the Earth, *J. Geophys. Int.* , 148, 3 443-475.

Pena, S. A. and Abdelsalam M. G., 2006. Orbital remote sensing for geological mapping in southern Tunisia: Implication for oil and gas exploration, *J. African Earth Sci.*, 44, 203-219.

Pirazzoli P. A., 1976a. Sea Level Variations in the northwest Mediterranean during Roman Times, *Science* 194, 519-521.

Pirazzoli, P. A., 1991. World atlas of Holocene sealevel changes, Elsevier, Amsterdam, 300 pp.

Pirazzoli, P.A., 2005. A review of possible eustatic, isostatic and tectonic contributions in eight late-Holocene relative sea-level histories from the Mediterranean area, *Quaternary Sci. Rev.* , 24, 1989-2001.

Pirazzoli P.A., Tomasin A., 2008. Return time of extreme sea levels in the central Mediterranean area, *Bollettino Geofisico* 31, 1–4, 19-33.

Pollitz, F. F., 2003. Transient rheology of the uppermost mantle beneath the Mojave Desert, California, *Earth Planet. Sc. Lett.* , 215, 89–104.

Post, E. L., 1930. *Generalized differentiation*, Transactions of the American Mathematical Society 32, 723–781.

Pritchard H.D., Arthern R.J., Vaughan D.G., Edwards L. A., 2009. Extensive dynamic thinning on the margins of the Greenland and Antarctic ice sheets, *nature* , 461, 971-974.

Profumo M.C., 2008. Archeologia della costa: la situazione marchigiana, by Terre di mare. Larcheologia dei paesaggi costieri e le variazioni climatiche (Trieste, 8-10 novembre 2007). *Atti del Convegno internazionale di Studi*, pp.360-368.

Ranalli, G., 1995. Rheology of the Earth, Chapman and Hall, London, 413 pp.

Ranalli, G., Murphy, D., 1987. Rheological stratification of the lithosphere, *Tectonophysics* 132, 281–295.

Ramillien, G., Lombard, A., Cazenave, A., Ivins, E. R., Llubes, M., Remy, F., Biancale, R., 2006. Interannual variations of the mass balance of the Antarctica and Greenland ice sheets from GRACE, *Global Planet. Change* 53, 198–208, doi:10.1016/j.gloplacha.2006.06.003.

Raymond, C.A., Ivins, E.R., Heflin, M.B., James, T.S., 2004. Quasi-continuous global positioning system measurements of glacial isostatic deformation in the Northern Transantarctic Mountains, *Global Planet. Change* , 42, 295303.

Reeh, N., Bøggild, C. E., Oerter, H., 1994. Surge of Storstrømmen, a large outlet glacier from the inland ice of north–east Greenland, *Rapp. Grønl. Geol. Unders.,*, 162, 201–209.

Reigber, Ch., Jochmann, H., Wnsch, J., Petrovic, S., Schwintzer, P., Barthelmes, F., Neumayer, K.-H., Knig, R., Frste, Ch., Balmino, G., Biancale, R., Lemoine, J.-M., Loyer, S., Perosanz, F., 2004. Earth Gravity Field and Seasonal Variability from CHAMP, in *Earth Observation with CHAMP– Results from Three Years in Orbit*, eds Ch. Reigber, H. Lhr, P. Schwintzer and J. Wickert, Springer, Berlin.

Ricard, Y., Sabadini, R., Spada, G., 1992. Isostatic deformations and polar wander induced by redistribution of mass within the Earth, J. Geophys. Res.97, (B10), 14,223–14,236.

Rignot, E., 2011. Is Antarctica melting?, *WIREs Climate Change*, 2, John Wi ley & Sons, Ltd. doi: 10.1002/wcc.110

Rignot, E., and Kanagaratnam, P., 2006. Changes in the velocity structure of the Greenland ice sheet, *Science* 311, 986–989.

Rignot, E., Bamber, J. L., van der Broeke, M. R., Davis, C., Li, Y., van der Berg, W. J., Meijgaard, E. V., 2008a. Recent Antarctic ice mass loss from radar interferometry and regional climate modelling, *Nature Geosci.*, doi:10.1038/ngeo102.

Rignot, E., Box, J. E., Burgess, E., Hanna, E., 2008b. Mass balance of the Greenland ice sheet from 1958 to 2007, Geophys. Res. Lett.35, L20502, doi:10.1029/2008GL035417.

Riva, R. E. M., Gunter B., C., Urban T., Vermeersen B. L.A., Lindenbergh R. C., Helsen M. M., Bamber J.L., Roderik S.W. van de Wal R. S. W., van den Broeke M. R., Schutz B., E., 2009. Glacial Isostatic Adjustment over Antarctica from combined ICESat and GRACE satellite data, *Earth Planet. Sc. Lett.* , 288, 516-523.

Riva, R. E. M., Bamber, J. L., Lavallee, D. A., Wouters, B., 2010. Sea–level fingerprint of continental water and ice mass change from GRACE, Geophys. Res. Lett.37, L19605, doi:10.1029/2010GL044770.

Rümpker, G., Wolf, D., 1996. Viscoelastic relaxation of a Burgers half-space: implications for the interpretation of the Fennoscandia uplift, *J. Geophys. Int.* , 124, 541–555.

Sabadini and Maier-Reimer, 2002 Gravity & Sea Level, *University College London*, http://esamultimedia.esa.int.

Sabadini, R., Yuen, D. A., Gasperini, P., 1988. Mantle rheology and satellite signatures from present-day glacial forcings, J. Geophys. Res., 93 (B1), 437–447.

Sammari, C., Koutitonsky, V., G., Moussa, M., 2006 Sea-level variability and tidal resonancein the Gulf of Gabes, Tunisia, *Cont. Shelf. Res.*, 26, 338-350. doi:10.1016/j.csr.2005.11.006.

Santini, S., Saggese, F., Megna, A., Mazzioni, S., 2011. A note on central-northern Marche seismicity: new focal mechanisms for events recorded in years 2003-2009, *Boll. Geof. Teor. Appl.* , 52. 1-11. doi: 10.4430/bgta0025.

Schmiedt G., 1972. Il livello antico del mar Tirreno. Testimonianze da resti archeologici, *E. Olschki, Florence* 323 p.

Schotman, H., 2008. *Shallow-Earth Rheology from Glacial Isostasy and Satellite Gravity - a sensitivity analysis for GOCE*, Thesis, Technische Universiteit Delft, 188 pp.

Schotman, H. H. A., Vermeersen, L. L. A., Wu, P., Drury, M. R., de Bresser, J. H. P, 2009. Constraints on shallow low-viscosity zones in Northern Europe from future GOCE gravity data, J. Geophys. Res., 178, 65–84, doi: 10.1111/j.1365-246X.2009.04160.x.

Schrama, E., Wouters, B., Vermeersen, B., 2011. Revisiting Greenland ice sheet mass loss observed by GRACE, J. Geophys. Res., 116, B02407, doi:10.1029/2009JB006847.

Schrama, E., Wouters, B., Vermeersen, B., 2011. Present day regional mass loss in Greenland observed with satellite gravimetry, *Surv. Geophys.*, doi:10.1007/s.10712-011-9113-7.

Schubert, G., Turcotte, D. L., Olson, P., 2001. *Mantle convection in the earth and planets*, Cambridge University Press.

Sheperd, A., Wingham, D., 2007. Recent Sea-Level Contributions of the Antarctic and Greenland Ice Sheets, *Science* 315, 1529–1532, doi:10.1126/science.1136776.

Shida, T., Matsuyama, M., 1912. Change of the plumb line referred to the axis of the Earth as found from the results of the internazional latitude observations, *Mem. College Sci. Engin. Kyoto Imperial University*, 4, 277–284.

Shum, C., K., Kuo C., Guo, J., 2008 Role of Antarctic ice mass balance in present-day sea-level change, *Polar Science*, 2, 149-161.

Simon, K. M, James, T. , Ivins, E. R., 2010 Ocean loading effects on the prediction of Antarctic glacial isostatic uplift and gravity rates, *J. Geod.*, 84, 305317, DOI 10.1007/s00190-010-0368-4.

Sivan, D., Lambeck, K., Touega, R., Rabana, A., Porathc, Y., Shirman, B., 2011. Ancient coastal wells of Caesarea Maritima, Israel, an indicator for relative sea level

changes during the last 2000 years *Earth and Planetary Science Letters* 222, 315 330, doi:10.1016/j.epsl.2004.02.007

Slobbe, D., Ditmar, P., Lindenbergh, R., 2009. Estimating the rates of mass change, ice volume change and snow volume change in Greenland from ICESat and GRACE data, *J. Geophys. Int.* 176, 95-106, doi:10.1111/j.1365-246X.2008.03978.x, 2009.

Smith, D. M., 1989. Efficient multiple–precision evaluation of elementary functions, *Math. Comput.*, 52, 131–134.

Solomon, S., Qin, D., Manning, M., Marquis, M., Averyt, K, Tignor, M. M. B., Miller, H. L., Chen, Z., 2007. *Climate Change 2007: the Physical Science Basis*, Cambridge University, Press.

Sørensen, L. S., 2010. Changes of the Greenland ice sheet derived from ICESat and GRACE data, *Ph. D. Thesis*, University of Copenhagen, 90 pp.

Sørensen, L. S., Simonsen, S. B., Nielsen, K., Lucas–Picher, P., Spada, G., Adalgeirsdottir, G., Forsberg, R., and Hvidberg, C. S., 2011. Mass balance of the Greenland ice sheet – a study of ICESat data, surface density and firn compaction modelling, *The Cryosphere* 5, 173–186, doi:10.5194/tc-5-173-2011.

Spada, G., Sabadini, R., Yuen, D. A., Ricard, Y., 1992. Effects on post-glacial rebound from the hard rheology in the transition zone, *J. Geophys. Int.* , 109 (2), 683-700. doi: 10.1111/j.1365-246X.1992.tb00125.x.

Spada, G., 2003. *The theory behind TABOO - a posT glAcial reBOund calculatOr*, Samizdat Press, Golden, White River Junction, pp. 109 (http://samizdat.mines.edu/).

Spada, G., Boschi, L., 2006. Using the Post–Widder formula to compute the Earth's viscoelastic Love numbers, *J. Geophys. Int.* , 166, 309–321. doi:10.1111/j.1365-246X.2006.02995.x.

Spada G. and Stocchi, P., 2006. The Sea Level Equation, Theory and Numerical Examples, *ISBN: 88-548-0384-7* 96 pp., Aracne, Roma.

Spada, G., Antonioli, A., Cianetti, S., Giunchi, C., 2006. Glacial isostatic adjustment and relative sea–level changes: the role of lithospheric and upper mantle heterogeneities in a 3–D spherical Earth, *J. Geophys. Int.* **165** (2), 692–702. doi: 10.1111/j.1365-246X.2006.02969.x.

Spada, G., Stocchi, P., 2007. SELEN: a Fortran 90 program for solving the "Sea Level Equation", *Comput. Geosci.,* 33, 4, 538–562. doi: 10.1016/j.cageo.2006.08.006.

Spada, G., 2008. ALMA, a Fortran program for computing the visco–elastic Love numbers of a spherically symmetric planet, *Comput. Geosci.,* 34,6, 667-687, doi: 0.1016/j.cageo.2007.12.001.

Spada, G., Colleoni, F., Ruggieri, G., 2011a. Shallow upper mantle rheology and secular ice–sheets fluctuations, *Tectonophysics* doi:10.1016/j.tecto.2009.12.020.

Spada, G., Barletta, V. R., Klemann, V., Riva, R. E. M., Martinec, Z., Gasperini, P., Lund, B., Wolf, D., Vermeersen, L. L. A., King, M., 2011b. A benchmark study for glacial–isostatic adjustment codes, **185**, 106–132, doi: 10.1111/j.1365-246X.2011.04952.x. *J. Geophys. Int.*

Spada, Ruggieri, G., Sørensen, S. L., Nielsen, K., Melini, D., Colleoni, F. (subm.) Greenland uplift and regional sea–level changes from ICESat observations and GIA modeling, *J. Geophys. Int.*

Steffen, H. and Kaufmann, G., 2005. Glacial isostatic adjustment of Scandinavia and northwestern Europe and the radial viscosity structure of the Earths mantle, J. Geophys. Res., 163, 801-802.

Steffen, H. and Wu, P., 2011. Glacial isostatic adjustment of Scandinavia – A review of data and modeling, *J. Geodesy* , 52, 169-204.

Stein, S. and Wysession, M., 2003. *Introduction to Seismology, Earthquakes, and Earth Structure*, Blackwell Publishing, Oxford.

Stocchi, P., Colleoni, F., Spada, G., 2009. Bounds on the timehistory and Holocene mass budget of Antarctica from sealevel records in SE Tunisia, *PAGEOPH*

Stocchi, P., and Spada, G., 2007. Postglacial sealevel in the Mediterranean Sea: Clarks zones and role of remote ice sheets, *Ann. Geophys.*, 50, 6, 741-761.

Stocchi, P., Spada, G., Cianetti, S., 2005. Isostatic rebound following the Alpine deglaciation: impact on sea–level variations and vertical movements in the Mediterranean region, *J. Geophys. Int.* 162, 137–147. doi:10.1111/ j.1365-246X.2005.02653.x.

Stocchi, P., Spada, G., 2009. Influence of glacial isostatic adjustment upon current sea–level variations in the Mediterranean, *Tectonophysics* doi:10.1016/j.tecto.2009.01.003.

Strasser D., Davoud E., Jeduoi Y. (1989). Carbonate Cements in Holocene beachrock: example from Bairet El Biban southeastern Tunisia, *Sed. Geol.*, 62 , 89–100.

Stewart, R.H., 1985. *Methods of Satellite Oceanography*, University of California Press, Berkeley, CA, 360 pp.

Stuiver, M., Reimer, P. J., and Reimer, R. W., 2005. CALIB 6.0, *www.calib.qub.ac.uk/calib*

Suess, E., 1906. *Face of the Earth*, Clarendon Press, Oxford.

Svendsen, J. I., Astakhov, V. I., Bolshiyanov, D. Y., Demidov, I., Dowdeswell, J. A., Gataullin, V., Hjort, C., Hubberten, H. W., Larsen, E., Mangerud, J., Melles, M., Moller, P., Saarnisto, M., Siegert, M. J., 1999. Maximum extent of the Eurasian ice sheets in the Barents and Kara Sea region during the Weichselian, *Boreas*, 28, 1, 234-242.

Tapley, B., Bettadpur, S., Watkins, M., Reigber, C., 2004. The gravity recovery and climate experiment: Mission overview and early results, Geophys. Res. Lett., 31, 9, L09607.

Tarasov L. and Peltier, W. R., 2002. Greenland glacial history and local geodynamic consequences, *J. Geophys. Int.* , 150, 198–229.

Tegmark M., 1996. An icosahedron–based method for pixelizing the celestial sphere, *ApJ Letters*, 470, 81-84.

Thomas, P. J., 2009. Luminescence Dating of Beachrock in the Southeast Coast of India–Potential for Holocene Shoreline Reconstruction, *J. Coastal Res.*, 25, 1-7.

Thomas, R., Akins, T., Csatho, B., Fahnestock, M., Gogineni, P., Kim, C. Sonntag, J., 2000. Mass Balance of the Greenland Ice Sheet at High Elevations, *Science* , 289, 426-430.

Thomas, R., King, M, Bently M., J., Whitehouse, P., L.,, J., 2011. Widespread low rates of Antarctic glacial isostatic adjustment revealed by GPS observations, Geophys. Res. Lett., 38, L22302, 1-6.

Toscano, M. A., Peltier, W. R. Drummond, R., 2011 ICE-5G and ICE-6G models of postglacial relative sea-level history applied to the Holocene coral reef record of northeastern St Croix, U.S.V.I.: investigating the influence of rotational feedback on GIA processes at tropical latitudes, *Quaternary Sci. Rev.* , 30, 21, 3032-3042.

Tsimplis, M., Spada, G., Marcos, M., Flemming, N., 2011. Multi–decadal sea–level trends and land movements in the Mediterranean Sea with estimates of factors perturbing tide gauge data and cumulative uncertainties, *Global Planet. Change*, 76, 63-76.

Tuccimei, P., Onac, B. P., Dorale, J. A., Gines J., Fornos J. J., Gines, A., Spada, G., Ruggieri, G., Mucedda, M., 2011, in press. Decoding Last Interglacial sea-??level variations in the Western Mediterranean using speleothem encrustations from coastal caves in Mallorca and Sardinia, *Quaternary Int.* .

Tucker M. E., 1981. *Sedimentary petrology: an Introduction*, Blackwells, Oxford, pp.255.

Tushingham A. M., Peltier, W. R., 1991. ICE-3G–A new global-model of Late Pleistocene deglaciation based upon geophysical predictions of postglacial relative sea-level change, J. Geophys. Res., 96, B3, 4497-4523.

Valko, P. P., Abate, J., 2004. Comparison of sequence accelerators for the Gaver method of numerical Laplace transform method, *Comp. Math. Appl.* 48, 629–636.

van der Wal, W., Schotman, H. H. A., Vermeersen, L. L. A., 2004. Geoid heights due to a crustal low viscosity zone in glacial isostatic adjustment modeling; a sensitivity analysis for GOCE, *Geoph. Res. Lett.*, 31, 10.1029/2003GL019139.

Velicogna, I., and Wahr, J., 2005. Greenland mass balance from GRACE, Geophys. Res. Lett., 32, L18505, doi:10.1029/2005GL023955.

Velicogna, I., Wahr, J., 2006. Acceleration of Greenland ice mass loss in spring 2004, *nature* ,443, 329-331, doi:10.1038/nature05168.

Velicogna, I., Wahr, J., 2006. Measurements of Time-Variable Gravity Show Mass Loss in Antarctica, *Science* 311, 1754. doi: 10.1126/science.1123785

Velicogna, I., 2009. Increasing rates of ice mass loss from the Greenland and Antarctic ice sheets revealed by GRACE, *Geophys. Res. Lett.*, 36, L19503, doi:10.1029/2009GL040222.

Vermeersen, L. L. A., Sabadini, R., 1997. A new class of stratified viscoelastic models by analytical techniques, *J. Geophys. Int.* , 129, 531–570.

Vermeersen, L. L. A., 2003. The potential of GOCE in constraining the structure of the crust and lithosphere from post-glacial rebound, *Space Science Rev.* 108, 105–113.

Visser, P.N.A.M., Rummel, R., Balmino, G., Snkel, H., Johannessen, J., Aguirre, M., Woodworth, P.L., Le Provost, C., Tscherning, C.C., Sabadini, R., 2002. The European Earth explorer mission GOCE: Impact for the geosciences, in: *Ice Sheets, Sea Level and the Dynamic Earth*, AGU Geodynamics Series 29, American Geophysical Union, Washington, DC.

von Grafenstein, U., Erlenkeuser, H., Mller, J., Jouzel, J., Johnsen, S., 1998. The cold event 8200 years ago documented in oxygen isotope records of precipitation in Europe and Greenland, *Climate Dynamics*, 14, 7381, doi: 10.1007/s003820050210.

Vousdoukas, M. I., Velegrakis A. F., Plomaritis T. A., 2007. Beachrock occurrence, characteristics, formation mechanisms and impacts, *Earth Sci. Rev.*, 85, 23–46.

Wahr, J.M., Trupin, A., DaZhong, H., 1995. Predictions of vertical uplift caused by changing polar ice volume, and a method for removing the effects of viscoelastic rebound, Geophys. Res. Lett., 22, 977-980.

Wahr, J., Leuliette, E., van Dam, T., Larson, K. M., Francis, O., 2008. Geodetic measurements of postglacial adjustments in Greenland, J. Geophys. Res.113, B02402, doi:10.1029/2007JB004956.

Wahr, J., van Dam, T., Larson, K. M., Francis. O., 2001, Geodetic measurements in Greenland and their implications, J. Geophys. Res., 106, (B8), 16,567–16,582.

Wahr, J., D. Wingham, C. Bentley. 2000. A method of combining ICESat and GRACE satellite data to constrain Antarctic mass balance, J. Geophys. Res., 105-B7, 279-294.

Wessel, P. and Smith, W. H. F., 1998. New, improved version of generic mapping tools released, *Eos Trans. AGU*, 79, 579.

Whitehouse, P., 2009. *Glacial isostatic adjustment and sea–level change. State of the art report, SKB TR–09–11*, Swedish Nuclear Fuel and Waste Management Organization (SKB), 105 pp.

Widder, D. V., 1934. The inversion of the Laplace integral and the related moment problem, *Transactions of the American Math. Soc. Translations*, 36, 107–200.

Widder, D. V., 1946. *The Laplace Transform*, Princeton University Press, Princeton, NJ, 406 pp.

Wieczerkowski, K., Wolf, D., 1998. Viscoelastic tidal dissipation in planetary models. In: Ducarme, B., Paquet, P. (Eds.), Proceedings of the 13th International Symposium on Earth Tides, *Observatoire Royal de Belgique*, 277–285.

Willis, J. K., Chambers, D. P., Kuo, C., Shum, C. K., 2010 Global Sea Level Rise Recent Progress and Chall enges for the Decade to Come, *Oceanography*, 23, 4, 26-35.

Wingham, D. J., Shepherd, A., Muir, A., Marshall, G.J., 2006. Mass balance of the Antarctic ice sheet, *Phil. Trans. R. Soc. A* 364, 1627-1635, doi:10.1098/rsta.2006.1792

Woodroffe, S.A. and Horton, B.P., 2005. Holocene sea-level changes in the Indo-Pacific, *J. of Asian Earth Sci.* 25, 2943.

Woodroffe, S.A., Horton, B.P., Larcombe.P.E., Whittaker, J.E., 2005. Intertidal mangrove foraminifera from the central Great Barrier Reef shelf, Australia: Implications for sea-level reconstruction, *J. Foram. Res.*, 35, 259-270.

Woodward, R. S., 1888. On the form and position of mean sea level, United States, *Geol. Survey Bull.*, 48, 87-170.

Woodworth PL, Player R. 2003. The permanent service for mean sea level: An update to the 21st century, *J. Coastal Res.*, 19, 287-95.

Woppelmann G., Martin Miguez B., Bouin M.N., Altamimi Z., 2007. Geocentric sea level trend estimates from GPS analyses at relevant tide gauges worldwide, *Global Planet. Change* , 57, 396-406.

Wouters B., Chambers D., Schrama E., 2008. GRACE observes small–scale mass loss in Greenland, Geophys. Res. Lett.L20501, doi:10.1029/2008GL034816.

Wu, P., Ni. Z., 1996. Some analytical solutions for the viscoelastic gravitational relaxation of a two–layer non–self–gravitating incompressible spherical earth, *J. Geophys. Int.* , 126, 413–436.

Wu, P. and Peltier, W. R., 1982. Viscous gravitational relaxation, *Geophys. J. R. astr. Soc.* ,70, 435–486.

Wu, X., Heflin, M. B., Schotman, H., Vermeersen, B. L. A., Dong, D., Gross, R., Ivins, E. R., Moore, A. W., Owen, S., 2010. Simultaneous estimation of global present–day water transport and glacial isostatic adjustment, *Nature Geoscience,* 3, 642–646, doi:10.1038/ngeo938.

Wunsch C., Ponte R. M., Heimbach P., 2007. Decadal trends in sea level patterns: 19932004. *J. Clim.*, 20, 5889, 5911, doi:10.1175/2007JCLI1840.1

Yokoyama, Y., Lambeck, K., De Dekker, P., Johnston, P., Fifield, L. K., 2000. Timing of the Last Glacial Maximum from observed sea-level minima, *nature* , 406, 6797, 713-716.

Yu, Shi-Yong, Bjrn E., Berglund, Sandgren, Per, Colman, Steven M. ,2007. Holocene organic carbon burial rates in the southeastern Swedish Baltic Sea. *The Holocene* 17,5, 673681.

Yuen, D., Peltier, W. R., 1982. Normal modes of the viscoelastic earth, *Geoph. J. Royal Astr. Soc.*, 69, 495–526.

Yuen, D. A., Sabadini, R. C. A., Gasperini, P., Boschi, E., 1986. On transient rheology and glacial isostasy, *geoph. J. Res,*, 91, 11,420–11,438.

Zachos, J., Shackleton, N., Revenaugh, J., Palike, H., Flower, B., 2001. Climate response to orbital forcing across the Oligocenee-Miocene boundary, *Science* 292, 274-278.

Zanutta A., Vittuari L., Gandolfi S., 2008 Geodetic GPS-based analysis of recent crustal motions in Victoria Land (Antarctica), *Global Planet. Change* 62, 115131.

Zoller and Heinrich, 1960 Pollenanalytische Untersuchungen zur Vegetationsgeschichte der insubrischen Schweiz", *Denkschriften der Schweizerischen Naturforschenden Gesellschaft*, 83, 45156. ISSN 0366-970X.

Zuffa G. G., 1979. Hybrid arenites: their composition and classification, *J. Sed. Petrology*, 50, 21–29.

Zwally, H.J., Giovinetto, M.B., Li, J., Cornejo, H., Beckley, M.A., Brenner, A.C., Sabam, J.L., Yi, D., 2005. Mass changes of the greenland and antarctic ice sheets and shelves and contributions to sea-level rise: 19922002, *J. Glac.* 51, 509527.

Zwally, H. J.,Giovinetto, M. B., 2011. Overview and Assessment of Antarctic Ice-Sheet Mass Balance Estimates: 19922009, *Surv. Geophys.*, 32, 351-376 doi: 10.1007/s10712-011-9123-5

Zwally, H. J., Li, J., Brenner, A. C., Beckley, M., Cornejo, H. G., DiMarzio, J., Giovinetto, M. B., Neumann, T., Robbins, J., Saba, J. L., Yi, D., Wang, W., 2011. Greenland ice sheet mass balance: distribution of increased mass loss with climate warming; 2003- 07 versus 1992–2002, *J. Glaciol.,* 57, (201), 88–102.